POLITECNICO DI MILANO

DEPARTMENT OF ENERGY

DOCTORAL PROGRAMME

ENERGY AND NUCLEAR SCIENCE AND TECHNOLOGY

CFD MODELING AND EXPERIMENTAL CHARACTERIZATION OF UREA/WATER SOLUTION INJECTION INSIDE SCR SYSTEMS OF DIESEL ENGINES

Doctoral Dissertation of:

Lorenzo Nocivelli

Supervisor:

Prof. Gianluca Montenegro

Co-supervisor:

Dr. Panayotis Dimopoulos Eggenschwiler

Tutor:

Prof. Angelo Onorati

The Chair of the Doctoral Program:

Prof. Carlo Enrico Bottani

2017 - XXIX Cycle STEN

to my parents

Acknowledgements

I would like to express my gratitude to my supervisor Prof. Gianluca Montenegro for the support and the trust he put in my path in the project development.
I would also like to thank my tutor Prof. Angelo Onorati, who took care of my PhD programme and allowed me to work in the Internal Combustion Engine Group.

Sincere thanks must also go to Dr. Panayotis Dimopoulos Eggenschwiler for the constant supervision during my period at EMPA and to Christian Bach who welcomed me in the Automotive Powertrain Technology department.

Abstract

The present work focuses on the characterization of the low-pressure driven injection applied to the pre-catalytic section of a Selective Catalytic Reduction system for vehicle applications.
Phase Doppler Anemometry represents the main technique to assess the spray kinematic features in cross-flow conditions in a very confined environment. The experiments are mostly carried out in a test bench able to reproduce Diesel engine exhaust after-treatment operating conditions, providing size and velocity distributions of the droplets generated by two different commercially available injectors.
The data are used, coupled with qualitative Shadow Imaging visualizations of the sprays, to initialize a numerical injection model for each nozzle, to be included in a Lagrangian-Eulerian framework handled with the open-source platform OpenFOAM®. The CFD simulation is validated on the near-nozzle behavior in quiescent air and on the data collected close to the primary impingement surface in cross-flow conditions.
A conspicuous fraction of the liquid mass impacts the surface and its quantification is carried out with a mechanical patternator, producing spatially resolved mass distributions and showing that the entrainment in cross-flow is always less than the $50\,\%$ of the injected mass. The simulation is used to estimate the intrusiveness of the instrument in the system, and then it is compared to the mass flux data, highlighting the improvement produced by the *fixed number of droplets per parcel* approach in the definition of the dispersed phase.
A literature based spray-wall interaction model is implemented in the CFD code, introducing a thermal threshold on the interaction regime identification and the conductive heat transfer between spray and walls, which are solved in their thermal transients.
The direct interaction of the droplets with the solid surfaces is identified as the paramount term in the walls energy balance, and is represented with synthetic impingement maps. On the other hand the impact on the walls is found to be the only source of break-up for the primary droplets, which are not deflected by the flow.

Keywords SCR, CFD, PDA, Low-pressure injection, Spray-wall interaction

Riassunto

Il lavoro proposto pone l'attenzione sulla caratterizzazione dell'iniezione a bassa pressione utilizzata nella sezione pre-catalitica di un sistema per la riduzione di ossidi d'azoto (Selective Catalytic Reduction) applicato a veicoli.
La Phase Doppler Anemometry rappresenta il principale strumento per la valutazione delle proprietà cinematiche di uno spray in condizioni operative realistiche. La dimensione e la velocità delle gocce iniettate da due diversi iniettori è misurata principalmente attraverso l'uso di un banco prova in grado di riprodurre le condizioni termo-fluidodinamiche di un sistema di rimozione inquinanti.
I dati sono utilizzati, in accoppiamento con la visualizzazione della morfologia dello spray attraverso Shadow Imaging, per inizializzare i modelli di iniezione da inserire in simulazioni CFD con approccio Lagrangiano-Euleriano realizzate con il software open-source OpenFOAM®. I risultati numerici sono validati sulla base di dati raccolti rispettivamente nella regione d'iniezione e vicino alla superficie solida di impatto dello spray.
La cospicua frazione di massa liquida che interagisce con le pareti del sistema è quantificata attraverso un patternator meccanico in grado di produrne una distribuzione spaziale. Le misure mostrano che più' della metà del liquido iniettato impatta con la parete solida del sistema, in qualsiasi condizione di flusso gassoso. Le simulazioni fluidodinamiche sono usate per valutare l'intrusività dello strumento nel sistema e successivamente sono comparate ai risultati di flusso di massa liquida, sottolineando come l'assegnazione di un numero costante di gocce ad ogni parcel computazionale migliori la rappresentazione dello spray.
Un modello di interazione spray-parete basato su dati di letteratura è stato implementato nel codice, introducendo una soglia termica nell'identificazione del regime di impatto e risolvendo lo scambio termico con le superfici del sistema.
L'interazione termica diretta tra gocce e solido è identificata come il termine principale nel bilancio termico delle pareti solide, ed è rappresentata con mappe di impatto che sintetizzano il fenomeno. Dal punto di vista dello spray, l'interazione con le pareti rappresenta l'unica sorgente di break-up delle gocce primarie, che non riescono a essere deviate dal flusso gassoso.

Keywords SCR, CFD, PDA, Iniezione a bassa pressione, Interazione spray-parete

Contents

List of Figures

List of Tables

Nomenclature

Abbreviations and Acronyms

3H	Three hole injector
6H	Six hole injector
Ca	Capillarity Number
K	Kinematic (Mundo) Number
La	Laplace Number
Nu	Nusselt Number
Oh	Ohnesorge Number
Pr	Prandtl Number
Re	Reynolds Number
Sc	Schmidt Number
Sh	Sherwood Number
We	Weber Number
ASC	Ammonia Slip Catalyst
CFD	Computational Fluid Dynamics
CHT	Conjugate Heat Transfer
DDM	Discrete Droplet Model
DL	Diffusion Limit
DOC	Diesel Oxidation Catalyst
DOI	Duration Of Injection
DR	Data Rate
ED	Effective Diffusion
HCs	Hydrocarbons
L-E	Lagrangian-Eulerian
LIR	Local Impingement Rate
NEDC	New European Driving Cycle
NO_x	Nitrogen Oxides
PDA	Phase Doppler Anemometry
PM	Particulate Matter
RANS	Reynolds Averaged Navier-Stokes
RM	Rapid Mixing
RNG	Re-Normalization Group
ROI	Region Of Interest
RR	Rosin-Rammler distribution
RSF	Relative Span Factor
RSM	Reynolds Stress Model
SCR	Selective Catalytic Reduction
SI	Shadow Imaging
SMD	Sauter Mean Diameter
SOI	Start Of Injection
UWS	Urea Water Solution

Greek symbols

β	Ejection/cone aperture angle
χ	Blending factor
δ	Rosin-Rammler scale parameter
Γ	Diffusion coefficient
γ	Size ratio
λ	Thermal Conductivity

μ	Viscosity
ν	Mass fraction
ϕ	Generic conserved variable
ψ	Deviation angle
ρ	Density
σ	Surface tension
τ	Viscous stress
ε	Turbulent kinetic energy dissipation rate
ζ	Normalized velocity scale

Latin Symbols

$\dot{y}$	Oscillation velocity
A	Area
B	Spalding number
C	General model coefficient
c_p	Specific heat
d	Diameter
h	Enthalpy
k	Turbulent kinetic energy
L	Injector channel length
m	Mass
n	Rosin-Rammler shape parameter
p	Pressure
Q	Thermal energy
r	Droplet radius
S	Generic source terms
T	Temperature
t	Time
W	Molar weight
Y	Mass fraction
F	Force
U	Velocity

Subscripts and Superscripts

$*$	Dimensionless
0	Initial/primary
∞	Far-field
$cell$	Computational cell
con	Contact
D	Drag
$drop$	Droplet
dyn	Dynamic component
$evap$	Evaporation
$face$	Computational face
$flow$	Average gas flow
gas	Gaseous phase
inj	Injection
L	Lift
mix	Multicomponent mixture
$nozzle$	Nozzle hole
rel	Liquid-Gas relative
s	Surface
sat	Saturation
sp	Spray
$turb$	Turbulent component
v	Volume
vap	Vapor
w	Wall

CHAPTER 1

Introduction

Selective Catalytic Reduction for automotive applications

Nitrogen Oxides (NO_x) production is a characteristic feature of the technologies involving air temperatures higher than 1500° C, like combustion and engines [61]. NO represents the prevalent specie generated from engines and the majority of the emitted flux oxidizes to NO_2 in the atmosphere. NO_2 is reactive with hydrocarbons to form ozone, which, if present in high concentrations, significantly deteriorates the air quality in urban environments. Moreover high NO_x concentrations in urban areas, which is related for more than the 40 % to vehicle emissions, has a toxic potential for humans, contributing to respiratory diseases [28].

For the current Diesel engines, the efficiency improvement resulting from lean combustion conditions and high in-cylinder temperatures is in trade-off with an excessive production of NO_x [37]. Moreover the reduction of particulate matter (PM) can be obtained improving the uniformity of the fuel-air mixture and the combustion efficiency,

creating conflicting requirements for the fulfillment of the overall regulation limits [38], as shown in Fig. 1.1.

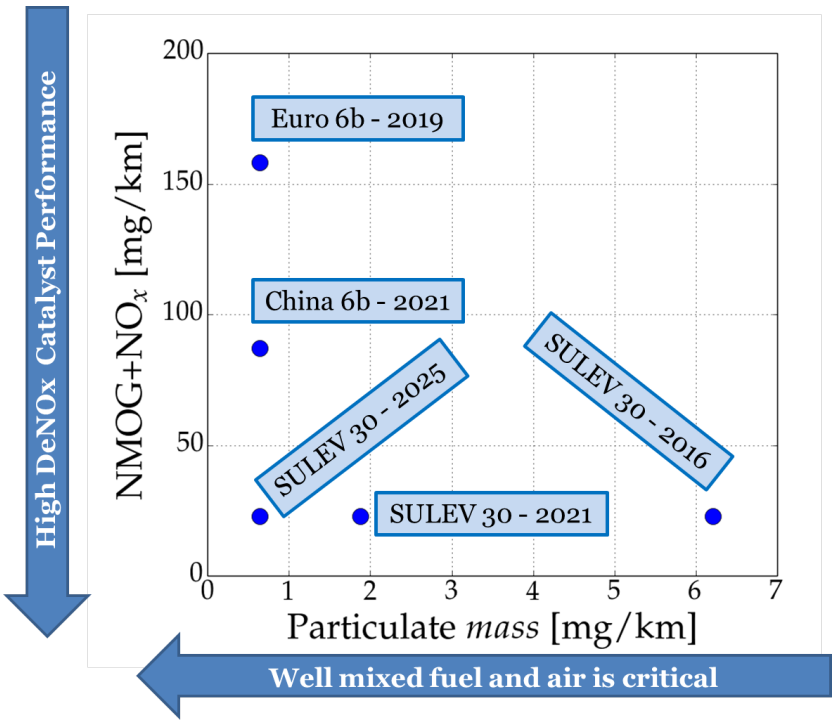

Figure 1.1: *Emission regulation comparison (adapted from [38]).*

Within this framework the tailpipe emission reduction becomes one of the leading approaches to control the emissions and to reduce the fuel consumption.

The three way catalyst represents the most effective NO_x reduction system for spark ignition engines and requires the absence of oxygen, allowing the reduction of NO_x by unburnt CO and HCs on rhodium active sites. Unfortunately, this technology is not applicable to lean-burn Diesel engines, since the large fraction of oxygen out of the combustion process provides an oxidant source for the unburnt hydrocarbons and adsorbs on Rhodium active sites saturating them, excluding the NO_x from the reaction scheme.

In this scenario a Selective Catalytic Reduction (SCR) of nitrogen oxides using ammonia (NH_3) as a reductant, which is a robust technology commercialized for decades in the stationary sector and capable of providing high selectivity and efficiency across a substantial temperature range [83], becomes an interesting solution to the NO_x emis-

sion control.

The key SCR reactions, catalyzed on Vanadia, copper zeolite or iron zeolite [100], are the following:

$$NH_3 + NO + \frac{1}{4}O_2 \rightarrow N_2 + \frac{3}{2}H_2O \qquad \text{standard SCR} \tag{1.1}$$

$$NH_3 + \frac{1}{2}NO + \frac{1}{2}NO_2 \rightarrow N_2 + \frac{3}{2}H_2O \quad \text{fast SCR} \tag{1.2}$$

$$NH_3 + \frac{3}{4}NO_2 \rightarrow \frac{7}{8}N_2 + \frac{3}{2}H_2O \tag{1.3}$$

Reaction (1.1) involves only NO and is always present, but is slower than (1.2) which requires NO_2. For this reason the usual configuration of an exhaust after-treatment system [16], (depicted in Fig. 1.2) includes a Diesel Oxidation Catalyst (DOC) before the SCR section to oxidize a fraction of the NO with the excess oxygen (1.4).

$$NO + \frac{1}{2}O_2 \rightarrow NO_2 \tag{1.4}$$

This process needs to be well designed, because if an NO_2/NO ratio higher than one is produced by the DOC, the excess of NO_2 can yield to a strong greenhouse gas, N_2O, production through (1.5):

$$NH_3 + NO_2 \rightarrow \frac{1}{2}N_2 + \frac{1}{2}N_2O + \frac{3}{2}H_2O \tag{1.5}$$

To avoid the toxic ammonia slip produced by unbalanced feed or insufficient gaseous mixing an Ammonia Slip Catalyst (ASC) is put at the end of the tailpipe, providing the reaction (1.6):

$$NH_3 + \frac{3}{4}O_2 \rightarrow \frac{1}{2}N_2 + \frac{3}{2}H_2O \tag{1.6}$$

In mobile applications, since the ammonia is toxic and flammable, the SCR technology is based on the injection of Urea Water Solution (UWS). The liquid mixture, 32.5 $\%$ w/w of urea in distilled water, corresponds to the eutectic composition providing the minimum freezing point (-11°) and represents a safe and stable ammonia carrier. The urea based system introduces an injection unit, located before the SCR catalyst as in Fig. 1.2, which involves a tank and a low-pressure dosing unit.

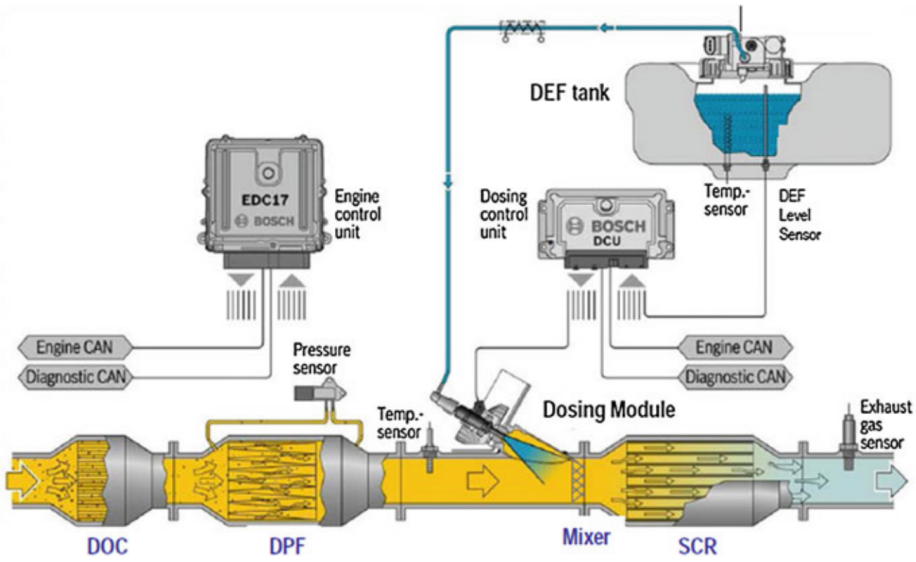

Figure 1.2: *Common layout of a Diesel engine tailpipe system [16].*

The ammonia feed preparation process is defined by the evaporation of the mixture and the thermolysis of the urea into ammonia and isocyanic acid [79] (1.7):

$$(NH_2)_2 CO \rightarrow NH_3 + HCNO \tag{1.7}$$

In presence of water vapor, the isocyanic acid reacts, generating another mole of ammonia (hydrolysis) (1.8).

$$HNCO + H_2O \rightarrow NH_3 + CO_2. \tag{1.8}$$

Static mixers represent the most common tool to enhance the reacting mixture spatial uniformity [18, 67] at the catalyst inlet, which has been found poor and independent on the exhaust cross flow magnitude for low pressure-driven UWS sprays [86]. Since a vigorous conversion of the urea has been found to be active only above 150° C [13,103] and the catalyst light-off temperature is set at 200° C [30], the New European Driving Cycle (NEDC) (Fig. 1.3) for passenger cars does not provide satisfactory thermal conditions in a significant fraction of its extension. The graph reported in Fig. 1.3, proposed by [30] on the basis of the data provided by [75] reports the exhaust temperature evolution at the UWS system key points (injection and catalyst inlet), underlining the

need of a fast heat-up of the system, as well as an extension of the mixture preparation to low temperature, through the increment of the residence time and the mixing efficiency. The design of a fast and uniform mixture feed to the catalyst needs to take

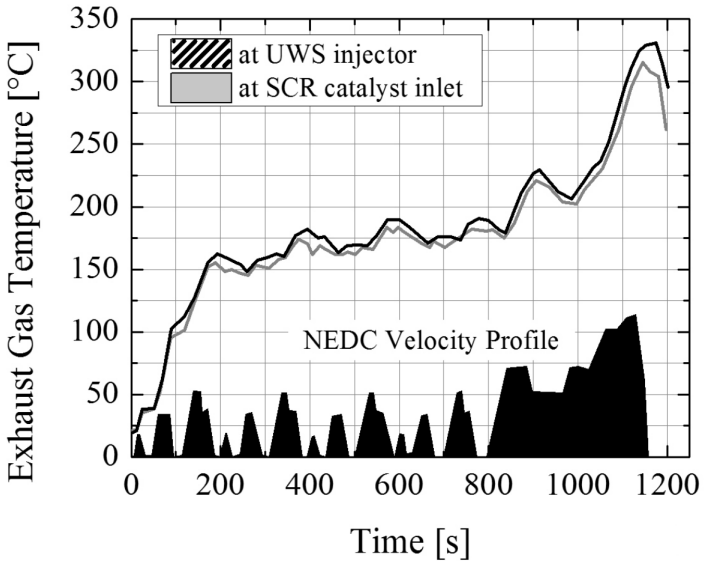

Figure 1.3: *New European Driving Cycle temperature transient [30, 75].*

into account the interaction with the gas flow and its solid boundaries (pipe walls and mixers) over a wide range of time scales, as sketched in Fig. 1.4.

The most critical issue is represented by an excessive spray-wall interaction which may lead to the deposition of a fraction of the injected solution and, in the worst case, to permanent solid by-product formation, as shown in Fig.1.5. These unwanted deposits can generate an alteration of the fluid dynamics of the system, a back pressure increase and eventually the deterioration of the system components [110].

A correct description of the UWS spray is the key point for a sufficient ammonia mixture preparation strategy, allowing an efficient operation of the system and its coupling with the engine over a wide range of load conditions.

Objective, approach and structure of the thesis

The objective of this work is the characterization of the pre-catalytic section of an urea based SCR system for automotive applications. The focus is put on the experimental investigation of commercially available pressure-driven injector behaviors in a confined

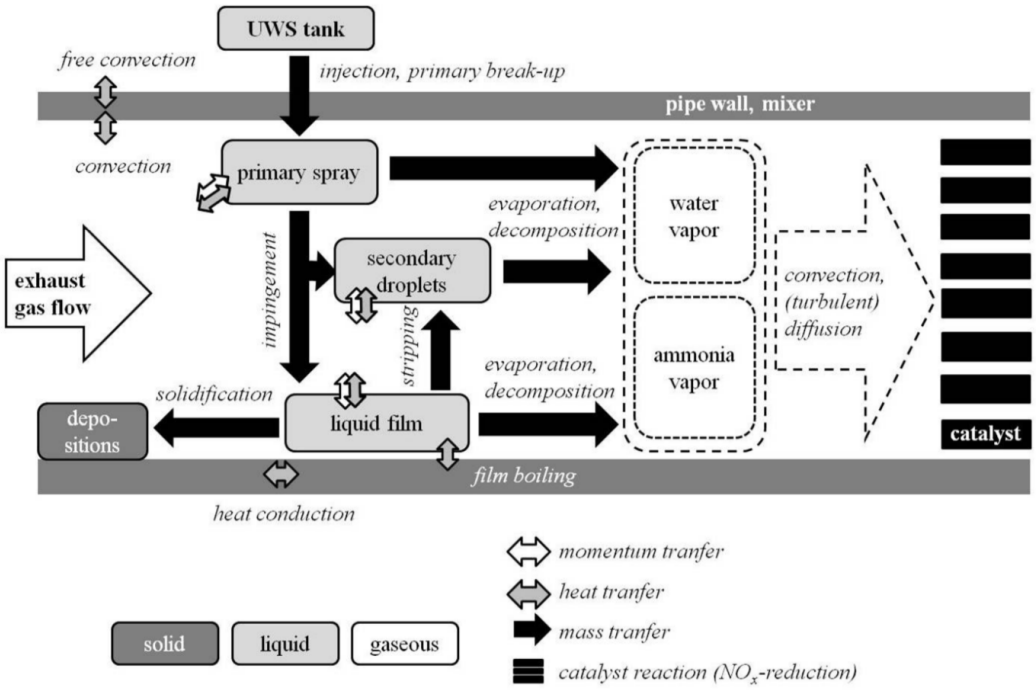

Figure 1.4: *Processes involved in the dosing module of an urea based SCR system [30].*

environment across the engine operating conditions and the definition of numerical models to be included in a Computational Fluid Dynamic platform. Major attention is put on the validation of the simulation results and the construction of a low computational cost tool able to represent the relevant thermo-kinematic phenomena in a full size test case. The experimental activity is based on optical techniques to characterize the spray evolution in cross flow conditions: Phase Doppler Anemometry (PDA) and Shadow Imaging (SI) represent the main activity, which has been carried out at Empa laboratories[1]. The simulation activity is completely covered by the open-source 3D finite volume software OpenFOAM® which has been extended and developed to handle the phenomena involved in the system. The core of the numerical campaign involves a Lagrangian description of the dispersed phase representing the spray, coupled with a finite volume Eulerian approach for the gaseous and solid phases, within the Unsteady Reynolds Averaged Navier Stokes (URANS) turbulence description framework. The thesis follows the path of the UWS solution in the system and can be summarized in three key points:

[1] Swiss Federal Laboratories for Materials Science and Technology, Dübendorf, Switzerland

Figure 1.5: *Urea by-product deposits on a static mixer [62].*

- characterization of the injection and the spray interaction with gaseous atmosphere. The behavior of two commercially available injectors is measured for distilled water and AdBlue® in quiescent air at the closest accessible location. The collected data are used to characterize and validate a robust and reliable numerical injection model. Then the injectors are installed on an engine-less test bench which reproduces exhaust after-treatment operating conditions, and the spray properties are assessed through PDA and coupled with previously collected Shadow Imaging data. The test-rig is reproduced with the simulation, validating the code behavior with relevant spray-cross flow interaction;

- assessment of the spray near-wall behavior. The spray path towards the catalyst is retraced by the experimental and numerical activities, including the spray interaction with the wall. The numerical simulation of the whole test-rig provides an assessment of the performance of a newly developed mechanical patternator able to sample the spray mass flow directed to the system walls. The measured mass flux on the wall is then numerically reproduced and a new spray impingement model describing both the kinematic and the thermal interaction model is implemented and tested, including the simulation of the thermal transients of the solid walls;

- evaluation of full-size system characteristics at engine operating conditions. The developed and validated simulation tool is applied to the experimental test rig to estimate the realistic behavior of a complete injection pulse to the catalyst inlet and to point out the strengths and the drawbacks of the low-pressure driven injection to prepare an uniform reactive gaseous mixture.

CHAPTER 2

Fundamentals of SCR injection

Low pressure-driven injection represents the commercial standard for Selective Catalytic Reduction applications and it has been the focus of experimental and numerical research activities in the recent past [8, 12, 13, 15, 45, 46, 77, 84–86, 91, 95].
In this chapter a critical analysis of the phenomena and their handling in literature is provided to build the basis for the simulation campaign of this work.

2.1 Numerical framework

The numerical activity in this thesis is carried out through Computational Fluid Dynamics (CFD), which indicates the numerical solution of multidimensional flow problems [88]. The pre-catalytic section of an SCR system is governed by conservation principles for mass, momentum, energy and species representable with a set of partial differential equations in terms of time and space which can be integrated numerically.

2.1.1 Transport equations for the gas phase

The finite volume approach [97] is chosen for the discretization and the solution of the equations and it is handled by the open-source platform OpenFOAM®. The differential form of a conservation equation can be expressed as (2.1), where ϕ represents a generic conserved variable, **U** the velocity, Γ the diffusion coefficient and S_ϕ the source term [97].

$$\frac{\partial (\rho \phi)}{\partial t} + \bigtriangledown \cdot (\rho \phi \boldsymbol{U}) = \bigtriangledown \cdot (\Gamma \bigtriangledown \phi) + S_\phi \tag{2.1}$$

It is usually called the *transport equation* of ϕ and it is composed of:

- rate of increase of ϕ of fluid element - rate of change;
- net rate of flow of ϕ out of fluid element - convective term;
- rate of increase of ϕ due to diffusion - diffusive term;
- rate of increase of ϕ due to sources - source term.

and setting ϕ equal to 1, U_i, h (enthalpy), Y_i (mass fraction of the i^{th} specie) results in the conservation of mass, i^{th} component of the momentum, energy and i^{th} specie.
The diffusion coefficient Γ for the momentum equation is a result of the Newtonian assumption applied to the fluid. In fact the governing equation development leads to the introduction of the viscous stresses τ_{ij} to take into account the forces balance on the boundaries of an arbitrary control volume. In many fluid flows the viscous stresses can be expressed as functions of of the local deformation rate, which is composed of the linear deformation component and the volumetric deformation component in 3D problems.
The volumetric deformation is given by the three linear elongating deformation components (2.2)

$$\frac{\partial U_x}{\partial x} + \frac{\partial U_y}{\partial y} + \frac{\partial U_z}{\partial z} = \bigtriangledown \cdot \boldsymbol{U} \tag{2.2}$$

and the viscous stresses are proportional to the rates of deformation. For compressible flows, two constants of proportionality (viscosities) are introduced: μ to relate the stresses to the linear deformation and λ, usually considered equal to $-3/2\,\mu$, for the volumetric components.

$$\begin{aligned} \tau_{ii} &= 2\mu \frac{\partial U_i}{\partial x_i} \\ \tau_{ij} &= \tau_{ji} = \mu \left(\frac{\partial U_i}{\partial x_j} + \frac{\partial U_j}{\partial x_i} \right) \end{aligned} \tag{2.3}$$

For the energy conservation, the shear stresses can be rearranged to define a volumetric dissipation function which acts as a source term.

The integration of (2.1) over a three dimensional volume V constitutes the key step of a finite volume method (2.4)

$$\int_V \frac{\partial (\rho \phi)}{\partial t} \, dV + \int_V \bigtriangledown \cdot (\rho \phi \boldsymbol{U}) \, dV = \int_V \bigtriangledown \cdot (\Gamma \bigtriangledown \phi) \, dV + \int_V S_\phi \, dV \tag{2.4}$$

which, thanks to the Gauss' divergence theorem can be re-written as (2.5) to highlight the convection and diffusion of ϕ across the control volume boundaries A.

$$\frac{\partial}{\partial t} \left(\int_V \rho \phi \, dV \right) + \int_A \boldsymbol{n} \cdot (\rho \phi \boldsymbol{U}) \, dA = \int_A \boldsymbol{n} \cdot (\Gamma \bigtriangledown \phi) \, dA + \int_V S_\phi \, dV \tag{2.5}$$

In time-dependent problems, like the ones simulated in this work, it is necessary to integrate the equations with respect to time t over a small interval Δt. Further details on the Eulerian finite volume approach can be found in [29, 97].

2.1.2 Turbulence handling

For many engine applications, the focus of the numerical calculation is put on the mean flow behavior and on the effect of turbulence on mean flow properties. Moreover a comprehensive simulation of a turbulent flow requires a space and time discretization capable of resolving the Kolmogorov microscale and the characteristic time associated with it [29]. For this reasons the approach chosen to handle the Navier-Stokes equations involves the modeling of the turbulent phenomena, and is based on the time averaging process leading to the Reynolds Averaged Navier-Stokes (RANS) equations in which the average of the fluctuating component gives rise to an additional term in (2.1). This term is derived to be coupled with the diffusion one where an *effective* diffusion coefficient is introduced as the sum of the dynamic and the turbulent components (2.6).

$$\Gamma^{'} = \Gamma_{dyn} + \Gamma_{turb} \tag{2.6}$$

The determination of the value of the turbulent viscosity μ_t is the main scope of the turbulence model. In this work the standard $k-\varepsilon$ model is used and introduces two transport equations for the turbulent kinetic energy k and its dissipation rate ε. These two new transported variables represent the basis for computing the turbulent viscosity μ_{turb} as (2.7) and on which deriving the diffusion coefficient for energy and specie balances.

$$\mu_{turb} = \rho C_\mu \frac{k^2}{\varepsilon} \tag{2.7}$$

The RANS modeling of the transport equations represents the most common approach to simulate the UWS injection sections, mainly because of the large domains involved in the computations and the necessity to simulate for relevant duration to capture the thermal and reacting phenomena involved in the mixture preparation [8, 12, 13], as the wall temperature transients (Fig. 2.1-a) and the ammonia conversion (Fig.2.1-b).

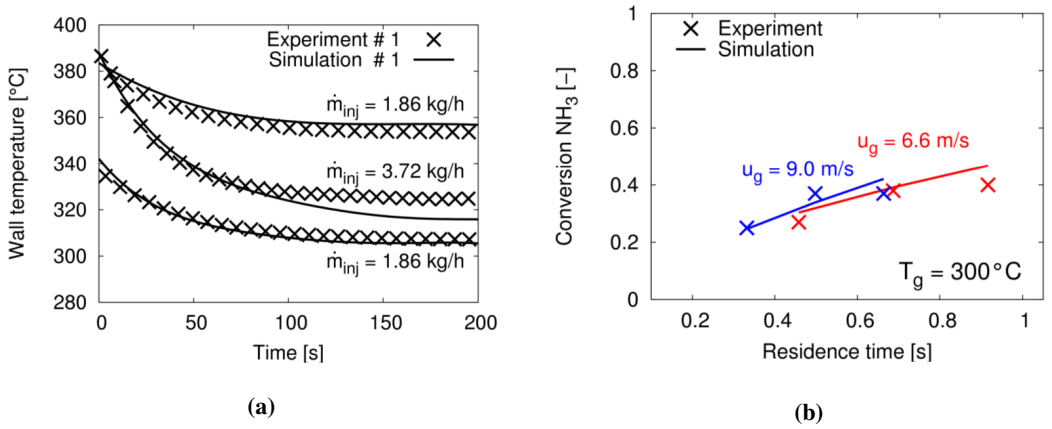

(a) **(b)**

Figure 2.1: *Characteristic time of the solid wall thermal transient [12] (a) and of the ammonia conversion process [12] (b) .*

No relevant agreement is found in the choice of the turbulence model: some authors [91, 95, 96] used the RNG $k-\varepsilon$ [64], others [15] the realizable $k-\varepsilon$ [81]. The simulation of stronger swirling flows has been carried out recently with $k-\zeta-f$ model [34] by [8] and with the Reynolds Stress Model (RSM) by [31]. Since this uncertainty does not define a prevalent way to proceed, the choice in the presented work is driven by the experience with the OpenFOAM® software for Lagrangian-Eulerian engine spray applications [47, 50, 93].

2.1.3 Liquid injection handling

Liquid injection can generate a great number of droplets (up to 10^8) with diameters in the range of 10^{-5} m. To be able to represent this phenomenon, a statistical averaging technique becomes necessary with additional submodels in order to describe the subscale processes. The so-called spray equation [106] defines the probable number of drops per unit volume at time t, that are located between position $\boldsymbol{x}$ and $\boldsymbol{x} + d\boldsymbol{x}$ and characterized by a velocity between $\boldsymbol{U}$ and $\boldsymbol{U} + d\boldsymbol{U}$, a radius between $r + dr$ and a temperature between $T + dT$ through a probability density function f with nine independent variables (2.8):

$$\frac{probable\ number\ of\ droplets}{unit\ volume} = f\ (\boldsymbol{x}, \boldsymbol{U}, r, T, t)\, d\boldsymbol{U}\, dr\, dT \tag{2.8}$$

To take into account the droplet shape deformation two additional variables need to be included: droplet distortion parameter y and its temporal rate of change $\dot{y}$. The temporal and spatial evolution of the distribution function is described by a conservation equation, which can be derived phenomenologically in analogy to the conservation equations of the gas phase, usually called spray equation (2.9),

$$\begin{aligned}\frac{\partial f}{\partial t} = &-\frac{\partial}{\partial x_i}(f\,U_i) - \frac{\partial}{\partial U_i}(f\,F_i) - \frac{\partial}{\partial r}(f\,R) - \frac{\partial}{\partial T}\left(f\,\dot{T}\right) \\ &- \frac{\partial}{\partial y}(f\,\dot{y}) - \frac{\partial}{\partial \dot{y}}(f\,\ddot{y}) + \dot{f}_{coll} + \dot{f}_{bu}\end{aligned} \tag{2.9}$$

F_i is the acceleration along the spatial coordinate x_i, R, $\dot{T}$ and $\ddot{y}$ are the time rates of the change of droplet radius r, temperature T and oscillation velocity $\dot{y}$. The source terms $\dot{f}_{coll}$ and $\dot{f}_{bu}$ account for droplet collision and break-up.

The mathematical description of the phenomenon is complex and the numerical implementation of (2.9) with an Eulerian finite volume scheme is very demanding in terms of computational cost because of the necessity of discretization of f in eleven independent dimensions. For these reasons, a more practical approach, represented by the Discrete Droplet Model (DDM) proposed by [24] and available in the OpenFOAM® platform, is used in all the practical applications of the SCR technology. The model features a Monte-Carlo based solution technique for the spray equation, that describes

the spray droplets by stochastic particles which are usually referred to as parcels [14]. These parcels produce a statistical representation of the spray reducing the number of computational objects which can be viewed as representative classes of identical, non-interacting droplets, tracked through physical space in a Lagrangian manner.
With this approach, the interface between a single droplet and the gas phase cannot be resolved because of computer limitations, and an averaging of the flow processes over a scale that is greater than the typical droplet diameter becomes necessary. Consequently, additional submodels are needed to describe the phase interaction [88].

Liquid Atomization

Since the Lagrangian description of the liquid phase requires the existence of drops, the simulation of spray formation always begins with drops starting to penetrate into the system. The injector modeling strategy is in charge of providing the assignment of the initial conditions of the computational parcels, such as initial radius, velocity components (and the consequent spray angle) which in reality are dependent on the flow conditions inside the nozzle holes [9].

Blob-Method The simplest and most common way of defining the starting conditions of the first droplets at the nozzle hole exit of full-cone sprays is the blob-method [73]. It assumes that atomization and drop break-up within the dense spray near the nozzle are indistinguishable processes and can be represented by the injection of large spherical droplets with uniform size equal to the nozzle hole diameter as in Fig. 2.2.
The number of the injected parcels is extracted from the injected mass flow rate, which

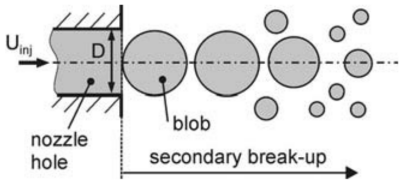

Figure 2.2: *Blob-method sketch [9].*

can be provided by direct measurements or derived from the Bernoulli equation (2.10).

$$U_{inj,max} = \sqrt{\frac{2\,\Delta\,p_{inj}}{\rho}} \tag{2.10}$$

$U_{inj,max}$ defines also the upper limit for the injection velocity. The low-pressure driven sprays used for SCR application work with a $\Delta\,p_{inj}$ below 10 bar, reaching a maximum velocity approximately of 40 m/s, which is much lower than the usual range of application for in-cylinder fuel injection.

One of most common correlations for the determination of the spray aperture angle is given by [72] and provides the aperture angle β_{sp} as a function of the geometrical ratio between the length of the injector internal channel and the nozzle diameter L_f/d_f.

According to [42, 71] the primary break-up can be classified in four major regimes, which are shown in Fig. 2.3-a: Rayleigh regime, first or second wind-induced regime or atomization, depending on the Reynolds number referred to the nozzle Re_{nozzle} (2.11) and Ohnesorge number Oh (2.12).

$$Re_{nozzle} = \frac{\rho\,\bar{U}_{nozzle}\,d_{nozzle}}{\mu} \tag{2.11}$$

$$Oh = \frac{\mu}{\sqrt{\rho\,\sigma\,d_{nozzle}}} \tag{2.12}$$

According to [83] the pressure driven injectors for SCR applications experience a second wind-induced regime (Fig. 2.3-b) where the main droplets are created from the core break-up and are smaller than the nozzle diameter. The development of surface waves due to shear stress leads to the stripping of very small droplets from the liquid core, completing the break-up of the jet only a few diameters after the injection. In the numerical description of the spray, the *blob-droplet* break-up by aerodynamic forces generated by the interaction of the liquid with the surrounding air is described through the Weber number referred to the gaseous phase (2.13).

$$We_{gas} = \frac{\rho_{gas}\,U_{rel}^2\,d}{\sigma} \tag{2.13}$$

According to Fig. 2.4 a substantial aerodynamic break-up is present only if the We_{gas} is higher than ≈ 12 which represents a value typical of the drops generated by an injector

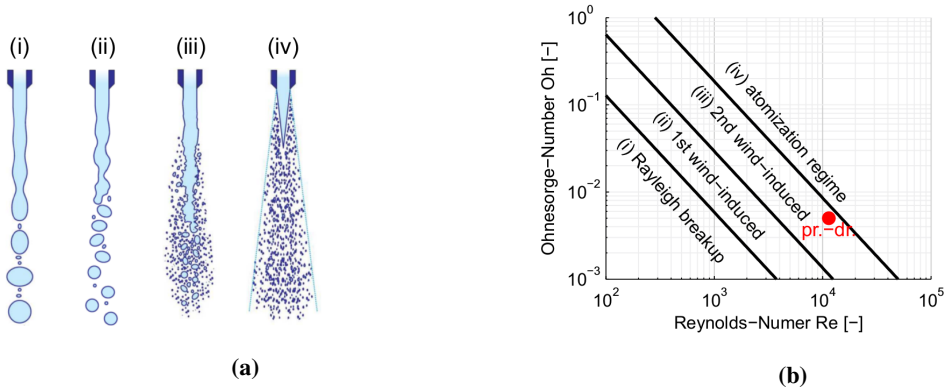

Figure 2.3: *Representation of the four primary break-up regimes [42, 71] (a) and mapping on Re_{nozzle} and Oh numbers highlighting the position of a typical pressure-driven injector for SCR applications [83] (b).*

for SCR applications [83]. Therefore, the applicability of the most common break-up models for the Lagrangian DDM spray framework [74,92] is not suited for the injection phenomena under investigation. Moreover [95] tested the blob-injection coupled with the break-up model by [73] strongly over estimating the droplet size, excluding the blob method from the proposed framework.

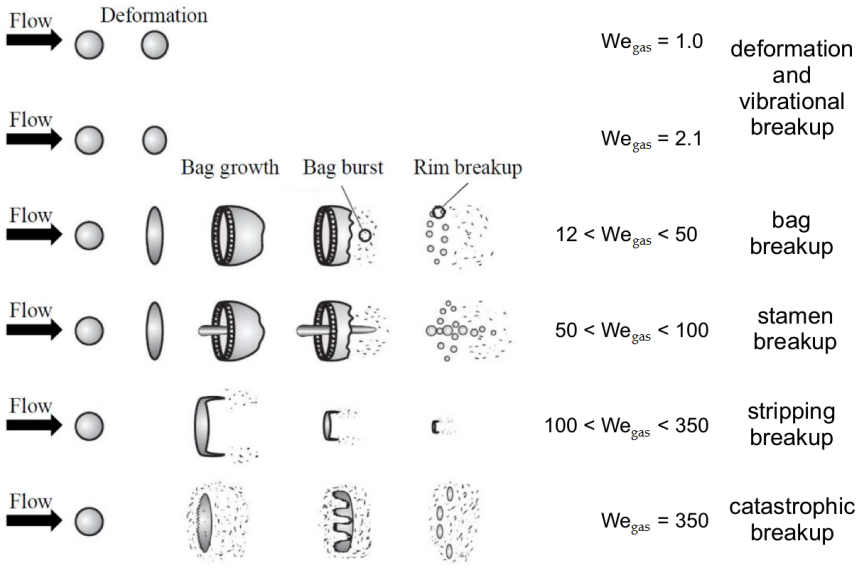

Figure 2.4: *Aerodynamic droplet break-up regimes [25, 68].*

Distribution functions This method assumes that the liquid is already fully atomized at the nozzle exit and that the distribution of drop sizes can be described by mathematical

functions. This approach skips the detailed modeling of the relevant processes during primary break-up and needs to be calibrated iteratively on far-field drop size values, accessible by experimental measurements (e.g. PDA).
The behavior of high pressure Diesel full cone sprays has been found in good agreement with the χ^2-law as the one proposed by [49] and reported in (2.14),

$$P\left(d\right) \;=\; \frac{1}{6\,\bar{D}^4}\,d^3\,e^{-d\,\bar{D}} \tag{2.14}$$

where $\bar{D}$ is estimated as (2.15). The Sauter Mean Diameter (SMD) value can be extracted from the injection parameters through semi-empirical correlations [52].

$$\bar{D} \;=\; \frac{SMD}{6} \tag{2.15}$$

Urea SCR literature reports the Rosin Rammler [76] probability function, shown in its cumulative form in (2.16), as an adapt formulation for the droplet size distribution [13, 91, 96] gathered from experimental data,

$$F_m\left(d\right) = 1.0 - \exp\left[-\left(\frac{d}{\delta}\right)^n\right] \tag{2.16}$$

but no clear agreement or formalization on the definition of the $scale$ parameter δ and the $shape$ parameter n is proposed by the authors.

Droplet motion equation

From the Newton's law, the motion equation of a droplet can be stated as follows:

$$m\,\frac{d\,\boldsymbol{U}}{d\,t} \;=\; \boldsymbol{F} \tag{2.17}$$

where $\boldsymbol{F}$ is the resultant of the forces acting on it and through which the coupling with the gaseous phase is realized. The choice of the relevant contributions to the balance is made *a priori* on the basis of previous assessments. According to [91] the most commonly encountered forces are listed in Tab. 2.1. Some features can be excluded from the simulation of a pressure-driven injection for SCR applications, since the characteristics of the spray and its interaction with the gas phase generate negligible contributions. In fact, the virtual mass force is not significant since the ratio between the liquid and

force	due to
virtual mass	acceleration of the surrounding gas at droplet acceleration
brownian motion	collisions with individual molecules of the gas phase
drag	relative velocity between droplets and gas
lift	velocity gradient in the normal direction to the particle trajectory
rotational	rotation of the droplet
buoyancy	gravitation
history	build-up of continuous phase boundary layer at acceleration of droplet

Table 2.1: *Summary of the most common encountered force in the Eulerian-Lagrangian framework [91].*

the gas densities is extremely high ($\approx$ 1000). Moreover, the Brownian motion effect becomes relevant only for droplets with size approaching the mean free path of the continuous phase (1-2 μm according to [3]) which represent a negligible fraction of the total injected mass in the application under investigation [44]. A detailed analysis of the force contributions has been carried out by [91] on a cylindrical channel, sketched in Fig. 2.5, representing an heavy-duty engine SCR section and allowing the complete development of the spray in the flow field, excluding a relevant interaction with the solid boundaries.

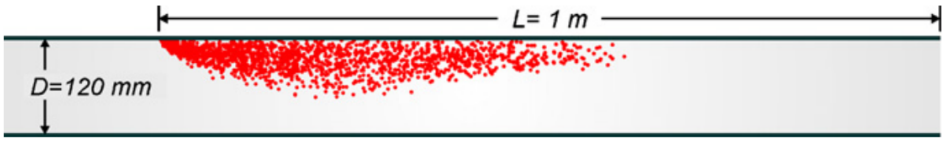

Figure 2.5: *Sketch of the system employed by [91].*

The investigation ranges from a cross-flow linear velocity of 25 m/s and T_{gas} equal to 300° C to an *extreme* condition working with $\bar{U}_{flow}$ = 100 m/s and T_{gas} = 500° C. The drag force F_D is found to be the predominant contribution in the spray system balance, and should always be included in the simulation of pressure-driven UWS injection. It is computed through a drag coefficient C_D, explicitly defined by (2.19) as a function of the Reynolds number Re_{gas} (2.20), through the formulation reported in (2.18).

$$\boldsymbol{F}_D = \frac{\pi d^2}{8} \rho C_D |\boldsymbol{U} - \boldsymbol{U}_{gas}| \, (\boldsymbol{U} - \boldsymbol{U}_{gas}) \tag{2.18}$$

$$C_D = \begin{cases} \frac{24}{Re_{gas}}\left(1 + \frac{Re_{gas}^{2/3}}{6}\right) & Re_{gas} \leqslant 1000 \\ 0.424, & Re_{gas} > 1000. \end{cases} \tag{2.19}$$

$$Re_{gas} = \frac{\rho_{gas}\, U_{rel}\, d}{\mu_{gas}} \tag{2.20}$$

This formulation assumes the sphericity of the droplets, and is taken into account as the reference value to be compared with the other force magnitudes. The effect of droplet deformation in the drag definition [35] has been tested, showing that for the lowest gas flow conditions, which are representative of medium/high loads of the test bench used in this work [83], the change in the results are of minor importance.

The lift force, function of the lift coefficient $C_L = f(\alpha^*)$, where α^* is the dimensionless shear rate of the fluid [41] has been found to be negligible over the whole cross-flow conditions spectrum, as well as the rotational force.

The effect of the buoyancy force is dependent on the orientation of the gas flow, of the injector, and on the retention time of the spray in the system. It has always been included in the simulation setup proposed in this thesis.

Also the history force can be neglected for the typical size of the SCR technology droplets, since it is relevant only for rapid acceleration or deceleration of the spray and decreases for dense sprays and with the particle diameter.

Finally, the effect of the stochastic perturbation of the droplet drag has been modeled taking into account a Gaussian distribution function to estimate the fraction of the velocity fluctuation based on the turbulent kinetic energy $\sqrt{\frac{2k}{3}}$. This contribution has been found important in the trajectory definition by [91] and therefore it is always included in the presented simulation.

Droplet mass conservation

The effect of the evaporation $\dot{m}_d$ of the liquid droplet is the only term that appears in the mass balance of a single liquid droplet (2.21).

$$\frac{dm}{dt} = \dot{m}_{evap} \tag{2.21}$$

The evaporation process is governed by conductive, convective and radiative heat transfer from the hot gas to the colder droplet and by the simultaneous diffusive and convective mass transfer of the species vapor from the boundary layer at the drop surface into the gas environment [88]. Since it is not feasible in terms of computational cost to directly resolve the flow field around each droplet, spherical shape and averaged flow conditions are assumed to determine heat and mass coefficients at the interface. The mass evaporation rate for each specie can be calculated as (2.22)

$$\dot{m}_{evap} \;=\; -\pi\, d\, \Gamma\, \rho_{vap} \ln\left(1 \;+\; \frac{Y_{vap,s} - Y_{vap,\infty}}{1 \;-\; Y_{vap,s}}\right) Sh \tag{2.22}$$

where the mass fraction of each component at the interface $Y_{vap,s}$ is calculated through the Raoult's law (2.23).

$$Y_{vap,s} \;=\; \frac{p_v\,(T)}{p_{gas,cell}}\,\frac{W}{W_{mix,s}} \tag{2.23}$$

$p_v\,(T)$ is the saturation pressure at the droplet temperature T and W and $W_{mix,s}$ are the molar weights of the i^{th} component and the gaseous mixture at the the droplet surface, respectively. The properties of the gas are calculated through the $1/3$ law, as the surface temperature (2.24)

$$T_s \;=\; \frac{2}{3}\,T \;+\; \frac{1}{3}\,T_{gas} \tag{2.24}$$

The Sherwood number Sh present in (2.22) can be evaluated resorting on the Ranz-Marshall formulation [70], shown in (2.25), where Re_{gas} refers to (2.20) and Sc is the Schmidt number for the gaseous phase defined as $(\mu_{gas}\, c_{p,gas})/\Gamma$ which reports the ratio between the momentum diffusivity and the specie diffusivity Γ.

$$Sh \;=\; 2.0 \;+\; 0.6\, Re^{1/2}\, Sc^{1/3} \tag{2.25}$$

This approach constitutes the basis of the engine-related literature [9, 88] and has been widely used in the SCR field with small variations in the definition of the Sherwood number [12, 13, 91].

Droplet energy conservation

The droplet energy conservation equation, defined according to the coordinate system reported in Fig. 2.6, involves the contribution related to the phase change and the one

generating a temperature evolution of the droplet (2.26).

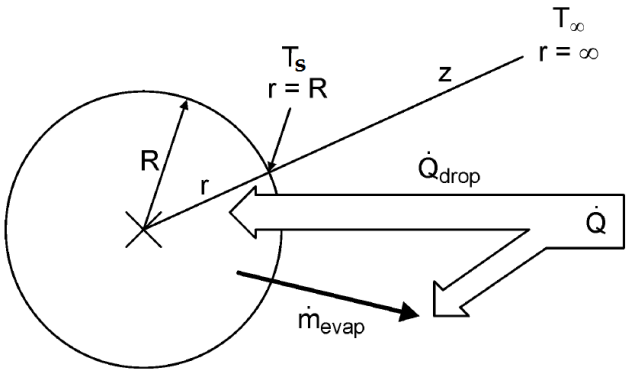

Figure 2.6: *Definition of the coordinate system for mass and heat fluxes [9].*

$$\dot{Q}_{drop} = \dot{Q}_{heating} + \dot{Q}_{evap} \tag{2.26}$$

Re-arranging the equation (2.26) to extract the droplet temperature variation (2.27) it is possible to isolate the convective heat flux which can be described through the gas Nusselt number Nu defined according to the Ranz-Marshall model [70] (2.28).

$$\frac{dT}{dt} = \frac{1}{m\,c_p}\left(\frac{dQ_{drop}}{dt} - \Delta\,h_{evap}\frac{dm_{evap}}{dt}\right) \tag{2.27}$$

$$Nu = 2.0 + 0.6\,Re^{1/2}\,Pr^{1/3} \tag{2.28}$$

The Prandtl number Pr, defined for the gas phase ${}^{(\mu_{gas}\,c_{p,gas})}/_{\lambda_{gas}}$ is calculated for the boundary layer, through the ${}^{1}/_{3}$ law to determine the thermophysical properties. The latent heat related to the evaporation of the liquid is calculated at the temperature of the droplet $\Delta\,h_{evap} = f\,(T)$ resumed in (2.29)

$$\frac{dT}{dt} = \frac{\pi\,d\,\lambda_{gas}\,Nu\,\left(T_{gas}-T\right)}{m\,c_p}\,f - \frac{1}{c_p}\,\frac{\pi\,d\,\Gamma\,\rho_{vap}\,\ln\left(1+B\right)\,Sh\,\Delta\,h_{evap}}{m} \tag{2.29}$$

where B is called the Spalding number and is defined as (2.30) as a result of the evaporation mass rate formulation (2.22)

$$B = \frac{Y_{vap,s} - Y_{vap,\infty}}{1 - Y_{vap,s}} \tag{2.30}$$

and f is a corrective factor which takes into account the reduction of the heat transfered to the liquid parcel corresponding to the simultaneous liquid evaporation. As for the the mass conservation equation, the reported approach has been developed for fuel sprays and in-cylinder applications [9,88] and used to simulate SCR systems with some different semi-empirical correlation for the determination of the Nusselt number by some authors [12, 13, 91].

UWS mixture modeling

Particular care must be paid to the way the urea–water solution is modeled. A limited number of works have been published on the modeling of UWS injection, each of them resorting to specific simplifications of the problem [13, 39, 48, 77]. The main source of uncertainty is the lack of characterization of urea–water solutions at various temperature levels [61]. By reviewing the literature in the field of UWS injection, the state of aggregation of urea is not clear during the evaporation of UWS. Actually, it can be varied among solid, molten and gas phases, depending on the local thermophysical conditions. In particular, the high gas temperature can be a source of strong deviation from the so-called D^2-law of the droplet [103], as shown in Fig. 2.7. This is caused

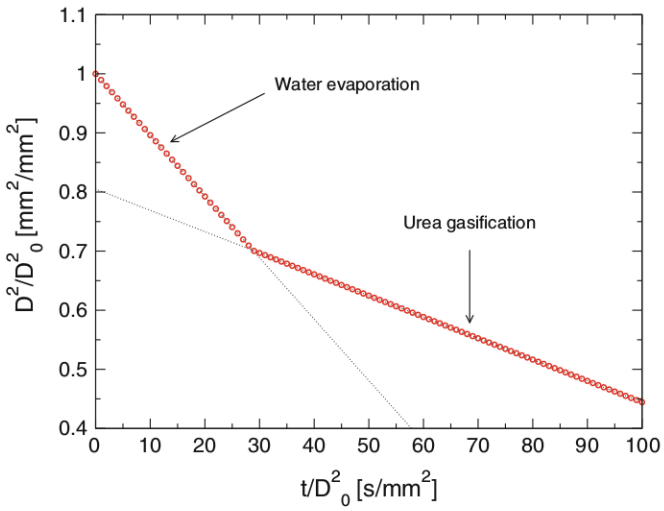

Figure 2.7: *Two phases of the D^2-law during evaporation of AdBlue® at T_{gas} = 423 K, ambient temperature and quiescent air [103].*

by the fact that the concentration of the two components in the solution changes during

the evaporation, leading to high concentration of urea, which may result in formation of solid components. The result is a formation of a solid crust around the droplet which, due to the boiling of the inner liquid core, will cause a sudden explosion of the droplet when the inner pressure increases above a threshold level [46, 57, 103]. A comparison among the Rapid Mixing model (RM) which considers infinite high transport coefficients accounting only for the temporal variation of temperature, concentration and thermophysical properties, the Diffusion Limit (DL) considering only the diffusive transport of energy and species inside the drop, and the Effective Diffusion (ED) taking into account the internal recirculation due to forced convection [13] (Fig. 2.8). The

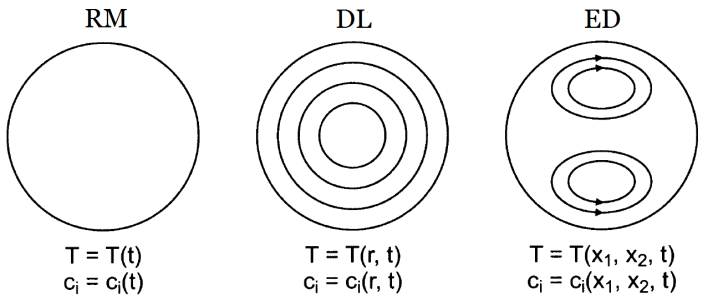

Figure 2.8: *Illustration of the three evaporation models tested by [13]: Rapid Mixing (RM), Diffusion Limit (DL) and Effective Diffusion (ED).*

influence of urea on the evaporation of UWS reported a decrease in the vapor pressure due to increasing concentration of urea in the droplet, resulting in a continuous increment of the droplet temperature and a slower evaporation compared to pure water [13]. The Rapid Mixing model predicts a lower urea concentration at the surface compared to the more detailed approaches, but does not strongly influence the droplet diameter during the evaporation at exhaust conditions. For this reason, the RM model is the one chosen to be applied to the proposed simulation campaign. In the present work, no urea chemistry is taken into account because of the very short residence time of the spray in the facility, including just the correlation proposed by [13] to reproduce its vapor pressure (2.31).

$$p_{v,urea}\left(T\right) = \exp 12.06 - 3992/T \tag{2.31}$$

The focus is put on the liquid mixture behavior in operating conditions, using the urea evaporation just as a tracker for the ammonia production locations.

CHAPTER 3

Spray - Flow Interaction

The correct CFD representation of the spray characteristics inside an SCR system is a mandatory feature for the design of the mixing performance and for the achievement of high conversion efficiencies of the SCR catalyst. As shown by [91, 96] the direct assignment of the diameter distribution is the most effective way to describe the injection of low pressure-driven sprays with the Lagrangian tracking of the dispersed phase. Previously available Phase Doppler Anemometry (PDA) campaigns [44, 95] measured the droplet sizes and velocities inside an engine-less test bench, run at the EMPA laboratories[1] with a dry air cross flow, operating over a wide range of momentum and temperature conditions. Due to the necessity of a closer estimation of the spray features to build a reliable numerical model, the focus of the experimental activity has been put to the near nozzle region.

[1] Swiss Federal Laboratories for Materials Science and Technology, Dübendorf, Switzerland

3.1 Near nozzle injection in quiescent air

The target of the investigation is put on two substantially different injectors in term of geometry and design, which operate at the same pressure (9 bar) and represent a common industrial standard for SCR applications. The first one, labeled 6H and shown in Fig.3.1-a, exhibits six parallel holes evenly arranged on a 1.36 mm diameter circle and elaborates a mass flow of 13.8 kg/h. Each hole has a diameter of 210 μm and the declared single spray cone angle is 13°. The second nozzle, 3H, injects a static mass flow of 7.2 kg/h through three 190 μm holes, arranged on a 1.9 mm circle (Fig.3.1-b). Each jet is deviated by 11° from the geometric axis and generates a 9° cone, according to the producer specifications.

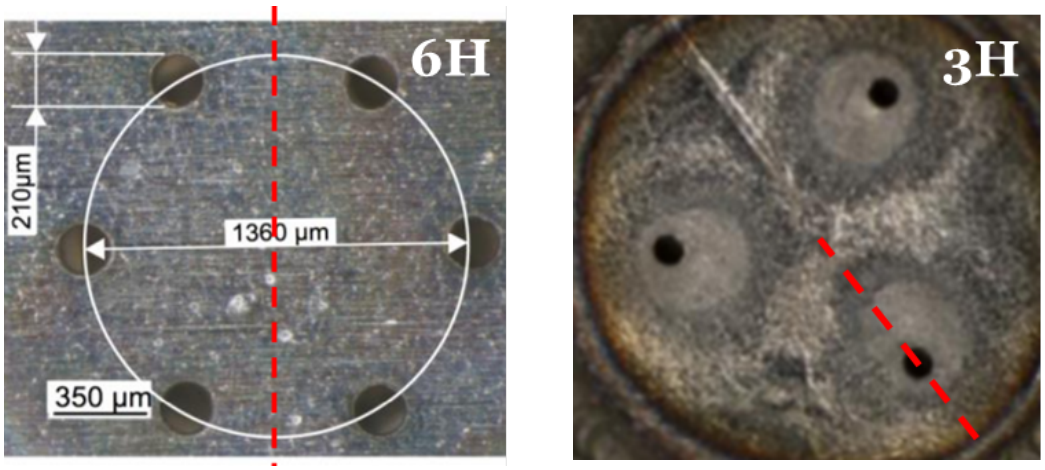

(a) (b)

Figure 3.1: *Nozzle heads with open-air sampling lines. 6H (a), 3H (b)*

3.1.1 Experimental setup

The injectors are installed in open-air conditions, setting the axis vertically. The measurement sampling lines are chosen in such way to cross the spray along their centerlines, at constant axial distance. The spray traversing is operated thanks to a horizontally adjustable injector support, as shown by the system sketch in Fig.3.2.

Injection pressure system The pump back-pressure is set to approximately 12 bar. The actual pressure acting on the nozzle is controlled by a pressure regulating valve. Two hydraulic dampeners, pre-charged at 10 bar, stabilize the pump back-pressure mitigat-

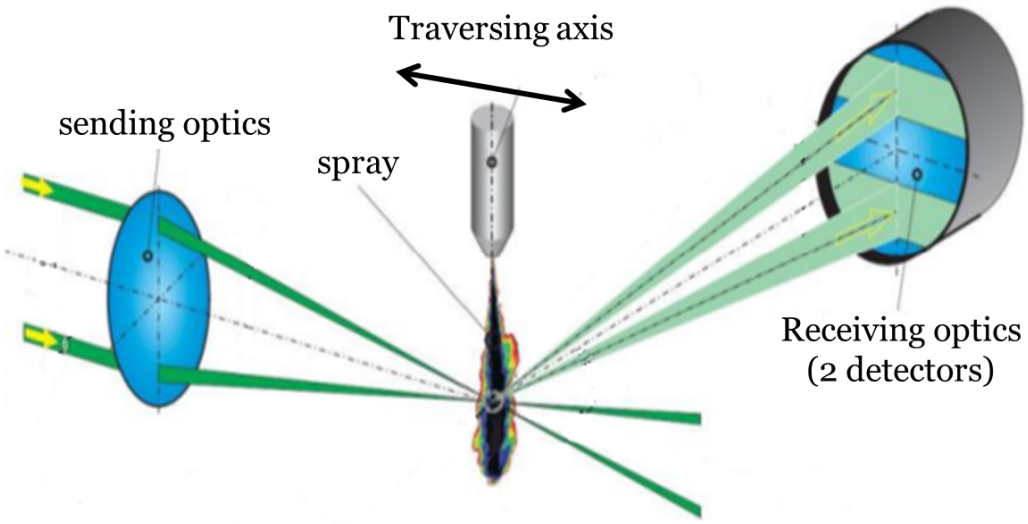

Figure 3.2: *Open-air PDA test bench sketch*

ing the fluctuation of the pumping system and reducing the pressure drop during the injection process. Initial pressure is set to 9.3 bar and drops by 0.5-1 bar during the 100 ms injections operated by an electronically triggered nozzle valve. The detailed description of the system can be found in [83]. The quality of the pumping system has been tested on the most critical injector available, the six hole nozzle (6H) with the maximum mass flow rate declared by the supplier. The actual mass flow rate was determined [98] by weighting the liquid collected injecting 2000 times in a tank. The mass was gathered setting the Duration Of Injection (DOI) to 50 ms, 100 ms and 150 ms reporting a constant mass flow rate equal to 3.87 g/s, as shown in Fig. 3.3. For this reason the PDA measurements are taken imposing a DOI of 100 ms assuming negligible both the injector opening and closing times.

Phase Doppler Anemometry system This technique provides the measurement of the velocity and of the size of individual spherical particles collecting the light scattered by their interaction with a fringe pattern generated by laser beams. In this work the subjects of the experiments are the liquid droplets generated by the pressure-driven injection, which scatter the fringe pattern in the measurement volume towards two photomultipliers. The frequency of the light seen by the photomultipliers corresponds to the droplet velocity, and the phase difference corresponds to the curvature radius as a direct repre-

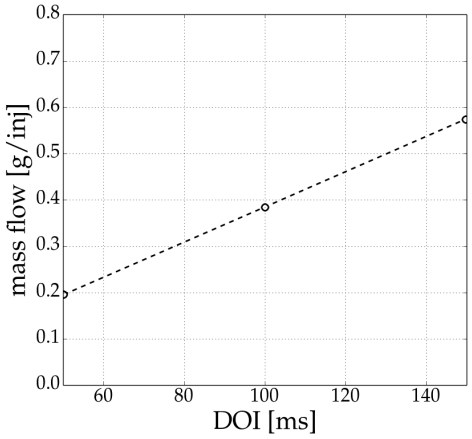

Figure 3.3: *Mass flux of the 6 hole pressure injector [98].*

sentation of the drop diameter .

The setup is based on the configuration proposed by [95, 105]. It employs a diode laser tuned to the $Ar^{+} - Ion$ wavelength of 514.5 nm. The beam vertical split and the frequency shift (40 MHz) are obtained through a Bragg cell (Fig. 3.4).

The separated beams are expanded and collimated at a designated beam separation

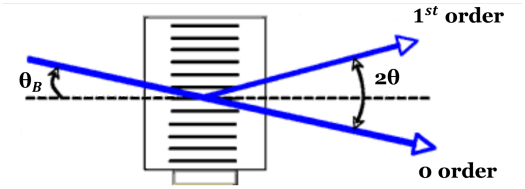

Figure 3.4: *Bragg cell beam separation and phase shifting [104].*

distance s_{beam} before being focused by a sending lens with 350 mm focal length in the measuring volume, as shown in Fig. 3.5. Operating with fixed lens focal length, the trade-off between the measurable velocity range and the precision produces the necessity of setting s_{beam} to 46 mm [83]. Brewster scattering angle (70°) is chosen to exploit the linear relation between the phase shift and the diameter (Lorentz-Mie-Theory) available if a single order of scattered light is dominant (p_{Mie}) with a sufficient light intensity for the detection guaranteed by the high power laser employed. The scattered light is collected by the DANTEC 57X10 PDA receiving optics with a 350 mm front lens and transferred into electrical signals by 3 photomultipliers. The signals are

processed by a DANTEC 58N10 system.

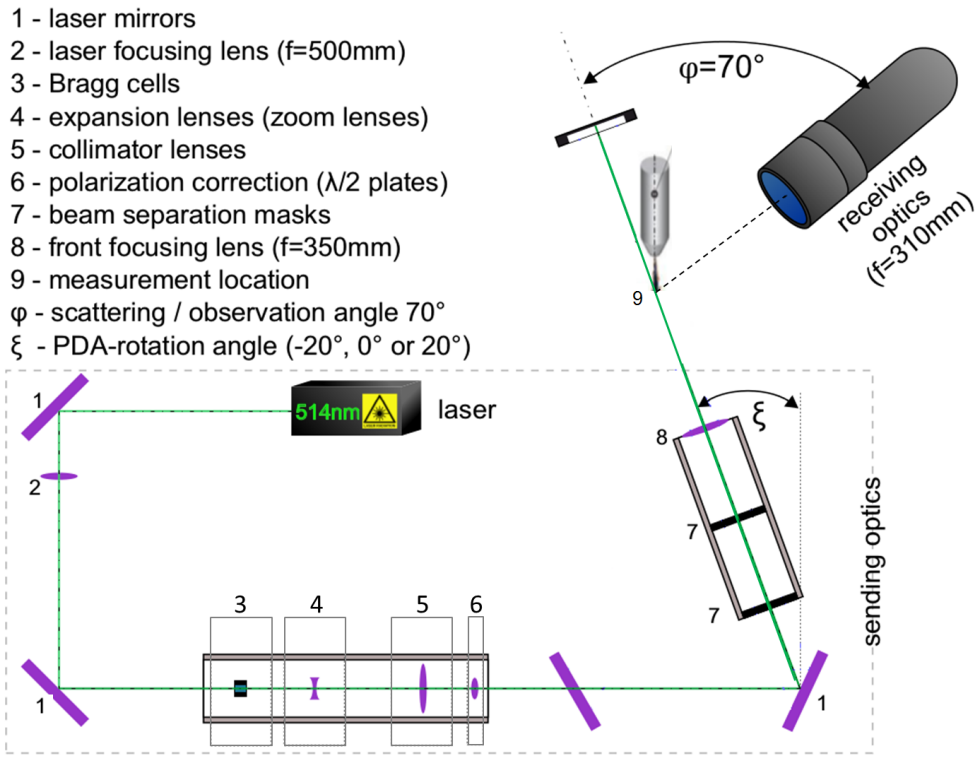

Figure 3.5: *Schematic of the single-beam PDA setup applied to the quiescent air measurements [83].*

Shadow Imaging system The near nozzle liquid injection process is background illuminated to capture the reduction of brightness, mostly due to the light Mie scattering in presence of droplets. The light source is provided by a 436 W cavitar cavilux smart diode laser, that provides monochromatic incoherent pulses at 640 nm. The light is fed to a laser beam expander which is focused on a ground glass plate, which provides the background illumination to the spray. A 12 bit Sensiscam QE CCD-camera captures the images at a resolution of 1376×1040 pixels [83, 85]. This experimental campaign is carried out with a pulse duration of 20 ns to reduce the drop motion blur effect to a resolution lower than the pixel size. A sketch of the system setup is provided in Fig. 3.6. The image analysis can lead to the qualitative evaluation of the spray shape and characteristic angles, and to the estimation of the liquid mass distribution. To obtain the latter information, 100 images without injection are collected for each measurement to obtain a background subtraction and uniformly highlight the spray behavior. Through

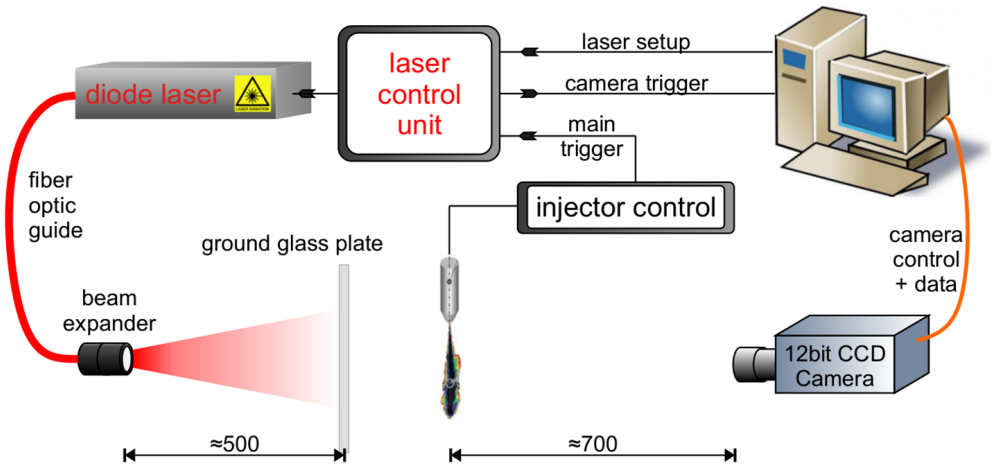

Figure 3.6: *Schematic of the Shadow Imaging system [83].*

the calculation of the $Bhattacharyya\ \ distance$ - d_{Bha} - [11] over a 75×75 pixels box the quality of the match between any spray image on an available background is computed. The spray images which show a match index lower than 99 % are removed from the stack. Then for each spray image (Fig. 3.7-a), the background one reporting the maximum d_{Bha} (Fig. 3.7-b) is subtracted to produce the net light extinction profile (Fig. 3.7-c). These results are used to qualitatively estimate the liquid mass flux over the traversing axis.

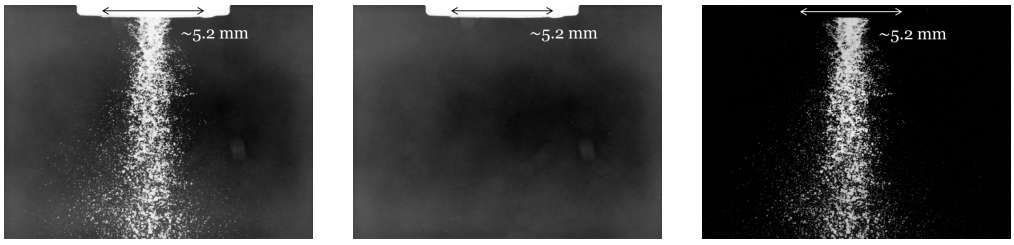

(a) **(b)** **(c)**

Figure 3.7: *6H - Near nozzle Shadow Imaging: original jet image (a), background image (b), net light extinction after substraction (c).*

3.1.2 Experimental results and discussion

The spray sizes and axial velocities are measured traversing the injector footprint centerline at 32 mm from the nozzle head. This distance has been chosen as the closest to produce sufficiently reliable data, ensuring the sampling validation rate higher than

60 % both in the spray cone core and in its periphery. The geometrical axis of the injector is designated as the origin - 0.0 mm - of the traversing axis. Due to a slight misalignment in the 6H installation, the sample location are shifted to match the actual symmetric behavior of the jet.

Water injection

Distilled water is injected to estimate the jet characteristics with a thermophysically known fluid and to build a reference framework over which to evaluate the effect of the presence of an urea fraction in the liquid solution.
The water properties employed in the experimental activity are gathered from [10], and linearly interpolated from the tabulated values.

Six hole Injector - 6H The traversing measurement is carried out with a spatial resolution of 2.5 mm. As reported by previous data [83], the single hole jets merge in a liquid stream from the very initial jet breakup stage (Fig.3.8-a). The resulting spray cone qualitatively behaves like a full cone along the nozzle central axis. The overall measured Sauter Mean Diameter d_{32} [80] of 75.11 μm and average diameter d_{10} equal to 39.52 μm are generated by a widely spread size distribution, as reported in Fig.3.8-b. The local average diameter trend (Fig. 3.9-a) shows its minimum value in correspon-

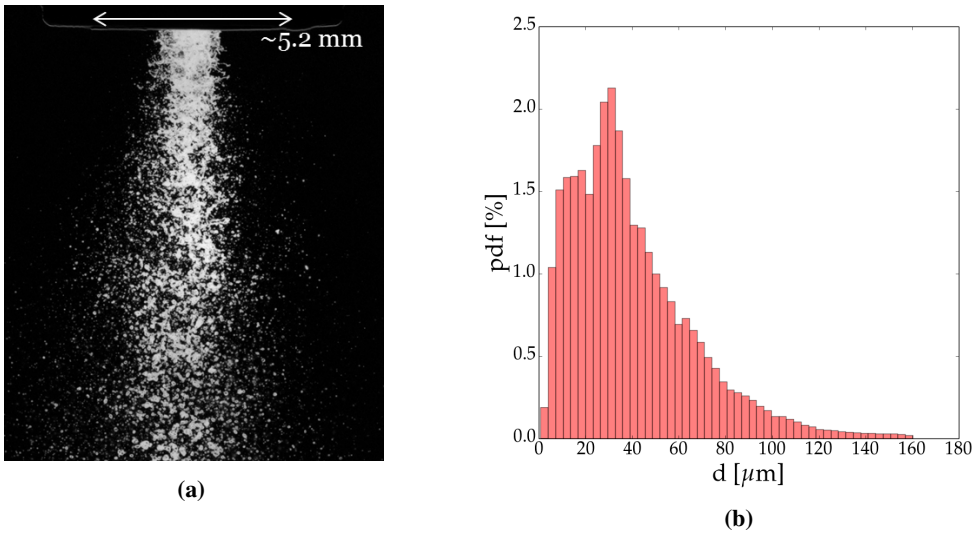

(a) **(b)**

Figure 3.8: *6H - Near nozzle liquid jet visualization through Shadow Imaging (a) and overall drop size distribution (b).*

dence to the nozzle axis which represents the strongest nozzle-to-nozzle interaction region. The spray core is also the maximum axial velocity location (Fig. 3.9-b) because of the null direction deviation from the measurement reference axis (vertical), the minimum interaction with the surrounding air and the maximum liquid mass flux as depicted by the averaged spray image in Fig. 3.10.

The graphs reporting the average values of diameters and velocities include *error bars* corresponding to the standard deviation of the collected data. It is used as a common parameter to easily represent the width of the measured distributions.

The Relative Span Factor (RSF), defined in (3.1) is chosen to represent the size dis-

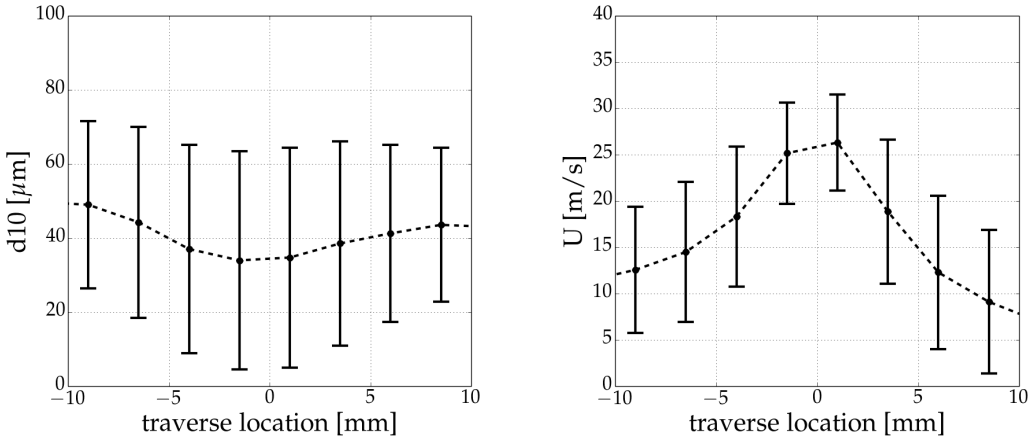

Figure 3.9: *6H - Average diameter (a) and axial velocity (b) in open-air conditions at 32 mm from the injector head.*

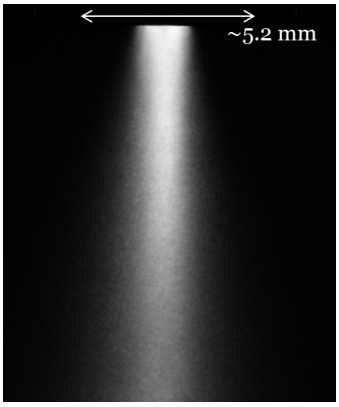

Figure 3.10: *6H - Spray average Shadow Image.*

tribution width, pointing out that from the inner core to the periphery, the liquid jet

breakup generates droplets of size ranging from 1 μm to 160 μm with a strongly non-uniform frequency distribution, as reported by Fig. 3.11. The dashed lines represent $d_{v,10}$ (green), $d_{v,50}$ (red) and $d_{v,90}$ (black), which are the drop diameters such that respectively the 10 %, the 50 % (volume median diameter), and the 90 % of the total liquid is in drop of smaller size.

$$RSF = \frac{d_{v,90} - d_{v,10}}{d_{v,50}} \tag{3.1}$$

From Fig. 3.11 it is possible to appreciate the differences between the behavior of the core (Fig. 3.11-a,b) and of the periphery (Fig. 3.11-c,d) of the spray cone: the paramount fraction of the collected droplets in the neighborhood of the jet axis has a size smaller than 40 μm, which corresponds to a reduced portion of the injected mass, shifting the drop volume median $d_{v,50}$, to $\approx$ 100 μm. The discrepancy between the droplet count distribution and the corresponding injected mass is less relevant in the periphery, where the fraction of the droplets with sizes lower than 20 μm is significantly reduced.

Tab. 3.1, summarizes the 6H spray characteristics over the sampling line. The collected data define an overall RSF of 1.1214, as a result of $d_{v,10} = 44.275$ μm, $d_{v,50} = 86.275$ μm and $d_{v,90} = 140.87$ μm.

Location	d_{10}	RSF	U_{avg}	Data rate	DR$_{norm}$
$[mm]$	[μm]	$[-]$	$[m/s]$	$[kHz]$	$[-]$
-9.0	48.99	1.15	12.57	0.107	0.04
-6.5	44.24	1.13	14.49	0.510	0.19
-4.0	37.03	1.05	18.30	1.802	0.66
-1.5	33.96	0.96	25.16	2.721	1.00
1.0	34.73	0.93	26.31	2.717	0.99
3.5	38.54	1.04	18.85	0.994	0.37
6.0	41.26	1.09	12.29	0.317	0.12
8.5	43.55	1.18	9.11	0.156	0.06

Table 3.1: *6H - Traverse property summary. DR$_{norm}$ represents the normalized data rate in order to estimate the droplet measurement frequency.*

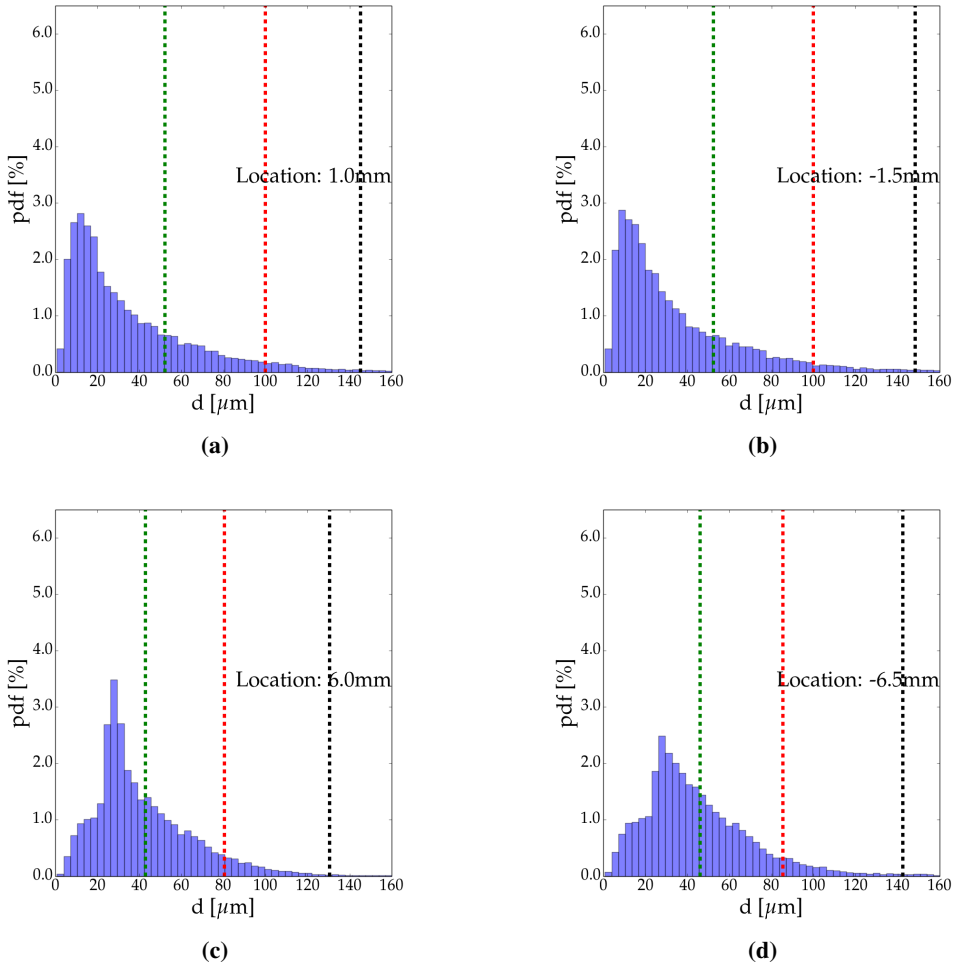

Figure 3.11: *6H - Local traverse size distributions. Spray core (a),(b) and periphery (c),(d). The dashed line represent the volumetric quantiles, $d_{v,10}$ (green), $d_{v,50}$ (red) and $d_{v,90}$ (black).*

Fig. 3.12 reports the correlation between drop sizes and velocities over the overall spray volume density distribution, averaged for each reported diameter bin. Even if the largest droplets carry the highest momentum, the spray mass core, which can be identified in the $[60 - 100]$ μm range, confirms an average axial speed consistent with the value of 27.4 m/s proposed by [84].

Three hole Injector - 3H Because of the clear separation among the single liquid streams [43] visualized through lateral Shadow Imaging (SI) and the reduced spray cone angle aperture, a sampling resolution of 1.25 mm has been chosen to traverse one of the three cone centerlines. The overall drop size distribution, reported in Fig. 3.13-b, can be synthesized by a d_{32} equal to 66.35 μm and a number average diameter d_{10} of 33.27 μm.

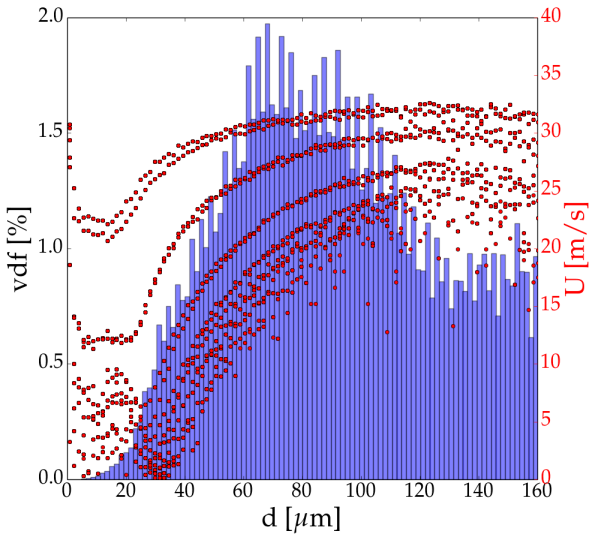

Figure 3.12: *6H - water injection - Volume density distribution and diameter-to-axial velocity correlation.*

The width of the distribution is of the same order of the 6H, reporting the poor quality of a low pressure-driven liquid atomization, represented by a RSF equal to 1.1367. The

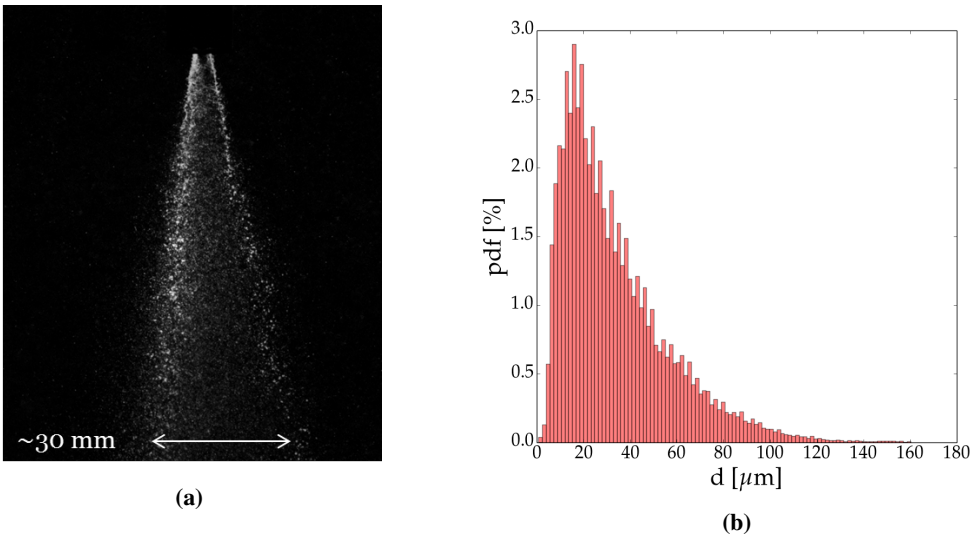

(a) **(b)**

Figure 3.13: *3H - Near nozzle liquid jet visualization through Shadow Imaging (a) and overall drop size distribution (b).*

diameter-to-axial velocity correlation follows the same trend shown by the 6H, with the highest velocities carried out by the biggest droplets. The spray mass core, corresponding to the size range [50-110] μm as reported by the volume density distribution

(Fig. 3.16), moves with a velocity of 32 m/s, confirming the supplier specification. The local average drop sizes and velocities are reported in Fig. 3.14, showing a peak in the particle size and velocity around the spray axis as supposed for full cone injections. Fig. 3.15, shows the drop size distributions over the spray cone traversing locations, on

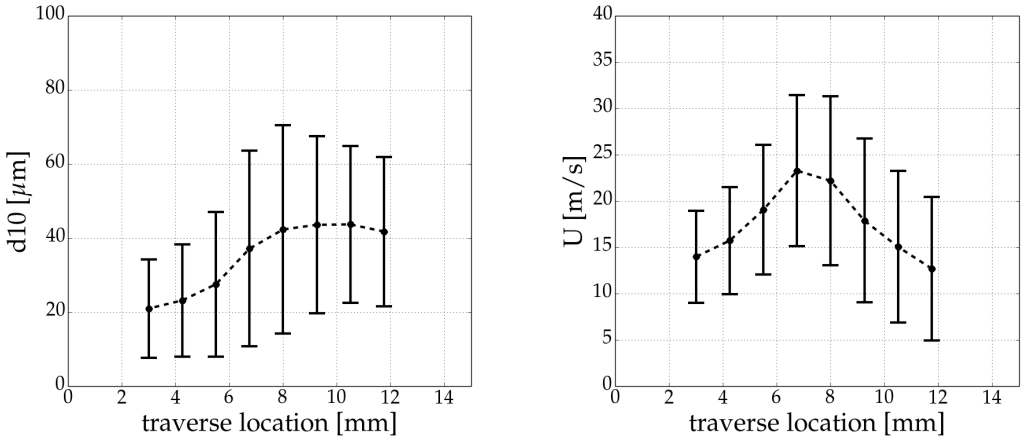

(a) **(b)**

Figure 3.14: *3H - Average diameter (a) and axial velocity (b) in open-air conditions at 32 mm from the injector head.*

which $d_{v,10}$, $d_{v,50}$ and $d_{v,90}$ are drawn.

The width of the droplet volume distribution generated by 3H, represented by the

Location	d_{10}	RSF	U_{avg}	Data rate	DR$_{norm}$
$[mm]$	[μm]	$[-]$	$[m/s]$	$[kHz]$	$[-]$
3	20.97	1.30	13.97	0.981	0.91
4.25	23.17	1.26	15.72	0.985	0.92
5.5	27.53	1.20	19.04	1.025	0.95
6.75	37.12	1.01	23.27	1.074	1.00
8.0	42.31	0.98	22.17	0.785	0.73
9.25	43.56	0.98	17.89	0.228	0.21
10.5	43.66	0.90	15.05	0.071	0.07
11.75	41.76	0.95	12.71	0.033	0.03

Table 3.2: *3H - Traverse property summary. DR$_{norm}$ represents the normalized data rate in order to estimate the droplet measurement frequency.*

volume quantiles ($d_{v,10}$, $d_{v,50}$ and $d_{v,90}$) in Fig. 3.15, is comparable with the behavior of 6H (3.11). The inclination of the measured jet produces a discrepancy in droplets characteristics in the outer peripheral location Fig. 3.15-d, where the average collected diameter is shifted to higher values and the size probability distribution flattens. As reported by Fig. 3.16 the drop volume probability function is narrower than the one

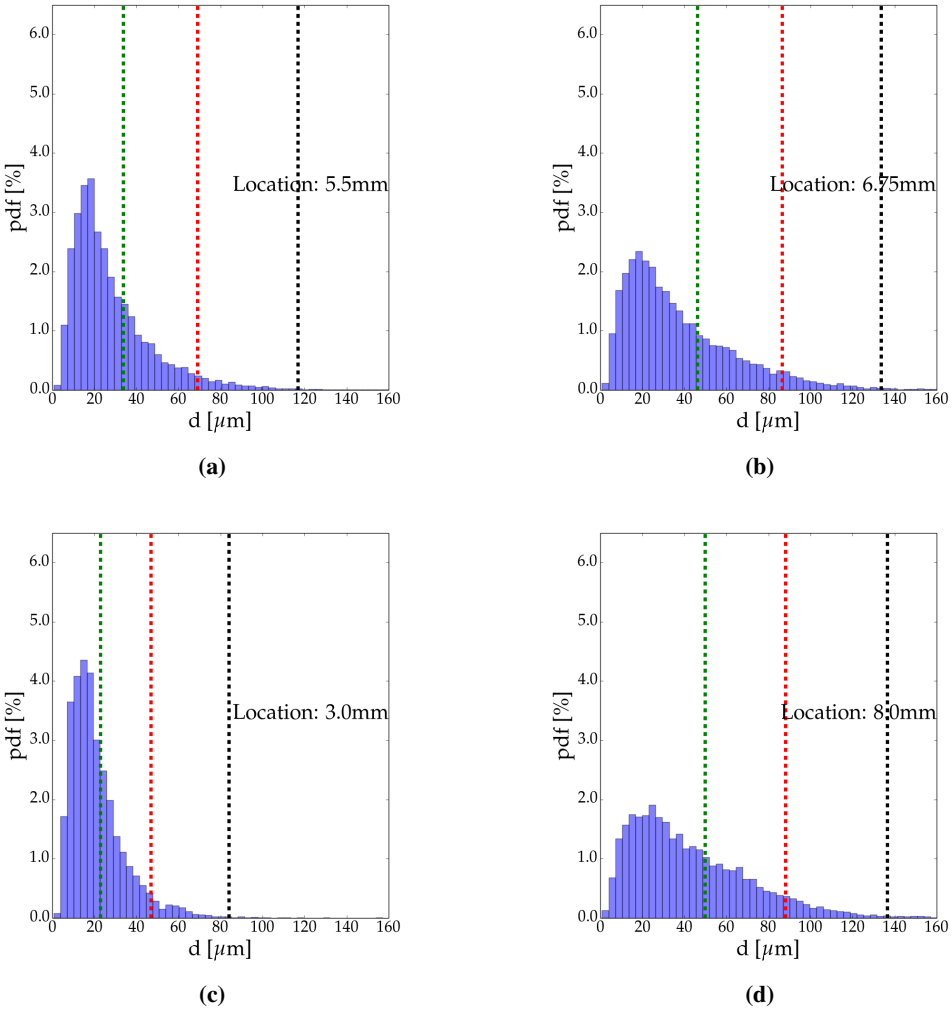

Figure 3.15: *3H - Local traverse size distributions. Spray core (a),(b) and periphery (c),(d).*

produced by 6H (Fig. 3.12), the atomization is improved and a steeper proportionality between droplet size and axial velocity is observed.

AdBlue injection

The same measurement routine is carried out with urea Water Solution (UWS) in its eutectic mixing ratio (urea - 32.5 $wt\%$) on the 6H injector. No substantial difference is found in the injector behavior, confirming what has been measured by [84].

Six hole Injector - 6H The jet generated by the coalescence of the single cones has the same width as the one produced by distilled water: both the local and averaged features

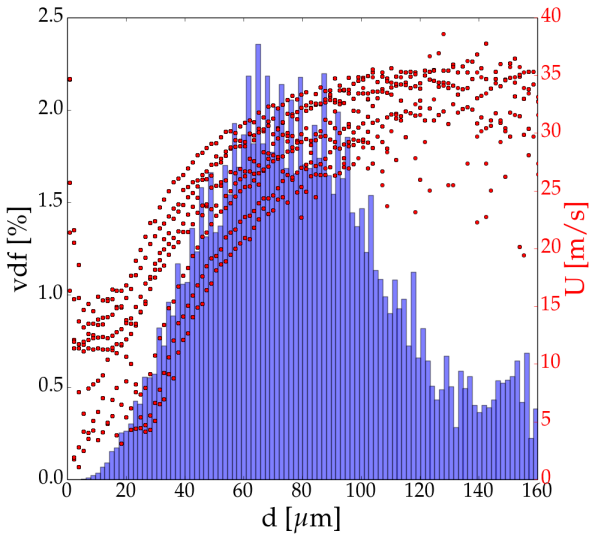

Figure 3.16: *3H - Volume density distribution and diameter-to-axial velocity correlation.*

extracted by the PDA measurements correspond. Fig. 3.17 shows the average diameter d_{10} and axial velocity U trends traversing the spray core region. The diameter-axial

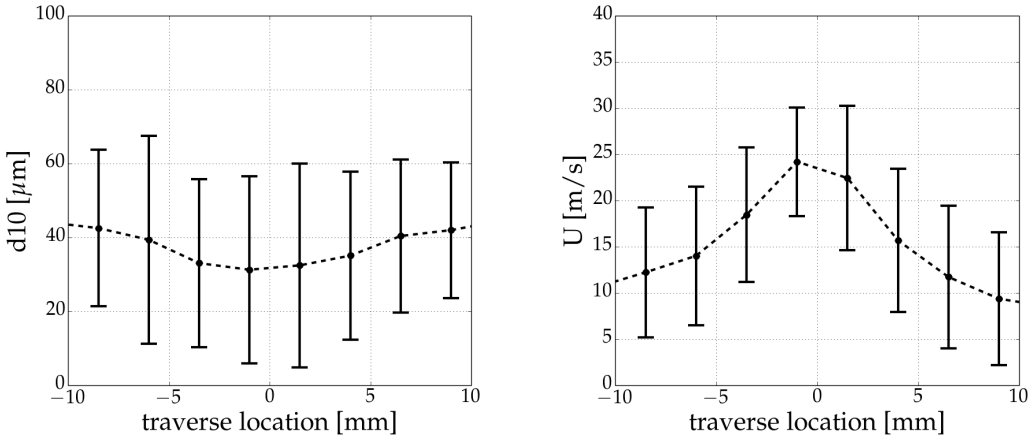

(a) **(b)**

Figure 3.17: *6H - UWS injection - Average diameter (a) and axial velocity (b) in open-air conditions at 32 mm from the injector head.*

velocity plot - Fig. 3.18 - denotes the same relationship presented by the water injection, confirming the spray injection velocity estimation.

Tab. 3.3, reports the summary of the spray characteristics along the sampling line, showing that the average size and velocity of the UWS droplets are slightly lower than the ones measured injecting distilled water (Tab. 3.1). No significant difference is

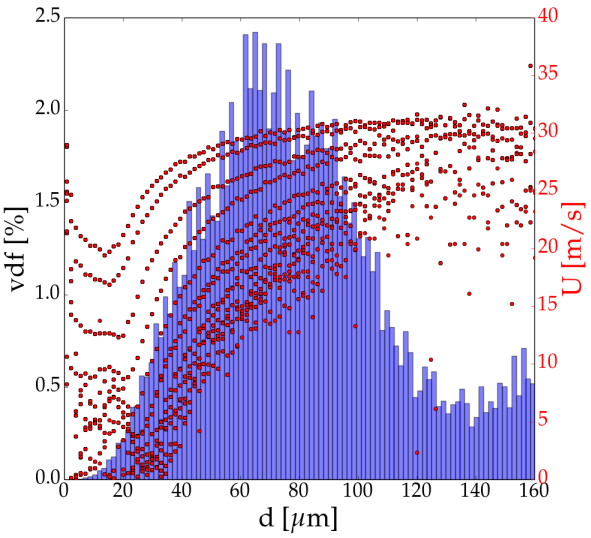

Figure 3.18: *6H - UWS injection - Volume density distribution and diameter-to-axial velocity correlation.*

reported in the extension of the spray cone resulting from the six jets coalescence, which produces relevant data in a $\pm 8.5\,mm$ range around the injector axis on a plane set $32\,mm$ from the nozzle head.

Location	d_{10}	RSF	U_{avg}	Data rate	DR_{norm}
$[mm]$	[μm]	$[-]$	$[m/s]$	$[kHz]$	$[-]$
-8.5	42.53	1.18	12.23	0.126	0.04
-6.0	39.38	1.03	14.02	0.352	0.12
-3.5	33.06	1.13	18.46	1.366	0.48
-1.0	31.28	1.10	24.21	2.830	1.00
1.5	32.47	1.04	22.43	2.037	0.72
4.0	35.09	0.98	15.69	0.737	0.26
6.5	40.40	0.94	11.73	0.215	0.08
9.0	41.99	0.92	9.37	0.082	0.03

Table 3.3: *6H - UWS injection - Traverse property summary. DR_{norm} represents the normalized data rate in order to estimate the droplet measurement frequency.*

3.1.3 Numerical modeling

The reported data define the basis on which numerical models are built and tested. Injection of distilled water through 6H is used as reference case to define the injector

model setup in quiescent air within the Lagrangian-Eulerian (L-E) framework.
The injection of distilled water with 3H and the behavior of 6H operating with UWS are respectively used to test the quality of the model definition routines on a very different nozzle head (Section 3.1), and to assess the liquid urea water solution model influence at low temperatures.

Mesh and gas phase definition

The initial mesh consists in a cubic box, as shown in Fig. 3.19 defined by a lateral extension of 62 mm, and a height of 40 mm. The injector is set in correspondence to the grid vertical axis, 0.5 mm inside the top surface to avoid any interference with the system boundary.

The symmetry plane present both in the injector heads and in the gaseous system

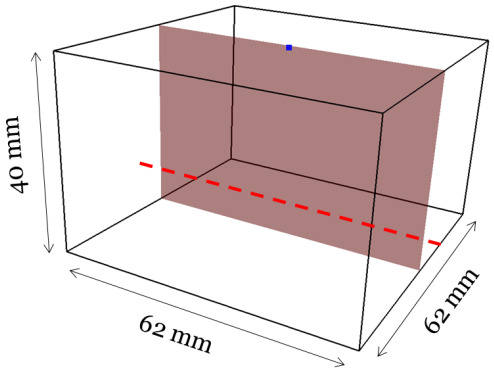

Figure 3.19: *Numerical simulation system bounding box. The dashed red line represents the spray traversing path and the blue point the nozzle head location.*

and reported in red in Fig. 3.19, cutting the system along the PDA traversing line, is exploited to reduce the mesh size and therefore the computational cost.

Initial and Boundary conditions Dry air at room conditions, defined as an ideal mixture of nitrogen and oxygen (Y_{N_2} = 76.6 $wt\,\%$), is used to represent the gaseous environment. The thermophysical properties of the species are defined according to the 7-coefficient polynomials proposed by [32]. The initial conditions are summarized in Tab. 3.4. Since the injector head is installed on a drilled metal plate, a solid wall boundary is defined on the top of the meshed box. The symmetry plane employs a reflecting boundary

T_{gas}	K	293
P_{gas}	bar	1.0
U_{gas}	m/s	0.0
$Y_{N_2,gas}$	$[-]$	.766
$Y_{O_2,gas}$	$[-]$	.234

Table 3.4: *Gas phase initial conditions.*

condition and the remaining patches behave according to the open-air boundaries. To minimize the effect of the latter boundaries a wave-transmissive approach [69] is applied on the pressure field. The condition set is reported in Tab. 3.5.

Fig. 3.20 shows the $coarse$ mesh test case, highlighting the solid top-wall (black), the

	top-wall	open-air
$\mathbf{U}_{gas}$	No slip	∂**U**/∂**n**=0
P_{gas}	∂P/∂**n**=0	wave-transmissive [69]
T_{gas}	T = 293 K	∂T/∂**n**=0
$Y_{i,gas}$	$\partial Y_i/\partial$**n**=0	$\partial Y_i/\partial$**n**=0

Table 3.5: *CFD boundary condition summary.*

symmetry plane (red) and nozzle head location (white spot). The turbulence is handled

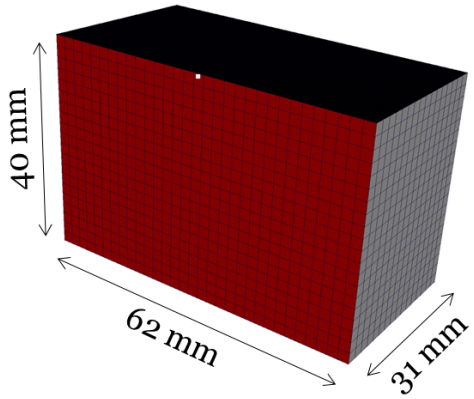

Figure 3.20: *Visualization of the coarse mesh test case.*

with the standard k-ε model, setting the boundary layer on the top-wall to be one-cell thick since scalable wall functions are used.

Spray simulation

Liquid injection in quiescent air at room temperature involves a limited thermal energy and mass exchange between the two phases, because of the weak temperature gradient

present at the drop interface coupled with the distance of the thermodynamic conditions of the system from the saturation line of both distilled water and AdBlue®. The purpose of this section is in fact the generation of a reliable setup of the injection model, purifying it from the influence of the submodels concerning the just above mentioned phenomena, to reproduce the near-nozzle spray behavior. The full two-way coupling, involving mass, momentum, energy and specie, between the dispersed and continuous phase is kept to test the solver behavior on the simplest available case, but the focus is put on the injection and on the momentum exchange modeling. The spheric drop assumption has been found to be a good representation in the determination of the drag coefficient C_d, through which the drag force is calculated, as stated in the very first simulation campaign done within this project [78]. A more detailed analysis of the injection modeling and the drop-drop stochastic collision modeling is carried out in the next sections.

6H - water injection setup The maximum Weber number (3.2) [88] of a drop injected in quiescent air, assumed to have the nozzle diameter ($d_{drop} = d_{nozzle}$ = 210 μm for 6H) and the Bernoulli velocity (42.4 m/s) is equal to 6.03, which is below the critical threshold defined by [68] for the bag breakup of a droplet.

$$We = \frac{\rho_{gas}\, d_{drop}\, U_{rel}^2}{\sigma} \tag{3.2}$$

For this reason the $blob$ injection strategy, coupled with the primary breakup models by [68, 73] is not able to accurately predict the widely spread diameter distribution measured through PDA. These considerations are confirmed in the work by [96] which tested the $blob$ injection method overestimating the drop size distribution of 6H in cross-flow conditions. A better prediction of the dispersed phase behavior can therefore be achieved assigning a diameter to each computational parcel through a drop size probability function built on the basis of the experimental data and tuning its direction and velocity to reproduce the spray cone angle and momentum profile. To synthetically represent the spray size population, a Rosin-Rammler (RR) distribution function [76] is used because of its flexibility and capability to reproduce a spray nozzle behavior [20], [55].

The cumulative probability function is reported in (3.3),

$$F_m(d) = 1.0 - \exp\left[-\left(\frac{d}{\delta}\right)^n\right] \tag{3.3}$$

where δ and n are respectively the scale and the shape parameters. To reproduce the whole 6H spray, a function fit is performed on an equivalent drop population, obtained weighting each PDA traverse measurement with its data rate value (reported in Tab. 3.1) to enhance the influence of the core on the overall spray. The resulting scale parameter δ is equal to 42.106 μm and the shape parameter n equal to 1.406. The latter value is in between the one proposed by [91] for an SCR injection system and the value tested for 6H by [96] showing that no clear literature evidence is available for low pressure-driven injector description. Each droplet velocity is set to 27.4 m/s [84], according to the value extracted from the peak of volumetric distribution reported in Fig. 3.12. To fulfill the observed sudden overlap of the six single spray cones (Fig. 3.8-a) and to cover the relevant traversing extension detected by the PDA measurement (Fig. 3.9), each single cone angle has been set to 36 °.

Being the injection the only momentum source for the gaseous phase, the air is strongly affected by the liquid motion in the form of a clear counter-rotating vortex structure, which has the strongest influence on the flow field in the near-nozzle location, as shown in Fig. 3.21. The effect of this structured motion is the segregation of the smallest

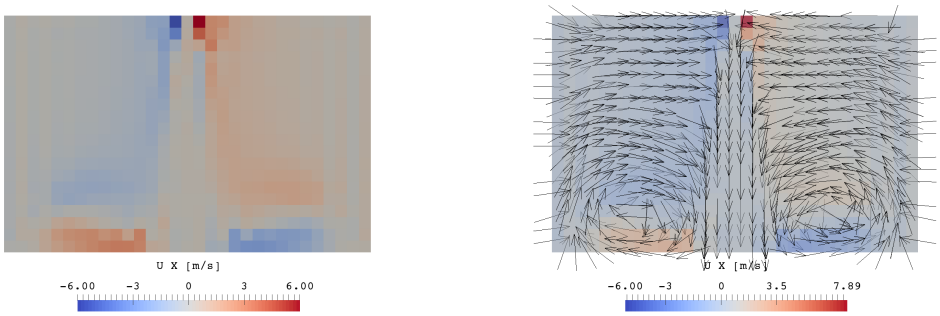

(a) **(b)**

Figure 3.21: *6H - Water injection - Horizontal gas velocity component (a) and counter-vortex direction visualization on the symmetry plane (b). Time = .1 s after SOI.*

droplets in the injector axis neighborhood, which is visible in the double hump d_{10} profile collected by the PDA measurements (Fig. 3.9). The largest and therefore most

inertial drops tend instead to keep their direction.

The influence of the boundaries on the gas recirculation is estimated extending the gaseous domain, shown in Fig. 3.22-a, keeping constant the dispersed phase modeling. It is possible to notice that the gas flow field motion is subjected to the pressure and velocity boundary conditions but the counteracting horizontal structure in the near nozzle is still present (Fig. 3.22-b). Fig. 3.23 shows how the recirculation motion variation does not affect the spray pattern because its magnitude is relevant only in the near nozzle region.

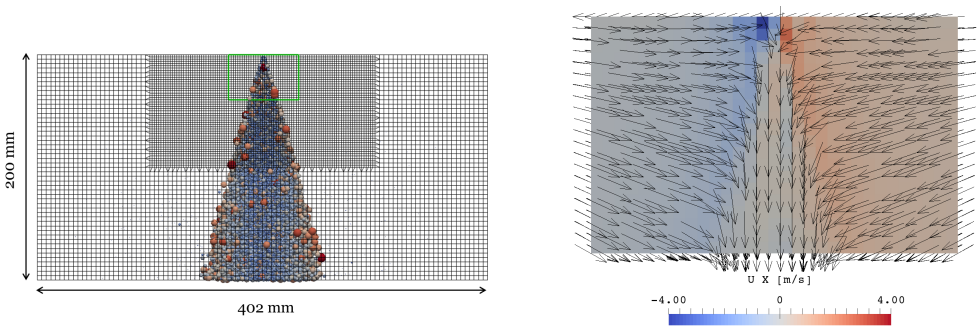

(a) (b)

Figure 3.22: *6H - Water injection - Large mesh outline, reporting in green the base system outline (a) and counter-vortex direction visualization in the near nozzle region (b). Time = .1 s after SOI.*

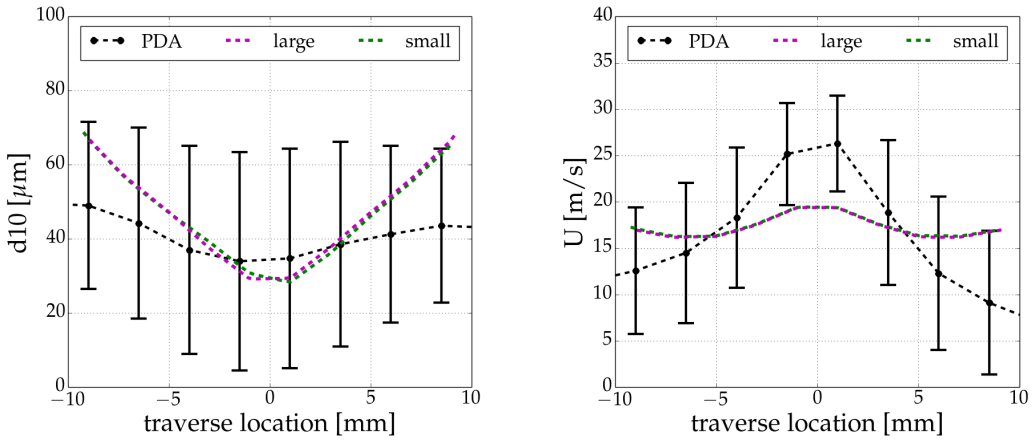

(a) (b)

Figure 3.23: *6H - Standard mesh vs large mesh spray property simulation.* d_{10} *(a) and* U *(b) profiles.*

Parcel discretization method The key point of a reliable representation of this behavior in the Lagrangian-Eulerial framework is the discretization of the spray in parcels. The validation process based on the comparison with PDA data, which provides the spatial distribution of the spray characteristic, forces the numerical simulation to reproduce the local diameter and velocity distributions as well as the spatial evolution of the jet cone. For this reason the determination of the mass and momentum numerical discretization plays as fundamental role in the injection process. The standard model by OpenFOAM® assigns to each parcel a mass dependent on the liquid flow rate injection law and a diameter according to the size probability distribution, calculating the number of particles in each parcel through the mass conservation principle. This approach is very solid and guarantees mass conservation especially with complex injection laws, but can lead to a wrong prediction of the spray characteristics, particularly if the drop size population is as wide as the one measured in this work. For this reason a different approach is used to simulate the low pressure-driven spray under investigation, assigning the diameter through the size pdf, constraining the number of particles per parcel and calculating the resulting liquid mass. For a continuous and uniform injection law, the overall mass conservation is kept defining the parcel injection rate to reproduce the injector specification. In Fig. 3.24-a it is possible to notice that the discrepancy between the two approaches is negligible, even at the beginning of the injection, where the low number of parcels makes their size assignment statistically relevant. The d_{10} profile

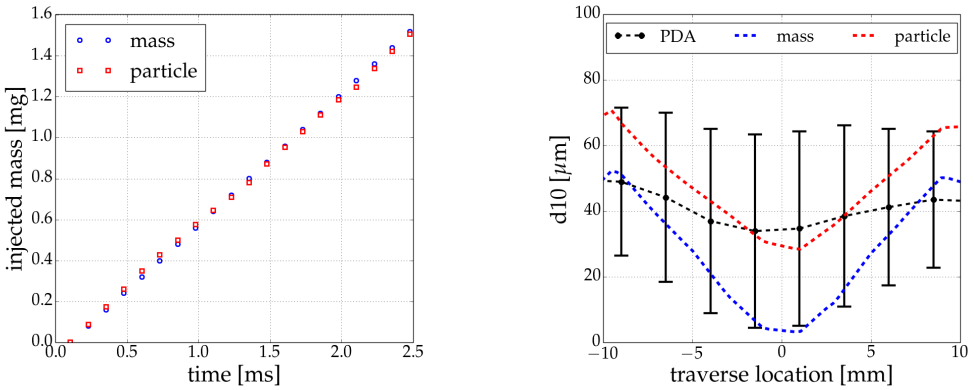

(a) **(b)**

Figure 3.24: *6H - fixed mass vs fixed particle per parcel injection during the first 2.5 ms after the SOI (a) and resulting d_{10} profile on the PDA traversing line (b).*

resulting from a constant mass parcel assignment shows a great underestimation of the drop size in the core of the spray, which is carrying the paramount part of the injected liquid. The spray simulation obtained by the constant particle approach instead, over predicts the average diameter in the periphery of the resulting cone but is consistent with the PDA data in the jet core (Fig. 3.24-b). The misalignment in the profiles comparison on the coarsest mesh is due to the simulation post processing routine, which assigns to each computational cell an average diameter which is updated at any parcel crossing and therefore is strictly dependent on the spatial discretization of the system. According to the comparison evidence, the latter approach, which keeps the number of particles per parcel constant, is chosen to simulate 6H.

Grid refinement It is known that the numerical solution of the Navier-Stokes equations becomes more and more accurate if the grid is refined, thanks to the accuracy in the discretization of differential equations. This assumption is valid only for continuous fluids represented through the Eulerian approach. Within the L-E framwork, it is impossible to reduce the grid size to resolve the gas phase up to the scale of the physical phenomena involved in a liquid injection, because this would violate a basic requirement for the Lagrangian liquid phase description, which is the fulfillment of a $void\ fraction$ (ratio between the gas and the liquid volume in a computational cell) close to one [9]. In this work, a gradual mesh refinement is applied to the test case: first the whole mesh is refined, then a secondary conical refinement is applied to the spray path. The three meshes, hex-dominant, are reported in Fig. 3.25 and described in Appendix B. Fig.

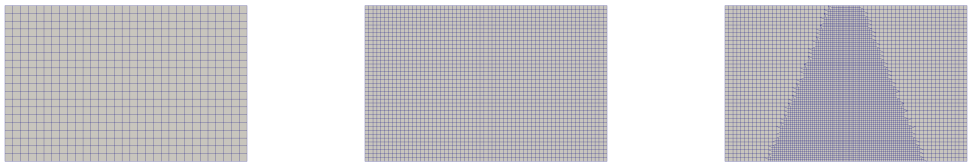

(a) (b) (c)

Figure 3.25: *Injector symmetry plane mesh: coarse (a), mid (b) and fine (c) test cases.*

3.26 shows the void fraction at the end of the injection (100 ms after SOI), highlighting how the L-E operating criteria is respected in each case with a minimum $void\ fraction$ of 0.8848 for the $fine$ mesh. The grid dependency on the spray tracking is evaluated

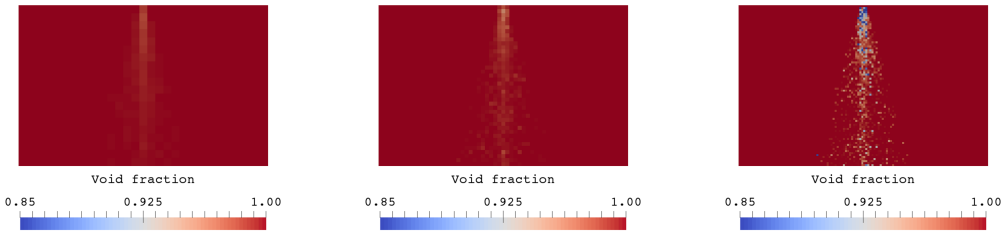

(a) **(b)** **(c)**

Figure 3.26: *6H - Void fraction: coarse (a), mid (b) and fine (c) test cases.*

over the experimentally collected d_{10} and the axial component of the velocity U profiles. The mesh refinement does not affect the spray average diameter profile (Fig. 3.27-a), but improves the results in the axial velocity plot (Fig. 3.27-b), due to the better discretization of the spatial gradients, especially in the near-nozzle region. In fact, the coarser the grid, the worse the spatial resolution of the gas velocity, and the worse the prediction of the gas-droplet momentum exchange, which depends on the relative velocity at the drop location [9]. A refined grid prevents an over prediction of the momentum diffusion due to the uniform distribution of the source term over the complete cell volume in which the parcel is located, and the underestimation of the gas velocity magnitude increment due to the higher mass contained in the gas cell. The latter effect, strongly affects the spray penetration transient, because small gas volumes are fast to be dragged by the first parcels, reducing the resistance to the path of the next droplets. Within this section the liquid penetration is not an issue because of the negligible opening and closing injector transients reported in tested conditions (DOI = 100 ms). The

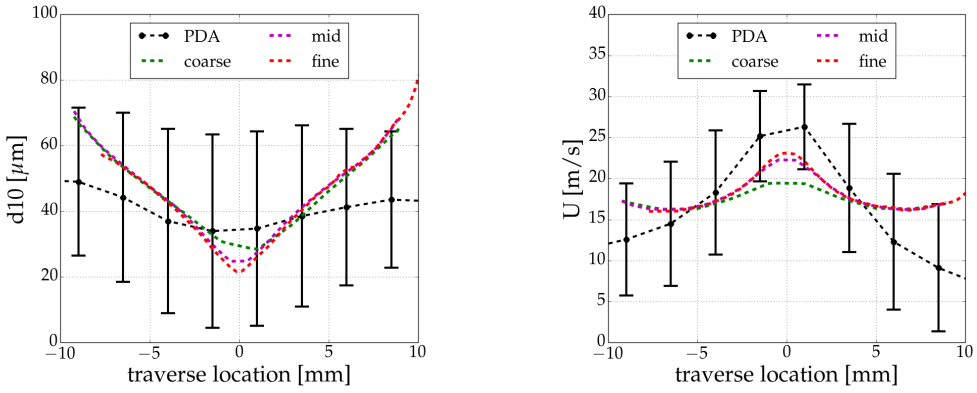

(a) **(b)**

Figure 3.27: *6H - d_{10} profile (a) and U profile (b) increasing the mesh refinement.*

described behavior, visible in Fig. 3.28, shows a more extended spray-gas momentum exchange region with the $fine$ mesh, which generates a faster gas flow ($U_{gas,max,fine}$ = 24.56 m/s, $U_{gas,max,coarse}$ = 22.95 m/s) in the spray core, reducing the drop velocity attenuation. In the $coarse$ mesh test case, the gas momentum increase is concentrated in the central cell column which includes the whole injector head, underestimating the lateral momentum exchange of the six jets.

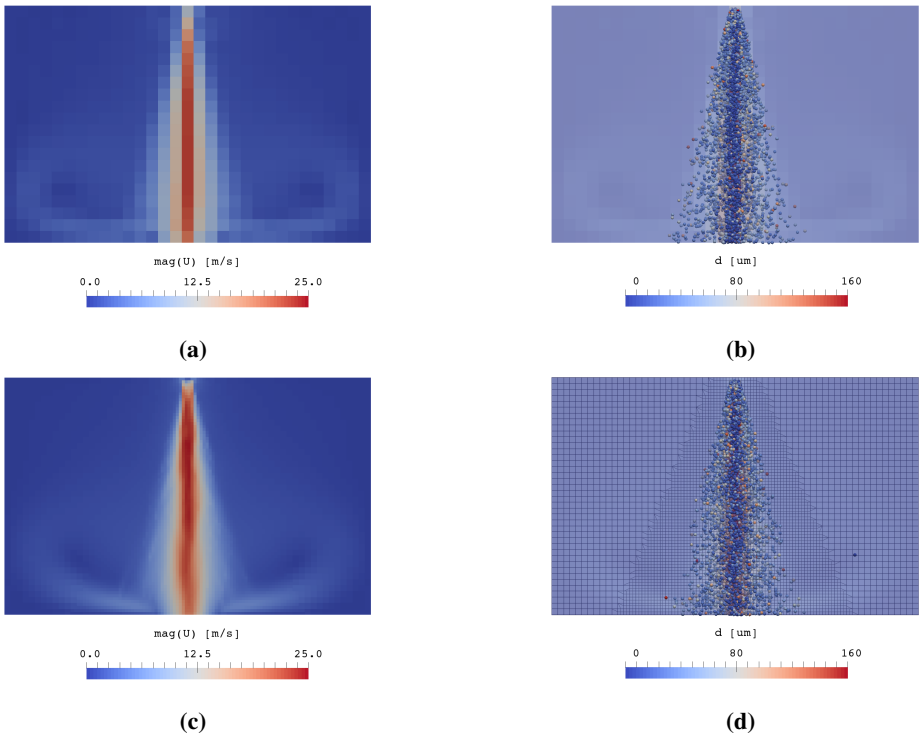

Figure 3.28: *6H - time = 100 ms after SOI - Gas velocity at the system symmetry plane: $coarse$ (a), and $fine$ (c). Spray path and drop diameters: $coarse$ (b), $fine$ (d).*

Thanks to the refined sampling grid provided by the $fine$ test case it is possible to produce a local drop size distribution analysis in the PDA traversing point neighborhoods, as shown in Fig. 3.29. Each probe is composed by 4 faces generating a sampling area of 1 mm^2: this configuration is the result of the trade-off between the necessity of a statistically relevant parcel pool, and the vicinity to the actual PDA sampling point. Therefore it is not a direct comparison, but a useful tool to understand the quality of the spray model. As shown by d_{10} profile plots, the spray core behavior is well captured (Fig. 3.30-a), but the simulation is less accurate in the representation of the periphery, producing a shift of the drop size distribution towards higher values (Fig. 3.30-b).

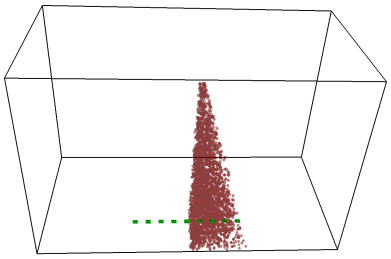

Figure 3.29: *Computational probes (green) used to generate the drop size distribution histograms around the PDA traversing points. The spray is cut in half for visualization purpose.*

These results are acceptable because the mass carried out the by core represents the paramount fraction, as shown in Fig. 3.30-c, and therefore the most important feature to be captured. In particular, more than the 35% of the total liquid mass is collected within a 9 mm^2 area around the injector axis.

Details about the mesh characteristics and the simulation setup are summarized in Appendix B.

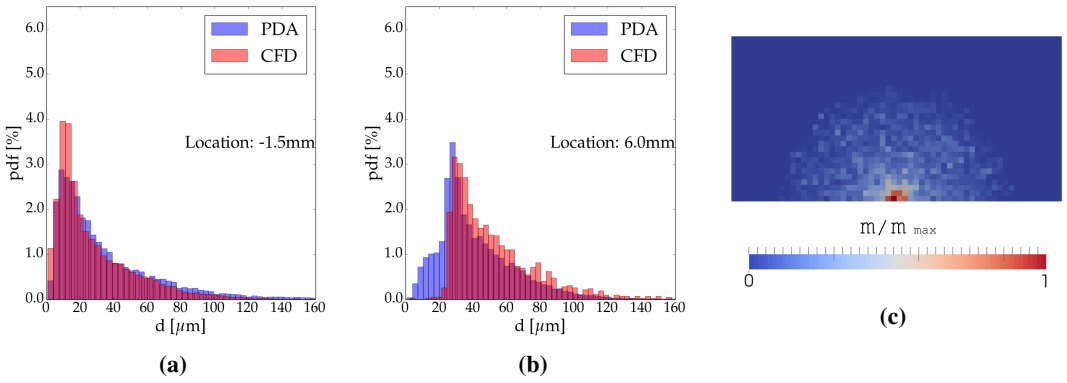

Figure 3.30: *6H - time = 100 ms after SOI - $fine$ test case - drop size distributions: core (a), periphery (b) and simulated normalized liquid mass flow rate at 32 mm from the injection location (c).*

Stochastic collision model The small droplets deviation by the recirculating gas flow and the consequent segregation in the injector axis zone is amplified by the simulation because of the absence of mutual interaction between the spray parcels. The drop-drop collisions have a strong effect on the mean droplet size and its spatial distribution [88] and, therefore, influence the reciprocal coupling between the dispersed and the continuous phases. The probability of two droplets to collide depends on their location, which can be easily quantified by the lower values of cell void fraction close the injector head

(Fig. 3.31-a), velocity and direction. Therefore in the simulated system the near nozzle region is the most probable location for the interactions to happen, as shown in Fig. 3.31-b. As stated in the previous chapter, the model by [63] is the most used in most engine spray simulations. The goal of the use of this model in the simulations is the addition of a shielding effect of the dense spray cloud present in the vicinity of the nozzle head to the recirculating motion of the parcels representing the smaller droplets. The

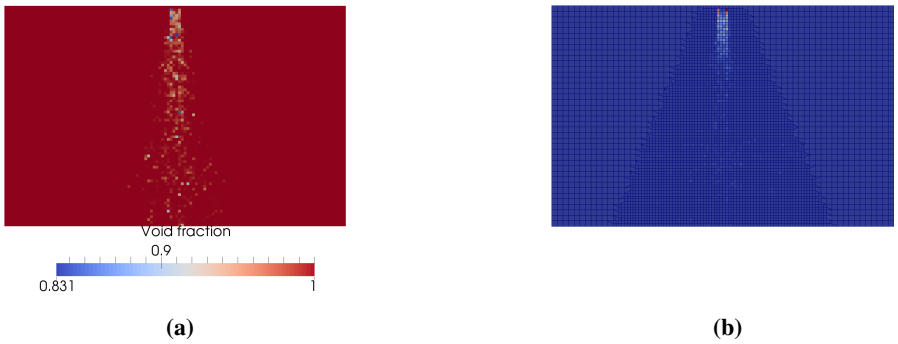

(a) **(b)**

Figure 3.31: *6H - $fine$ test case - Void fraction using the collision model (a) and parcel collision locations (normalized) (b) .*

model has been used just including grazing collisions between the parcels, avoiding any coalescence between pairs because of two major reasons. The first one is the absence of break-up phenomena, and therefore models, for low pressure-driven sprays, which will transport parcels representing large droplets resulting from the impact without taking into account their destructive interaction with the air. The second is the analysis of the discrepancies between the simulation and the experimental data, which shows an overestimation of d_{10} in the periphery of the spray and a drop size distribution lacking of small values. A partial deviation of the small droplets toward the peripheral locations is therefore the major aim of the representation of the droplet collisions. The addition of the collision model was tested on the $fine$ test case, as reported in Fig.3.32, not showing significant modification in the average diameter profile, but improving the axial U trend, mainly due to the momentum transfer from the biggest and most inertial drops to the smaller and deviated ones. The partial enhancement in the prediction of the spray kinematic properties is provided by the single jet shielding capability for the droplets recirculating to the nozzle axis region. The drawback of this feature is represented by the hollow liquid mass pattern generated on a plane set at the PDA sampling distance

(32 mm) from the injector head, reported in Fig. 3.33-a. In the *standard* numerical setup, where the numerical parcels do not mutually interact, the obtained liquid mass distribution is concentrated in the spray axis neighborhood (Fig. 3.33-b) and it is consistent with the findings of [98], who highlighted the pronounced spray mass peak in the axis location projection, collecting the liquid with a mechanical patternator set 75 mm from the nozzle head in quiescent air (Fig. 3.33-c). The reported difference in the spray mass distribution simulation represent a critical feature in the description of the mixture preparation and in the prediction of the effect on the liquid impingement on the wall thermal transients and does not justify the inclusion of the stochastic drop-drop collision model in the injection numerical setup.

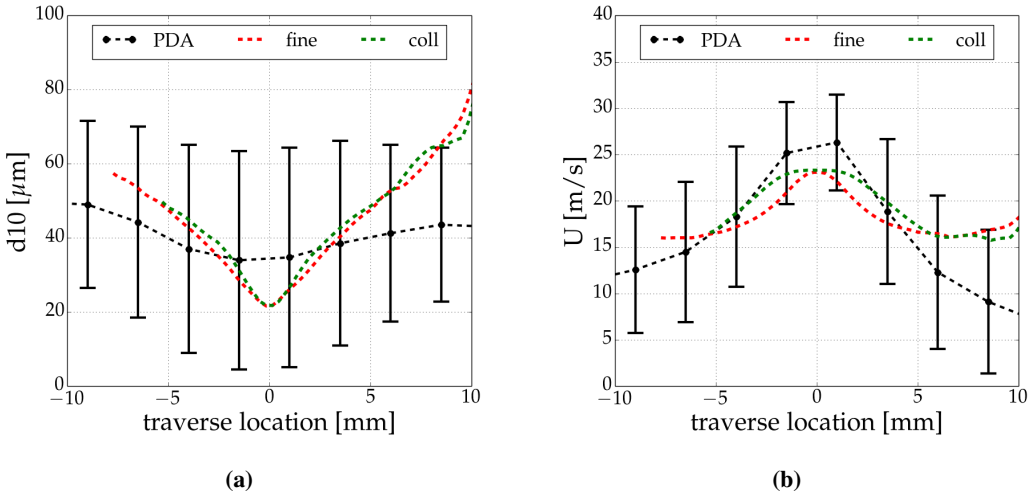

(a) **(b)**

Figure 3.32: *6H - fine test case - d_{10} profile (a) and U profile (b) including the stochastic collision model (labeled as coll).*

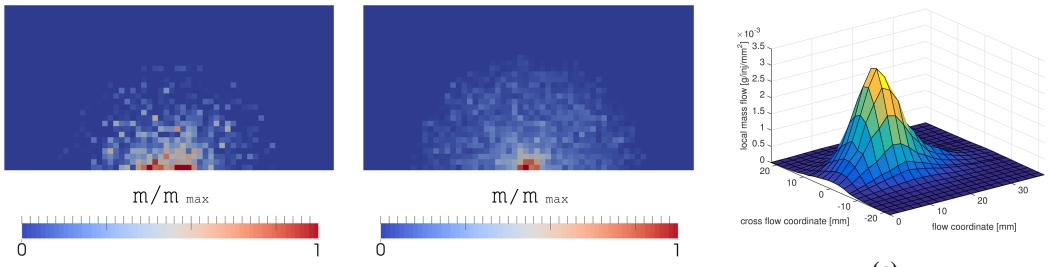

(a) **(b)** **(c)**

Figure 3.33: *6H - fine test case - simulated normalized liquid mass flow rate profile at 32 mm from the injector in quiescent air (fine mesh) adding the drop-to-drop collision model (a), with the standard setup (b) and liquid mass collected by patternation at 75 mm from the injector [98] (c).*

3H - water injection setup The quality and reliability of the method to initialize the Lagrangian model is assessed on the second available data set, represented by distilled water injection through the three hole nozzle (3H). As stated from the Phase Doppler Anemometry and Shadow Imaging campaigns, the clear jet deviation from the nozzle head axis and the consequent spray cone separation generates a negligible cone to cone interaction. Because of the strong influence of the spray on the gaseous flow field, the whole injector is simulated, exploiting the system and injector symmetry as shown in Fig. 3.34.

The Rosin-Rammler formulation fit on the weighted diameter distribution collected

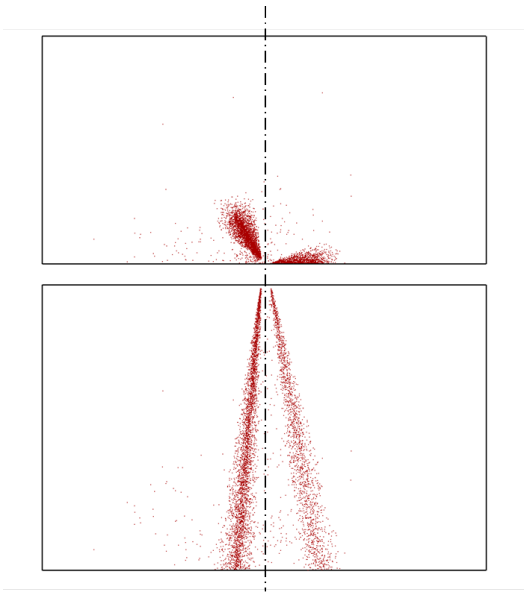

Figure 3.34: *3H - distilled water - CFD spray path for the injection in quiescent air.*

by the PDA produces a scale parameter δ equal to 38.90 μm and a shape parameter n equal to 1.578. The focus is put on the behavior of the single cone on its centerline, which lays on the system symmetric boundary. The single cone characteristic angles are defined according to the supplier specifications (Section 3.1) and the velocity is set to 32 m/s as derived from the PDA data (Paragraph 3.1.2). The reported results show a reasonable agreement between the simulated d_{10} and U trends (Fig. 3.35), showing how the developed approach is capable of reproducing the average kinematic properties of a low pressure-driven injector. Fig. 3.36-a shows that the void fraction constrain for the L-E simulations is fulfilled in the $fine$ mesh test case. The effect of the injection

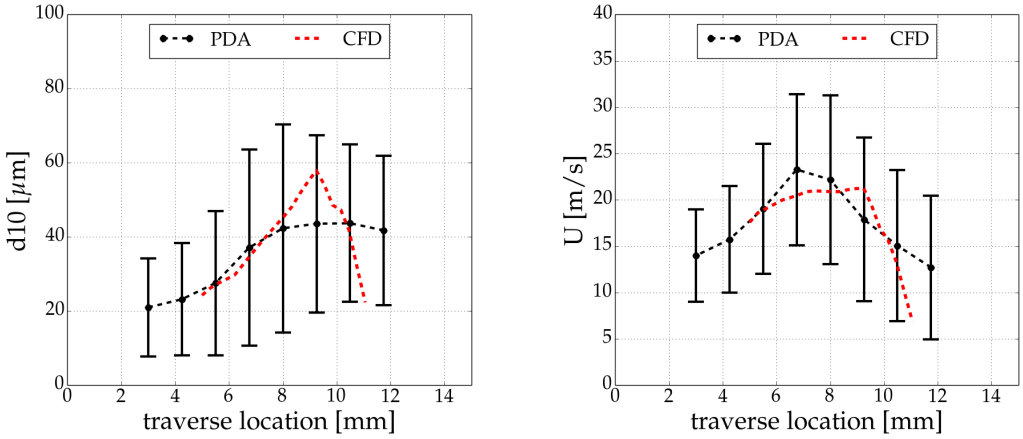

(a) **(b)**

Figure 3.35: *3H - distilled water injection - d_{10} profile (a) and U profile (b).*

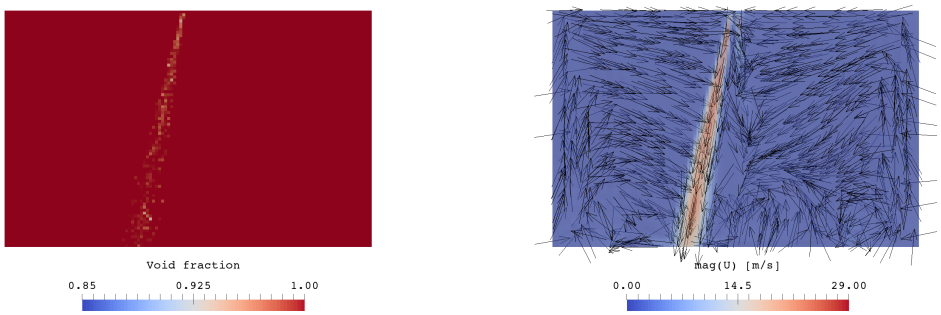

(a) **(b)**

Figure 3.36: *3H - distilled water injection - Void fraction (a) and U_{gas} field (b) at 100 ms after SOI.*

is still a relevant phenomenon in the development of the gas flow field, but the injector hole displacement and the spray cone deviation reduces the effect of the vortexes on the jet.

AdBlue injection

The method described for the extraction of the injector model parameter from the PDA results is applied also to the UWS spray dataset. The difference between the fluids in this operating conditions consists mostly on the different thermophysical properties of the liquid mixture, because no relevant mass transfer is present within the time-scale of the experiment. According to [13] if the surface temperature of the droplet is lower than the saturation temperature of the water (373 K at ambient pressure), the Rapid Mixing (RM) [26, 82] treatment of the UWS solution is a reliable approach to describe

the mass variation of a UWS droplet. It assumes infinite high transport coefficients for the liquid phase, eliminating temperature and concentration spatial gradients within the droplet but not their variation in time (RM in Fig. 2.8). A new set of thermophysical properties for the liquid urea is implemented in the software[2], based on the functions proposed by [109] as suggested by [77] and on the vapor pressure formulation proposed by [12]. A scale parameter equal to 41.45 μm and shape parameter equal to 1.605 are obtained through the fit of the Rosin-Rammler formulation (3.3) on the experimental droplet size distribution. Both the velocity and the single cone angle are kept respectively to 27.4 m/s and 36°. The reported results, shown in Fig.3.37 refer to the $fine$ mesh test case.

The simulation shows the same behavior reported by the water injection, capturing

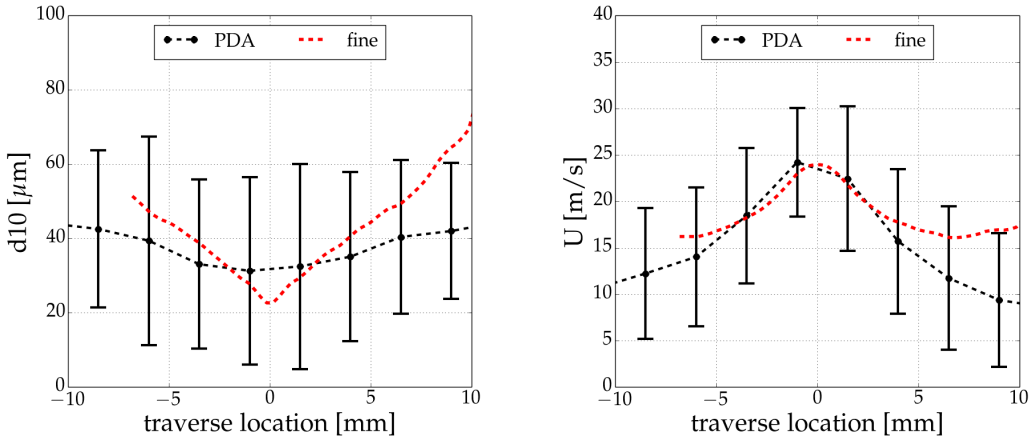

(a) **(b)**

Figure 3.37: *6H - UWS injection - d_{10} profile (a) and U profile (b).*

well the d_{10} and U trends along the traversing line, underestimating the average drop size in the core and shifting the diameter distribution towards higher values in the periphery (Fig. 3.38). No relevant variation is found in the numerical injection behavior in quiescent air conditions. The presence of urea has a negligible effect on the injection process and on the liquid distribution in the simulated domain. Therefore, an acceptable description of the near-nozzle characteristics of 6H is provided as a starting point for the analysis of the SCR spray in engine after-treatment thermal and kinematic conditions for both distilled water and UWS.

[2]See Appendix A

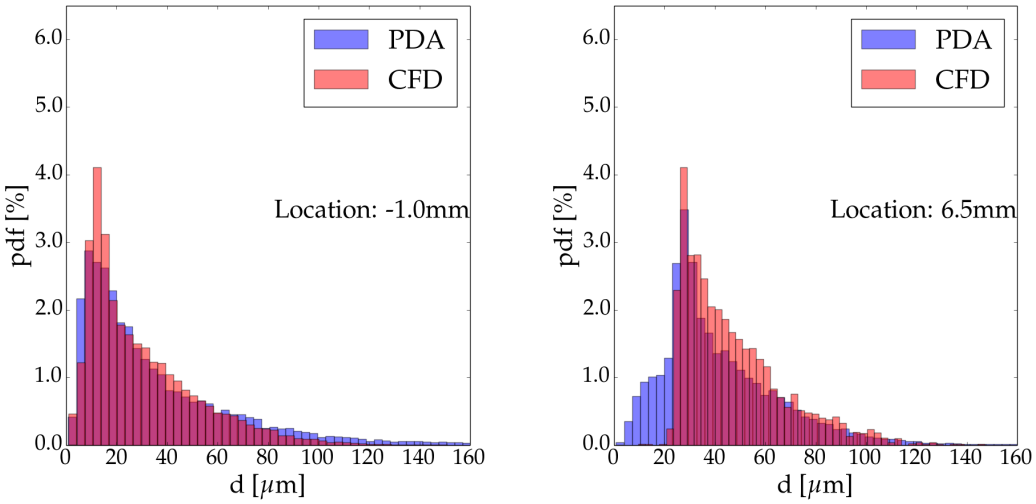

Figure 3.38: *6H - UWS injection - Spray core (a) and periphery (b) size distributions.*

The obtained probability density functions for the three test cases are reported in Fig. 3.39.

The droplet size distributions are subjected to the traverse population weighting based on the PDA data rate, and better reproduce the spray behavior in its core compared to the periphery. This results is part of the data extraction routine definition, which is aimed at building a solid and synthetic tool to investigate the spray behavior in a confined system like the exhaust after-treatment channel.

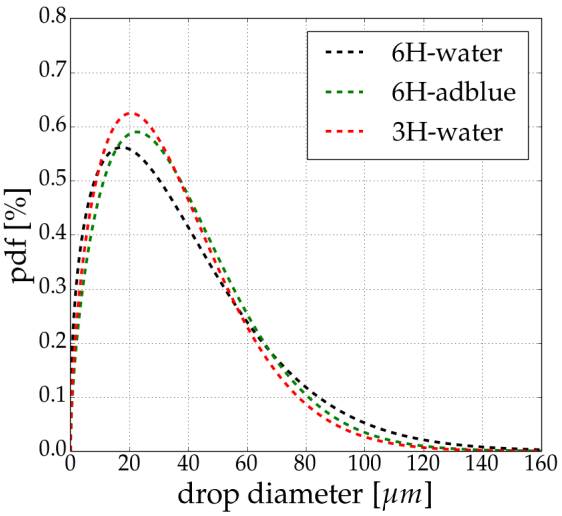

Figure 3.39: *Modeled diameter distribution functions (Rosin-Rammler functions).*

3.2 Spray in cross-flow

3.2.1 Experimental setup

The exhaust after-treatment conditions are reproduced by the engine-less test bench operated with dry air cross-flow shown in Fig. 3.40.

A detailed experimental campaign [43, 44, 84–86, 96] has been carried out on the low

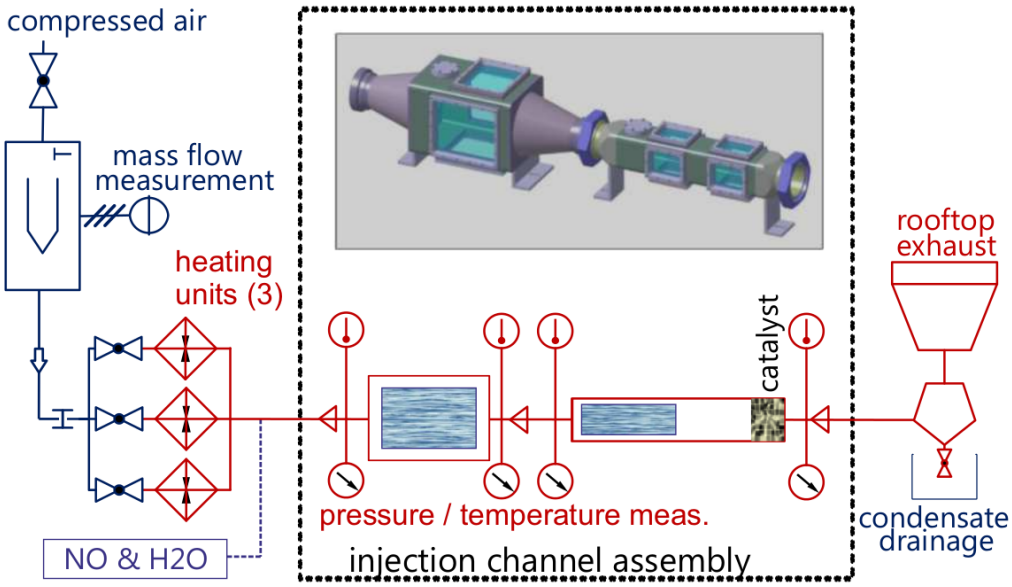

Figure 3.40: *Schematic of the engine-less test bench.*

pressure-driven injection behavior over a wide range of conditions through Shadow Imaging (SI), Phase Doppler Anemometry (PDA), and planar Mie Scattering campaign. The nozzles are top-mounted on the 80×80 square channel, highlighted by the section **B-B** in Fig. 3.41, with an inclination of 50° to the channel axial flow direction. The channel can be fed by a dry air mass flow up to 400 kg/h at a temperature ranging from room temperature to 500° C. Fig. 3.42 reports the flow maps highlighting how the controllable parameters, temperature and mass flow rate, affect the mean flow velocity and volume flow rate (Fig. 3.42-a), the Reynolds number (Fig. 3.42-b) and the flow momentum, $\rho_{gas}\, U_{gas}^2$ (Fig. 3.42-c). Tab. 3.6 summarizes the conditions at which the reported PDA data are collected for each injector.

The installation of the injector seats on the test-bench results in different absolute lo-

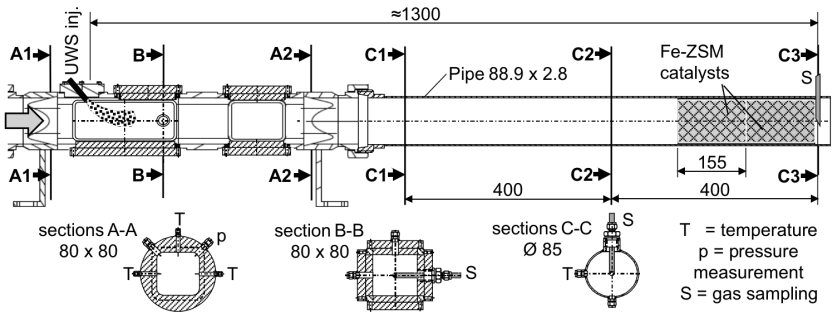

Figure 3.41: *Injection channel assembly sketch [83].*

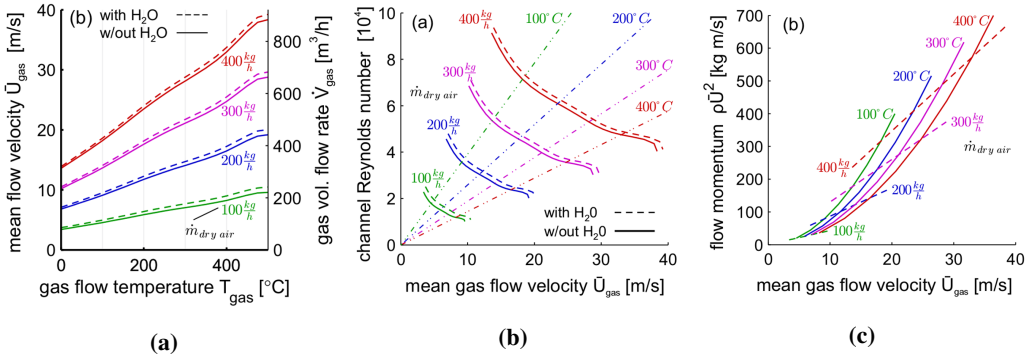

Figure 3.42: *Injection section flow maps [83]. Mean velocity and volumetric flow rate (a), Reynolds number (b) and flow momentum (c).*

cations of the nozzle heads. 6H and 3H are recessed respectively by 7.83 mm (6 mm in the vertical direction) and 22.19 mm (17 mm in vertical direction) along the injector axis. To be able to directly compare the reported results, the origin of a constant coordinate system is set at the intersection between the injector axis and the measurement plane as sketched in Fig. 3.43. As for the previous section, the PDA measurements give the most relevant information for the calibration of the numerical models and therefore represent the reference dataset. To estimate both the vertical and the horizontal component of the droplet velocities a second $Ar^+ - Ion$ laser tuned to the wavelength of 488 nm (blue) is added to the setup reported in Sec. 3.1.1. The beam is horizontally split and phase shifted by a second Bragg cell according to the setup reported in Fig. 3.44. The measuring section is connected with flexible pipes to the channel structure, to be able to modify the relative position of the spray to the PDA system, obtaining the traversing sampling line.

label	$\dot{m}_{gas}$	$U_{flow,gas}$	T_{gas}	Re	Nozzle
	$[kg/h]$	$[m/s]$	$[^\circ C]$	$[-]$	
t200f100	100	5.8	200	13.4 10^3	6H, 3H
t300f200	200	14.2	300	23.6 10^3	3H
t400f400	400	33.1	400	41.5 10^3	6H

Table 3.6: *Summary of the gas flow conditions in the injection section used in the PDA campaign.*

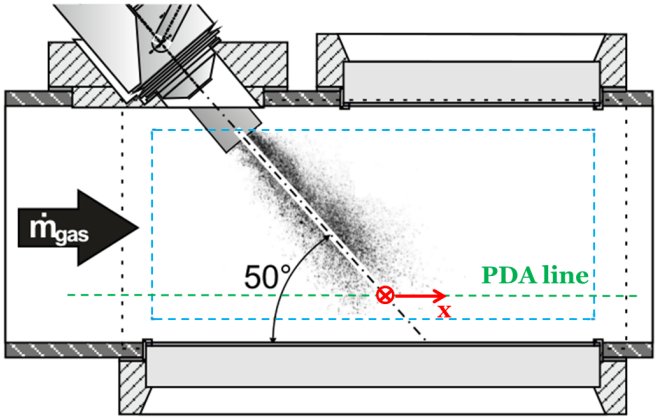

Figure 3.43: *Injector section and system coordinate reference point.*

3.2.2 Experimental results and discussion

The focus of the current analysis involves the influence of the cross flow thermal and momentum loads on the spray pattern inside the channel. Previous Shadow Imaging campaigns [44] showed that a consistent fraction of the liquid injected by the nozzles under investigation reaches the bottom plate of the chamber. This condition generates the arise of a relevant spray-wall interaction, which is the basis for the solid deposit formation and the most relevant phenomenon to be controlled in a in reliable and continual operation of urea based SCR systems. Therefore the PDA datasets of major interests are the farthest from the injector location, both to estimate the entrainment and the phase change in the liquid interaction with the cross flow and to evaluate the characteristics of the spray directed to the bottom surface.

Water injection

The proposed experimental results retrace the steps defined by the injection in quiescent air one, reporting the characteristics of distilled water spray produced by different nozzle configurations (6H, 3H) and the influence of the presence of urea in the liquid

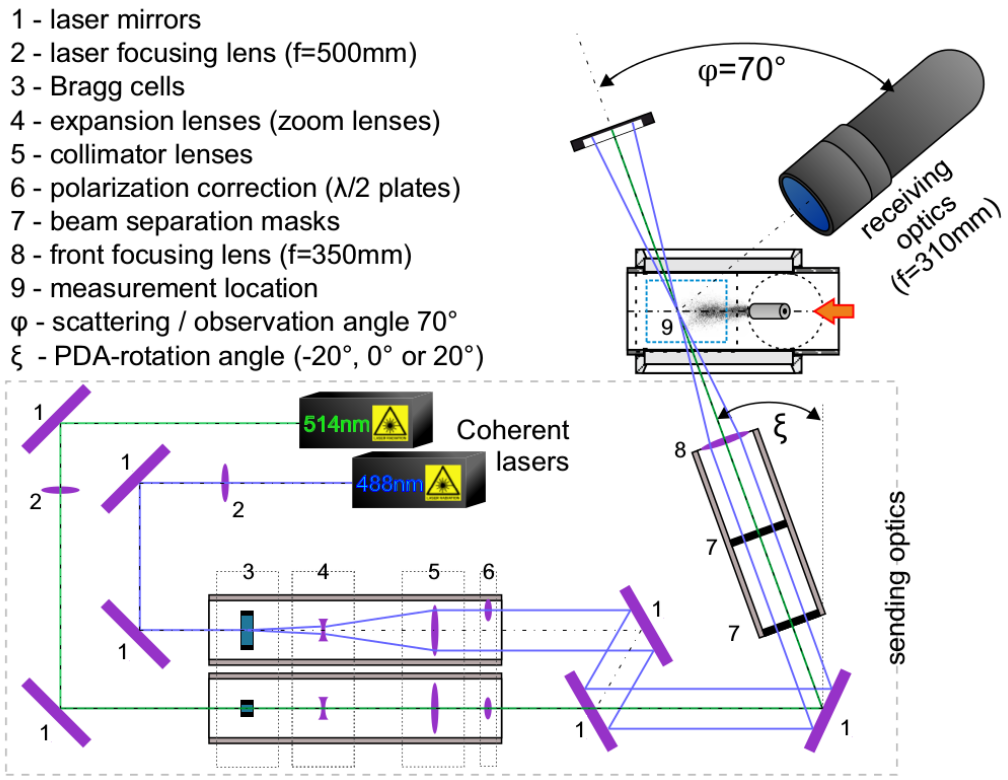

Figure 3.44: *Spray in cross flow PDA system setup [83].*

solution for 6H across the test-bench operating conditions.

6H - water injection The measurements of the spray pattern along the channel (and liquid jet) centerline at 26 mm from the bottom plate have been carried out by [96]. Mechanical constrains and the need of following the channel transversal symmetry, defined the nozzle head orientation, which is reported in Fig. 3.45. The liquid is injected with 1 Hz frequency and a pulse duration equal to 60 ms.

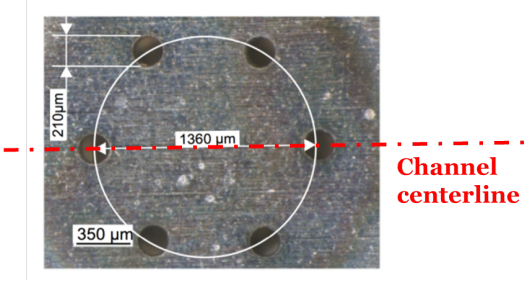

Figure 3.45: *Sketch of the 6H orientation in the channel.*

The spray is traversed by the laser fringe patterns with a spatial resolution of 5 mm (plus the most downstream point which is set 3 mm far from the previous location) in the neighborhood of the injection axis projection, which is set to be the measurement in-built origin (Fig. 3.44). This reference location is horizontally shifted by 50.35 mm from the injector location, as reported in detail in Appendix B. As discovered in the near-nozzle analysis, the six liquid jets overlap in a single conical structure which is not disrupted by the cross flow, as evaluated by [44] and reported in Fig. 3.46-a.

The increment of the gas flow load causes the entrainment and phase change of the

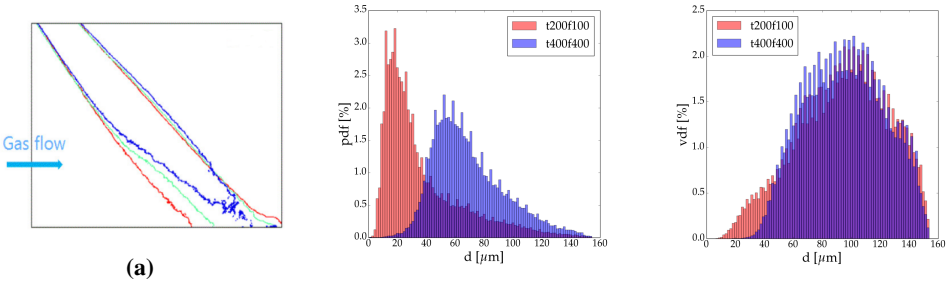

(a) (b) (c)

Figure 3.46: *6H - Shadow imaging contours at different flow conditions (gas flow conditions: 300° C, red: 100kg/h, green:200kg/h, blue: 300kg/h) [44] (a), droplet size probability distribution function (b) and droplet volume distribution (c).*

smallest droplets, which do not reach the PDA sampling plane, shifting the droplet size distribution towards higher values (Fig 3.46-b). In fact the paramount fraction of the spray mass, represented by the droplet volume distribution in Fig. 3.46-c, is only weakly affected by the cross-flow increment, confirming the behavior highlighted by the Shadow Imaging. The average diameter d_{10} and vertical U and horizontal V velocity component plots (Fig. 3.47) confirm that the spray conical structure is not able to shield the small particles from the entrainment causing a gradual decrease in the average drop size at the downstream traverses in both the low load (t200f100) and in the high load (t400f400) conditions. At t200f100 it is possible to notice that the vertical velocity profile (Fig. 3.47-c) partially preserves its original shape, showing a maximum around the 0.0 mm location, which represents the injector axis projection. At t400f400 the gas cross flow alters this behavior, highlighting how the larger droplets, carrying higher velocity and able to reach the sampling plane, do not represent the injected momentum profile.

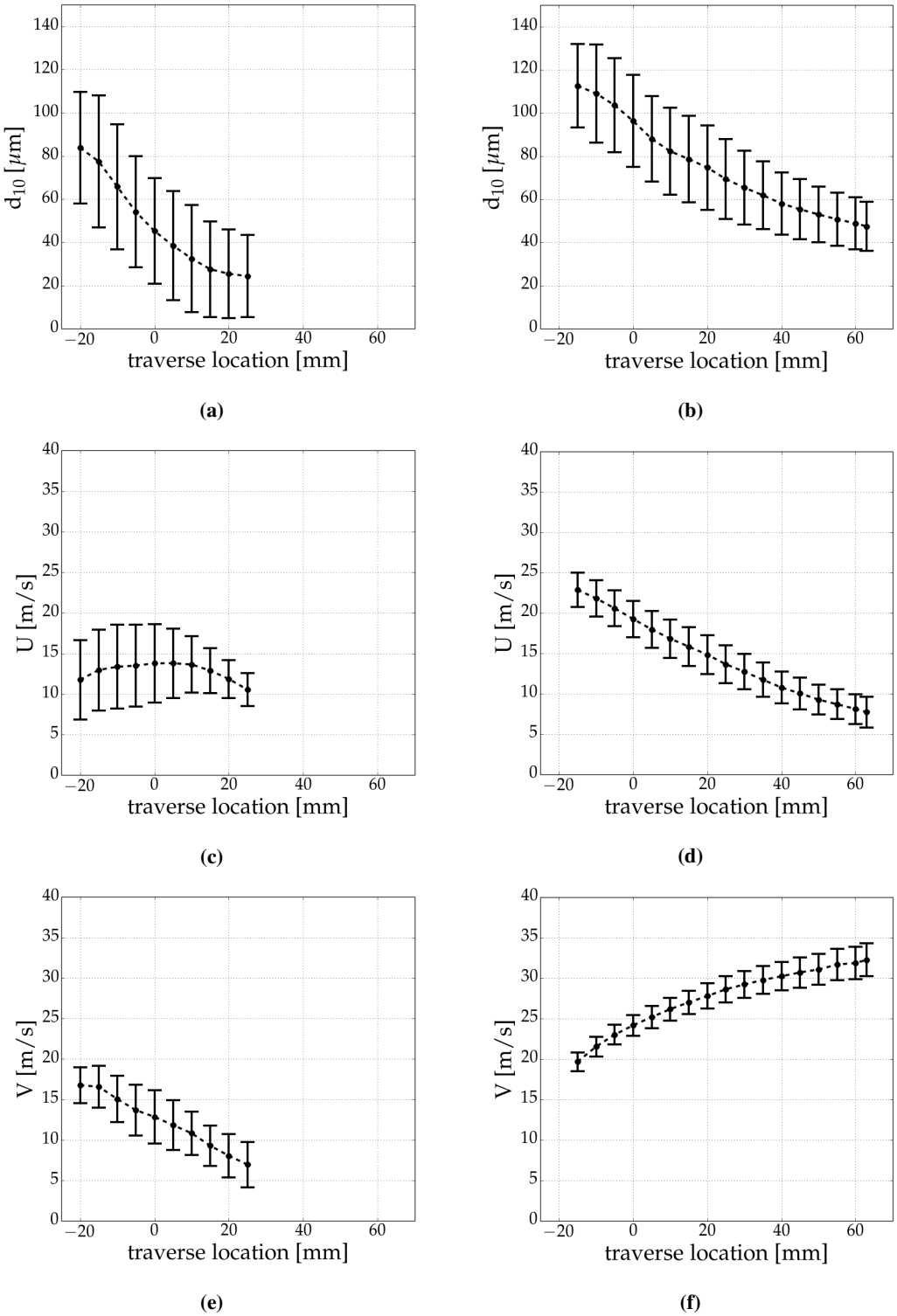

Figure 3.47: *6H - Spray average kinematic parameter profiles. Left: low load (t200f100): d_{10} (a), U (c) and V (e). Right: high load (t400f400): d_{10} (b), U (d) and V (f)*

The effect of the cross flow on the spray kinematics is well represented by the $d - U$ and $d - V$ correlations, especially at t400f400. Fig. 3.48 reports the scatter plot of the collected droplets over the volume distribution, showing that the larger ones conserve their momentum to the PDA sampling plane. The smaller droplets, instead, are deflected by the gas, reducing their vertical component U and being dragged and accelerated by the gas.

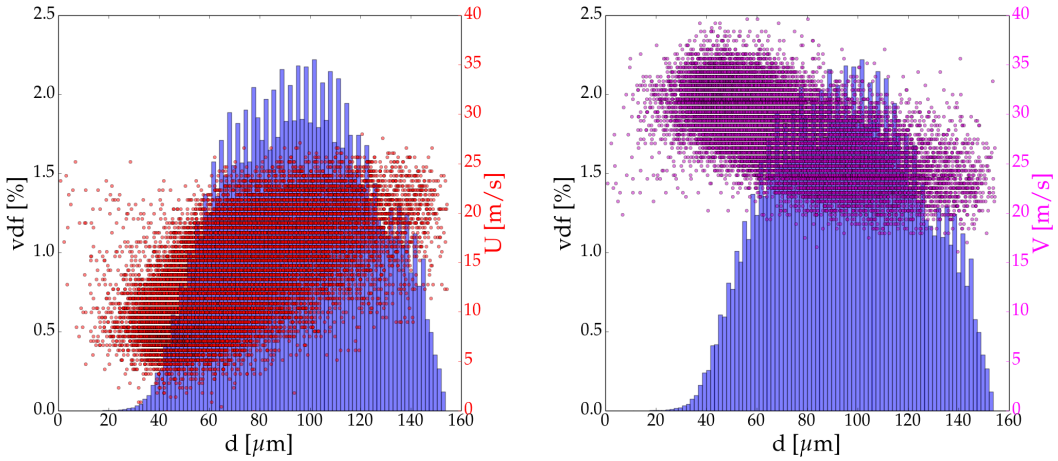

Figure 3.48: *6H - Spray size-velocity relations at high load flow (t400f400). $d - U$ (a), $d - V$ (b)*

3H - water injection The three hole injector is mounted on the test-rig in such way not to alter the channel transversal symmetry as sketched in Fig. 3.49. The most downstream hole, aligned with the channel horizontal, is the object of investigation. This setup is chosen to reduce the influence of the lateral walls on the droplets path and to separate the three spray cones to avoid mutual interactions. The liquid is injected with 3 Hz frequency and a pulse duration equal to 60 ms. The measurement campaign is carried out traversing the spray cone with a resolution of 4 mm along the channel centerline at the lowest optically accessible plane, set 18 mm above the bottom surface[3]. The reported results involve the low load condition (t200f100), and the intermediate condition (t300f200). The spray cones are only weakly affected by the cross flow and a clear separation is visible through lateral Shadow Imaging [44]. The influence of the cross flow interaction increment on d_{10}, U and V is less evident for the three hole injector

[3] See Appendix B for the detailed traverse geometric summary.

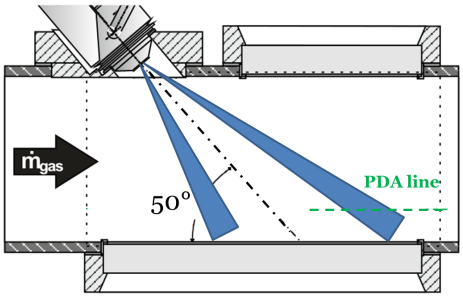

Figure 3.49: *Sketch of the 3H installation on the injection chamber.*

compared to 6H, as shown in Fig. 3.51. The reported profiles show a maximum in correspondence of the front cone axis projection, situated 31.7 mm downstream of the PDA reference system origin, both at t200f100 and t300f200. Fig. 3.50 reports, over the collected spray volume distribution at intermediate load conditions (t300f200), the average vertical and horizontal velocity components calculated for each size sampling bin, highlighting that the larger droplets maintain a large portion of their initial velocity which is visible from both the measured components. At this cross flow conditions, the mean flow velocity $U_{flow,gas}$ is equal to 14.2 m/s and corresponds to the lower threshold of the horizontal component of the droplet velocity (Fig. 3.50-b), underlining that the largest droplets carry a considerable fraction of their momentum. The same trend is clear in the vertical droplet velocity U plot (Fig. 3.50-a) which shows a relevant entrainment only for the droplets with small sizes.

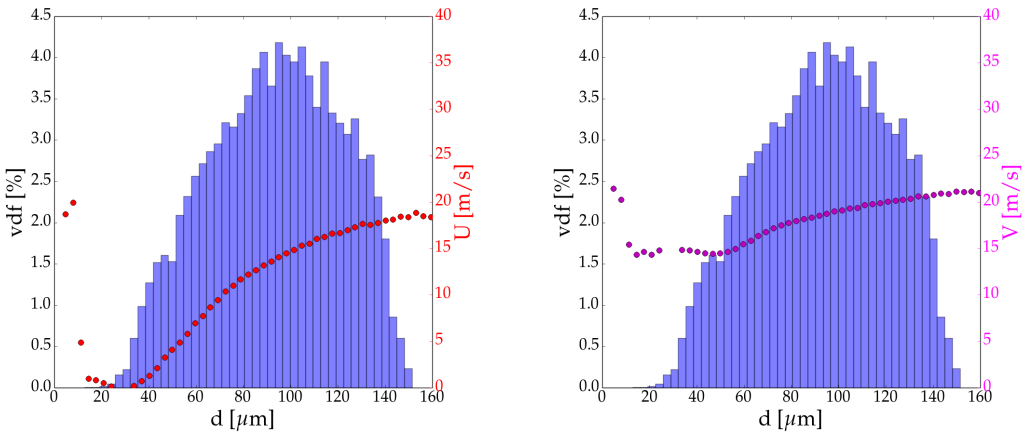

Figure 3.50: *3H - Spray size-velocity relations at intermediate load flow (t300f200). $d-U$ (a), $d-V$ (b)*

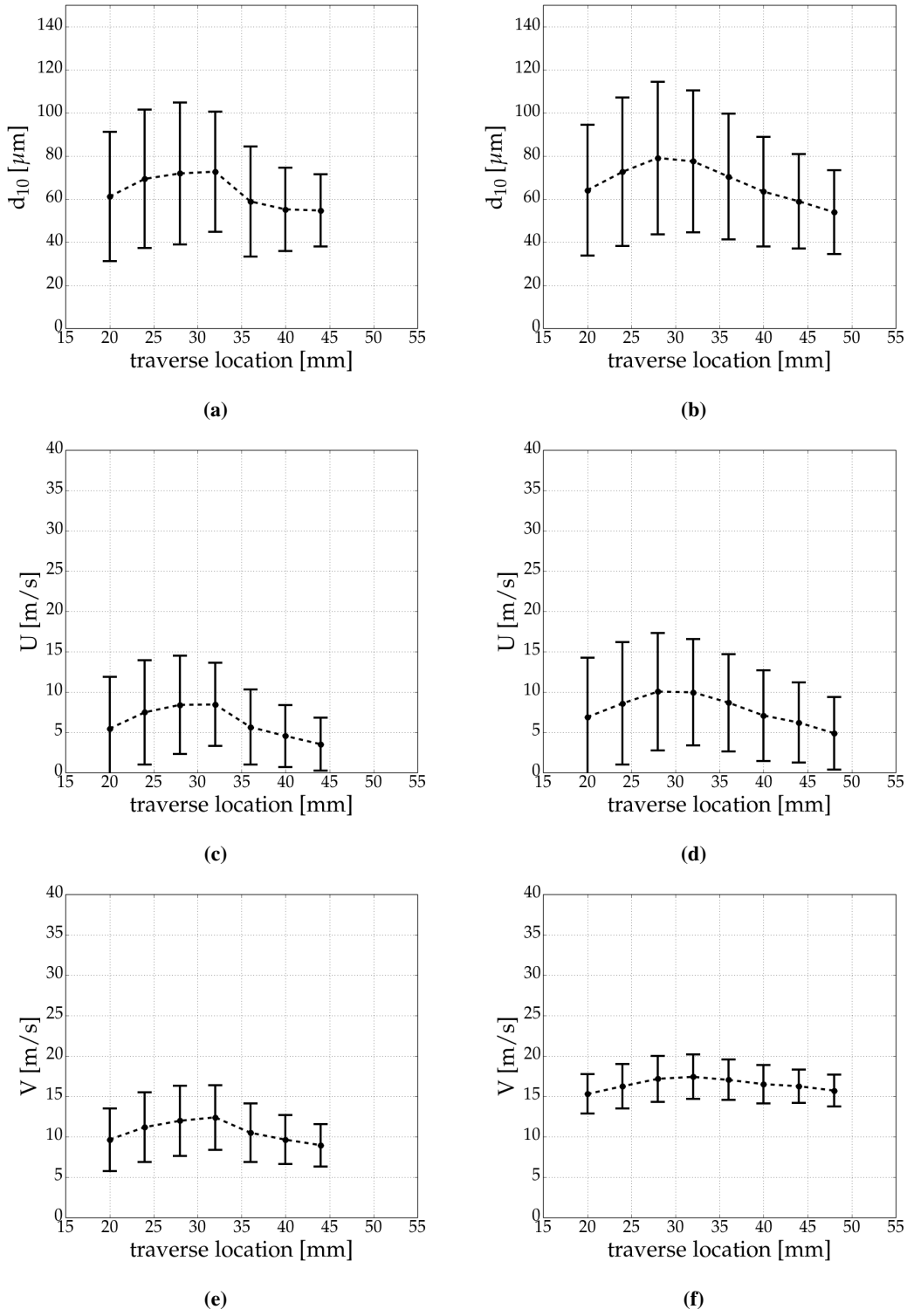

Figure 3.51: *3H - Spray average kinematic parameter profiles. Left: low load (t200f100): d_{10} (a), U (c) and V (e). Right: intermediate load (t300f200): d_{10} (b), U (d) and V (f)*

6H - AdBlue® injection Shadow Imaging and planar Mie scattering results across the test bench operating conditions [84], show no distinction between the water and UWS liquid distribution in the spray-gas interaction phenomenon.

Fig. 3.52 reports the spray lateral view contours constructed by averaging SI images, showing negligible difference both in the internal and in the cone periphery at high load conditions, $(\rho U^2_{flow})_{gas} = 404\ kg/(m\,s^2)$.

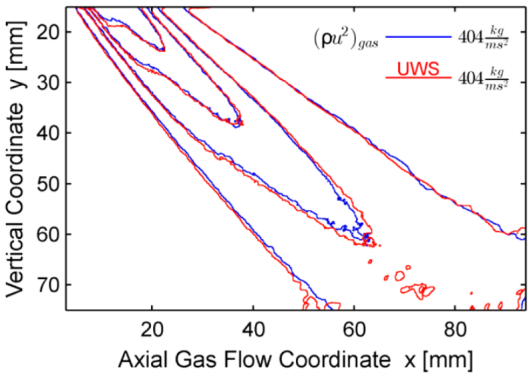

Figure 3.52: *6H - SI image intensity contours [83].*

The invariance in the kinematic behavior between water and UWS spray-gas interaction is confirmed by the PDA data. Fig. 3.53 shows the UWS droplets average d_{10}, U and V profiles, reporting the same trends exhibited by the distilled water ones. The scatter plots of $d-U$ and $d-V$ (Fig. 3.54) relations lead to the same conclusions drawn in the previous section, showing that the kinematic properties of the small droplets are strongly modified by the cross flow, which is not able to deflect the inner spray core.

3.2.3 Numerical modeling

The goal of this section is the generation of a reliable and robust numerical model to simulate the spray behavior at exhaust after-treatment real operating conditions. The injection section of the test-rig is reproduced and the spray model defined in Sec. 3.1.3 is applied to represent the near-nozzle behavior of the Lagrangian phase. The influence of the most important submodels is investigated on the basis of the comparison with average and local Phase Doppler Anemometry data.

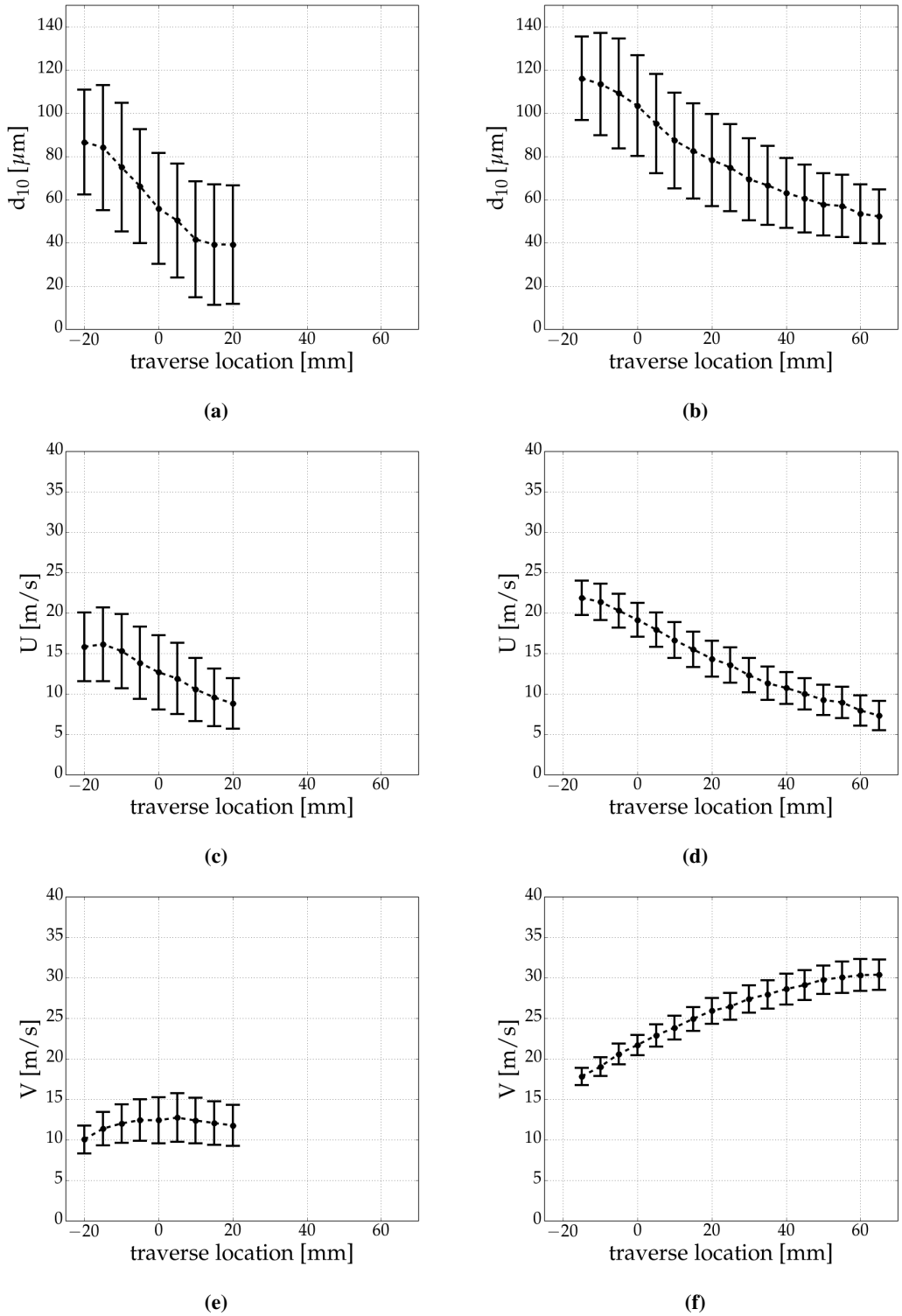

Figure 3.53: *6H - UWS injection - Spray average kinematic parameter profiles. Left: low load (t200f100): d_{10} (a), U (c) and V (e). Right: high load (t400f400): d_{10} (b), U (d) and V (f)*

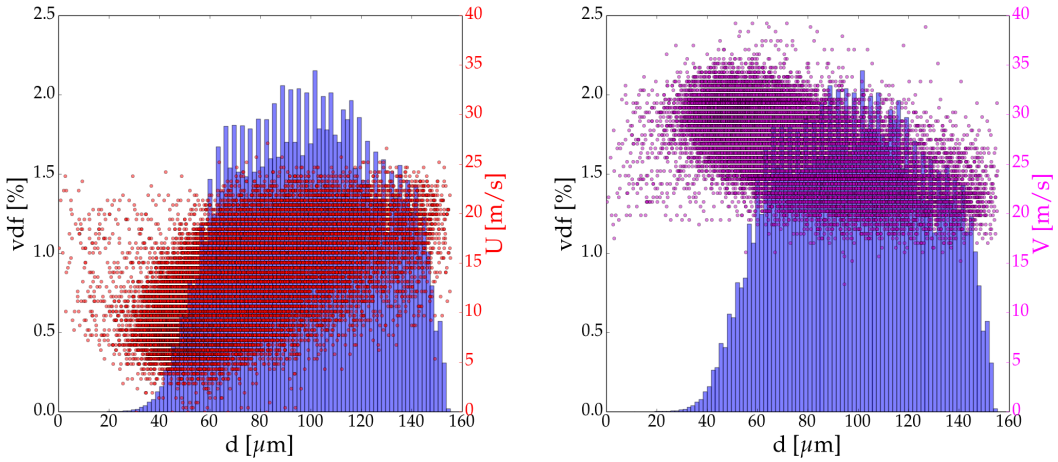

(a) **(b)**

Figure 3.54: *6H - UWS injection - Spray size-velocity relations at high load flow (t400f400). $d - U$ (a), $d - V$ (b)*

Mesh and gas phase definition

The optically accessible injection section, highlighted in Fig. 3.55-a, is a 80×80 mm square chamber and the phenomena under investigation in the analysis of the spray development are included in the axial range $[0 \ - \ 200]$ mm from the injector location. To reduce the interference of the boundaries in the development of both continuous and dispersed phases, the computational domain is defined to cover the axial range $[-120 \ - \ 280]$ mm, as reported by Fig. 3.55-b. A simplified squared section duct geometry simulates the computation system, as suggested by [95]. The injector channel is reproduced adding a square channel inclined according to the nozzle axis direction. Its length depends on the injector mount location which is specified in Sec. 3.2.1. The details of the mesh are reported in Appendix B.

Thanks to the transversal symmetry of the test-rig and of the nozzles, the numerical domain is split in half along the channel axis by a vertical plane to reduce the computational costs. Symmetry boundary conditions are applied on the resulting surface.

Initial and Boundary conditions Dry air, used as operating gas according to the specifications provided in in Sec. 3.1.3, is initialized providing fully developed fields for the velocity and the turbulence variables (k and ε according to the standard $k - \varepsilon$ model) at the domain. This conditions are reached running a steady-state incompressible flow

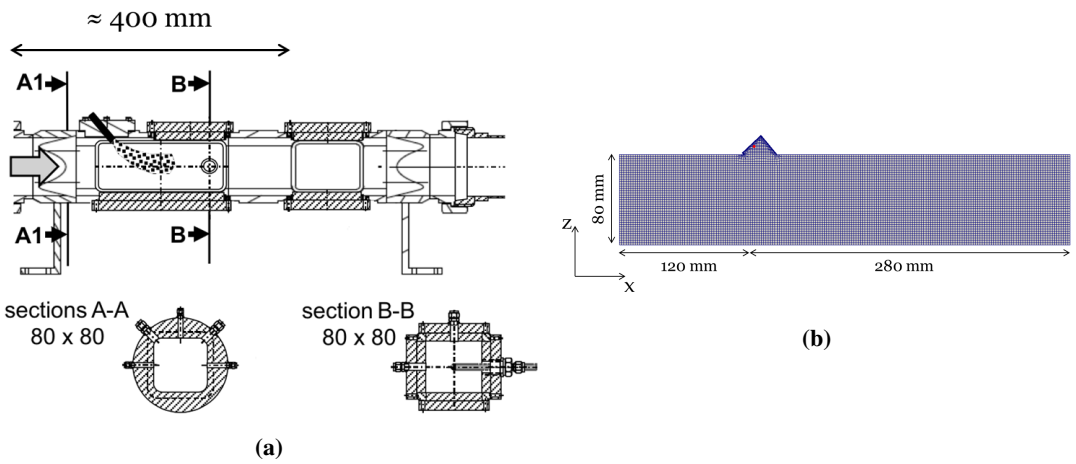

Figure 3.55: *Injection section of the test-rig (a) and simulation domain (b).*

simulation driven by a pressure gradient on an auxiliary mesh (Fig. 3.56-a) and mapping the outlet U_{gas}, k and ε fields on the inlet. The applied pressure gradient consists of an explicit source term applied to the momentum equation according to the average flow velocity. The solution of the simulation, providing the surface fields on an inlet patch shown in Fig. 3.56-b, allows the direct application to the channel mesh because of a full geometrical consistency. The fully developed flow initial condition setup on the

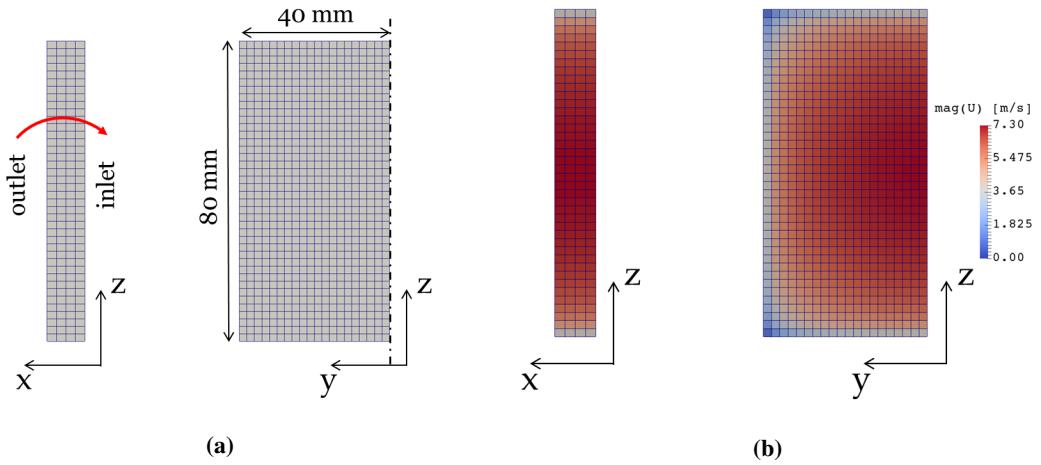

Figure 3.56: *Auxiliary computational grid (a) and steady-state velocity profile for low load conditions (t200f100) (b).*

channel domain is then obtained running a compressible steady-state simulation starting from quiescent air at the temperature of the simulated flow regime. The boundary conditions reported in Tab. 3.7 are applied to the steady-state preliminary simulation and to the spray tracking cases.

	solid walls	inlet	outlet	symmetry plane
$\mathbf{U}_{gas}$	No slip	$\mathbf{U}_{gas}$=$\mathbf{U}_{gas,developed}$	$\partial\mathbf{U}/\partial\mathbf{n}$=0	reflecting-symmetric
P_{gas}	∂P/$\partial\mathbf{n}$=0	∂P/$\partial\mathbf{n}$=0	wave-transmissive [69]	reflecting-symmetric
T_{gas}	$\partial T_{gas}/\partial\mathbf{n}$=0	T_{gas}=$T_{gas,0}$	$\partial T_{gas}/\partial\mathbf{n}$=0	reflecting-symmetric
$Y_{i,gas}$	$\partial Y_i/\partial\mathbf{n}$=0	$Y_{i,gas}$=$Y_{i,gas,0}$	$\partial Y_i/\partial\mathbf{n}$=0	reflecting-symmetric
k	scalable (all y^+)	k=$k_{developed}$	$\partial k/\partial\mathbf{n}$=0	reflecting-symmetric
ε	scalable (all y^+)	ε=$\varepsilon_{developed}$	$\partial\varepsilon/\partial\mathbf{n}$=0	reflecting-symmetric

Table 3.7: *CFD boundary condition summary.*

Spray simulation

The injector models developed within the injection in quiescent air framework, are applied to the channel domain as a starting point for the development of a robust simulation setup, including a correct characterization of the heat and mass exchange between the liquid and the gaseous phase. The analysis of 6H injecting distilled water is the reference test in the application of the spray submodels in cross-flow conditions, which is tested on the behavior of 3H. As for the injection in quiescent air, the influence of the effect of urea in the system is evaluated on 6H. Due to the consistency in the mesh structure and in the parcel-gas interaction kinematic characteristics, the near-nozzle modeling is kept as defined in the previous numerical campaign. In particular, no primary break-up models are applied to the spray, and a direct assignment of the initial conditions of each parcel in terms of size velocity and direction is explicitly defined by the conical nozzle injector model.

The extremely limited number of droplets clearly directed upwards collected in the PDA measurements, highlights the weak influence of the interaction with the bottom surface in the estimation of the kinematic properties of the spray at the sampling location. This assumption, coupled with the reduced injection frequency (1 Hz), allows considering a single injection pulse (DOI = 60 ms) as significant representation of the experimental conditions, neglecting the phenomena involving longer time scales than then injection period, as wall film development or spray recirculation. Therefore, the simulated spray involves a single pulse with constant injection law, and the reported results refer to the End Of Injection (EOI), to allow the complete development of the liquid in the channel and to collect enough parcel events to produce statistically valuable data. A simplified spray-wall interaction model, consisting in an artificial sticking

and de-coupling from the continuous phase of the parcels hitting a solid surface, is applied to the solid walls of the system.

Grid dependency The high load condition (t400f400) is taken into account to estimate the influence of the grid refinement on the spray evolution in the system, because of the strongest spatial gradients caused by the higher momentum and energy sources provided by the cross-flow. The average kinematic properties of the spray collected on the sampling line are reported in Fig. 3.58, showing no significant difference with an increment in the mesh refinement. The $coarse$ label refers to a grid composed of cubic cells with an edge size of 2 mm, in agreement with the injection in quiescent air cases. The mid test case involves a tridimensional refinement along the spray path conical projection which generates cubic cells with an edge size of 1 mm, as reported in Fig. 3.57-a, to reduce the computational expenses. Fig. 3.57-b, shows that the minimum void fraction is never lower than 0.9, allowing a consistent comparison between the two cases.

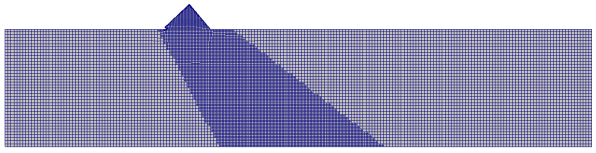

(a)

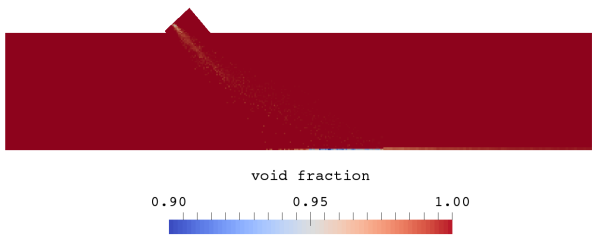

(b)

Figure 3.57: *6H - distilled water injection - high load t400f400 - mid test case conical refinement (a) and void fraction at 60 ms after the SOI at t400f400 (b).*

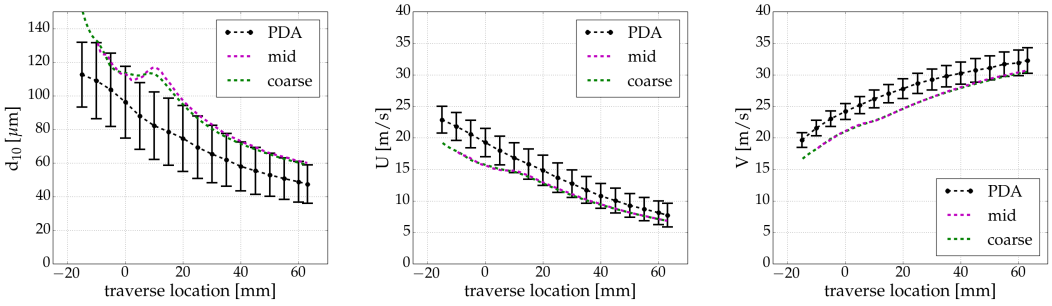

Figure 3.58: *6H - distilled water injection - high load t400f400 - Grid refinement effect on the average spray properties: average diameter d_{10} (a), vertical U (b) and horizontal V (c) velocity components.*

The development of the dispersed phase inside the system is shown in Fig. 3.59 in terms of size, velocity magnitude and temperature of the computational parcels, showing no remarkable differences. The dimension of the spheres corresponds to the representative diameter of each parcel, highlighting the results obtained analyzing the PDA results, where the larger drops are not deflected by the cross-flow and maintain a significant fraction of their initial momentum. On the contrary the smaller ones are accelerated by the flow and experience an approximately horizontal trajectory. The temperature of the liquid inside the chamber is always considerably lower than the saturation temperature, which is reached just by the smallest parcels, suddenly deflected to generate the top part of the spray wake. The grid refinement effect is negligible also for the gas phase, as shown in Fig. 3.60 which reports the velocity magnitude at 60 ms after the SOI, sampled on the section corresponding to the intersection of the injector axis with the top wall (left), with the bottom wall (center), and with the computational domain outlet (right).

From the reported results it is possible to notice that the trends of the average kinematic properties of the droplets are captured on the $coarse$ mesh, which becomes the reference test case for further simulation and discussion. The spray simulation at high flow conditions (t400f400) provides reasonable agreement with the experimental PDA data, slightly underestimating the droplet velocity, but over predicting the average diameter. The hump in the size profile (Fig. 3.58-a) is ascribed to the lack of a reliable mutual collision model, which can improve the momentum exchange within the liquid phase in the denser spray core.

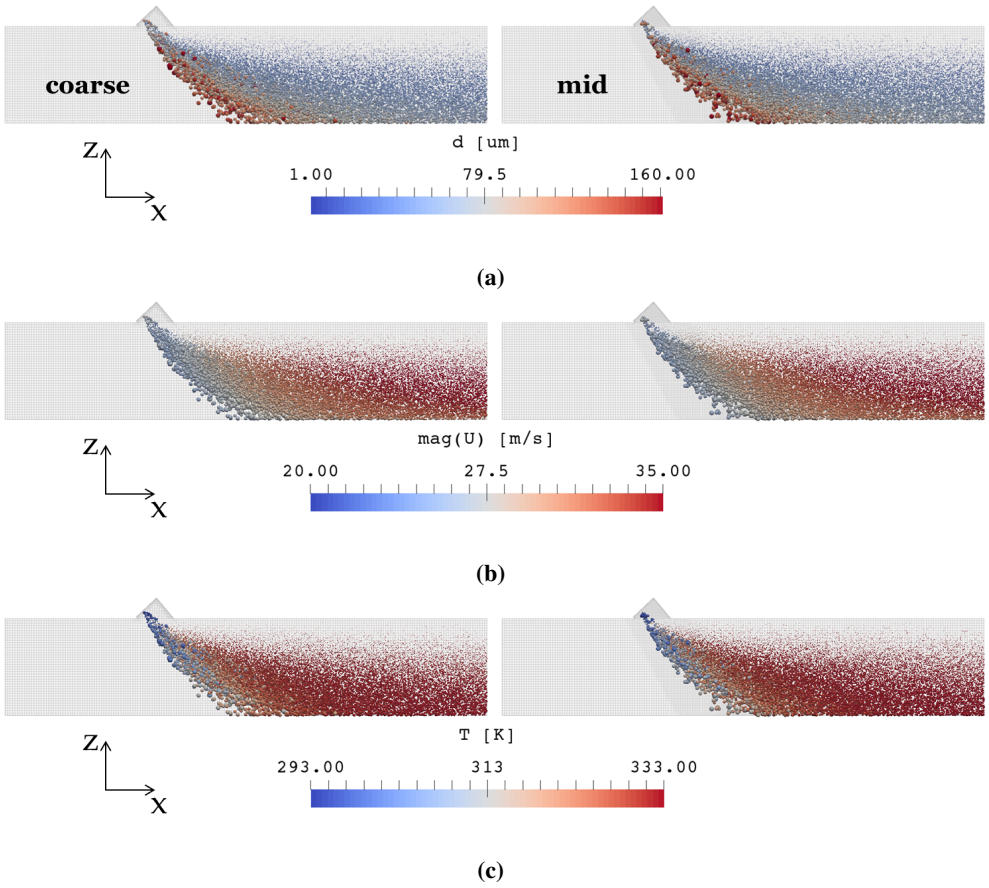

Figure 3.59: *6H - water injection - effect of the grid refinement on the spray at high flow conditions (t400f400) - time: 0.1 s after SOI. Drop size (a), velocity magnitude (b) and liquid temperature (c) of the injected spray.*

Parcel characterization method The influence of the method used in the parcel properties assignment is investigated at low load conditions (t200f100) where a better estimation of the effect of the cross flow on the spray is possible, avoiding the deflection of the paramount number of parcels representing the smaller droplets and the reduction the target of the investigation to only the most inertial ones able to reach the PDA traversing line. As stated in Sec. 3.1.3, the definition of a constant number of droplets per parcel has shown a better agreement with the PDA data collected injecting in quiescent air. The improvement of this approach is still evident at t200f100, where the constant mass approach, labeled $mass$ in Fig. 3.61-a, strongly underestimates the average droplet size from the core of the spray, ideally projected at 0.0 mm location, to the end of the liquid wake. Fig. 3.61-b shows the fully developed spray shape, at 60 ms after SOI, on the centerline of the system, restating the weak liquid entrainment.

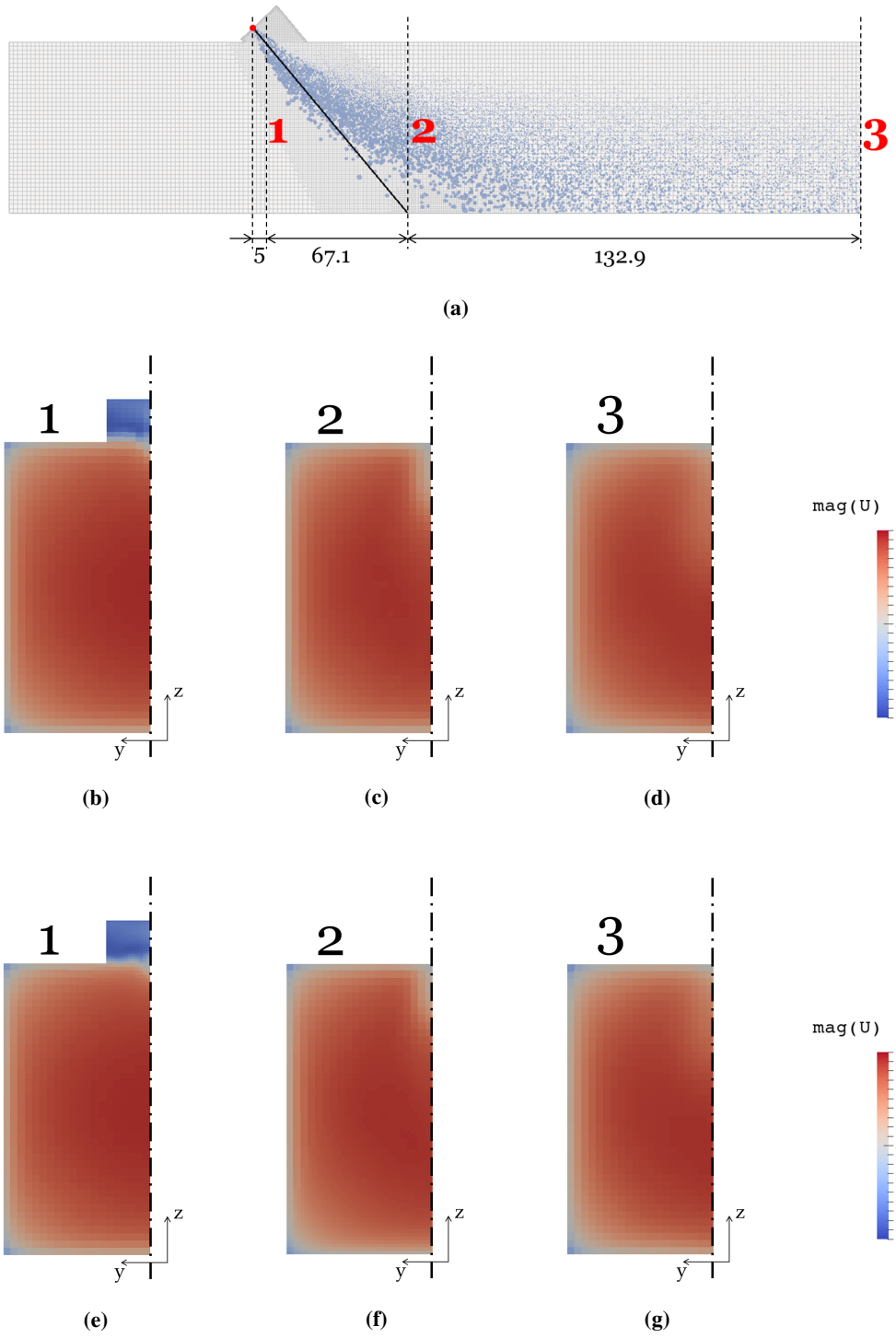

Figure 3.60: *6H - Distilled water injection - high load t400f400 - Gas flow velocity magnitude profiles at 60 ms after SOI. coarse test case (top row), and mid test case (bottom row). Section corresponding to the injector axis intersection with the top wall (a,e), with the bottom wall (b,f) and to the domain outlet (c,g).*

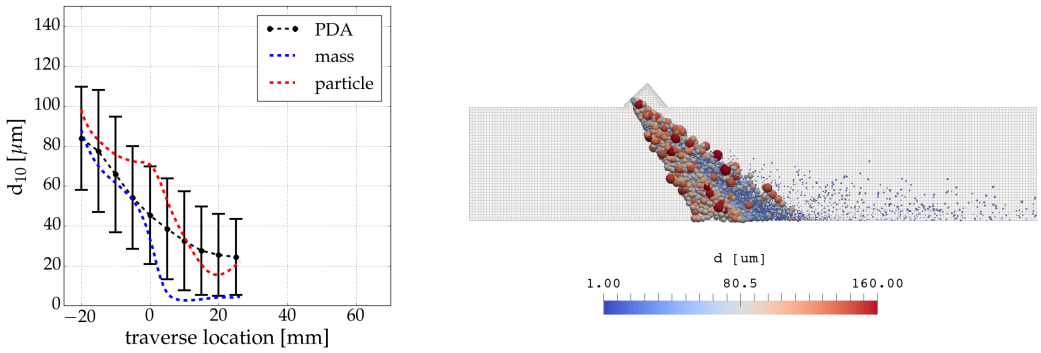

(a) **(b)**

Figure 3.61: *6H - distilled water injection - low load t200f100 - d_{10} profile (a) and fixed particle per parcel spray evolution (b).*

3H - water injection

The spray modeling in cross-flow conditions is tested on the same computational domain with the three hole injection. The nozzle position and orientation are set according to the sketch reported in Fig. 3.49 and the front hole is halved by the symmetry plane and crossed by the sampling line.

Fig. 3.62 reports the kinematic properties compared to the experimental PDA data. The simulation predicts a stronger cone deflection, which is clearer in the intermediate load conditions (t300f200) showing a shift of the spray location, which corresponds to the sampling range extension. Moreover, the strong overestimation of the average diameter is an indicator of the entrainment of an excessive fraction of the parcel representing small droplets, reported in Fig. 3.63. The three hole configuration, coupled with the thinner cone aperture, amplifies the drawbacks of the proposed simulation setup, which are attributable to the lack of characterization of the dense spray core features, represented by the drop-drop collisions and the primary breakup phenomenon.

6H - AdBlue® injection

The lack of characterization of the chemical reaction involved in the urea decomposition [8,13] and the choice of the Rapid Mixing model for the parcels in the estimation of the spray modeling behavior in the system, implicate a strong limitation of the characterization of the phase change of the UWS droplets. The findings of [83] are, however,

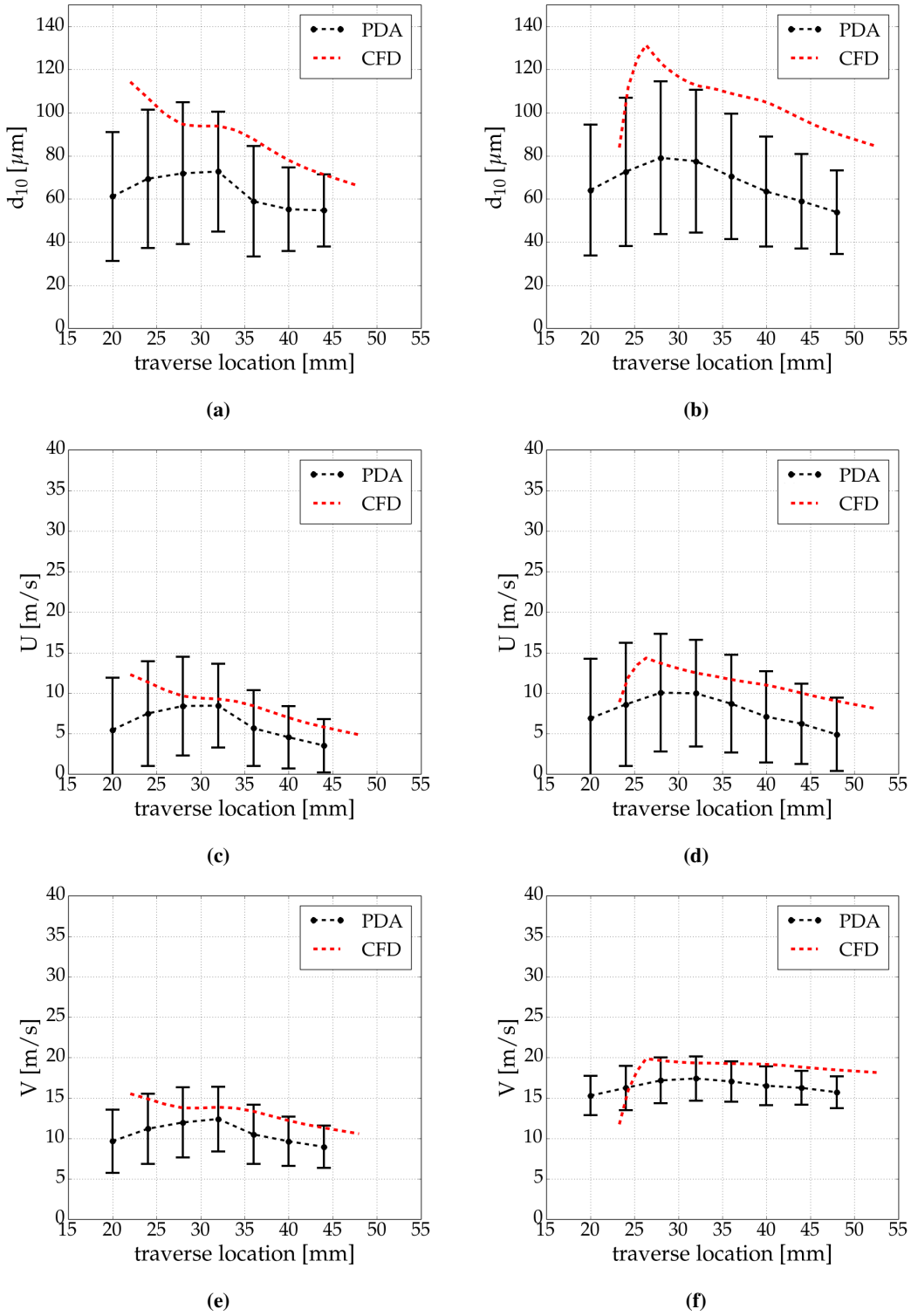

Figure 3.62: *3H - water injection - Spray average kinematic parameter profiles. Left: low load (t200f100): d_{10} (a), U (c) and V (e). Right: intermediate load (t300f200): d_{10} (b), U (d) and V (f).*

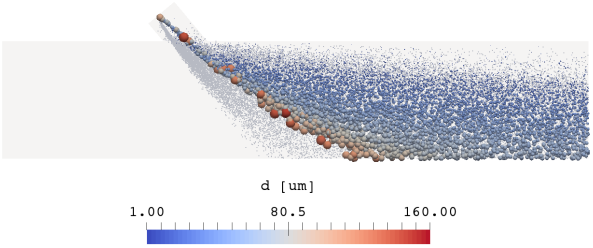

Figure 3.63: *3H - water injection - Spray diameter at intermediate load conditions (t300f200). Excessive entrainment of the small droplets. The upstream parcels are generated by the lateral injector cone.*

reproduced by the simulations up to the high load conditions (t400f400), which point out an average urea mass fraction Y_{urea} close to the injected one, as visible in Fig. 3.64-a. Fig. 3.64-b shows that the fraction of the simulated spray reaching a temperature $T > 360\ K$ does not cross the sampling plane. The comparison between the

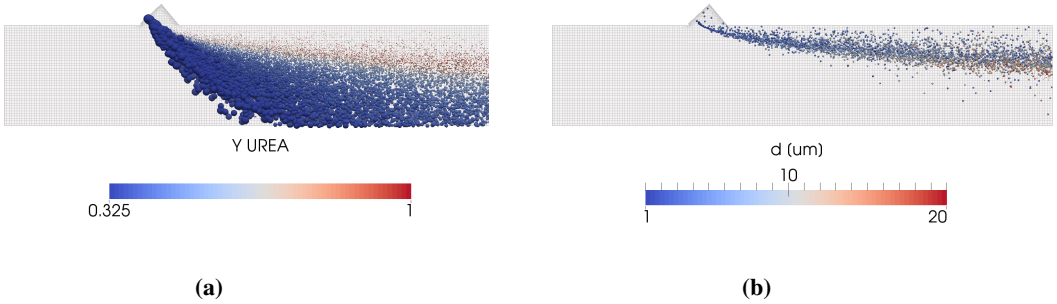

(a) **(b)**

Figure 3.64: *6H - UWS injection - high load t400f400 - urea fraction in the liquid mixture Y_{urea} (a) and diameter of the parcels reaching $T > 360\ K$ (b).*

average kinematic properties of the spray is reported in Fig. 3.65, showing reasonable agreement in capturing the spray trends. The left column refers to the low load conditions, t200f100, the right one to the high load ones, t400f400.

The measured and reported data provide a description of the interaction of the sprays generated by low pressure-driven injection over a wide range of operating conditions. This chapter represents also the starting point of the analysis of one of the most important features in the operation of the urea based SCR technology, which is represented by the spray-wall interaction. Starting from near-nozzle PDA data, the definition of the injector model properties is carried out, providing the kinematic properties of the

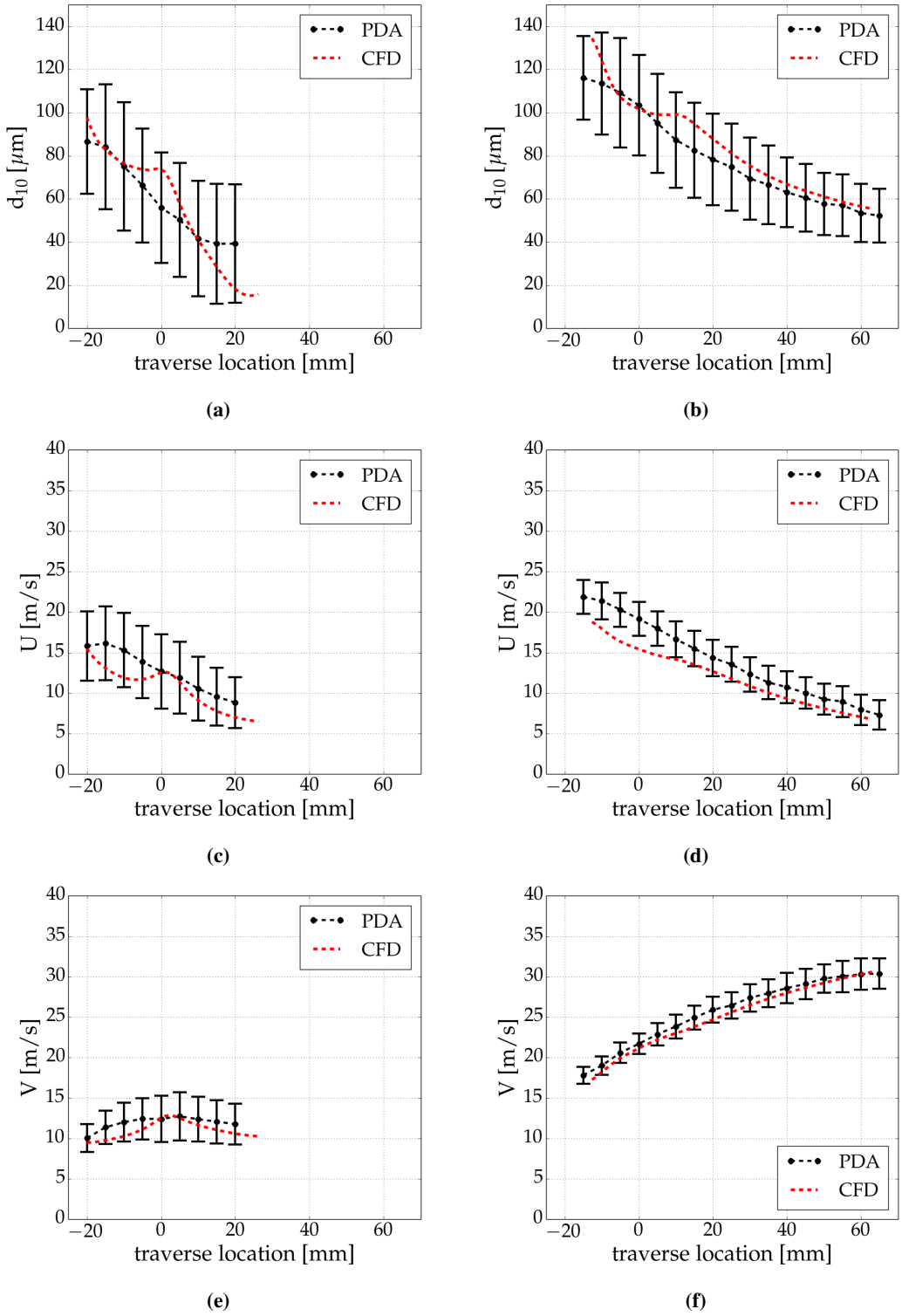

Figure 3.65: *6H - UWS injection - Spray average kinematic parameter profiles. Left: low load (t200f100): d_{10} (a), U (c) and V (e). Right: high load (t400f400): d_{10} (b), U (d) and V (f).*

injected parcels. A new approach for the $droplet - to - parcel$ relation has been proposed, highlighting the effectiveness of assigning a fixed number of droplets to every parcel in the description of wide drop size distributions. The models are then applied to exhaust after-treatment conditions, underlining that the proposed models are always able to catch the trends of the spray properties, generally overestimating the droplet sizes.

Although the injected diameter distributions are comparable (Fig. 3.39), the different morphology of the injected streams, six parallel liquid jets for 6H and three thinner and deviated cones for 3H, strongly influences the spray behavior in cross-flow conditions. In particular, 3H generates clearly separate streams, increasing the local liquid concentration but decreasing the overall influence of the injection on the flow field, highlighting the lack of droplet mutual collision modeling. The consequent overestimation of the entrainment of the small droplets is strongly affecting the average diameter representation (Fig. 3.62-a,b), but not modifying the spray cone momentum, as shown by the good representation of the normal and axial velocity components in the near-wall region (Fig. 3.62-c-e).

This effect is less evident in the simulation of 6H, since the importance of the collision modeling in the simulation of the small droplets path is weaker compared to the gas flow recirculation effect, underlined in the injection in quiescent air conditions (Figs. 3.21).

The effect of the urea in the liquid solution both from the experimental and the numerical point of view is found to be negligible in the description of the path of the spray to the wall.

The CFD results are acceptable within the framework of this project, which aims at providing a spray characterization able to handle the whole system geometry and operating conditions. In fact, the test cases are run in parallel on 4 Intel® Core™i7 CPU 870 @ 2.93 GHz never exceeding 6 hours for the injection in quiescent air test cases and 12 hours for the spray development in cross-flow condition, resolving a domain of a size comparable with a pre-catalytic section of a real SCR system.

CHAPTER 4

Characterization of the spray-wall interaction

The purpose of the characterization of the spray interaction with the walls is the prediction of its kinematic and thermal effects both on the droplets and on the solid structure of the system. This feature becomes vital in the prevention of liquid film formation and consequent possible solid deposit formation. According to the previous chapter, a substantial fraction of the liquid spray injected by low pressure-driven sprays impacts on the walls of the test-rig, which well represents the pre-catalytic section of a DeNO$_x$ exhaust after-treatment system. On the modeling side, the numerical simulation of the spray impingement is aimed at defining a modeling approach feasible to represent the conditions experienced in the system to be included in the Lagrangian-Eulerian framework built in the previous chapter.

4.1 Impinging spray properties

The parameters influencing an impact can be ascribed both to the liquid spray and to the solid walls characteristics. According to [40] the influence of the gravity is usually excluded from the modeling, as the acting forces are some order of magnitude less than surface tension and drag. Therefore from the spray side, the kinematic interaction with a solid surface can be described just through the dynamic properties of the drops, represented by velocity **U**, diameter d, density ρ, surface tension σ and dynamic viscosity μ. These parameters can be synthesized defining dimensionless numbers through the Buckingham Pi-Theorem which are able to improve the direct comparison of different conditions. The dimensionless numbers proposed by [40] are reported in Tab. 4.1.

Capillarity Ca	$\frac{U\,\mu}{\sigma}$
Laplace La	$\frac{\rho\,\sigma\,d}{\mu^2}$
Ohnesorge Oh	$\frac{\mu}{\sqrt{\rho\,\sigma\,d}}$
Weber We	$\frac{\rho\,U^2\,d}{\sigma}$
K [56]	$\frac{(\rho\,d)^{3/4}\,U^{5/4}}{\sigma^{1/2}\,\mu^{1/4}} = We^{5/8}\,La^{1/8}$

Table 4.1: *Dimensionless numbers in the kinematic spray wall interaction description.*

Six hole injector

According to [83], who extracted the K numbers from the PDA data collected injecting UWS at 60 mm from the nozzle location, at constant gas flow temperature equal to 300° C and three different gas cross flow loads (100 kg/h, 200kg/h, 300 kg/h). The K number distribution has been found to be determined by the droplet size distribution, as shown in Fig. 4.1.

Three hole injector

The same results have been gathered for water injection with 3H [45] at similar gas flow and temperature conditions, as reported in Fig. 4.2. The higher K numbers correspond to the larger droplets which are not relevantly affected by the cross flow. In fact the kinematic parameter distribution flattens increasing the liquid entrainment in the flow field, showing that the large droplets are not deflected and their velocity is not strongly reduced.

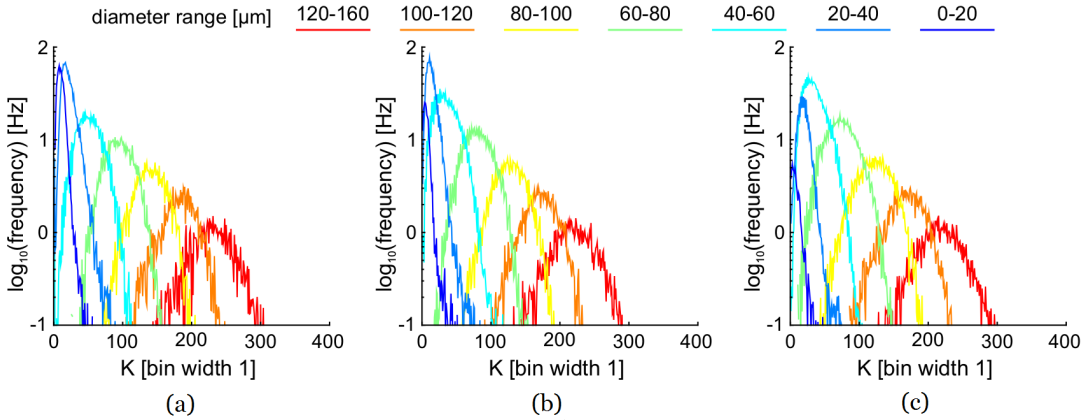

Figure 4.1: *6H - UWS injection - K number by diameter range at 60 mm from the nozzle at T_{gas} = 300° C, and mass flow equal to 100 kg/h (a), 200kg/h (b) and 300 kg/h (c) [83].*

The injection of distilled water with 3H at intermediate load conditions (t300f200) are simulated and validated in the previous chapter. The kinematic parameters of the droplets are collected on the PDA sampling plane and guide to the same considerations as shown in the left column of Fig. 4.3. The figures isolate the spray properties of the front cone at the sampling locations, represented by the PDA plane, and the bottom surface. The simulation includes the description of the lateral spray cone as well, to reproduce the spray-related flow field modification and its influence on the front jet development. The size of the colored spheres represents the droplet diameters, which are reported in Section 3.2.3 from Chapter 3. The core of the spray, carrying the paramount fraction of mass and vertical momentum shows the maximum values of K. The smallest droplets entrained in the gas flow and composing the $wake$ are not going to impact the bottom surface and, as visible from the velocity component normal to the bottom surface (U_{norm}) have a horizontal trajectory.

The simulation allows to track the behavior of the spray to the wall, as reported on the right column of Fig. 4.3. It is important to notice that the simulated spray maximum normal component of the kinematic parameter K drops from 94 to 82 (Fig. 4.3-d), highlighting that the PDA measurement at 18 mm from the bottom plate allows a good estimation of the spray properties in terms of velocity magnitude, diameter and absolute K, but not a reliable evaluation of the impact behavior which is dependent on the normal velocity component, according to [40].

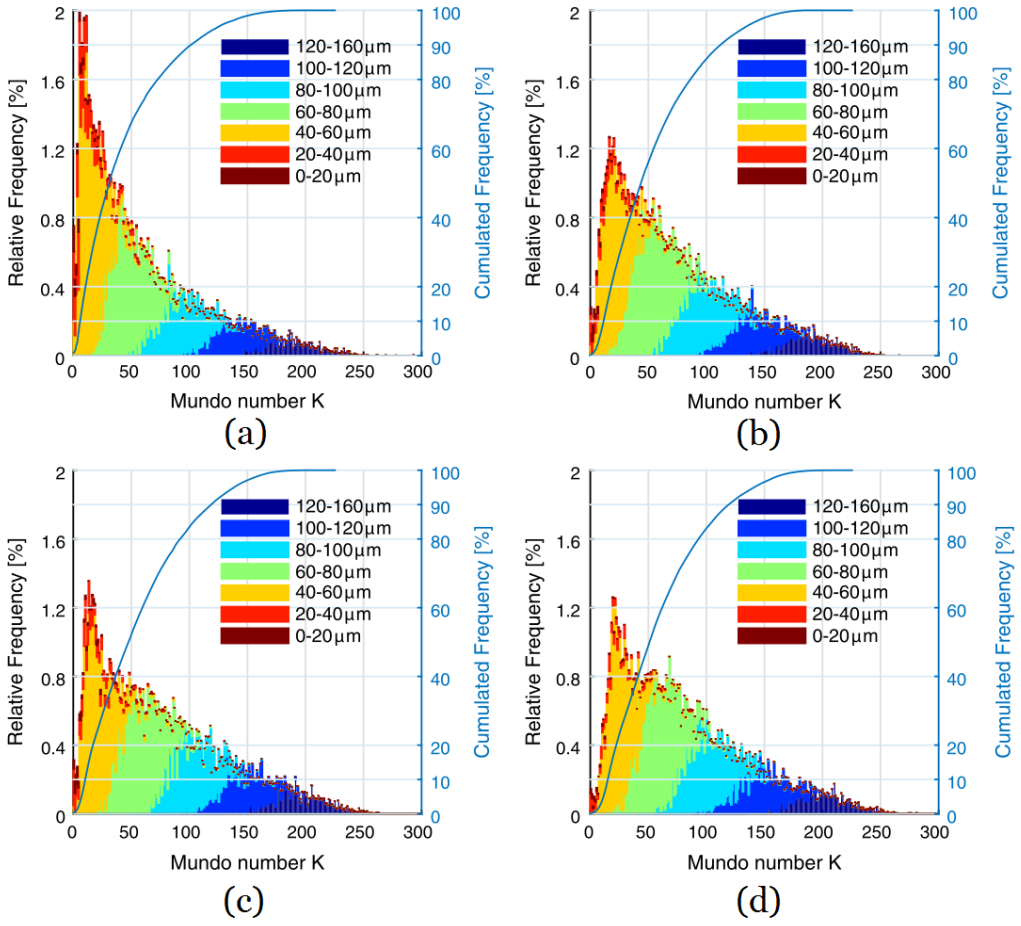

Figure 4.2: *3H - water injection - K number by diameter range at 80 mm from the nozzle location: T_{gas} = 200° C and $\dot{m}_{gas}$ = 200 kg/h (a), T_{gas} = 200° C and $\dot{m}_{gas}$ = 300 kg/h (b), T_{gas} = 300° C and $\dot{m}_{gas}$ = 200 kg/h (c), T_{gas} = 300° C and $\dot{m}_{gas}$ = 300 kg/h (d) [45].*

4.2 Impinging fluid mass quantification

Most of the measurement techniques, like Mie scattering [83] or high speed imaging [94] are able to determine qualitative characterization of the spray behavior as well as relative quantitative comparisons. Recently, high speed Schliren technique has been applied to highlight the effect of the wall interaction on the spray development and evaporation over a wide range of temperatures [53], providing as well a qualitative impingement behavior. The measurement of the absolute value of the spray volume flux has been performed through a complete Phase Doppler Anemometry sweep [65, 66] involving a full lateral optical access to the near surface region and a dense spatially distributed sampling matrix in a fuel spray context. The critical post-processing tech-

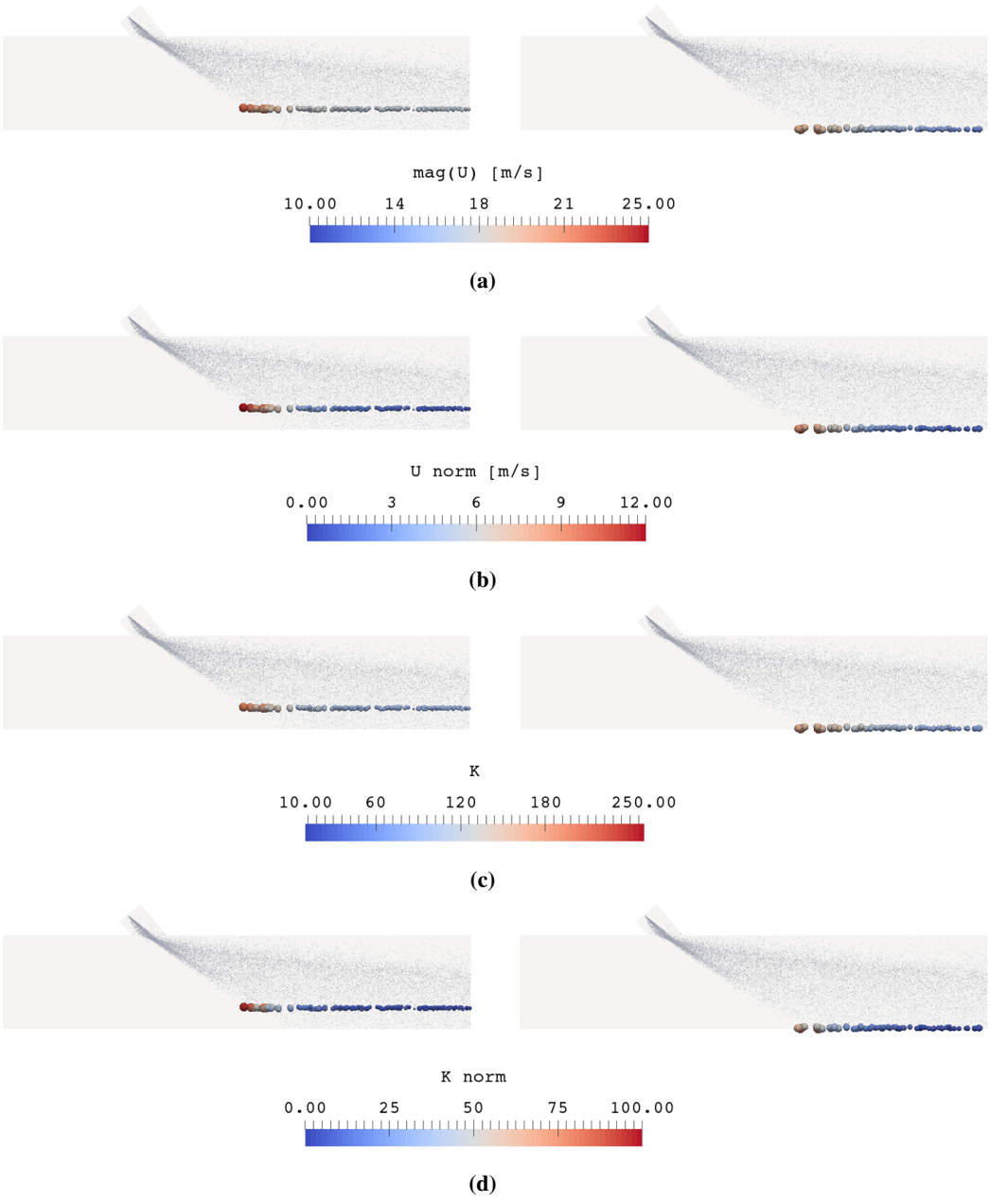

Figure 4.3: *3H - water injection - time = 100 ms after SOI. Front cone visualization of the velocity and the kinematic parameters (the size of the spheres represents the parcel characteristic diameter). left: PDA sampling plane, right: bottom surface. Droplet velocity magnitude (a) and component normal to the bottom surface (b). Absolute Kinematic parameter K (c) and normal component K_{norm} (d).*

nique highlighted by [6] and the necessity of a wide measurement grid to provide a complete mass flow map, excludes the application of this latter method from the framework of this project. Mechanical patternation is taken into account to provide a spatially distributed liquid mass measurement.

4.2.1 Experimental setup

A mechanical patternator has been designed and built at Empa [21, 98] to quantify the mass distribution at the lowest accessible sampling plane. The instrument is composed of a perforated plate where 24 circular probes, with a inner diameter of 5 mm, are installed as pictured in Fig. 4.4. The instrument characteristics are based on the design proposed by [90]. The tips of the probes are sharpened to reduce the influence of the

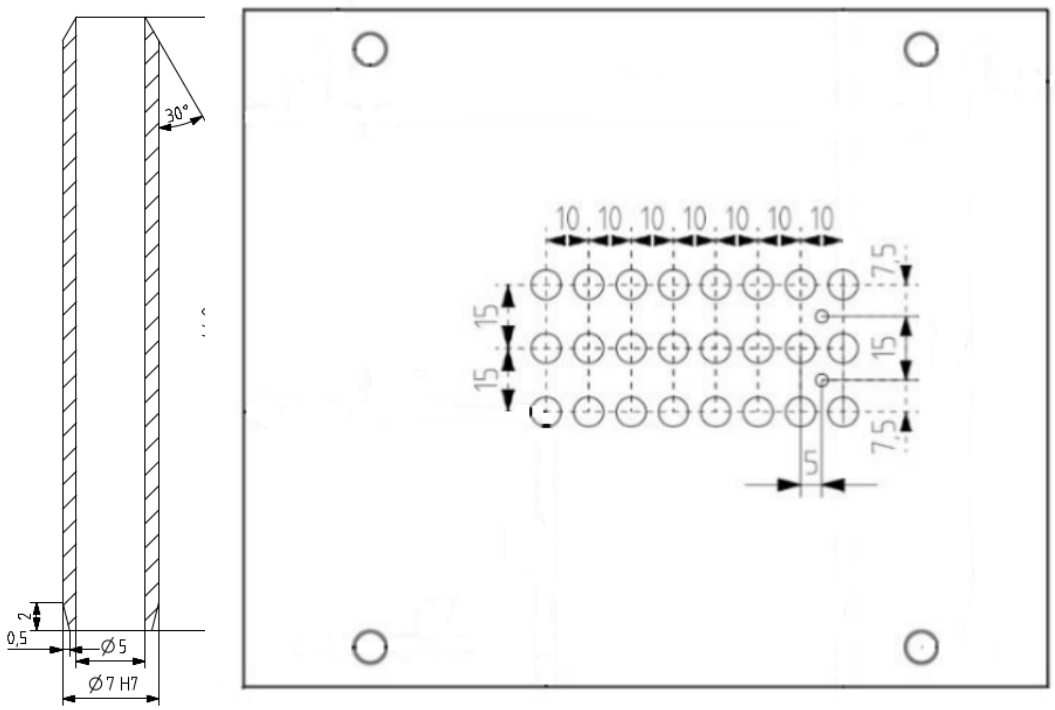

Figure 4.4: *Schematic of a single probe (a) and of their distribution on the perforated plate.*

walls interference in the mass collection process. The liquid gathered by each probe is collected in a polyethylene bottle with a capacity of 250 ml through a silicon tube. A vacuum pump generating an underpressure of 0.1 bar at the end of the collecting tubes, is connected to the bottles to generate the suction needed to avoid stagnation of the droplets on the probe channel walls due to capillary force. The plate is inserted in the injection chamber replacing the standard bottom wall, as sketched in Fig. 4.5. The patternation matrix, shown in Fig. 4.4-b has a resolution of 10 mm in the gas flow direction and of 15 mm along the transversal coordinate. The relative positioning between the flow channel and the instrument can be controlled along the two planar coordinates

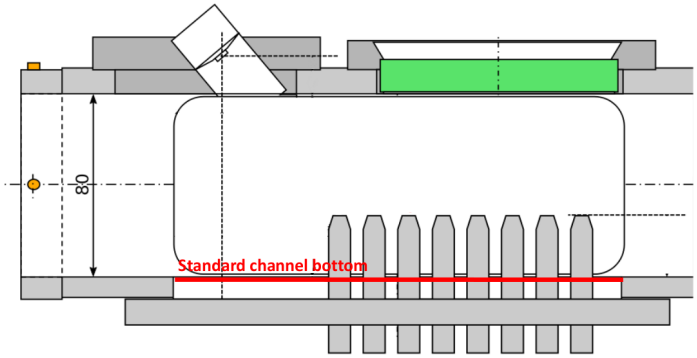

Figure 4.5: *Sketch of the patternator location inside the injection chamber.*

to perform sequential measurements and to increase the spatial resolution up to 2 $\times$ 2 mm, partially overlapping the probe areas as reported in Fig. 4.6.

Each measurement involves a statistically relevant number of injections (1700 to

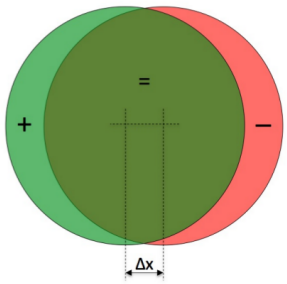

Figure 4.6: *Partial overlap of the sampling areas of a probe.*

3000). The mass collected by each bottle, corresponding to the sampling location is weighted with a scale with an accuracy of $\pm$0.01 g. A more detailed description of the design of the instrument is available in [98].

4.2.2 Evaluation of the intrusiveness of the instrument

Computational Fluid Dynamics is used to estimate the modification of both the gaseous flow field and the spray development inside the test rig [60].

Flow field modification The impact of the patternator on the gaseous field inside the test rig has been investigated through steady-state simulation of cross flow over the kinematic and thermal conditions range operated in the spray characterization campaigns,

summarized in Tab. 4.2. Mass, momentum and energy balances are discretized on the

label	$\dot{m}_{gas}$	$U_{flow,gas}$	T_{gas}	Re
	$[kg/h]$	$[m/s]$	$[^\circ C]$	$[-]$
t200f100	100	5.8	200	13.4 10^3
t300f200	200	14.2	300	23.6 10^3
t400f400	400	33.1	400	41.5 10^3

Table 4.2: *Summary of the gas flow conditions tested in the CFD campaign.*

real channel geometry. The resulting computational grid, which is reported in detail in Appendix B and shown in Fig. 4.7 exploits the transversal symmetry of the system, and therefore involves half of the geometry extension, applying a reflecting boundary condition of the vertical surface built on the channel axis and reducing the overall cell count.

To compare the gas flow development in the configuration implementing the patter-

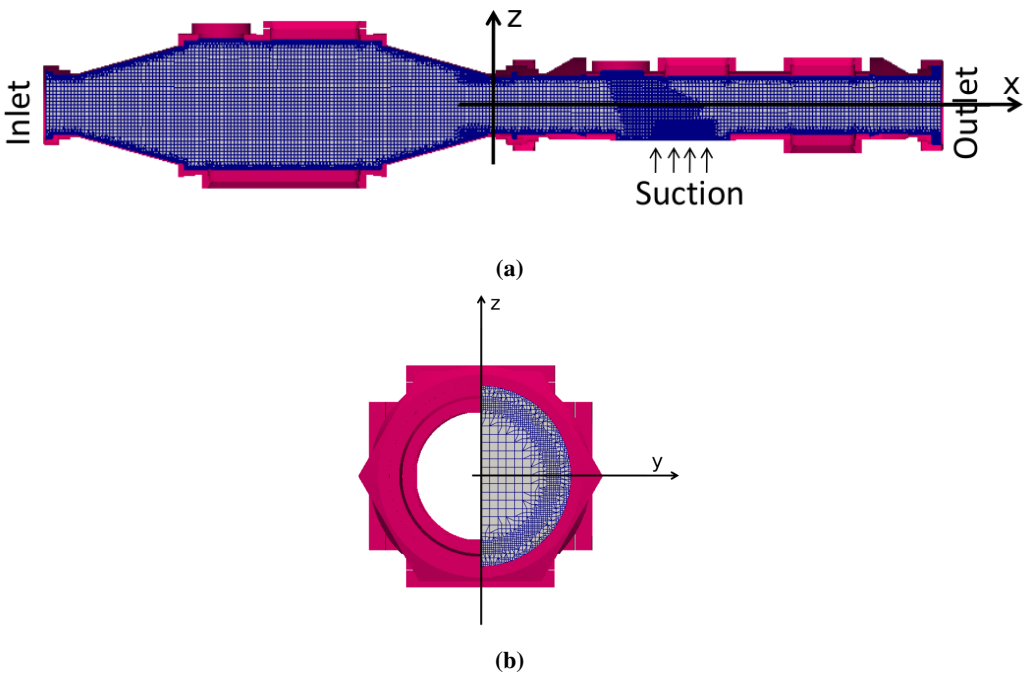

Figure 4.7: *Computational mesh for the patternator setup. Lateral view (a) and outlet section detail (b).*

nator with the $standard$ one, two grids are generated starting from cubic cells and refining and adapting to the geometry features through the use of prisms and polyhedra with $snappyHexMesh$ tool [33]. No slip conditions are applied to the velocity fields

at the solid walls, which are considered adiabatic. Turbulence is handled with the standard $k-\varepsilon$ model, setting the wall boundary layer to be one-cell thick since scalable wall functions are used. Dry air is treated as a perfect gas, according to the specifications reported in Appendix A.

The probe suction flow is reproduced imposing a 10 Pa underpressure at the probe base to match the estimated intake velocity of 5 m/s.

Tab. 4.3 summarizes the boundary condition setup.

	solid walls	inlet	outlet	sym plane	probe suction
$\mathbf{U}_{gas}$	No slip	$\mathbf{U}_{gas}$=$\mathbf{U}_{gas,flow}$	∂**U**/∂**n**=0	reflecting	∂**U**/∂**n**=0
P_{gas}	∂P/∂**n**=0	∂P/∂**n**=0	$P_{tot,gas} = P_{amb}$	reflecting	$P_{tot,gas} = P_{suction}$
T_{gas}	$\partial T_{gas}/\partial$**n**=0	T_{gas}=$T_{gas,0}$	$\partial T_{gas}/\partial$**n**=0	reflecting	$\partial T_{gas}/\partial$**n**=0
k	scalable (all y^+)	k=0.05I_{turb}	$\partial k/\partial$**n**=0	reflecting	$\partial k/\partial$**n**=0
ε	scalable (all y^+)	ε=$f(l_{turb})$	$\partial\varepsilon/\partial$**n**=0	reflecting	$\partial\varepsilon/\partial$**n**=0

Table 4.3: *CFD boundary condition summary.*

Fig. 4.8 reports the impact of the probes on the region involved by the spray development at intermediate load (t300f200), highlighting that the variation is confined to the patternator inlet plane, without affecting a large fraction of the channel section. The

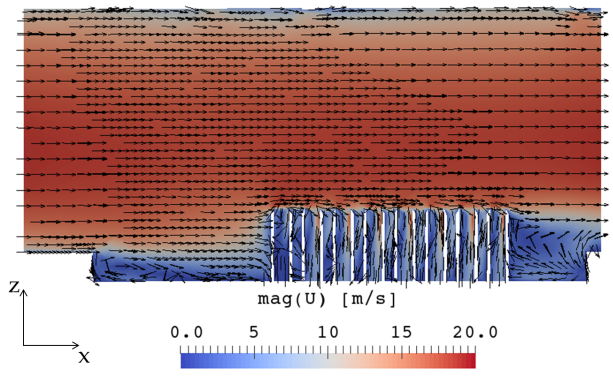

Figure 4.8: *Velocity profile and magnitude at t300f200 on the symmetry plane of the injection section.*

profiles of the component of the gas velocity along the channel axis ($U_{gas,x}$) are analyzed along the channel symmetry plane, which corresponds to the centerline vertical section. The influence of the instrument in the flow development is evaluated at three

different locations, representing the projected spray core center on the sampling plane (position 1), the last downstream edge (position 2) and a section 40 mm downstream of the last probe to quantify the modification of the path to the actual catalytic section of the rig (position 3) as shown in Fig. 4.9. The patternator is positioned in the most upstream position, to reproduce the most invasive situation from the spray development side.

Fig. 4.10-a,c,e report $U_{gas,x}$ over the channel vertical coordinate, normalized on the

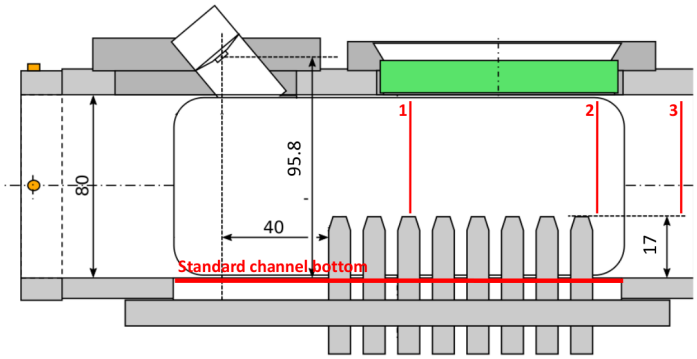

Figure 4.9: *Position of the sampling lines in the evaluation of the flow field modification. The patternator positioning refers to the 3H channel setup.*

average inlet velocity, reported in Tab. 4.2, since the gas flows in isothermal conditions. The differences in the velocity profiles are reported in Fig. 4.10-b,d,f, showing a discrepancy always lower than the 10% of the inlet average value. The steeper reduction of $U_{gas,x}$ close to the probe entrance is the result of both the vacuum pump suction and of the physical obstacle represented by the patternator iteself.

Spray-Patternator interaction

The 6H injector model was used to assess the probe interference on the development of distilled water spray from low pressure-driven sprays. The injection is simulated within the Lagrangian-Eulerian framework as described in Sec. 3.2.3 of Chapter 3. The mesh involved in the calculation reproduces the injection chamber of the test rig in its real geometry and it is extracted from the flow field mesh. A conical refinement is applied to the injector cone projection to be consistent with the PDA validation process. The two different grids referring to the standard channel configuration (Fig. 4.11-a) and to the patternator insertion in the system (Fig. 4.11-b) are described in detail in Appendix

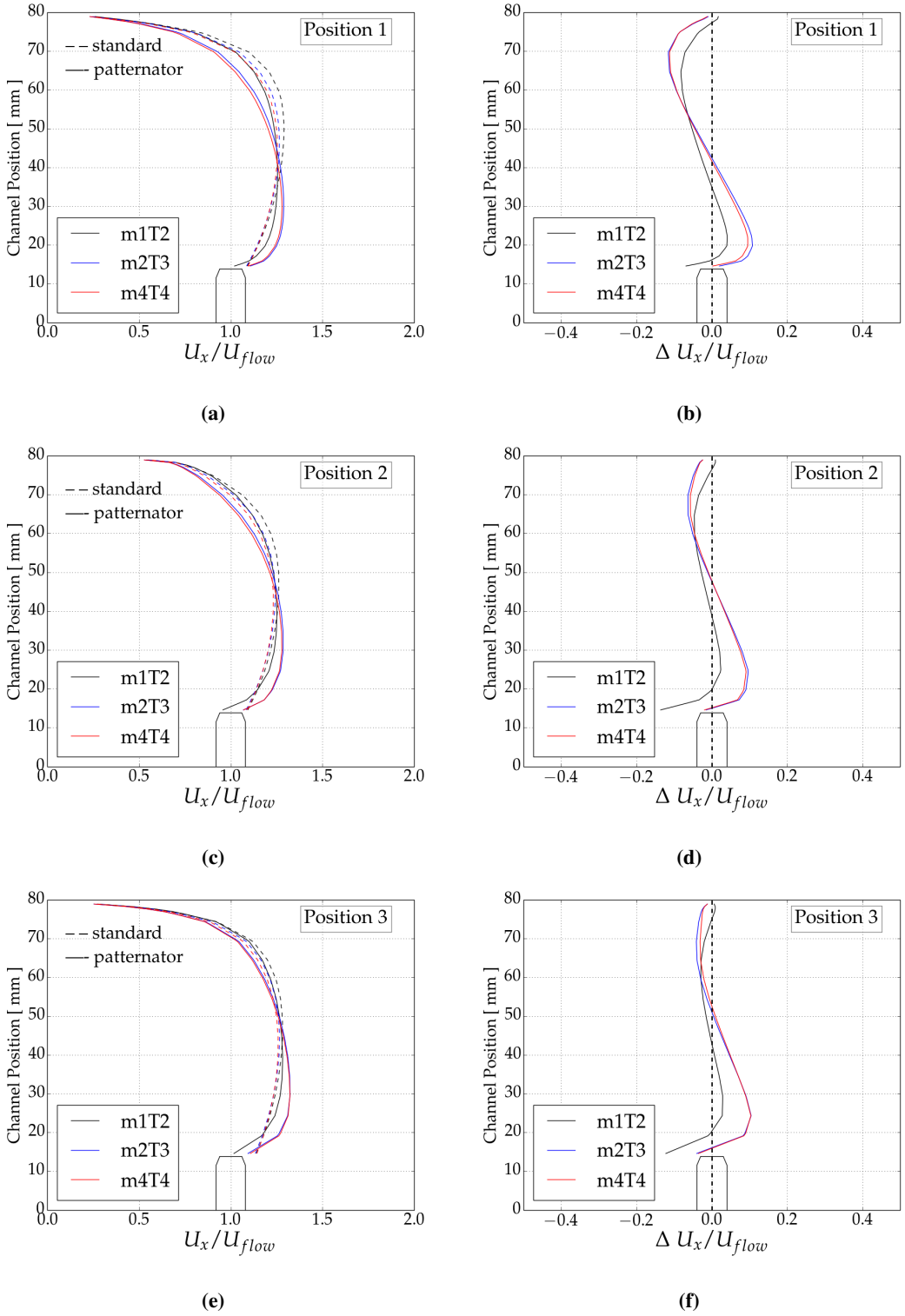

Figure 4.10: *Velocity profile on the centerline of the injection section (a,c,e) and difference in the velocity profiles introducing the patternator in the system, normalized on the average inlet velocity U_{flow} (b,d,f).*

B. The probe arrangement is kept fixed and represents the most upstream measurement

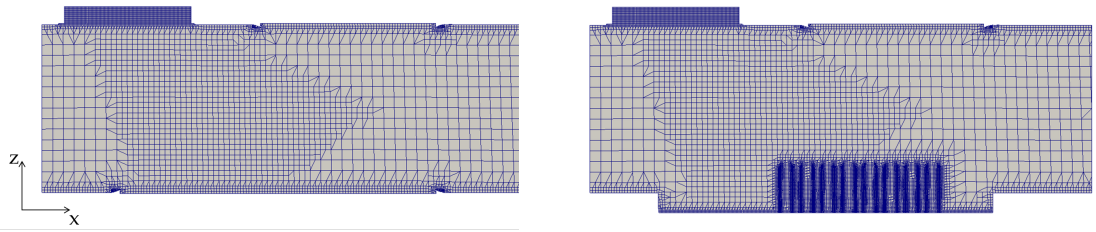

(a) (b)

Figure 4.11: *Computational meshes for the injection chamber in its standard configuration (a) and with the presence of the patternator (b).*

location, introducing the worst case condition in which the biggest portion of the spray experiences an interaction with the modified flow field. The injection duration is set to 100 ms and the reported results refer to the nozzle closing instant. Fig 4.12 reports the spray qualitative patterns at low (t200f100) and intermediate (t300f200) conditions, showing negligible influence of the patternator presence. The spray color is cut at the probes measuring plane for visualization purpose. The planar distribution of the spray

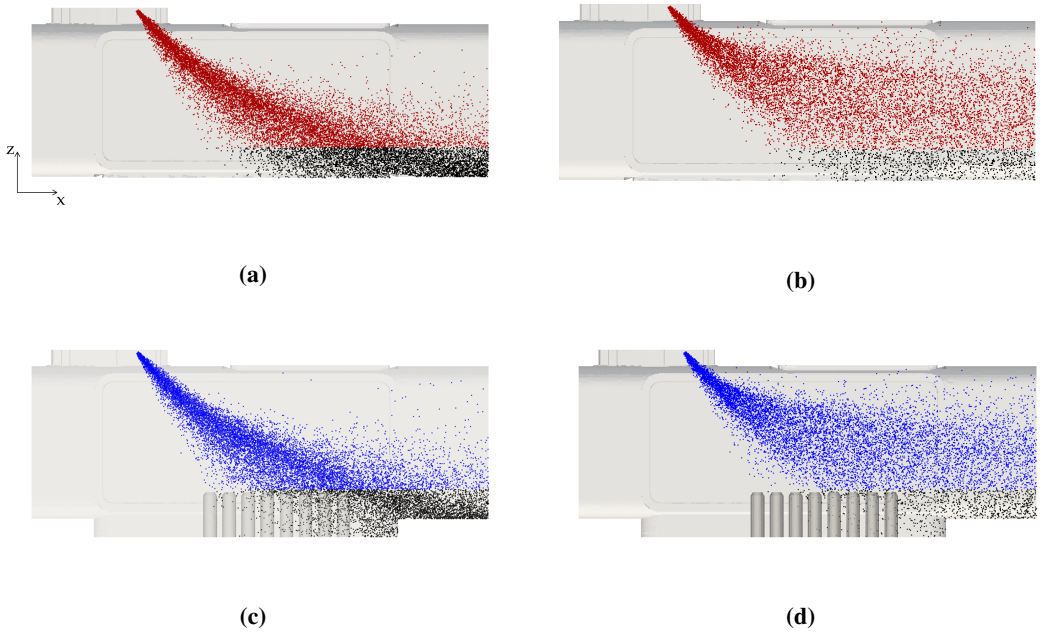

(a) (b)

(c) (d)

Figure 4.12: *Simulated spray path to the instrument measuring plane. t200f100 standard channel (a), t300f200 standard channel (b), t200f100 patternator channel (c) and t300f200 patternator channel (d).*

mass on a plane set 5 mm above the probe inlet is reported in Fig. 4.13, reinforcing

the assumption of a limited impact of the patternator geometry on the spray evolution under cross flow conditions. The coefficient of variation $c_{v,face_i}$ of the collected spray mass normalized on the total value collected by the sampling region is calculated for each computational face as defined in (4.1).

$$c_{v,face_i} = \frac{\sigma_{face_i}}{\bar{m}_{face_i}} \tag{4.1}$$

$c_{v,face_i}$ compares the local standard deviation σ_{face_i} and the mean value $\bar{m}_{face_i}$ obtained in the two channel configurations. Figs. 4.13-e,f report the coefficient of variation maps, showing that the wider differences are concentrated in the very periphery of the spray. Indeed, the average c_v over the whole sampling plane is 10.26 $\%$ for t200f100 and 15.54 $\%$ for t300f200, showing that the patternator influences the planar spray mass distribution within an acceptable deviation range.

Experimental results

The experiments have been carried out in [21] on the injection of distilled water by the three hole injector 3H. Standard injection settings correspond to a DOI of 150 ms and a frequency of 3 Hz. The patternator inlet plane is positioned 79 mm from the injector position as shown in Fig. 4.9. To assess the instrument performance inside the test rig, preliminary measurements were performed in the channel with quiescent air conditions, in order to collect the total footprint with a resolution of 2 $\times$ 2 mm and integrating the results to obtain the total injected mass value. This value has been then normalized to obtain a $mass\ per\ injection$ value that will be considered the reference to estimate the entrainment and the phase change due to cross flow interaction. To evaluate the accuracy of the instrument, the injector was removed from the channel and 2500 injection were collected in a closed tank at ambient temperature. The resulting $mass\ per\ injection$ value has been compared to the one obtained through patternation, as reported in Tab. 4.4. The higher value obtained with the patternator is ascribed to the recirculation of the droplets impinging and splashing/rebounding on the probe walls in absence of cross flow. The error has been considered small enough to perform the experimental campaign. Fig. 4.14 shows the spray mass footprint collected with the spray patternator in quiescent air at room temperature, where the axis origin (0,0) is

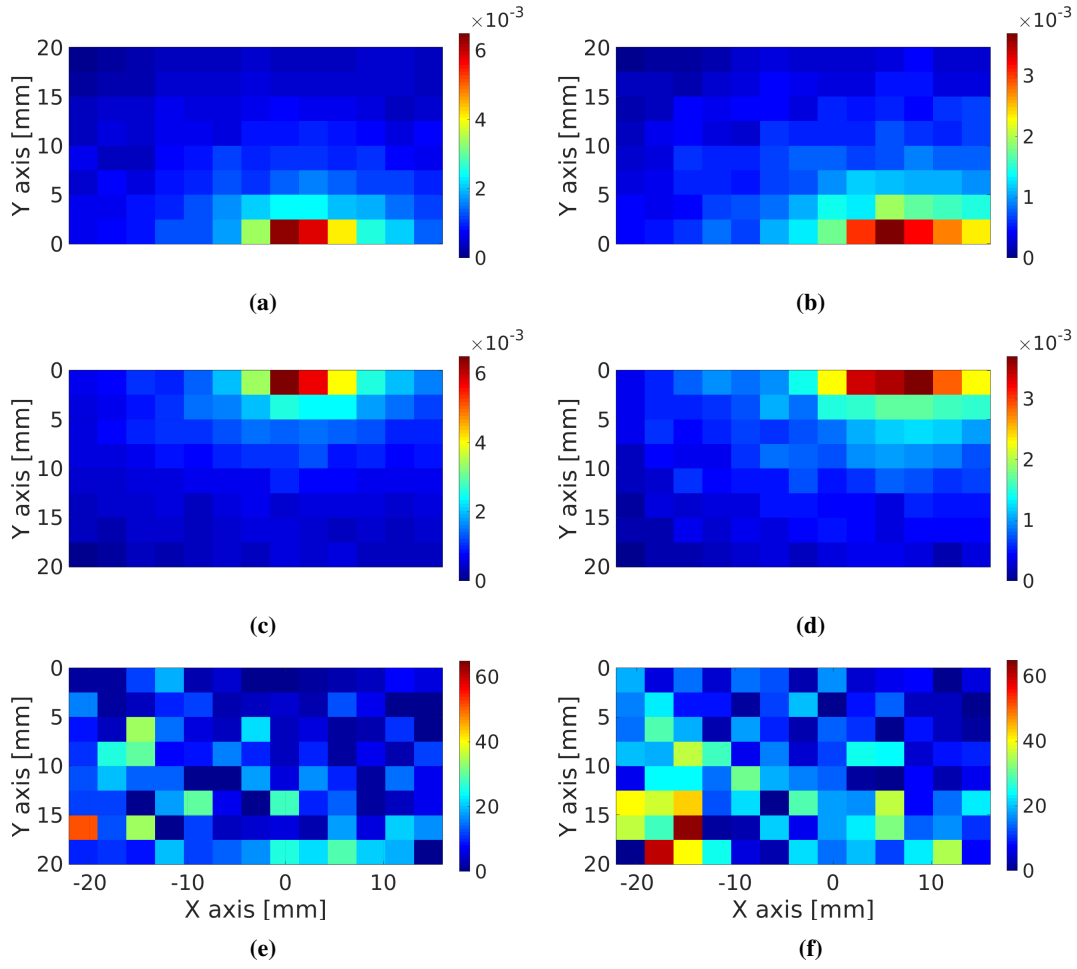

Figure 4.13: *Spray mass flux comparison at 5 mm from the patternator probe inlet plane. Maximum collected mass value: 6.3 10^{-3} g for t200f100 and 3.7 10^{-3} for t300f200. standard channel at t200f100 (a), standard channel at t300f200 (b), patternator channel at t200f100 (c) patternator channel at t300f200, $c_{v,face_i}$ map for t200f100 (e) and $c_{v,face_i}$ map for t200f100 (f).*

set by the initial position of the most upstream probe row, corresponding to an horizontal shift of 43.40 mm from the injector location. It shows three clearly separated peaks corresponding to the three injector hole spray cones. Therefore, in order to speed up the measurement campaign, only the front and most downstream cone has been analyzed.

To understand the separate influence of the thermal interaction with the flow field and the liquid evaporation, gas iso-momentum measurements have been carried out, assuming that air density is only temperature dependent: $\rho_{gas} = \rho(T)$. The chosen momentum value, ρU_{gas}^2 = 62.5 $kg/m\,s^2$, represents an intermediate condition for the test rig, and corresponds to a mass flux of 200 kg/h at room temperature. Then, the effect of the aerodynamic drag and the consequent entrainment has been estimated by

method	collected mass $[g/inj]$
tank	0.2927
patternation+integration	0.3102
relative error	5.64

Table 4.4: *Patternation accuracy estimation.*

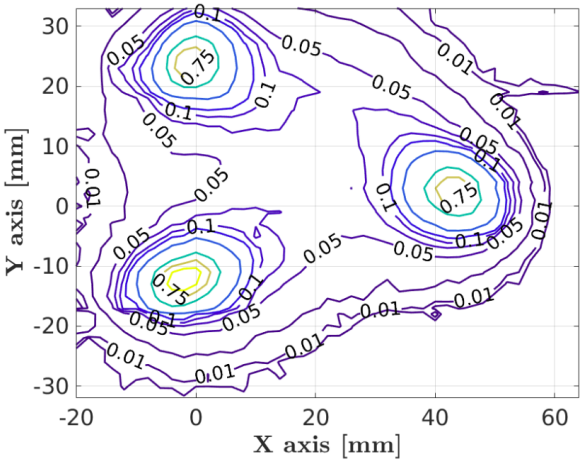

Figure 4.14: *Local Impingement Rate at zero flow conditions and room temperature. Reference value = 7.36* 10^{-4} $g/(injmm^2)$.

varying the cross flow momentum at room temperature. Tab. 4.5 summarizes the iso-momentum and iso-temperature conditions. To compare the spray mass distribution

T_{gas} [°]	gas mass flux $[kg/h]$
20	0
20	200
150	166
200	157
300	143
400	132
20	100
20	200
20	300

Table 4.5: *Iso-momentum and iso-temperature flow conditions.*

along the measurement matrix, a constant Region Of Interest (ROI) has been defined from the peak position defining a rectangle formed by the minimum extension of the footprint in each direction as reported by [21, 60]. The footprint has been presented as a specific mass flux normalized on a single injection pulse expressed as Local Impingement Rate (LIR, $[g/(inj\,mm^2)]$). The longitudinal and transversal distribution are reported in Fig. 4.15. Tab. 4.6 reports the front cone location, the integral value of

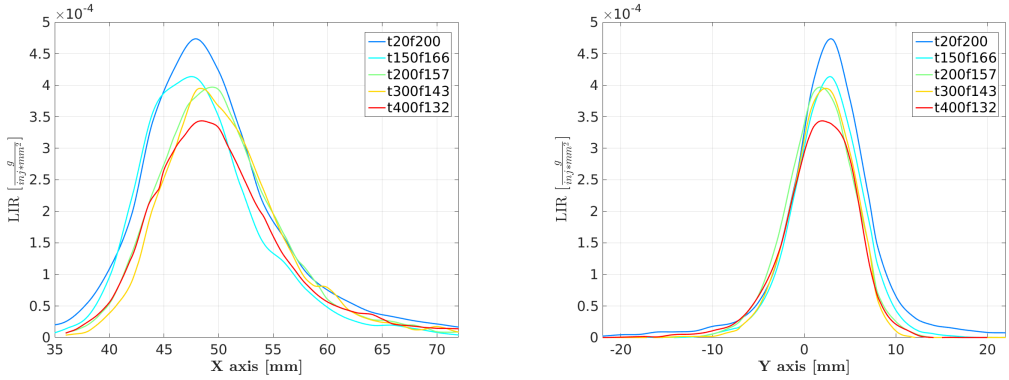

(a) **(b)**

Figure 4.15: *Iso-momentum Local Impingement Rate profiles: longitudinal (a) and transversal (b).*

the collected mass and Local Impingement Rate measured with the patternator at ambient temperature and no gas flow conditions (t20f0) which have been considered the references to estimate the effect of the gas flow on the spray behavior. The reduction

	t20f0
peak x position $[mm]$	43.57
max LIR $[g/(inj\,mm^2)]$	$7.36{\cdot}10^{-4}$
integral value $[g/inj]$	0.0847

Table 4.6: *Front cone footprint characterization at no flow conditions t20f0.*

of the total collected mass (4.2) due to the partial evaporation and the entrainment of the spray, as well as the decrease of the LIR peak (4.3) are reported in Tab. 4.7 for the iso-momentum conditions. No relevant displacement in measured mass flow peak has been found when increasing the temperature of the gas.

$$mass\ reduct_{tXfY} = \frac{(m_{tXfY} - m_{t20f0})}{m_{t20f0}} \tag{4.2}$$

$$peak\ reduct_{tXfY} = \frac{max\,(LIR_{tXfY}) - max\,(LIR_{t20f0})}{max\,(LIR_{t20f0})} \tag{4.3}$$

Fig. 4.16 shows the effect of the increased gas flow momentum keeping the gas at room temperature on the spray pattern. Increasing the flow velocity, the spray cone experiences a slight shift of the footprint position downstream and a less than linear LIR peak reduction. The results are summarized in Tab. 4.8. The LIR peak reduction and the mass reduction trends are plotted in Fig. 4.17, showing less than linear variation increasing both the drag and the phase change between spray and gas flow field. Even

	t20f200	t150f166	t200f157	t300f143	t400f132
Peak X position $[mm]$	47.90	47.50	49.42	48.33	48.47
Longitudinal ΔX$[mm]$	4.34	3.94	5.86	4.76	4.90
Max LIR $[g/(inj\,mm^2)]]$	4.74E-04	4.14E-04	3.97E-04	3.95E-4	3.45E-04
Peak reduction $\%$	35.68	43.82	46.09	46.35	53.10
Integral value $[g/inj]$	0.0685	0.0488	0.0479	0.0429	0.0444
Mass reduction $\%$	19.13	42.38	43.45	49.35	47.58
Phase change compared to t20f200 $\%$		23.25	24.32	30.22	28.45

Table 4.7: *Iso-momentum measurement summary.*

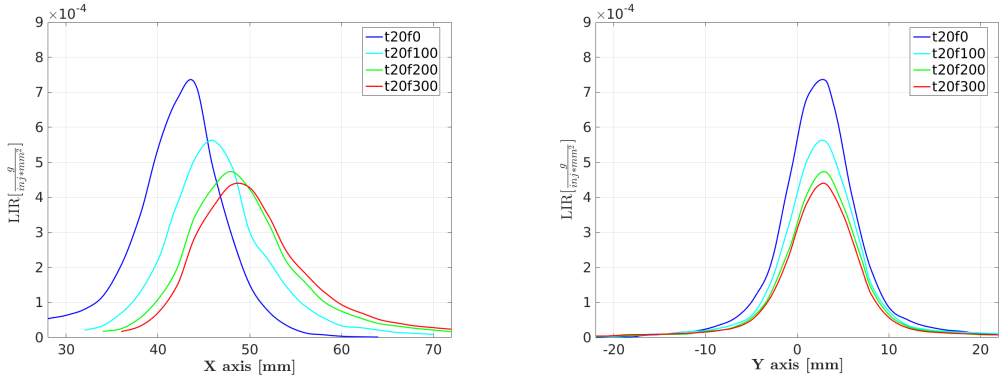

(a) **(b)**

Figure 4.16: *Iso-temperature Local Impingement Rate profiles: longitudinal (a) and transversal (b).*

at the highest gas flow conditions t20f300 at room temperature, the 77.5 $\%$ of the liquid crosses the patternation plane, and therefore is going to impact on the wall, generating strong cooling of the system walls and consequent liquid film formation. It is important to notice that the effect of an increased gas temperature generates a reduction of the Local Impingement Rate which is comparable to the entrainment one.

4.2.3 Numerical simulation of the impinging mass flux

The reported measurement campaign involved the characterization of the mass flux of the front cone of the three hole injector (3H), which does not represent the core of the numerical activity of this work and is used as a test for the validity of the modeling approach, as shown in Chapter 3. For this reason the assessment of the patternator influence on the test bench operating condition and on the spray development has been carried out during the design process employing 6H as a reliable representation of a pressure-driven injector for SCR application. Only two operating conditions are simulated in this section for the 3H injector, focusing on the effectiveness of the proposed

	t20f100	t20m200	t20m300
Peak X position $[mm]$	45.89	47.90	48.70
Longitudinal ΔX $[mm]$	2.33	4.34	5.14
Max LIR $[g/\ (inj\ mm^2)]$	5.63E-04	4.74E-04	4.40E-04
Peak reduction $\%$	23.54	35.68	40.20
Integral value $[g/\ inj]$	0.0742	0.0685	0.0657
Entrainment $\%$	12.40	19.13	22.43

Table 4.8: *Iso-temperature measurement summary.*

approach on the overall injector simulation quality.

The results of Section 4.2.2 determine an acceptable deviation of both the gas flow field and the spray development with the introduction of the patternator in the channel. To avoid the complex simulation of the impact of the parcels on the probe geometry, the spray mass planar distribution is collected sampling on a flat surface set in correspondence to the instrument inlet (79 mm from the injection location). This approach allows also to collect a $continuous$ mass distribution, without the necessity of moving the probe positions and spatially integrate the results.

The simulations are carried out on the simplified representation of the channel proposed in Chapter 3, initializing the fields according to a fully developed gas flow (described in detail in Section 3.2.3).

Injection without cross-flow The reference values in the experimental campaign, extracted injecting without cross flow, involve the determination of the injected mass distribution and the maximum Local Impingement Rate location and magnitude. The quality of the numerical representation of the mass flow pattern is therefore tested in this conditions, emphasizing the effect of the proposed approach to split the liquid mass in the computational parcels. The simulation involves a single injection pulse with a duration of 100 ms.

Fig. 4.18-a reports the longitudinal LIR profile, showing that the fixed number of droplets per parcel, labeled $parcel$, produces a good agreement with the experimental data. The constant mass per parcel, labeled $mass$, tends to smooth the mass flow profile, mostly because of the overestimation of the weight of the small size droplets and the consequent prediction of a lower inertia in the core of the spray. The planar spray mass distribution on the sampling plane at 100 ms after the SOI, normalized

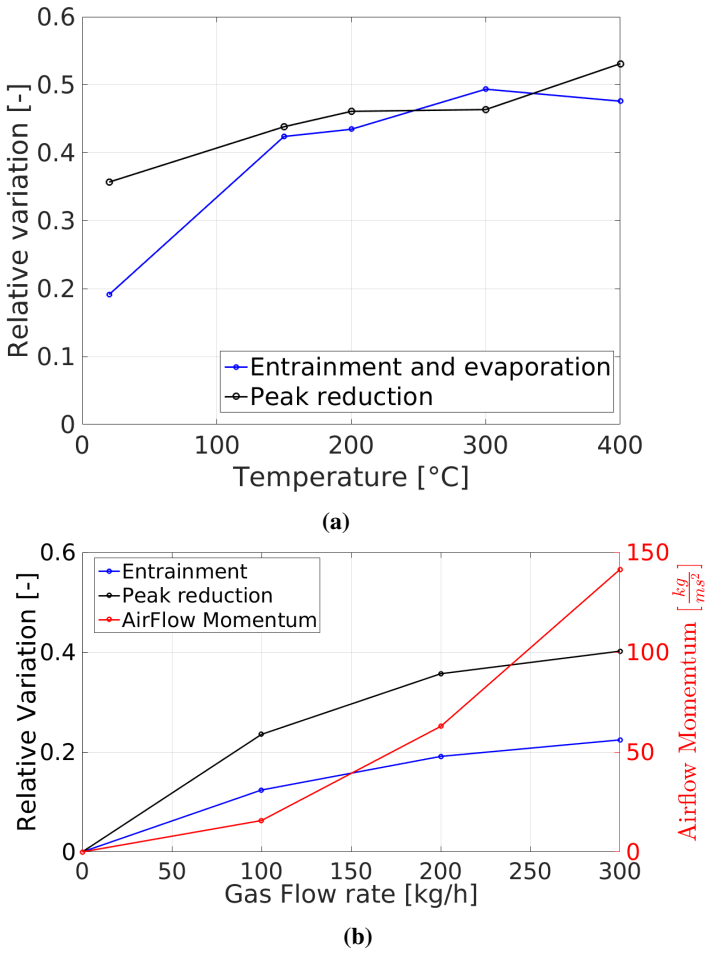

Figure 4.17: *LIR peak and integral mass reductions for iso-momentum (a) and iso-temperature (b) conditions.*

on the maximum collected value, is reported respectively for the $mass$ (Fig. 4.18-b) and for the $parcel$ approach (Fig. 4.18-c) underlining that the strong axial inertia of each cone measured through patternation is better represented by parcels composed of a constant number of droplets without taking into account their size.

Injection with cross-flow The behavior of the modeling framework is tested on the intermediate gas flow momentum conditions at room temperature (t200f20) representing the $\rho U_{gas}^2 = 62.5\ kg/m\,s^2$ value. The spray model of the 3H injector tend to overpredict the front cone displacement and the extension of the planar mass footprint. This result can be ascribed to the not perfect match found for the 3H injector kinematic properties over the PDA data in the previous chapter, and to the absence of a drop-to-drop colli-

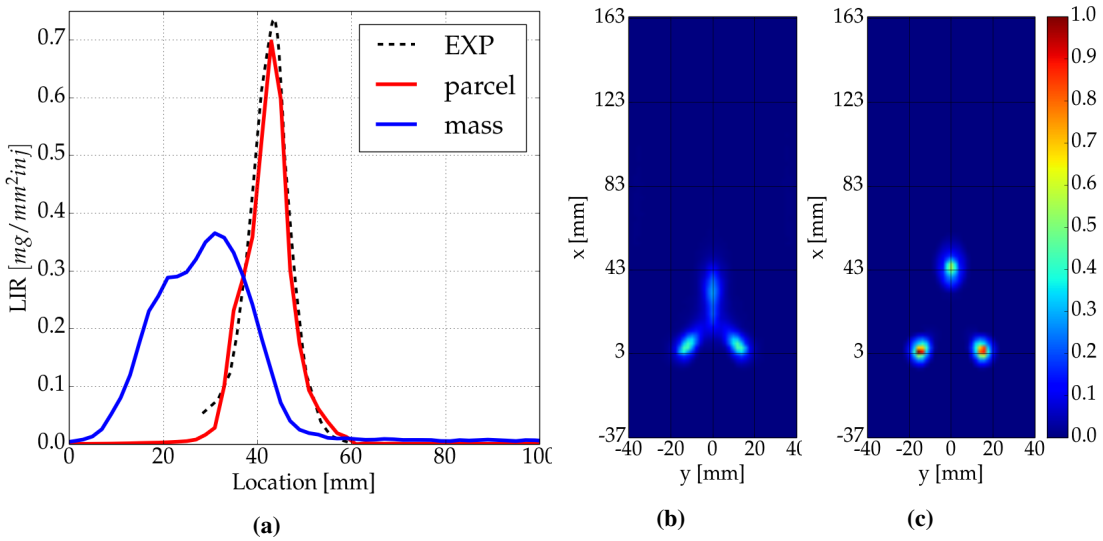

Figure 4.18: *Longitudinal profile of the Local Impingement Rate of the 3H injector without cross flow (t20f0) (a), planar mass distribution obtained with the* $mass$ *(b) and* $parcel$ *(c) approaches.*

sion model applicable to low-pressure driven sprays and the consequent overestimation of the small drops drag. The constant mass per parcel approach ($mass$) produces a strong overestimation of the entrainment, which is partially avoided with the $parcel$ approach as shown in Fig. 4.19-a. Fig. 4.19-b,c report the spray mass collected on the sampling plane, normalized on the maximum collected values, highlighting that the constant $mass$ approach is not able to describe the conservation of the spray core in presence of gaseous cross-flow.

4.3 Impingement modeling

As clearly stated by the experimental campaign, the representation of low pressure driven sprays in a confined environment as an exhaust after-treatment channel involves a substantial interaction with the solid boundaries of the system. Therefore the definition of a spray-wall interaction model which considers all the characteristics of the incoming drop, the wall, and environment provided by the simulations validated in the previous sections and determines the outcome of the impact (Fig. 4.20) is of vital importance.

Several models have been developed for the representation of the spray-wall interaction, determining different approaches in the phenomenon analysis or the introduction

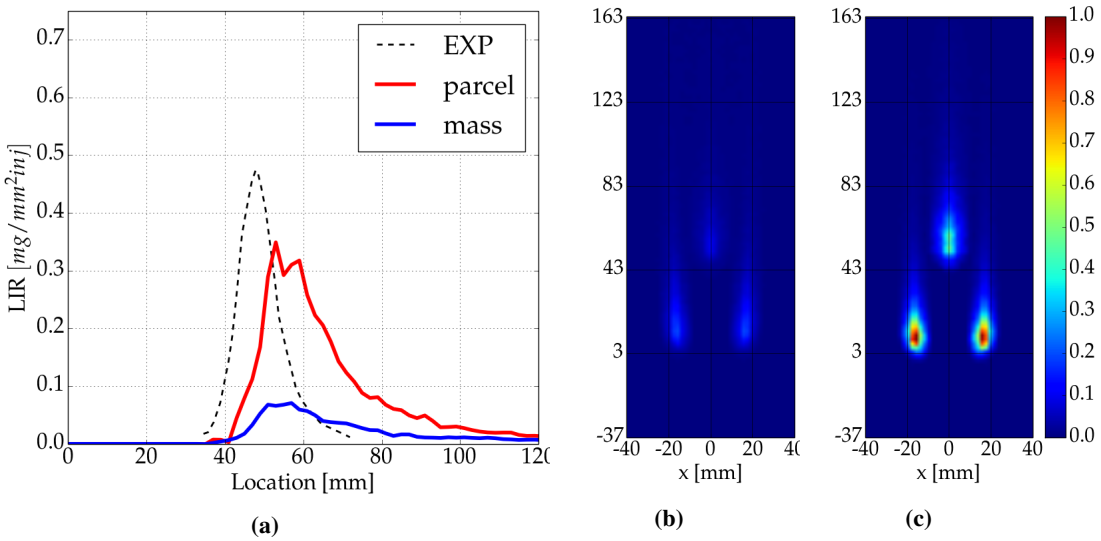

Figure 4.19: *Longitudinal profile of the Local Impingement Rate of the 3H injector at* $\rho U_{gas}^2 = 62.5$ $kg/m\,s^2$ *(a), planar mass distribution of with the* $mass$ *(b) and* $parcel$ *approach (c).*

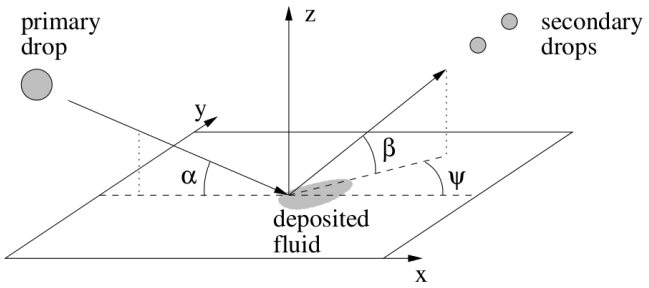

Figure 4.20: *Sketch of a droplet impact event [40].*

of different parameters for the regime classification (e.g. surface roughness [7] or the droplet frequency [87]). The work of [40] provides a critical analysis of the available modeling strategies and a synthetic representation of the semi-empirical correlation determining the phenomena description. It has been widely used in the CFD simulation of urea based Selective Catalytc Reduction systems [8,12,15,30] because of its applicability to the Lagrangian-Eulerian framework and because of the introduction of a thermal threshold on the impact regime recognition, which is fundamental in the determination of the possible wetting of the solid surface and the consequent identification of critical locations for solid deposit formation. Within this work, the model is implemented from scratch in the OpenFOAM® platform.

Impact regime classification

The classification of the impact regime is based on $critical$ values of a thermal parameter T^* (4.4) and a kinematic parameter which is the previously introduced K (Tab. 4.1). The regime transition criteria for single drop impingement are summarized in a general expression that accounts for dry and wet walls, covers the whole temperature range.

$$T^* = \frac{T_{wall}}{T_{sat}} \tag{4.4}$$

The whole impingement regime map, reported in Fig. 4.21-a is simplified by [40] as sketched in Fig. 4.21-b, defining four impact regimes: deposition, cold splash, rebound and thermal breakup.

Since no clear influence of the impingement angle is found in literature, the regime

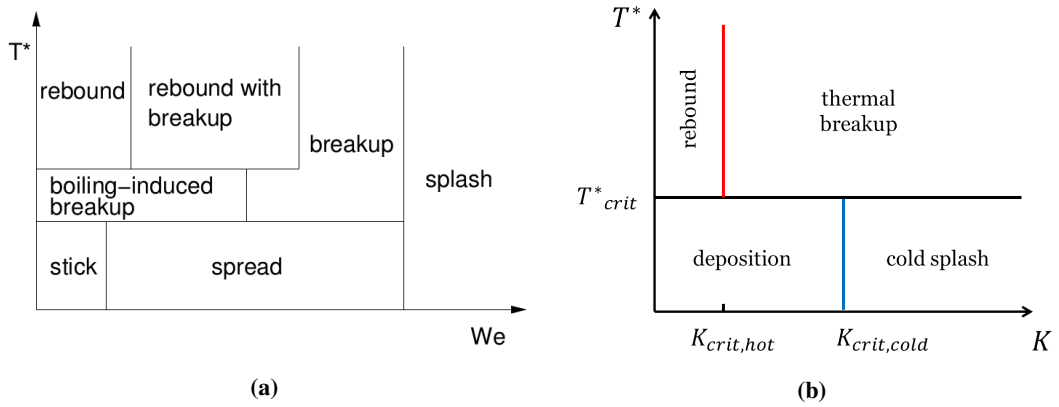

Figure 4.21: *Complete impact regime characterization [7] (a) and the regime map proposed by [40] and implemented in the code (b).*

recognition is dependent on the velocity component normal to the surface, and the consequent normal kinematic parameter K_{norm}. A critical dimensionless temperature $T^*_{crit} = 1.1$ is defined according to experiments by [2, 40], and separates the cold and hot wall behavior.

Above this threshold, the temperature of the wall tends to induce breakup considerably reducing the kinematic threshold between conservative and destructive impacts. No surface roughness influence is reported in the determination of the hot wall $K_{crit,hot}$ which is represented by a uniform probability function between 20 and 40 as shown in

(4.5)

$$K_{crit,hot} = rnd\,[20 - 40] \tag{4.5}$$

The cold wall conditions allow liquid deposition on the surface and therefore the regime recognition is dependent of the wall wetting. For cold and dry walls, the critical kinematic parameter is dependent on the dimensionless temperature and on the wall surface roughness, which are separated in the formulation by [40]. The minimum value of the kinematic parameter is considered a function of T^* as shown in (4.6), according to a limiting value $K_{T,min} = 54$, a maximum set by [56] as $K_{T,max} = 130$, the coefficient c_t equal to 13 and the transition tempeature T^*_{trans} = 1.05 in the OpenFOAM®.

$$K_{min}\,(T^*) = \begin{cases} K_{T,min} + (K_{T,max} - K_{T,min})\; e^{c_t\,(T^* - 1)}, & T^* \leqslant 1 \\ K_{T,max}, & 1 < T^* < T^*_{trans}. \end{cases} \tag{4.6}$$

A smooth function has been proposed to introduce the surface roughness dependence on the critical kinematic parameter as reported in (4.7), on the basis of [89]. The ε_a variable refers to the wall surface roughness normalized on the impinging drop size.

$$K_{cold,crit}\,(\varepsilon_a\, T^*) = K_{min}\,(T^*) - 12.75\;(\ln(\varepsilon_a) - \chi) + 12.75\sqrt{(\ln(\varepsilon_a) - \chi)^2 + 5} \tag{4.7}$$

$$\text{with} \quad \chi = -\frac{K_{min}\,(T^*) + 43.6}{25.5}$$

The transition between the hot and cold behavior is achieved through the blending function (4.8)

$$K_{crit}\,(\varepsilon_a\, T^*) = (1 - \lambda)\; K_{crit,cold} + \lambda\;(K_{crit,hot}) \tag{4.8}$$

$$\text{with} \quad \lambda = \frac{\arctan\,(p\,(T^* - T^*_{trans}))}{\pi} + \frac{1}{2}, \qquad p = \frac{\tan\left(\pi\left(\omega - \frac{1}{2}\right)\right)}{dT^*}$$

The parameters chosen in the implementation correspond to $T^*_{trans} = 1.05$, $dT^* = 0.05$, and $\omega = 0.999$.

Assuming constant spray properties, the resulting splashing threshold function $K_{crit} = f\,(\varepsilon_a\, T^*)$ increases with higher wall temperatures up to the hot wall thermal threshold, where the boiling induced breakup enhances a destructive impact interaction probabil-

ity. A rougher wall imposes a normal component to the tangential fluid movement by induced turbulence, facilitating a destructive interaction of the droplet with the wall. This trend is reduced increasing the temperature of the wall, because of the easier vapour generation in the surface depressions, which act as a cushion for the penetration of the liquid in the crevices. This behavior is depicted in Fig. 4.22-a, and its effect on the overall kinematic threshold map is reported in Fig. 4.22-b.

The presence of liquid on the surface, which implies cold wall conditions, alters the

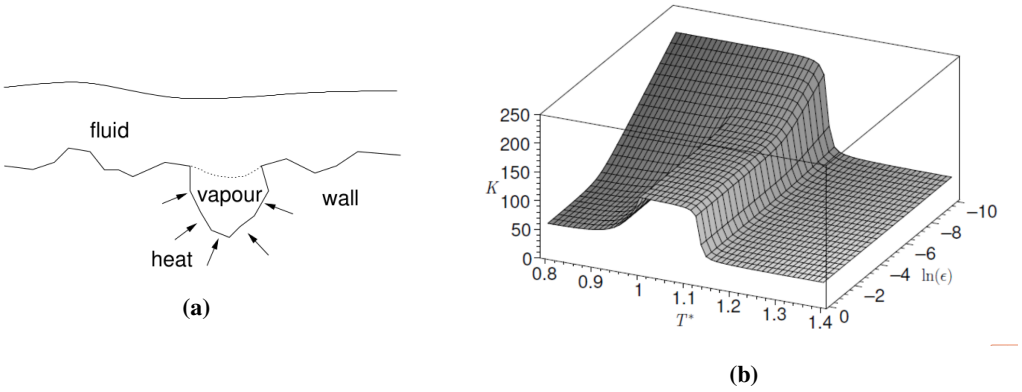

Figure 4.22: *Effect of the surface roughness coupled with the wall temperature on the impact (a) and kinematic threshold $K_{crit} = f(\varepsilon_a T^*)$ behavior [40] (b).*

droplet behavior on the surface and introduces the necessity of characterizing another surface property, which is defined as the liquid film thickness normalized on the droplet diameter (4.9).

$$\delta = \frac{h_{film}}{d} \tag{4.9}$$

A functional description of the kinematic parameter threshold literature data [19, 51, 101] for wet conditions has been generated in [40]. It employs a Weibull expression (4.10) and is defined according to the ϕ function (4.11) of δ and the droplet Laplace number La (Tab. 4.1).

$$Weibull\,(x, x_0, q) = \frac{q}{x_0}\left(\frac{x}{x_0}\right)^{q-1} e^{-\left(\frac{x}{x_0}\right)^q} \tag{4.10}$$

$$\phi\,(x, x_0, y_l, y_r, s) = \frac{y_r - y_l}{\pi}\arctan\left(\pi\, s\frac{x - x_0}{y_r - y_l}\right) + \frac{y_r - y_l}{2} \tag{4.11}$$

The definition of the K_{crit} for wet impact depends on the conditions reported in (4.12) and it refers to the δ_0 variable, which represents the values for the switch between low

La and high La behavior, defined in (4.13). The behavior of the wet splashing threshold is reported in Fig. 4.23.

$$K_{crit}\left(\delta\, La\right) = \phi\left(\delta,\, \delta_0,\, 125,\, 58.7,\, -100\right) + \left(408.4\,\delta_0 - 283.6\right) Weibull\left(\delta,\, \delta_0,\, 3\right) \tag{4.12}$$

$$\delta_0 = \phi\left(La,\, 600,\, 0.85,\, 1.08,\, 0.003\right) \tag{4.13}$$

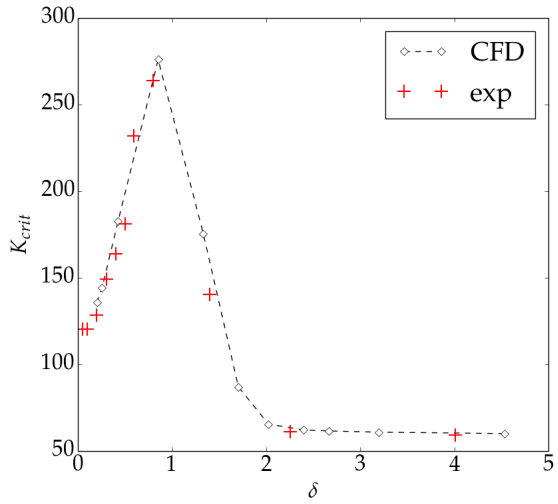

Figure 4.23: *K_{crit} threshold for impact on wet wall. Comparison between the implemented value and the data from [19, 51].*

Determination of the impact outcome

The relevant quantities of the droplets leaving the wall handled by the model are able to provide a detailed characterization of the momentum of a computational parcel. The outcome of the impact[1] can be therefore defined according to:

- mass fraction of the secondary drops $\nu_m = \frac{mass_1}{mass_0}$
- size ratio $\gamma = \frac{d_1}{d_0}$
- velocity magnitude

[1]The subscript 0 is used to refer to the impinging droplet. Each of the droplets ejected from the impact is labeled with the subscript 1

- trajectory (ejection angle toward the surface β and deviation angle ψ from the incident planar direction)
- number of particle per parcel to fulfill the overall mass balance.

Mass ratio The implemented semi-empirical function, based on [7], has been corrected by [40] to include the hot wall transition and the liquid film interaction is reported in (4.14). No liquid deposition is considered when the dimensionless temperature T^* is above the critical threshold. In case of presence of wet surface, the impact can remove a fraction of the mass of the liquid film obtaining $\nu_m > 1$.

$$\nu_m = \begin{cases} max\left(0, min\left(1, \frac{T^*-0.8}{1.1-0.8}\ (1-B)\ +\ B\right)\right), & \text{with } B = 0.2 + 0.6\,p, \text{ dry wall.} \\ max\left(0, min\left(1, \frac{T^*-0.8}{1.1-0.8}\ (1-B)\ +\ B\right)\right), & \text{with } B = 0.2 + 0.9\,p, \text{ wet wall.} \end{cases} \tag{4.14}$$

$$\text{where} \quad p = rnd(0\,,\,1)$$

Size ratio No clear temperature influence has been found in the determination of the size of the secondary droplets, guiding to the implementation of the same size ratio correlation in the CFD code. The formulation for dry wall impact by [40], couples the data of [36, 87] assuming a similarity to the formulation of [58], which provides the correlation for wet wall interaction. The average diameter of the ejected droplets is dependent on the Weber number We (Tab. 4.1) and the impingement angle α and reported in (4.15).

$$\gamma = \begin{cases} 3.3\, e^{3.6\left(\frac{\alpha}{\pi}\right)^2} We^{-0.65}, & \text{dry wall} \\ 2.2\, e^{3.6\left(\frac{\alpha}{\pi}\right)^2} We^{-0.36}, & \text{wet wall.} \end{cases} \tag{4.15}$$

The assignment of the size of each secondary droplet is then defined according to a Weibull distribution built around the average value γ which is used as $scale$ parameter, assuming a $shape$ parameter q equal to 2.
For the hot rebound interactions the droplet is assumed not to change its size.

Velocity ratio The velocity of the secondary drops is distinguished between rebound and atomization and no thermal characterization is expressed for the destructive in-

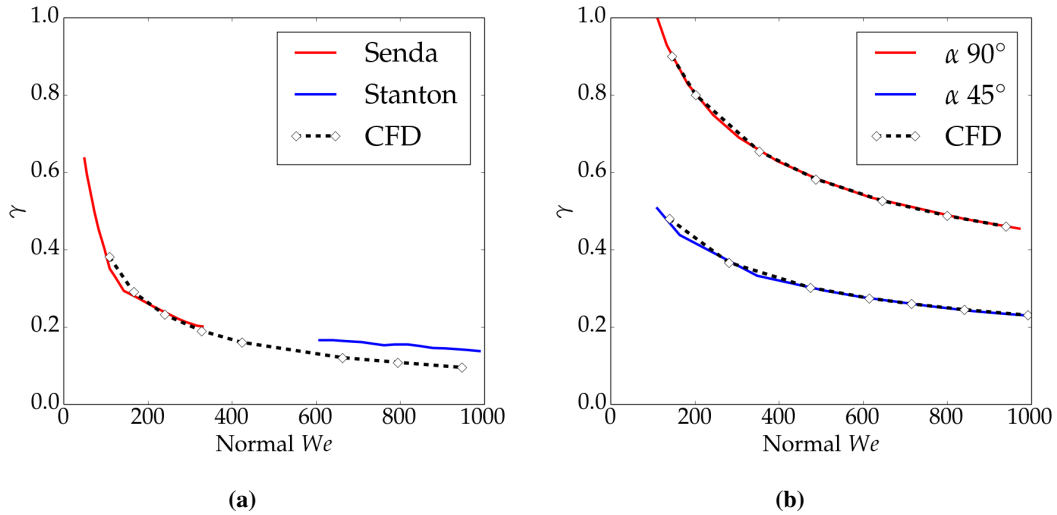

Figure 4.24: *Diameter ratio for dry [36, 87] (a) and wet [58] (b) impingement conditions.*

teractions. The rebound expresses a conservation of the tangential momentum of the droplet, and a reduction of the normal momentum component is defined as a function of the normal impact Weber number [99] reported in (4.16) and shown in Fig. 4.25

$$We_1 = 0.678\, We_0\, e^{-4.415\cdot 10^{-2}\, We_0} \tag{4.16}$$

The splashed droplet velocities in dry wall conditions are derived as function of the

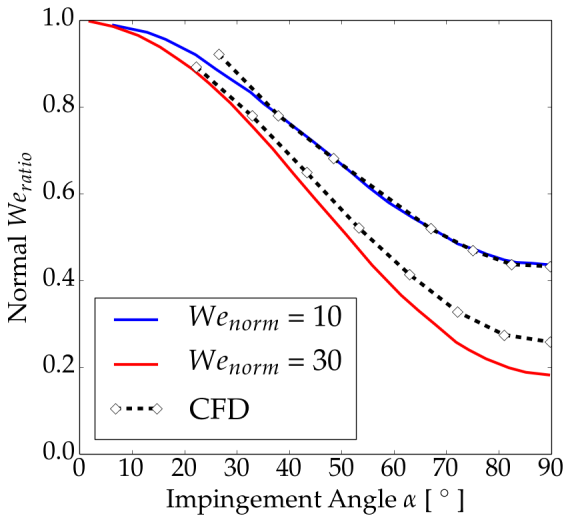

Figure 4.25: *Normal We reduction trend in the hot rebound interaction [99].*

absolute Weber number We_a and the angle impingement angle α according to (4.17).

$$We_{a,1} = \gamma\left(We_{a,0}\left(1-\eta^{'}\sin^2\alpha\right)+12\right)-\frac{12}{\nu_{32}} \quad \text{with } \eta^{'}=0.85 \text{ and } \nu_{32}=2 \tag{4.17}$$

For wet wall splash events, the formulation is dependent as well on the angle and on the absolute Weber number [58] as reported in (4.18).

$$max\left(51-7.1\,e^{3.4\frac{\alpha_r}{\pi}},\ c_\alpha We_{a,0}\right) \quad \text{with } c_\alpha=-0.378\left(\frac{\alpha_r}{\pi}\right)^2-0.123\,\frac{\alpha_r}{\pi}+0.156 \tag{4.18}$$

Fig. 4.26 shows the implemented model behavior against the experimental data gathered in [40]. The velocity of the single parcel is calculated in the code from the We

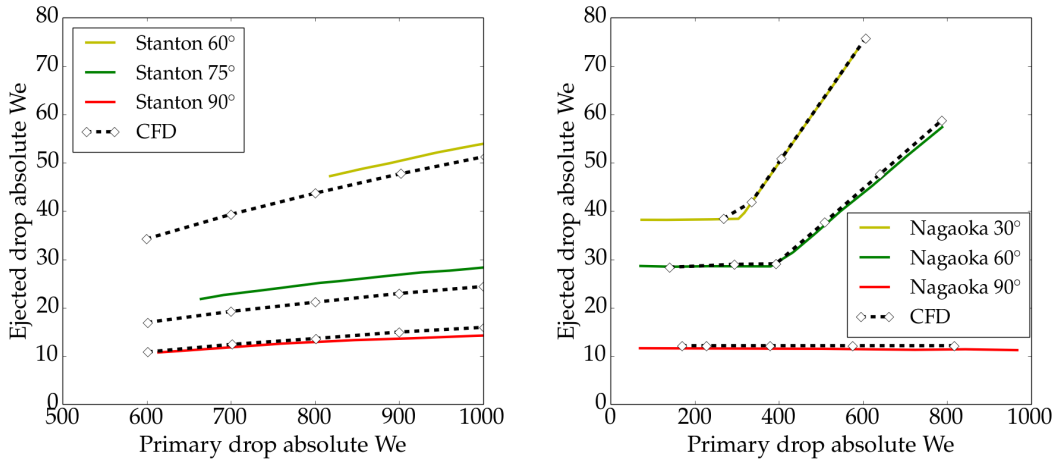

Figure 4.26: *Absolute We reduction correlation for dry [87] (a) and wet [58] (b) impingement conditions.*

definition, according to the characteristic droplet size calculated in the previous paragraph (4.19).

$$U_1 = \sqrt{\frac{\sigma\, We_{a,1}}{\rho\, d_{i,1}}} \tag{4.19}$$

Ejection angle For hot rebound conditions the trajectory of the droplets after the impact is a result of the reduction in the normal component of the momentum, and tends to flat on the surface. The ejection angle toward the surface β has been found dependent on the droplet incident direction [56, 58] in cold and wet wall conditions.

For impacts on hot surfaces, a strong dependence on the Weber number has been de-

scribed by [2, 40].

The resulting angles are distributed on the splashed droplets through a logistic distribution (4.20) around the average value calculated in (4.21).

$$logistic\left(\beta,\,\bar{\beta},\,\sigma_l\right) \;=\; \frac{1}{\sigma_l}\,\frac{e^{-\frac{\beta-\beta_0}{\sigma_l}}}{\left(1+e^{-\frac{\beta-\beta_0}{\sigma_l}}\right)^2} \qquad \text{with } \sigma_l \;=\; 4 \tag{4.20}$$

$$\bar{\beta} \;=\; \begin{cases} 9.3 \;+\; \ln\epsilon_z\,(2.7-0.03\,\alpha) \;+\; 0.22\,\alpha, & \text{cold dry wall} \\ 0.225\,\alpha\,e^{(0.017\alpha-0.937)^2}, & \text{wet wall.} \\ \alpha\,0.96\,e^{-0.0045\,We}, & \text{hot wall.} \end{cases} \tag{4.21}$$

The behavior of the code is reported in Fig. 4.27 for the three possible impact cases.

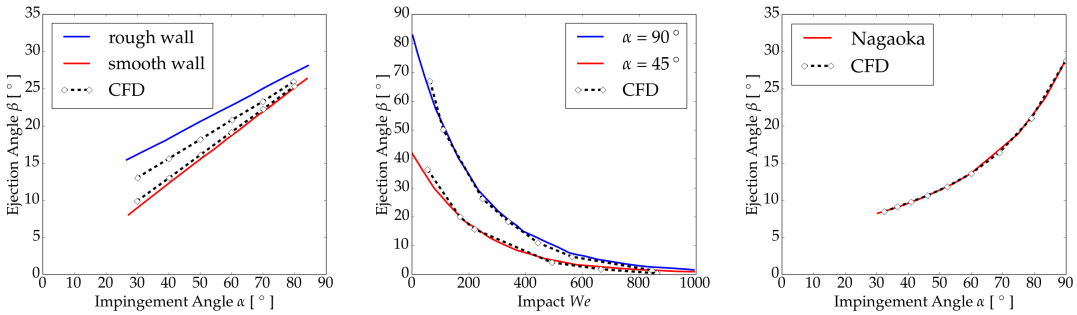

(a) **(b)** **(c)**

Figure 4.27: *Ejection angles β for cold-dry wall [56]: CFD smooth profile refers to ϵ_z=0.05, and CFD rough profile to ϵ_z=0.3 (a), hot wall [2] (b) and wet wall [58] (c).*

Deviation angle For orthogonal impingement, the secondary drops leave the impingement location with random planar direction. For smaller impact angle $\alpha < 90°$ the distribution is condensed at the leeward side and diluted at the windward side. This effect is directly related to the conservation of the tangential component of the momentum. The modeling approach proposed by [40] is based on mass and momentum conservation, assuming that the thickness of the sheet caused by the spray, in analogy with an impinging jet, is proportional to the probability of drop emission. The resulting

deviation angle ψ formulation is reported in (4.22).

$$\psi \;=\; -\frac{\pi}{\omega}\,\ln\left(1 \;-\; p\left(1\,e^{-\omega}\right)\right) \tag{4.22}$$

with

$$\omega \;=\; \begin{cases} \sqrt{\frac{1+8{,}872\,\cos 1.152\,\alpha}{1-\cos\alpha}}, & \alpha \;\leq\; 80^{\circ} \\ \frac{\pi^2}{2}\,\cos\alpha, & \alpha \;\geq\; 80. \end{cases}$$

Number of parcels A destructive interaction with the walls induces the fragmentation of the impinging drop into a variable number of secondary droplets. The size ratio formulation (4.15) provides the characterization of ejected droplet diameter, and therefore their number through the conservation of mass. Within the Discrete Parcel Model approach employed in the Lagrangian description of the spray proposed by this work, an additional assumption needs to be defined to characterize the droplet breakup. [40] proposes to generate three new parcels for each destructive impingement event, according to [87]. The cumulative Weibull distribution corresponding to the parameters defined in the size ratio analysis around the average value γ is therefore accessed with three random points to extract three characteristics diameters to be assigned to each computational parcel. The determination of the total number of droplets N_{tot}, composing the three parcels, is determined by the discretized mass balance (4.23).

$$\frac{\pi}{6}\,\rho\,,N_{tot}\sum_{i=1}^{N_{parcels}}\left(pdf_i\,d_i^3\right) \;=\; \nu_m\,m_0 \tag{4.23}$$

The Weibull pdf is accessed again to distribute the fraction of $Ntot$ to each of the ejected parcels.

Model outcome

The released OpenFOAM® library provides two spray-wall interaction models. The simplest one[2] constrains the behavior of the impinging parcel to a constant interaction type, neglecting the parcel and the system thermal and kinematic parameters.
A more detailed impingement model[3], based on [7] is available to characterize the in-

[2] $StandardWallInteraction$
[3] $ThermoSurfaceFilm$

teraction of the spray with cold walls, both wet and dry, through a routine comparable with the newly implemented one.

It is not suitable for the field of interest of this work, because it is not able to discriminate hot wall impingements from the purely kinematic interactions, as shown in Fig. 4.28, not allowing the identification of the events provoking wall cooling.

The new impingement model is tested in its hot and cold behavior and compared to the

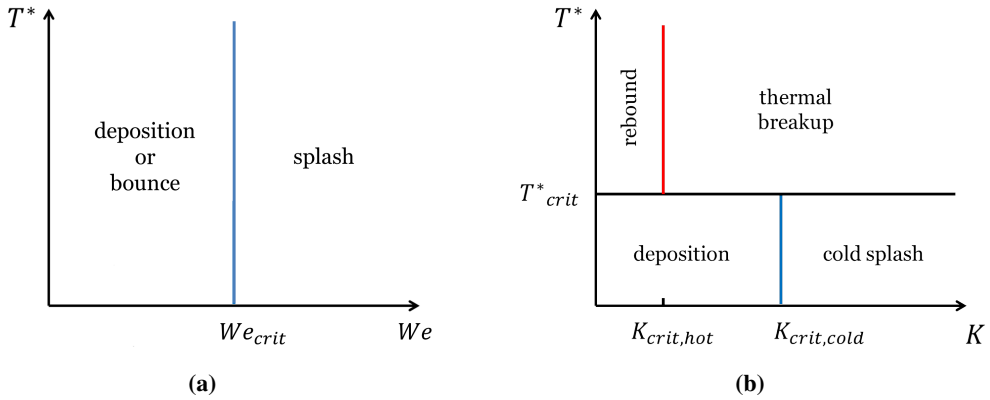

Figure 4.28: *Impingement map sketch for the OpenFOAM® model (a) and the one newly implemented on the basis of [40].*

state of the art of the available CFD platform involving dry wall conditions representing possible operating conditions of an SCR system. The graphs showing the agreement of the implement model results over the experimental data are generated testing the interaction of a distilled water single droplet impact on a flat surface, as sketched in Fig. 4.29.

The implemented spray-interaction model is able to handle both single and multi-region test cases, therefore to be consistent with the released model a single layer region is put in correspondence to the bottom wall, which acts as a thin liquid film with zero thickness. The surface temperature is kept constant and de-coupled from the gaseous and the dispersed liquid phases to 300 K ($T^* \approx 0.8$) to simulate the cold wall behavior, and to 450 K ($T^* \approx 1.2$) for the hot wall interaction. To be consistent with the OpenFOAM® standard model, the droplet We number is reported to compare different impingement regimes.

The first impact event involves a drop with normal We equal to 600 generating a destructive interaction according to both the model thresholds and the behavior is reported

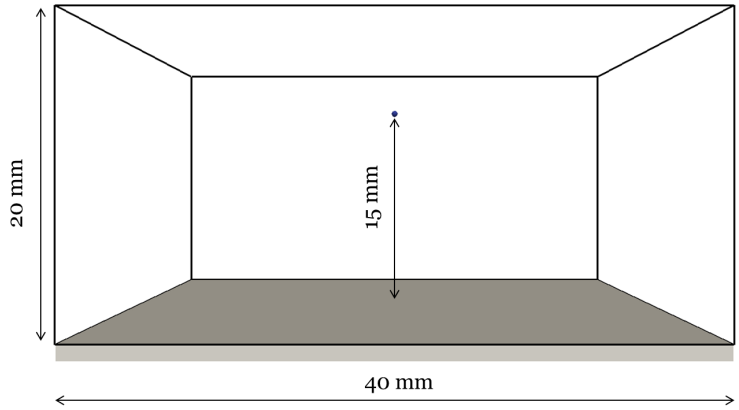

Figure 4.29: *Single droplet normal impingement test-case.*

in Tab. 4.9.

It is possible to notice that for normal impingement the new model provides a stronger

	std OpenFOAM®	*new* - cold wall	*new* - hot wall
We_{norm}	600	600	600
α [°]	90	90	90
T_{wall} K	300	300	450
T^*	0.8	0.8	1.2
γ	0.22	0.13	0.13
$\frac{U_1}{U_0}$	0.57	0.28	0.28
β [°]	20.22	28.33	5.67
ψ_1 [°]	145	-132	-132
ψ_2 [°]	112	-60	-60
ψ_3 [°]	[-]	66	66

Table 4.9: *Normal impingement modeling comparison.*

breakup, visible from the lower size ratio γ, which, coupled with the higher reduction in the velocity magnitude, provokes a higher dissipation of the impinging droplet momentum. It is possible to notice that the trajectory of the secondary droplets ejected from a hot wall thermal breakup is closer to the surface.

For the representation of the inclined impact on the surface, summarized in Tab. 4.10, a droplet with normal We equal to 350 and an impingement angle α of 60° is simulated, to point out the remaining features of the new model, which are the deviation angle characterization and the introduction of the thermal threshold.

The cold-dry wall behavior is not included in Tab. 4.10 since the impinging droplet de-

	std OpenFOAM®	new - hot wall
We_{norm}	350	350
α [°]	60	60
T_{wall} K	300	450
T^*	0.8	1.2
γ	0.39	0.109
$\frac{U_1}{U_0}$	0.87	0.52
β [°]	20.22	11.81
ψ_1 [°]	145	-44
ψ_2 [°]	112	-15
ψ_3 [°]	[-]	32

Table 4.10: *Inclined impingement modeling comparison.*

posits on the wall according to the newly implemented regime identification. From the reported data it is possible to appreciate the more dissipative impact which generates a stronger atomization. The trajectories of the secondary droplets exiting the impact are concentrated in the leeward direction, included in a $[-45, +45]$ ° range, which is more representative of the physical behavior of an inclined impact.

4.4 Thermal behavior of the impingement

The consistent spray fluxes impinging on the bottom surface of the system measured and simulated in the previous sections are source of wall cooling and the decrease in the temperature of a solid surface represents the trigger for the formation of liquid film and possible derived solid urea by-products deposits [27].

Heat transfer caused by spray impingement is significant in many fields of application [4, 54, 102]. Thermo-graphic measurements of the wall cooling derived by a low a pressure-driven spray [43] have shown heat flux peaks up to 10 MW/m^2, highlighting the paramount importance of the correct characterization of this phenomenon in the system overall energy balance. From the modeling side, the work by [12] proposed a thermal modeling of the impingement coupled with the already implemented kinematic interaction model which produced good results in the validation on solid temperature transient experimental data. For this reason the same approach is implemented in the OpenFOAM® platform within the framework described above. According to [107] the direct heat transfer between spray and wall is well described with the assumption of

contact between two semi-infinite bodies, represented by the droplet and the wall. This approach introduces the dependence of the energy balance on the respective thermal effusivities (4.24), where ρ is the density, λ the thermal conductivity and $c_{p,i}$ the specific heat[4].

$$b_i \;=\; \sqrt{\rho_i \, \lambda_i \, c_{p,i}} \tag{4.24}$$

The formulation of the exchanged energy is dependent on the contact time t_{con} and the contact area A_{con}, and is a function of the temperature difference between the wall and the drop, as reported in (4.25).

$$Q \;=\; A_{con} \, \frac{2\sqrt{t_{con}}}{\sqrt{\pi}} \, \frac{b_w \, b}{b_w \;+\; b} \, (T_w \;-\; T) \tag{4.25}$$

The contact time is a function of the impinging droplet properties and depends on the kinematic parameter K (Tab. 4.1) and the switch between the two formulations reported in (4.26) corresponds to the upper limiting value of the conservative hot wall interaction as reported in (4.5). The first case almost corresponds to the hot rebound interaction and the second one to the thermal breakup.

$$t_{con} = \begin{cases} \frac{\pi}{4} \sqrt{\frac{\rho \, d^3}{\sigma}}, & K \;\leqslant\; 40 \\ \sqrt{\frac{\pi}{2}} \left(\frac{\rho \, d^5}{\sigma \, U^2} \right)^{0.25}, & K \;>\; 40. \end{cases} \tag{4.26}$$

The contact area is defined as a function of the We, according to the maximum diameter expansion provided in [1] and shown in (4.27). The contact drop size evolution law is assumed to linearly increase up to the maximum value $d_{con,max}$ in correspondence to half of the t_{con}.

$$d_{con,max} = d \, 0.61 \, We^{0.38} \tag{4.27}$$

The temperature of the liquid droplet on a hot surface can largely raise, therefore the properties of the droplets are update every simulation time step, taking care of the two-way coupling with the gaseous phase.

[4]The subscript w is used to refer to the wall properties. The liquid drop characteristics are reported without any subscript

Multi-region solver

The interaction between spray and wall needs the transient description of the solid phase, which is realized extending the boundaries of the system including the walls in the simulation.

The solid energy conservation equation, which is only diffusive, is discretized according to the finite volume approach, constraining a direct face-to-face coupling with the grid defined for the gaseous environment. The solution of the two phases is carried out in a segregated way, thermally connecting the boundaries with a Conjugate Heat Transfer (CHT) approach. The overall energy balance and the temperature continuity assumption are handled matching the temperature of the two phases at the interfaces (4.28), and equalize the exchanged heat fluxes (4.29).

$$T_{i,fluid} = T_{i,solid} \tag{4.28}$$

$$q''_{i,fluid} = q''_{i,solid} \tag{4.29}$$

The heat exchanged within the spray-wall interaction is determined by (4.25) and applied to the liquid phase as a source term in the energy balance of the droplet, and to the solid phase as a volumetric source term for the boundary cell covering the impingement location.

Assessment of the model behavior

A simplified test case is built on the basis of Fig. 4.29, involving a constant size (d = 50 μm) droplet chain impinging the wall with a angle of 45°. The Lagrangian phase is introduced with a point injector, set 15 mm above the impingement surface, which elaborates 0.5 kg/h of distilled water assigning constant velocity to the droplets, equal to 20 m/s. A detailed description is provided in [59]. The solid wall is represented as a 1 mm thick foil discretized into four uniform thickness cells. The frontal surface of a computational face defines a 1 mm^2 area. Its thermophysical properties are kept constant. The system is initialized in thermal equilibrium at atmospheric pressure and T equal to 300° C. The setup of the test case generates a stream of dropltes that impinges always the same wall computational face, bringing to the extreme level the wall cooling

effect and pointing out the numerical behavior of the system.

Application of the Conjugate Heat Transfer The effect of the gas-wall CHT on the overall energy balance is investigated comparing the fully coupled system with an artificial simulation, in which the solid surface is kept adiabatic to the gaseous field, experiencing only the drop impingement source. Fig. 4.30 reports the temperature profile along the solid foil thickness when the surface reaches the critical temperature level $T^* = 1.1$. The label 0 refers to the impact location, and $+1\ mm$ to the neighbor cells, not directly affected by the interaction with the spray. The CHT has a negligible influence on the heat flux and on the surface temperature. Moreover the lateral thermal conduction has a very restrained influence on the solid behavior highlighting that the time scale of the spray cooling is much shorter than the other thermal phenomena. This results

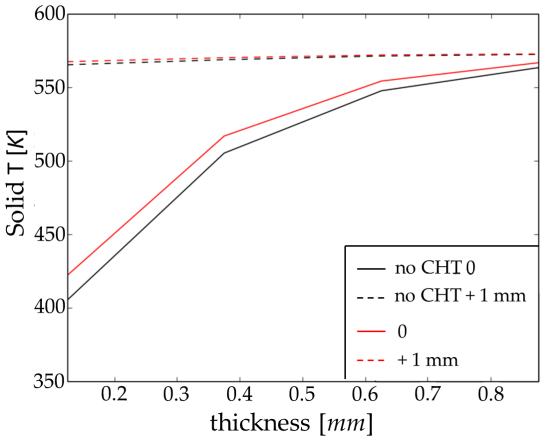

Figure 4.30: *Solid temperature profile at the onset of the liquid deposition.*

emphasizes the importance of a correct prediction of the impingement location in the design of an urea based SCR system.

Grid refinement effect The solid mesh is refined to estimate the effect of the thermal numerical inertia of the interaction between the Lagrangian spray and the Eulerian wall mesh. A refinement of the grid along the thickness direction, labeled $fine\ \ thickness$, generates layers of cells with uniform size equal to 0.125 mm. The grid tightening on the surface, $fine\ \ surface$, generates cells with 0.250 mm^2 area. The refinements are then coupled into the $fine\ \ mesh$ test case.

This process aims to estimate the different influence of the lateral conduction and of the normal temperature gradient effect on the thermal behavior of the solid surface.

Fig. 4.31-a reports the effect of the grid refinement on the temporal evolution of the

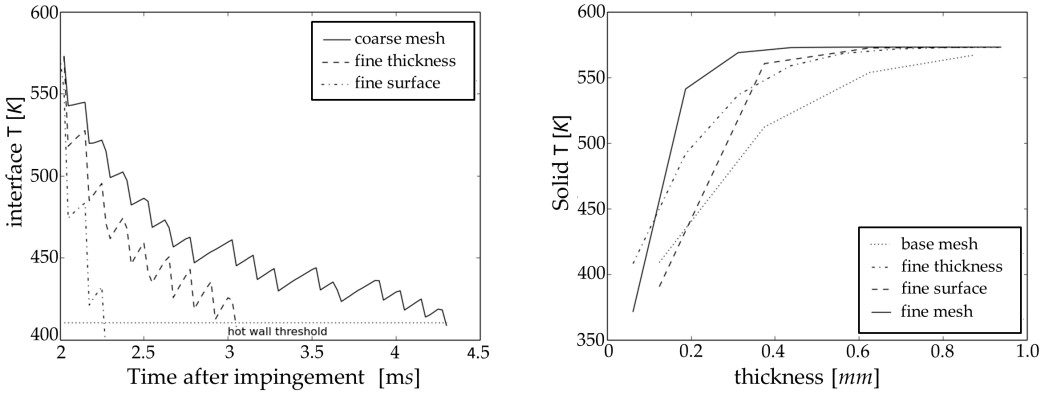

(a) **(b)**

Figure 4.31: *Time evolution of the solid surface temperature (a) and temperature profile along the thickness of the solid foil (b).*

thermal profile at the location of the impingement. The paramount heat source provided by the spray cooling implies that the volume of the solid cell is the only important parameter in the representation of the spray-wall interaction and determines the transient length to the thermal wetting threshold. The same consideration is drawn from Fig. 4.31-b which reports the influence of the mesh refinement on the temperature gradient along the solid foil thickness, showing that both the lateral conduction and the axial conductive heat fluxes are of negligible influence during the liquid impact on the wall.

The measurements and simulations of the spray reported in Sec. 4.1 show that the normal component of the kinematic parameter in the core of the spray is higher than the critical thermal break-up threshold defined by the implemented model ((4.4), Fig. 4.21-b). Since a destructive impact generates droplets with sizes and velocities considerably smaller than the primary ones (Figs. 4.24-a, 4.26-a), the addition of the kinematic modeling of the spray-wall interaction introduces a strong modification in the spray evolution in the pre-catalytic region.

The computed liquid mass footprints (Figs. 4.19, 4.18), in good agreement with the experimental results, show that the impingement is concentrated in the neighborhood

of the spray cone projection and represents a fundamental contribution in the system energy balance, which need to include the solid wall thermal transients.

CHAPTER 5

SCR spray heat-transfer

The measurement of the full spray-wall thermal interaction transients has been carried out on the three hole nozzle (3H) reporting wall temperature maps and extracting the heat flux values for a single injection pulse (60 ms) of distilled water [43, 45]. No data is available for the 6 hole nozzle (6H) representing the core of the simulation campaign, whose behavior is extensively analyzed through the models implemented in the code and coupled with the kinematic characterization of the low-pressure driven spray in cross-flow conditions.

5.1 Experimental results

A stainless steel (type 304) plate with a thickness of 0.3 mm is inserted 14 mm above the bottom surface of the injection chamber, as sketched in Fig. 5.1. The chamber is equipped with a high transmissivity bottom optical access, to allow thermographic measurements on the rear surface of the plate, which is not wet and maintains a constant

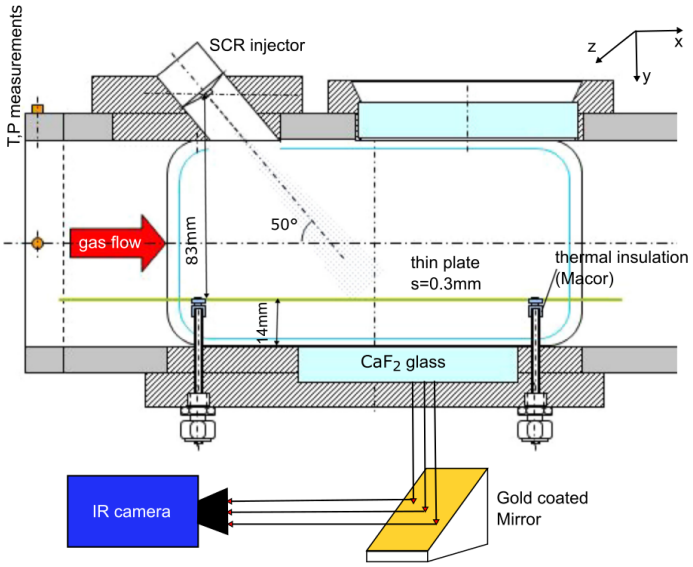

Figure 5.1: *Illustration of the experimental setup for the heat transfer evaluation [45].*

emissivity. The infrared camera is a Cedip Jade III, with a 50 mm lens. The radiation detector is an InSb quantum detector that is sensitive in the 3.6-5.1 μm wavelength range and is cooled by a Stirling engine to 77 K. 150 frames per second are taken at a resolution of 320 $\times$ 240 pixels at 0.245mm/pixel, allowing the visualization of the whole injector footprint [45]. The measurements are taken on the 3H injector in cross-flow, keeping the gas temperature constant at 300° C and increasing the mass flow rate $\dot{m}_{gas}$ from 100 $^{kg}/_{h}$ to 300 $\frac{kg}{h}$.

The calculation of the spray cooling heat flux is realized solving the inverse heat conduction problem with a finite element scheme, assuming 1D heat transfer through the thickness according to [5, 23] and to the estimation obtained in Section 4.4 from Chapter 4 for a single droplet impact. The measured rear surface temperature profile is reported on the left column in Fig. 5.2, beside the estimated front wall thermal footprint (center) and the calculated heat flux at the front surface (right column) for the spray impingement with gas flow at T_{gas} =300° C and $\dot{m}_{gas}$ =200 $^{kg}/_{h}$. The clear separation of the three spray cones is evident from the temperature profiles, in accordance with the patternator measurements, showing that the spray mass flux strongly influences the cooling heat flux. Moreover, the temperature drop is substantial for each spray jet and there is a time shift in the profiles due to the different traveling distance from the injec-

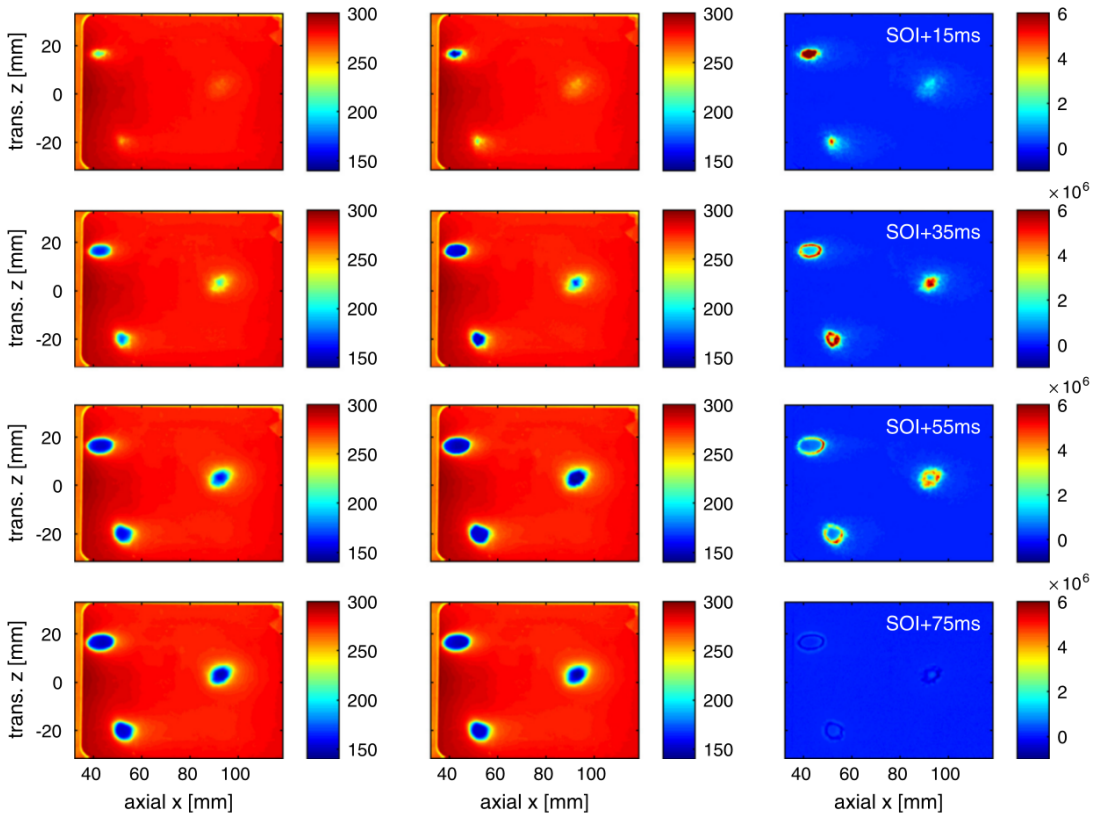

Figure 5.2: *Spatial distribution of the plate rear surface measured temperature (a), front surface calculated temperature (b) and of the calculated front surface heat flux (c) [45]. The injector is operated with a DOI of 60 ms.*

tor nozzle to the surface. In the lowest cross-flow loads, corresponding to the minimum entrainment of liquid in the air, the local heat flux magnitude can reach 10 $^{MW}/_{m^2}$. The lowest temperature of the three footprints are quite similar, showing that there is a limit to which extent the plate can be cooled by the spray and this limit is independent from the local mass flux. A time lag between the front and the rear surface temperature profiles is visible from the thermal sampling on the centerline of the most downstream cone as shown in Fig. 5.3 that contributes to highlight the negligible magnitude of the lateral conduction in the plate, visible in the conservation of the profile after the end of the injection ($t > 68ms$). The temporal variation of the plate front surface temperature, averaged on a 2.7 mm circular area around the T_{min} peak and reported in Fig. 5.4-a, shows that the spray cooling effect decreases with increasing gas flow rate. The maximum heat flux over the same sampling area amounts up to 4.5 $^{MW}/_{m^2}$ at T_{gas} =300° and $\dot{m}_{gas}$ =100 $^{kg}/_{h}$ and 3.0 $^{MW}/_{m^2}$ at T_{gas} =300° and $\dot{m}_{gas}$ =300 $^{kg}/_{h}$, and is

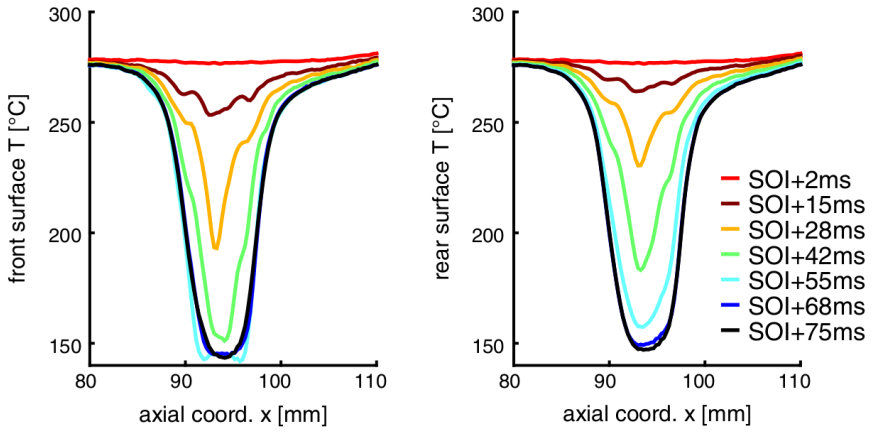

Figure 5.3: *Plate surface temperature profiles along the centerline of the front cone footprint: front surface (left)) and rear surface (right). DOI=60 ms, T_{gas} =300° C and $\dot{m}_{gas}$ =200 $^{kg}/_{h}$ [45]*

reached earlier in the case of lower flow rate, as in Fig.5.4-b.

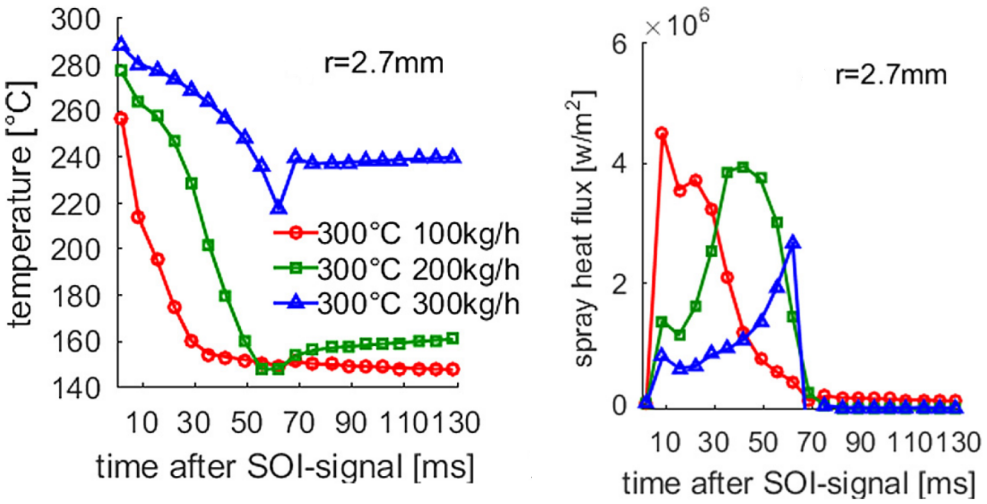

(a) **(b)**

Figure 5.4: *Temporal evolution of the coldest spot in the front cone footprint: front surface temperature (a) and front surface heat flux (b). DOI=60 ms, and sampling circular area corresponding to r=2.7 mm [45].*

5.2 Simulation results

The main simulation campaign as in Chapter 3 refers to the representation of the six hole injector 6H, which numerical behavior has been validated on the PDA measurement in cross flow at low and high load conditions, labeled as t200f100 and t400f400

to recall the temperature t $[^\circ C]$ and the flow f $[^{kg}/_h]$ values.
Although the results are not directly comparable to the experimental data, the measured qualitative behavior and magnitude of the phenomena under investigation are used as a reference for the understanding of the simulation reliability.

Mesh and Eulerian phase definitions

The grid is built on the basis of the simplified geometry proposed in Section 3.2.3 to represent the injection chamber. A 0.3 mm thick plate generated 14 mm above the bottom surface and isolated from the gaseous domain is discretized with 8 uniform cell layers along its thickness. The plate covers the whole transversal section, splitting the cross flow in two separate regions, respectively considered the main (top) and the bypass (bottom). The longitudinal extension of the solid mesh, $[-39\,,\,+205]$ mm from the nozzle location, is included in the gaseous domain, to correctly represent the flow split in different operating conditions. As shown in Fig. 5.5, a progressive refinement of the gaseous phase grid is generated both to better describe the split and rejoining of the flow at the plate edges and to reduce the aspect ratio between the cells of the two phases.

As for the kinematic characterization of the spray, the domain is halved along the

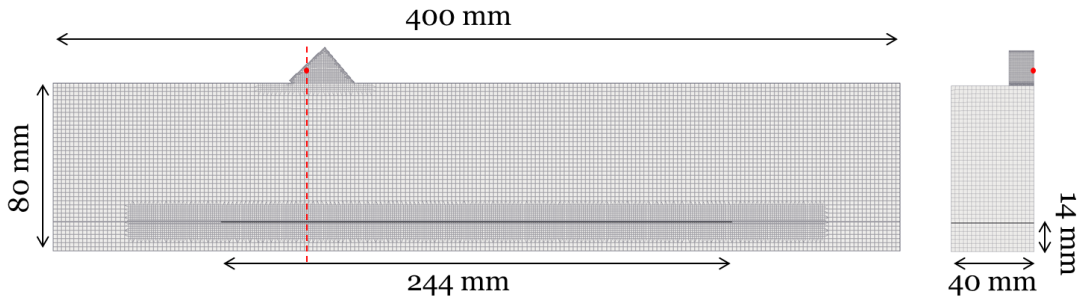

Figure 5.5: *Computational grid of the injection chamber equipped with the suspended plate.*

vertical plane built on the channel axis and a reflecting-symmetry boundary condition is applied to the obtained surface. A detailed mesh description is reported in Appendix B. The gas phase is defined as dry air according to Appendix A. The solid phase thermophysical properties are constant and reproduce the stainless steel type 304 [10] as reported in Tab. 5.1.

ρ_{solid}	kg/m^3	8055
$c_{p,solid}$	$J/kg\ K$	480
λ_{solid}	$W/m\ K$	15.1

Table 5.1: *Summary of the solid phase thermophysical property values.*

Initial and Boundary conditions The initial condition of the gas phase is generated according to the method resumed in Section 3.2.3 on the new grid: a periodic cylindrical mesh is used to generate a fully developed inlet flow profile, which is used to calculate the steady state condition in the mesh. The solid phase is initialized at constant pressure and temperature, which are in equilibrium with the gaseous phase. Conjugate Heat Transfer (CHT) boundary conditions (Section 4.4) are applied at all the interfaces between the phases to ensure the temperature and heat flux continuities and to simulate the heat flux provided by the gas by-pass to the rear surface of the plate. The multi-region solver described in Section 4.4 handles the solution of the gaseous and the solid transients, coupling them through boundary conditions. The full setup of is reported in Tab. 5.2

Gas Phase					
	external walls	interface walls	inlet	outlet	symmetry plane
$\mathbf{U}_{gas}$	No slip	No slip	$\mathbf{U}_{gas}$=$\mathbf{U}_{gas,developed}$	$\partial\mathbf{U}/\partial\mathbf{n}$=0	reflect-symm
P_{gas}	∂P/$\partial\mathbf{n}$=0	∂P/$\partial\mathbf{n}$=0	∂P/$\partial\mathbf{n}$=0	wave-trans [69]	reflect-symm
T_{gas}	$\partial T_{gas}/\partial\mathbf{n}$=0	CHT	T_{gas}=$T_{gas,0}$	$\partial T_{gas}/\partial\mathbf{n}$=0	reflect-symm
$Y_{i,gas}$	$\partial Y_i/\partial\mathbf{n}$=0	$\partial Y_i/\partial\mathbf{n}$=0	$Y_{i,gas}$=$Y_{i,gas,0}$	$\partial Y_i/\partial\mathbf{n}$=0	reflect-symm
k	scalable (all y^+)	scalable (all y^+)	k=$k_{developed}$	$\partial k/\partial\mathbf{n}$=0	reflect-symm
ε	scalable (all y^+)	scalable (all y^+)	ε=$\varepsilon_{developed}$	$\partial\varepsilon/\partial\mathbf{n}$=0	reflect-symm
Solid Phase					
	external walls	interface walls			
T_{solid}	$\partial T_{solid}/\partial\mathbf{n}$=0	CHT - $\partial T_{solid,i}/\partial\mathbf{n}_i$=$\partial T_{gas,i}/\partial\mathbf{n}_i$ and $T_{solid,i}$=$T_{gas,i}$			

Table 5.2: *CFD boundary condition summary.*

Water spray simulation

The simulation of the liquid injection retraces the Section 3.2.3 but the spray-wall interaction that includes both the kinematic and the thermal modeling introduced in Section 4.3. Distilled water is taken as the reference fluid for the characterization of the phenomena. The duration of the injection (DOI) is set to 100 ms to assess a wide range of impinging conditions and to analyze a significant thermal transient of the wall. The presence of the plate acts as an obstacle for the flow, modifying its development and

the consequent interaction with the spray, changing the location of the impingement. Moreover the modeling of the impingement introduces new source terms in the spray, which affects the gas through the two way coupling. The change in the gaseous field is visible in Fig.5.6, where the stream-lines of the flow are reported in two sections, corresponding respectively to the spray *core* path (left column) to the wall and to the spray *wake* development region (right column), as sketched in Fig.5.6-a.

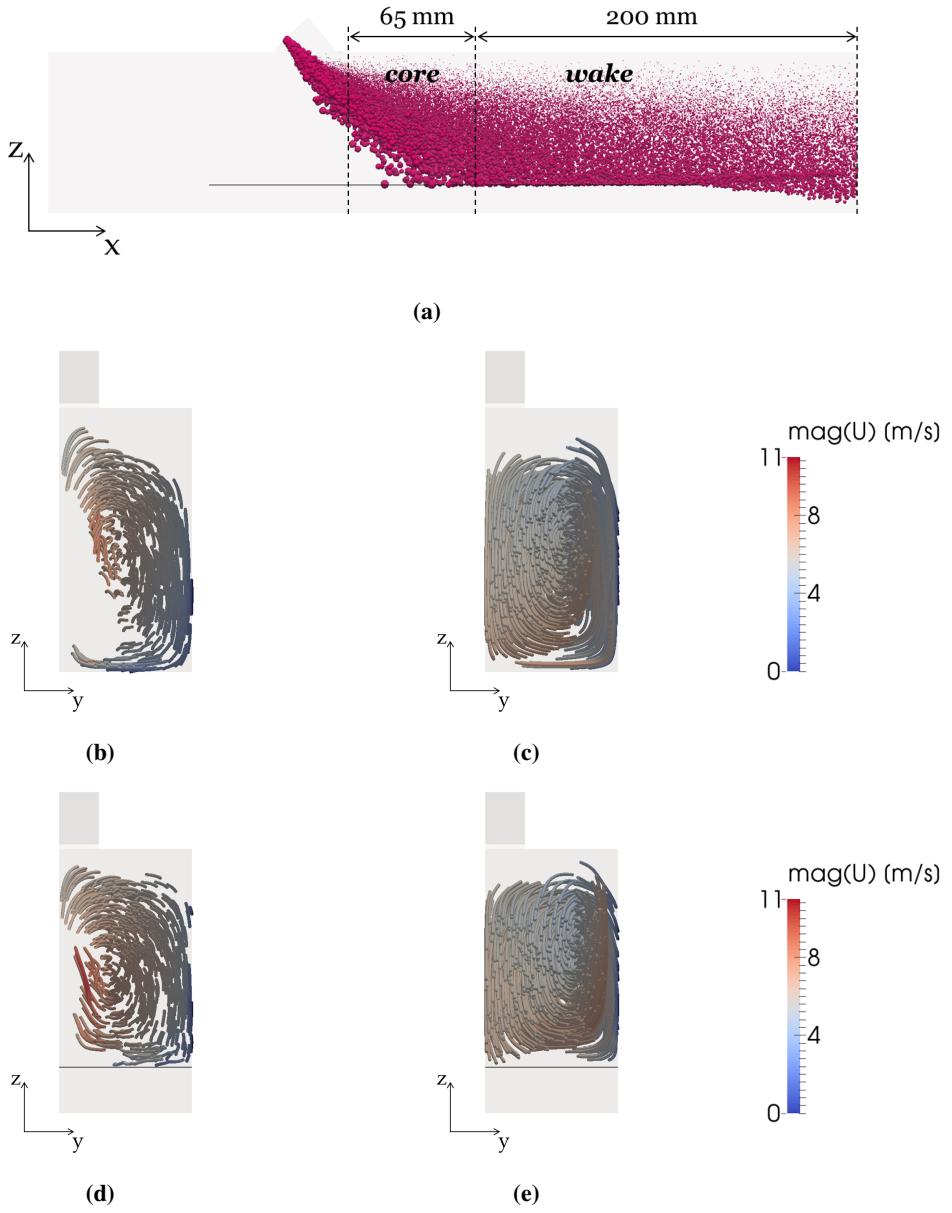

Figure 5.6: *6H - water injection - t200f100 - left column:core section, right column:wake section. Comparison between the gaseous flow stream-lines in the standard channel configuration (b-c) and the plate insertion (d-e).*

In low load conditions (t200f100) the presence of the plate confines the vortex generated by the spray in a smaller section, extending its influence to a larger part of the spray path, especially in the *wake* region. At high load (t400f400) the flow field is only slightly affected by the injected liquid momentum. The increase in the velocity magnitude due to the presence of the plate is not relevant for the injection section as reported in Fig 5.7.

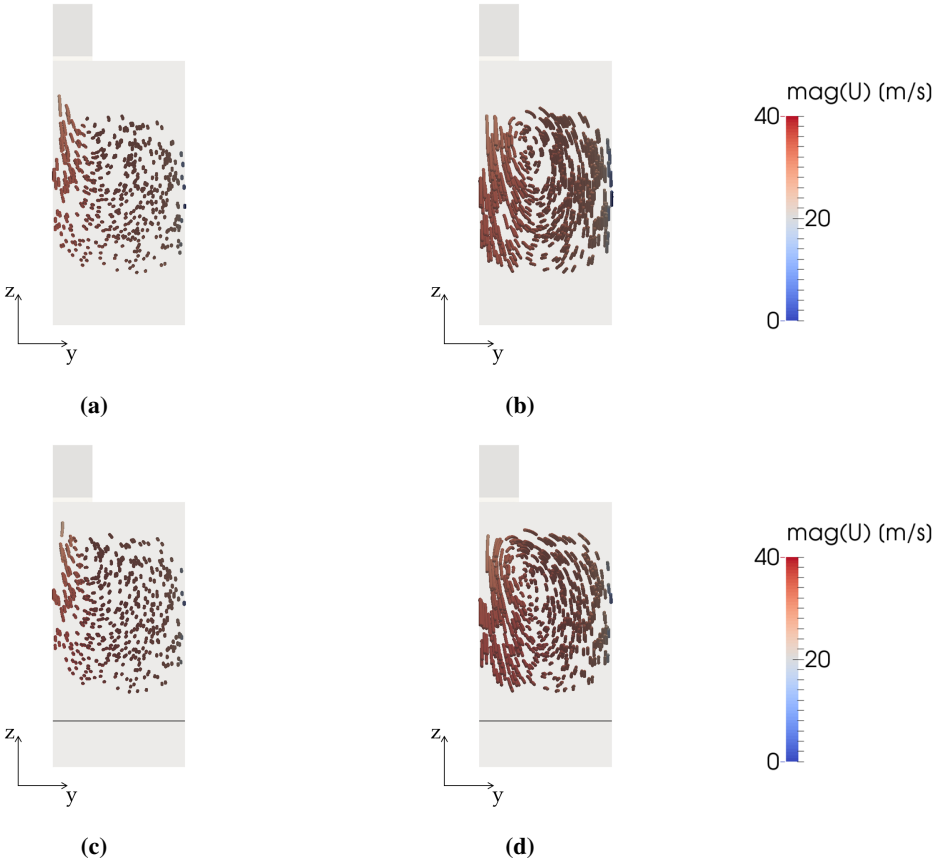

Figure 5.7: *6H - water injection - t400f400 - left column:core section, right column:wake section. Comparison between the gaseous flow stream-lines in the standard channel configuration (b-c) and the plate insertion (d-e).*

The variation of the system geometry and its influence on the flow field development are not strong enough to provoke a relevant change in the behavior of the spray path to the wall. Fig. 5.8 shows that the introduction of the plate in the system does not affect the primary droplets kinematic properties, which are still compatible with the PDA experimental data.

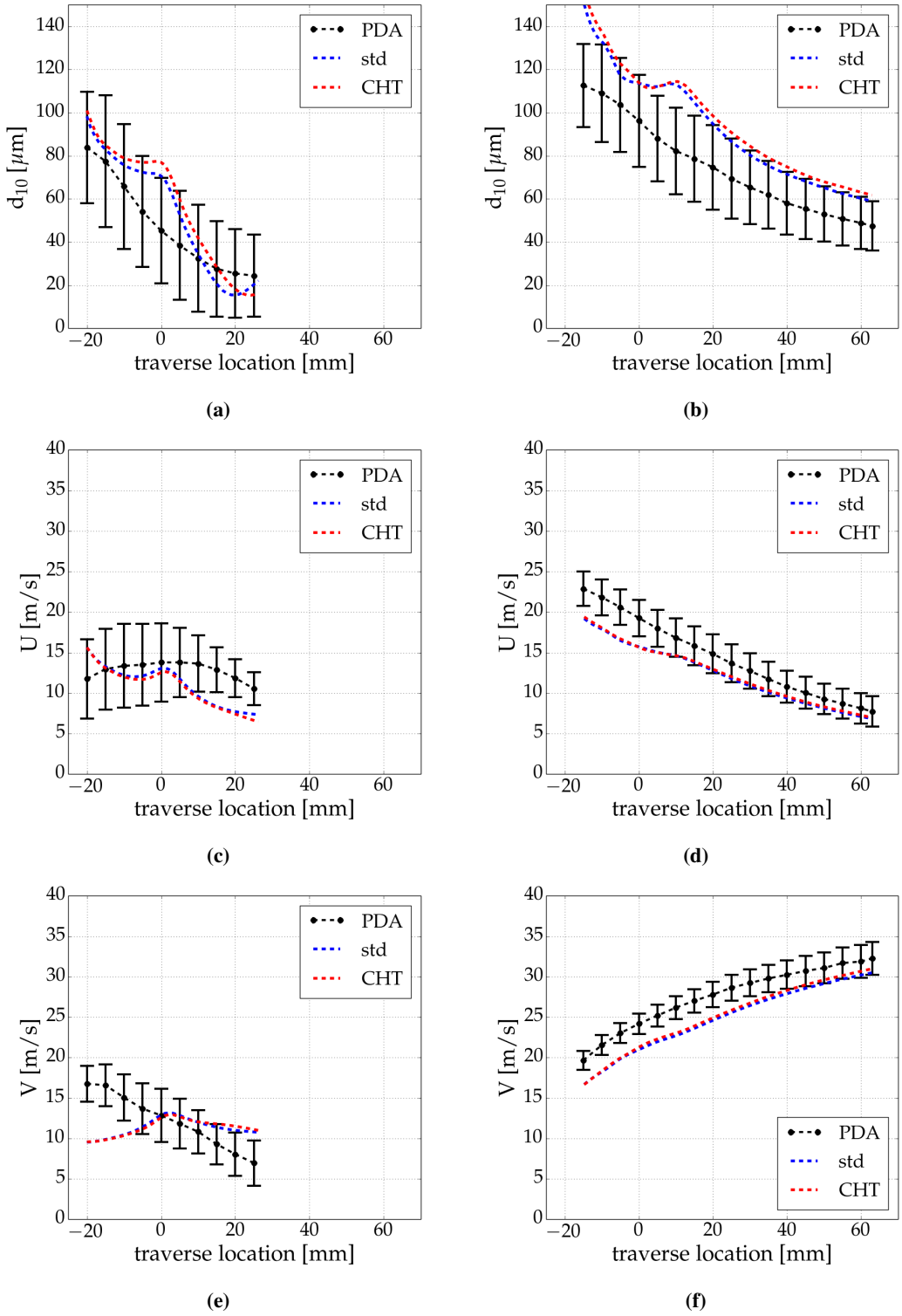

Figure 5.8: *6H - water injection - Spray average kinematic parameter profiles. Left: low load (t200f100): d_{10} (a), U (c) and V (e). Right: high load (t400f400): d_{10} (b), U (d) and V (f). The red lines refer to the complete spray-wall treatment on the suspended plate CHT, compared with the standard channel std configuration.*

These results are confirmed by the very similar spray patterns in the *core* section reported in Fig. 5.9 for low and high load conditions.

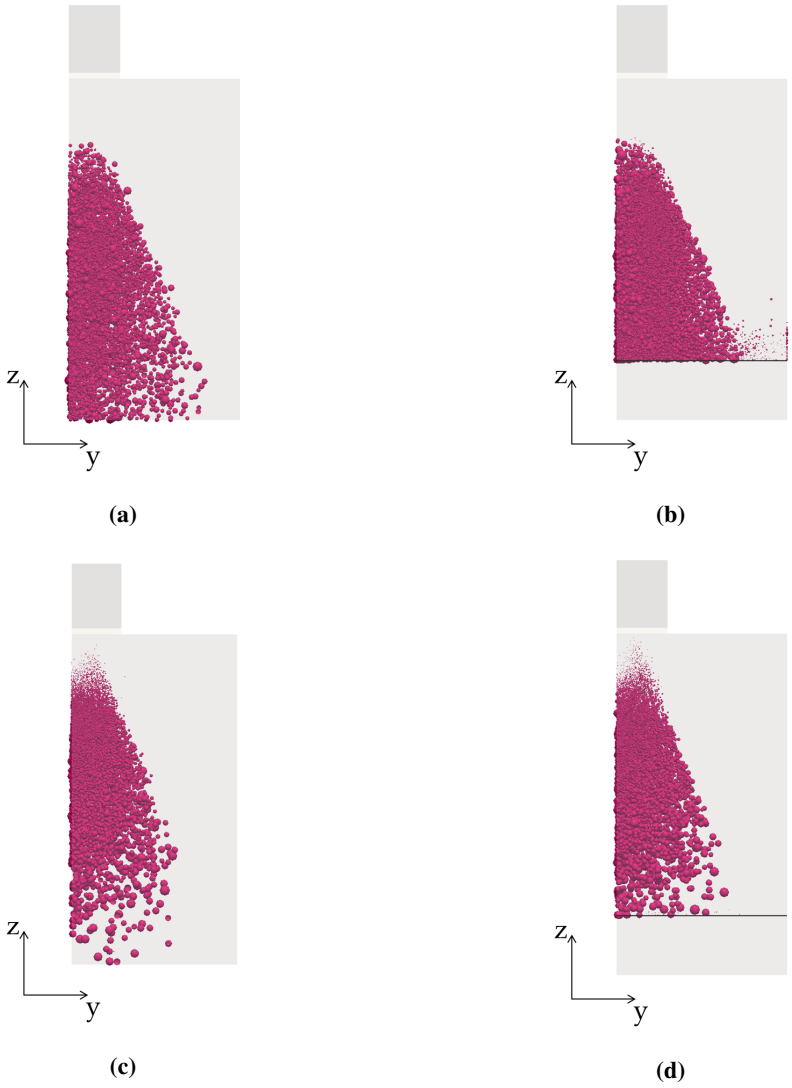

Figure 5.9: *6H - water injection - Spray development in the core section. left column: std channel, t200f100 (a) and t400f400 (c). right column: channel with suspended plate, t200f100 (b), and t400f400 (d).*

The interaction with the solid plate, generates a strong modification of the wake (Fig. 5.10), which is constituted of parcels with a small characteristic diameter generated by the impact. Their initial trajectory is close to the plate front surface but is deviated from the gaseous vortex in the farthest wake. These phenomena are clearer for the t200f100 case, since the gas flow entrainment is reduced and the liquid injection has a stronger impact of the overall fluid-dynamic behavior of the system.

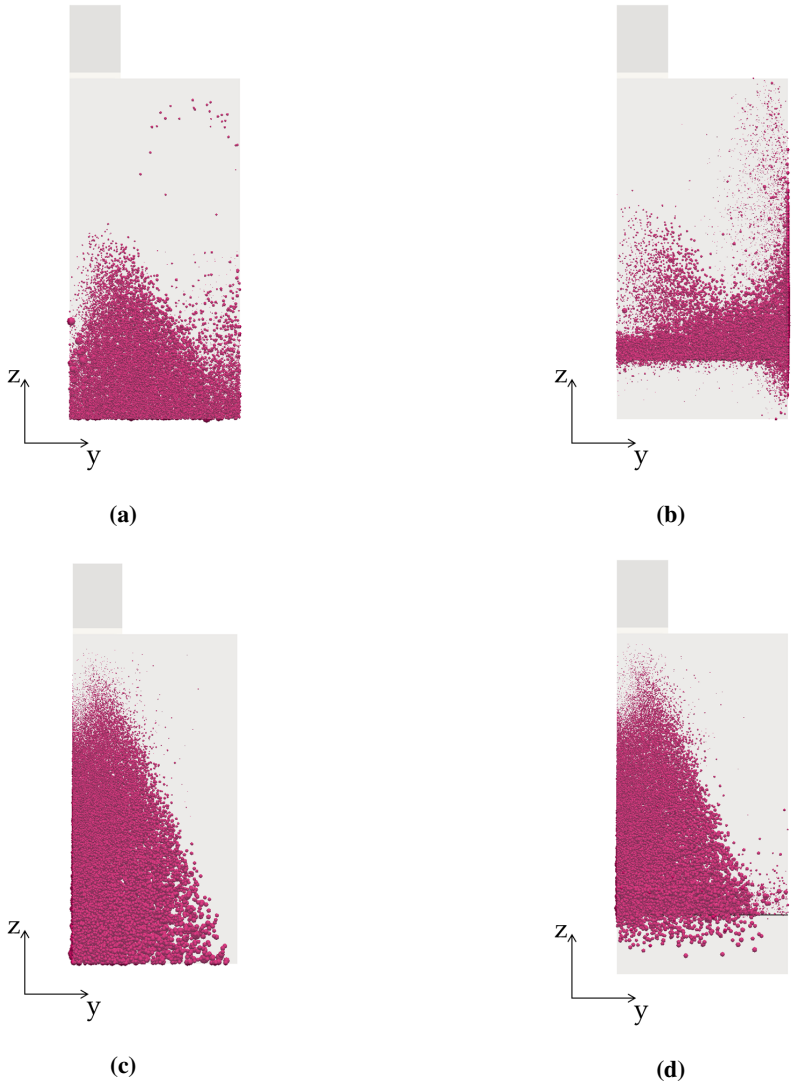

Figure 5.10: *6H - water injection - Spray development in the wake section. left column: std channel, t200f100 (a) and t400f400 (c). right column: channel with suspended plate, t200f100 (b), and t400f400 (d).*

Thermal transients

As stated in the previous chapter with the single droplet impingement test, the spray impact on the plate front surface represents the paramount source term in its energy balance. Since the focus is put on the assessment of critical wall cooling, always dry-wall impact conditions are taken into account in this section, avoiding the simulation of the wall film formation. The impingement model identifies the four dry wall regimes, $deposition$, $hot\ \ rebound$, $cold\ \ splash$ and $thermal\ \ break-up$, always taking into account the heat directly exchanged by the spray and the solid phase. If a partial or

complete deposition on cold surfaces is identified for a parcel, the fraction of the mass is artificially removed from the system after completing the thermal interaction. Since the characteristic heat transfer and phase change times are much longer than the average droplet ones, this approach is chosen in accordance with the always-dry impact to avoid an overestimation of the cooling effect of the spray on the wall.

The spray core conservation in cross flow conditions is clear in the temperature profile on the centerline channel, shown in Fig. 5.11, where the strongest temperature drop is confined where the larger drops impact on the surface.

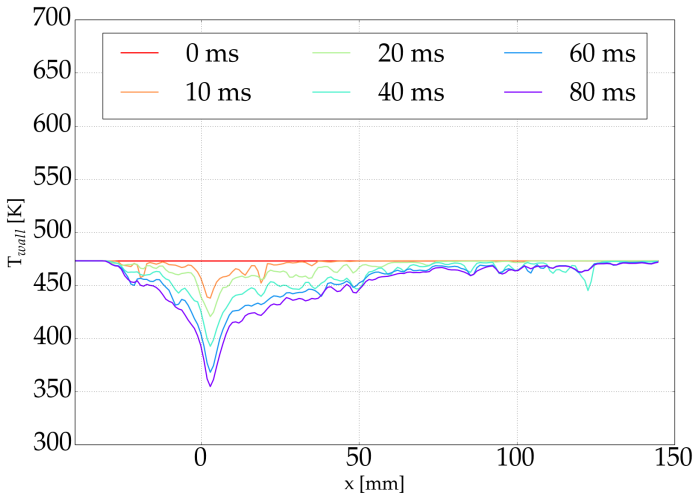

(a)

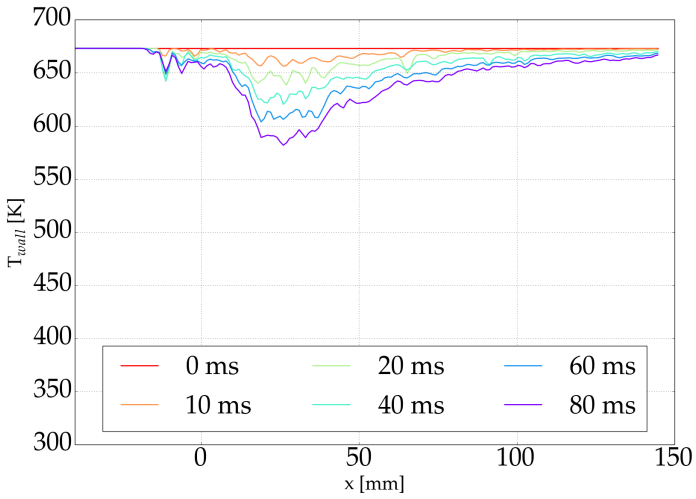

(b)

Figure 5.11: *6H - water injection - Plate front surface temperature profile on the centerline of the system. t200f100 (a) and t400f400 (b).*

The reference system origin, $x = 0 \ \ mm$ is set at the intersection between the nozzle geometrical axis and the front surface of the plate. Fig. 5.12 shows the temporal evolution of the front surface temperature in its coldest spot, represented by a 1 mm^2 face, situated 3.1 mm and 21.2 mm downstream of the projected nozzle axis location, respectively for the t200f100 and t400f400 conditions.

The plate temperature planar distribution at t200f100 reported in the left column of in Fig. 5.13 is compared with the mass distribution collected 4 mm from the impingement surface in a simulation without the presence of the solid plate to provide information only on the spray primary flux to the wall.

The thermal footprint reports the same peak but is affected by the impacts of the droplets ejecting from the primary impingement, which involve a portion of the surface not yet cooled by the spray core.

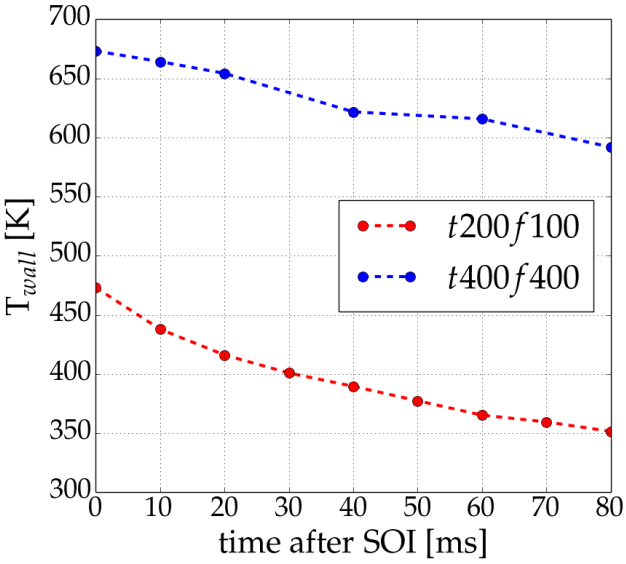

Figure 5.12: *6H - water injection - Coldest spot surface temperature evolution.*

At t400t400 the mass and thermal footprints are shifted downstream and flattened by the interaction with the stronger cross flow (Fig. 5.14). The magnitude of the temperature is comparable since the higher wall temperature difference acts as a stronger driving force for the conductive heat exchange defined by the formulation by [107] shown in (4.25). In fact the temperature difference approaches the null values for a single injection pulse of 100 ms at low load conditions.

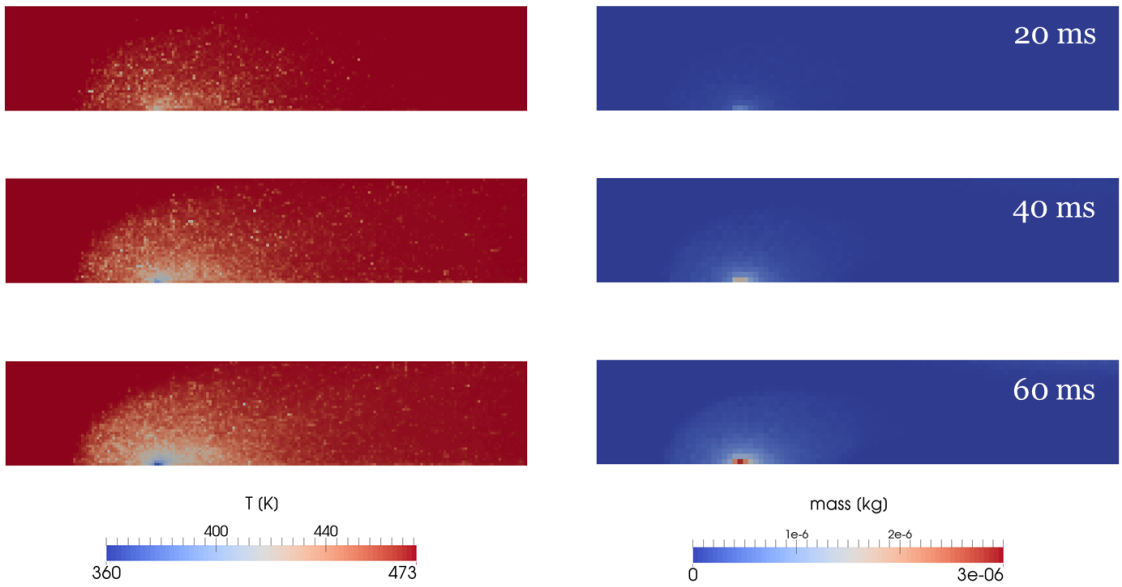

Figure 5.13: *6H - water injection - low load conditions t200f100 - temporal evolution of the front surface temperature pattern (left) and liquid mass distribution on a sampling surface set 4 mm above the location of the plate, collecting only the primary spray.*

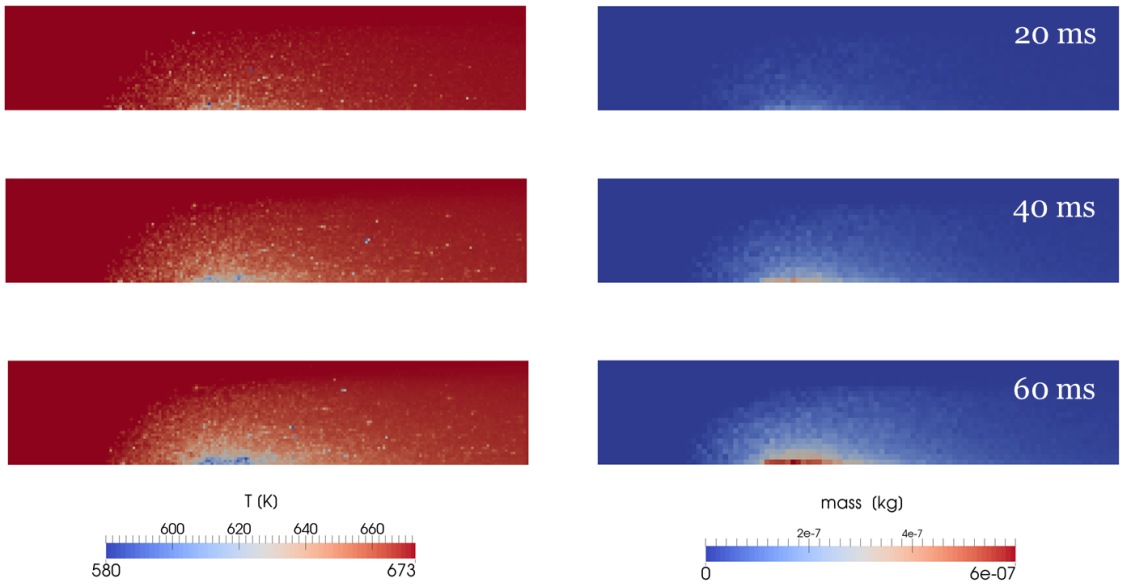

Figure 5.14: *6H - water injection - high load conditions t400f400 - temporal evolution of the front surface temperature pattern (left) and liquid mass distribution on a sampling surface set 4 mm above the location of the plate, collecting only the primary spray.*

Fig. 5.15 proposes a comprehensive representation of the impact, where a normalized kinematic parameter $^{K}/_{K_{crit}}$ defined for the ith impinging droplet as (5.1) represents the x-axis:

$$^{K}/_{K_{crit}} = \frac{K_i}{K_{crit}\,(drop, wall)} \tag{5.1}$$

where K_i (see Tab. 4.1) is the kinematic parameter of the ith droplet and $K_{crit}\,(drop, wall)$ is its critical value according to the implemented model as a function of the droplet and wall thermal and kinematic properties (see Section 4.3).

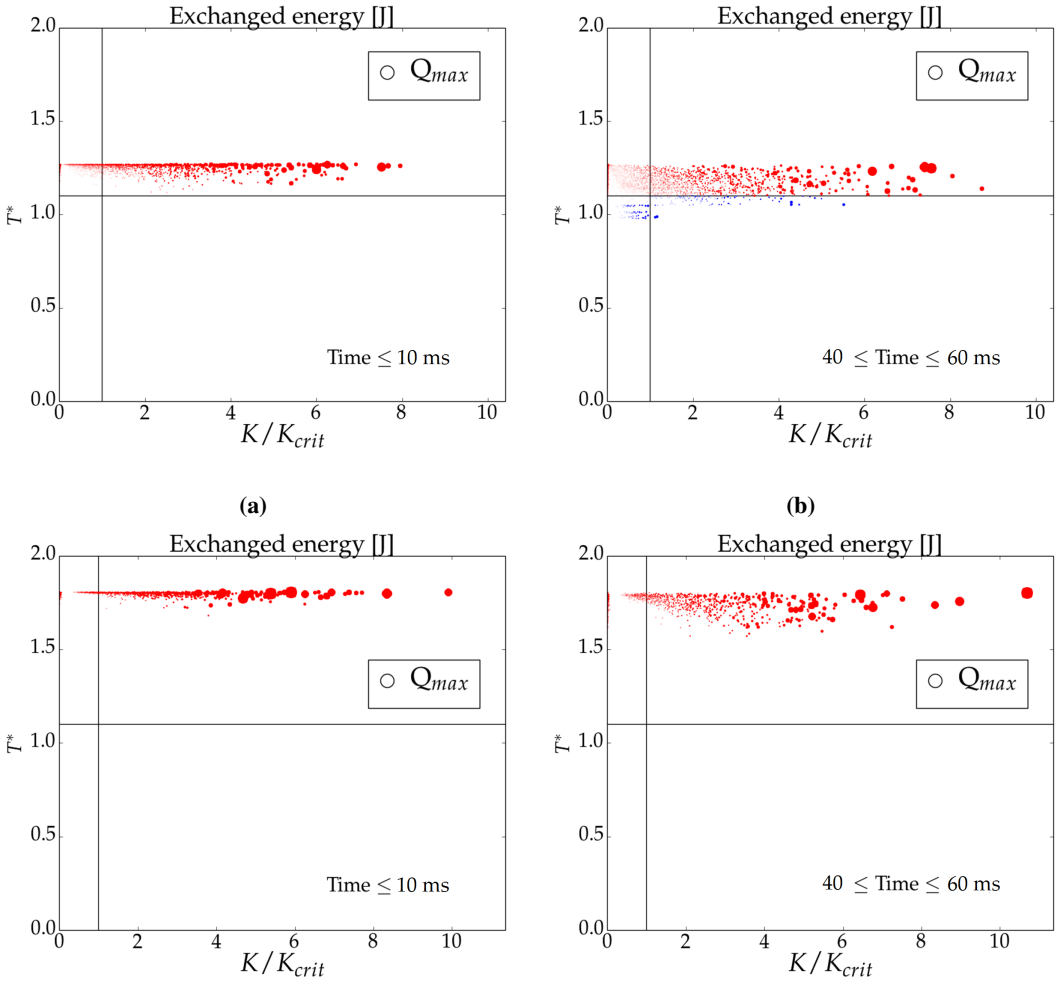

Figure 5.15: *6H - water injection - Exchanged energy: t200f100 (a-b), Q_{max} = 7.08e^{-03} J. t400f400 (c-d), Q_{max} = 1.37e^{-02} J.*

In this way, a uniform representation of the destructive interaction threshold can be obtained, characterizing in a clearer manner the properties of the impact. The scatter-plot reports in red and blue the hot-wall and the cold-wall interactions, respectively. The size of the dot is a linear function of the exchanged energy Q ($[J]$) according to (4.25). At low load conditions, a completely dry surface is estimated only for the first 10 ms after SOI, making the wall cooling very critical and a fast mixture preparation impossible in the operation of this injector in a simple cross flow. The necessity of a flow mixing generator is therefore obvious to introduce swirling flow and to produce a more distributed impact on the surface.

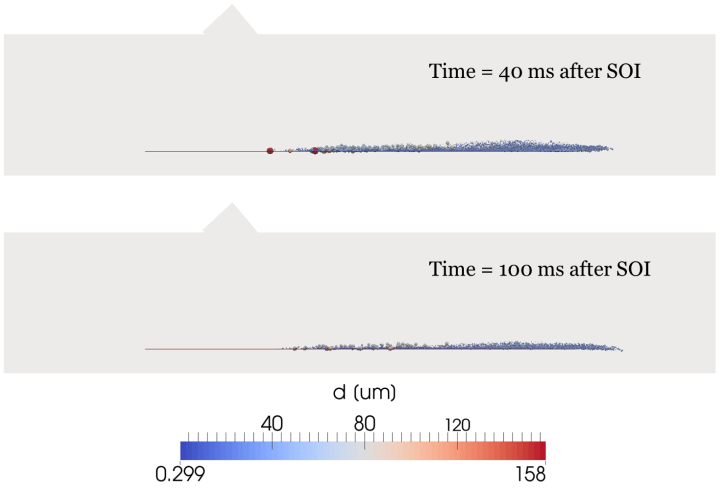

(a)

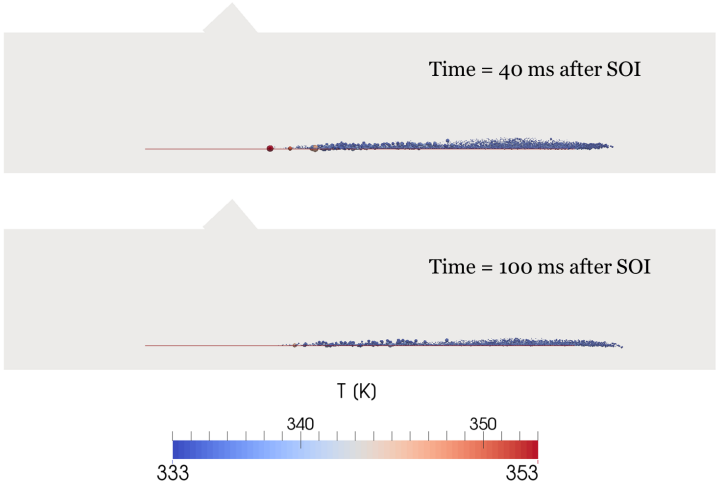

(b)

Figure 5.16: *6H - water injection - Characteristics of the droplets with a temperature higher than 333 K. Drop size (a) and Temperature (b).*

At high load conditions, although strong cooling of the plate is provoked by a single injection pulse, the onset of liquid film is not allowed yet, according to the implemented model, which sets the critical surface wetting temperature equal to $\approx 410\ K$ (1.1 times the saturation temperature of the liquid mixture).

The exchanged energy is clearly dependent on the surface temperature, as it drops as soon as colder faces are encountered by the impinging parcels, and on the kinematic intensity of the impact, represented by the K/K_{crit} parameter. Therefore, from the point of view of the wall cooling, the higher momentum carried by the droplets, the more critical the impingement.

On the other hand, the impact of the spray on the wall can be identified as the primary source of droplet break-up in the operation of an SCR system. The parcels with temperature higher than 60° C, visualized in Fig. 5.16, are confined to the near wall region, and their characteristic diameter is very small in the wake of the impingement location. Moreover they evaporate completely before the channel outlet till the end of the injection pulse, when the temperature of the wall is far below the initial one, showing that the amplification of the interaction area between droplets and gas due to the break-up is the most important feature in the phase change evolution.

Fig. 5.17 reports the exchanged energy of the impact from the spray side, specified on the parcel mass. It is possible to notice that in the simulation, the energy exchanged by smaller parcels is still lower than the primary and destructive impacts, but relevant for the phase change and the gaseous mixture preparation. Fig. 5.18 shows the water mass fraction at the plate front surface on the centerline of the system. The spray cone impingement location, which is the source of the major break-up, is visible just in the low load conditions (t200f100) at the first reported time, highlighting that the evaporation is due mostly to the smaller droplets impacting the wall. Moreover, at higher load, the small droplets do not reach the wall, and therefore the evaporation is only present in the wake of the impact event.

The higher temperature of the plate and the surroundings provokes a local increment of the evaporation, which is confined to the spray-wall interaction region, as shown in Fig. 5.19-b, where the water vapor mass flux distribution at the outlet is reported at 40 ms after SOI. Fig. 5.19-a shows that, at low load conditions, the vortex generated by the

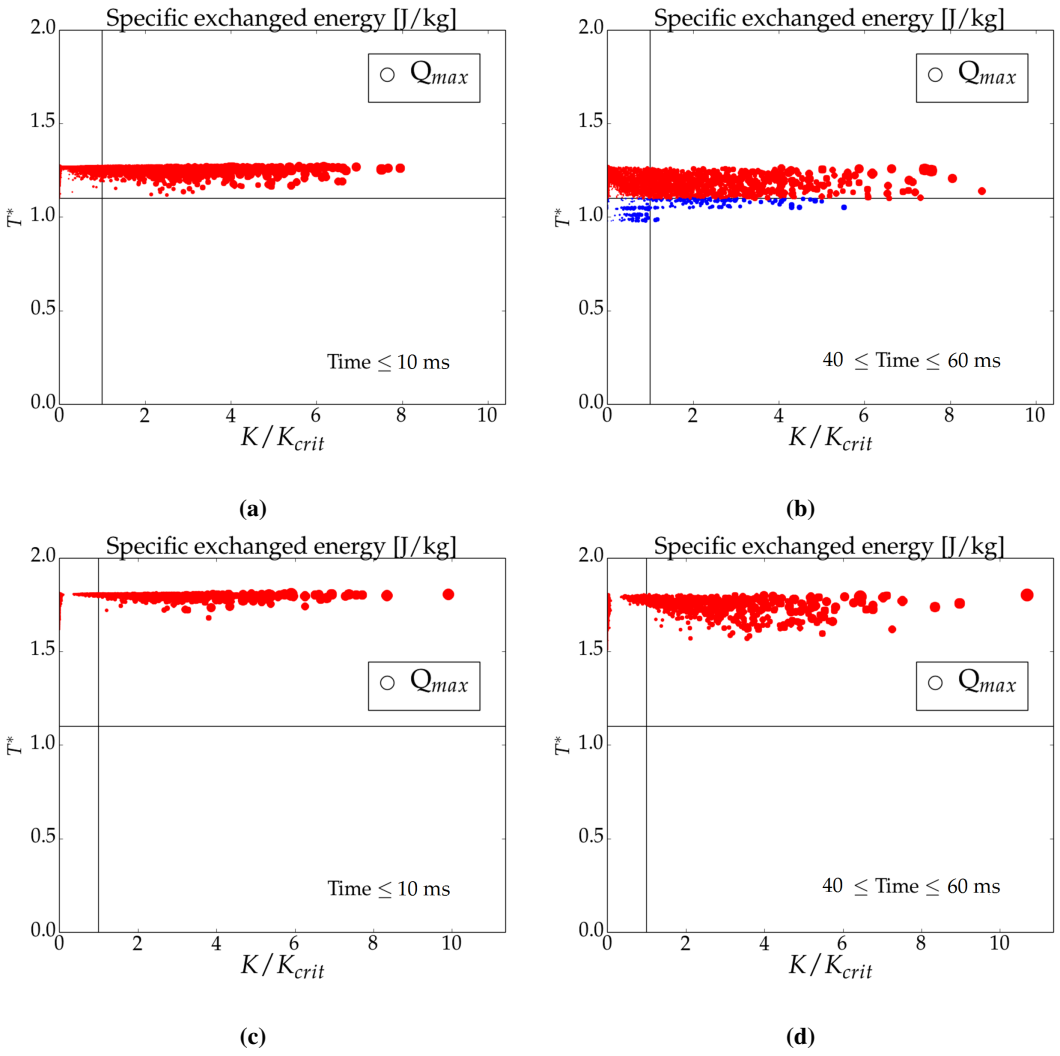

Figure 5.17: *6H - water injection - Specific exchanged energy: t200f100 (a-b),* Q_{max} *=* $6.83e^{05}$ $^{J}/_{kg}$*. t400f400 (c-d),* Q_{max} *=* $1.38e^{06}$ $^{J}/_{kg}$

impingement carries out the paramount fraction of the secondary droplets generated by the impact, dislocating the region of major evaporation.

The test bench setup is not able to handle the injected mass and to provide the the complete evaporation of the liquid in none of the reproduced operating conditions. The system configuration involves a cylindrical channel generating an almost straight flow field, which determines a too short path for the spray evolution and a strong localization of the impingement primary surface, provoking not acceptable wall cooling. The necessity of a larger impact map is clear also by the separation of the primary impacts from the secondary ones provided in Fig. 5.20, which shows that the secondary droplet kinematic parameters are close to zero, exchanging negligible energy with the wall.

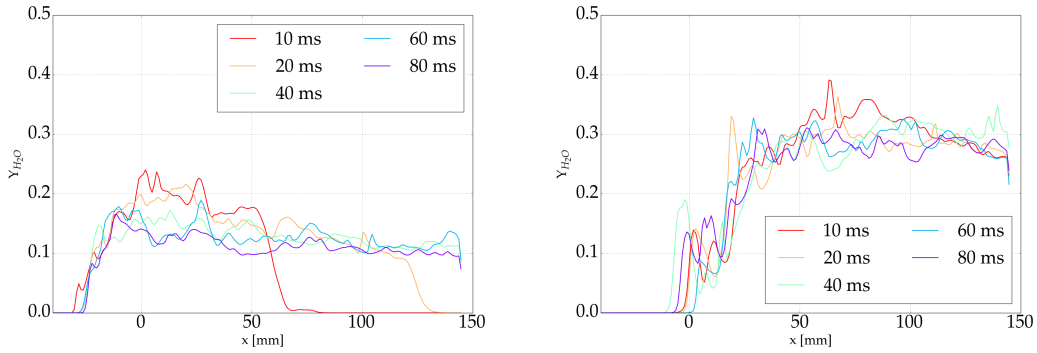

(a) **(b)**

Figure 5.18: *6H - water injection - Water mass fraction in the gaseous phase at the interface with the plate front surface: t200f100 (a) and t400f400 (b).*

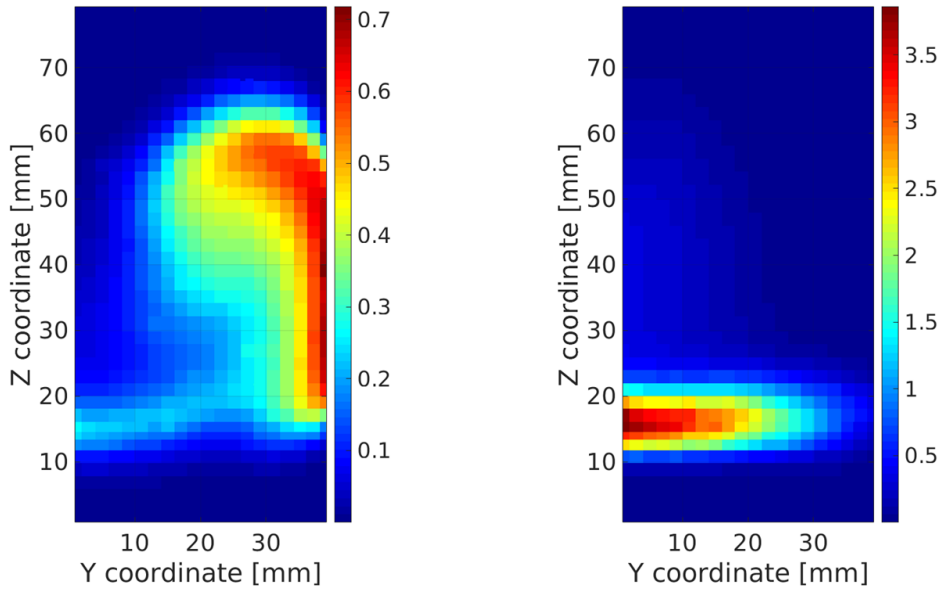

(a) **(b)**

Figure 5.19: *6H - water injection - Water vapor mass flow rate* $[kg/m^2\,s]$ *at the domain outlet: t200f100 (a), t400f400 (b).*

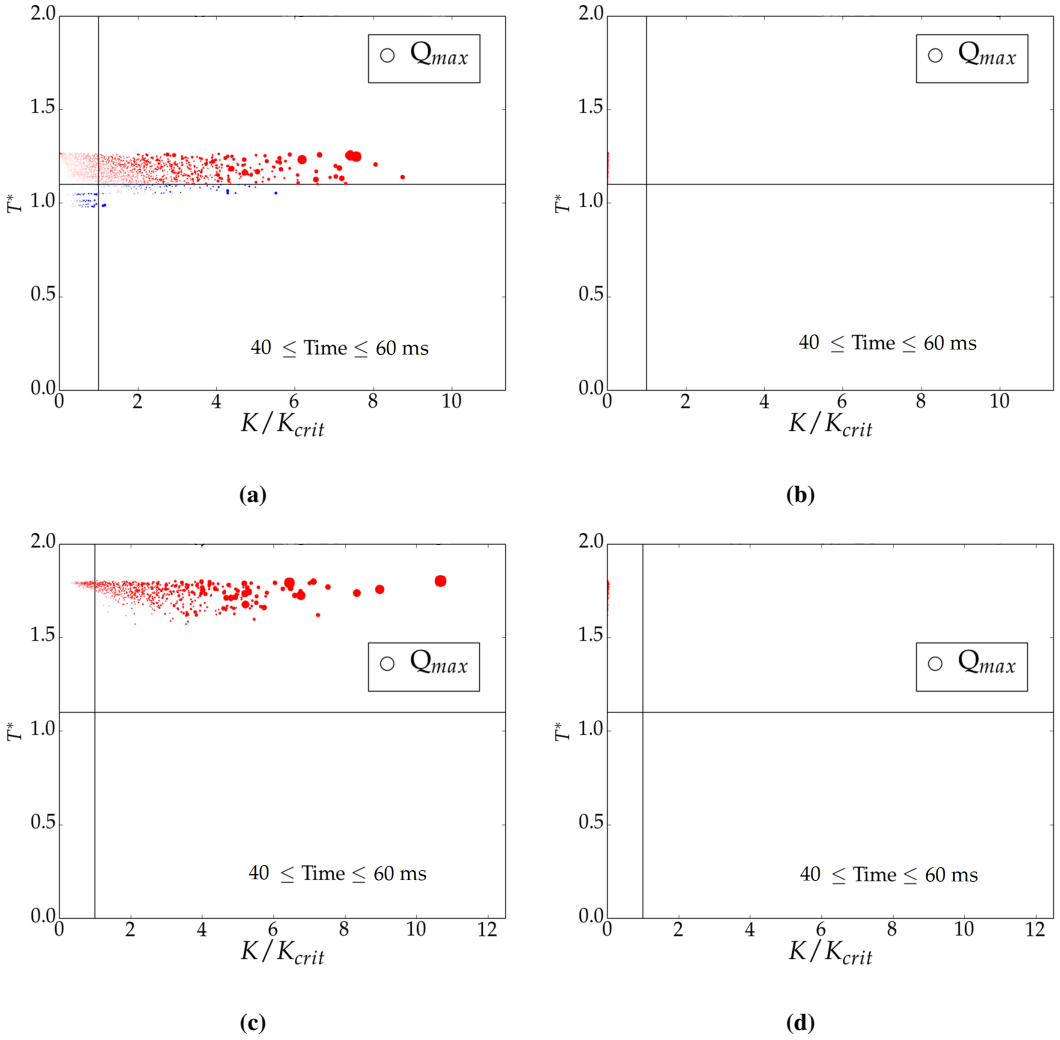

Figure 5.20: *6H - water injection - Impact exchanged energy. t200f100: primary (a) and secondary (b) droplets, Q_{max} = 7.08e^{-03} J. t400f400 primary (c) and secondary (d) droplets, Q_{max} = 1.37e^{-02} J.*

The interaction is smaller, but not negligible in terms of specific energy, determining a continuous interaction with the wall, and an amplification of the heating effect provided by the gas, as shown in Fig 5.21.

The number of secondary impingement events is an order of magnitude higher than the primary ones, because of the flat trajectory generated by the impact. Within this configuration, the localization of the spray core footprints provides the necessary information for the determination of the risk on onset of liquid wall film, but the characterization of the evaporation is strictly dependent on the path of the secondary droplets. Fig. 5.22-a reports the water mass flow rates for the gaseous and the liquid phases, showing that at higher load conditions (labeled 44 and referring to t400f400) the flow momentum tends

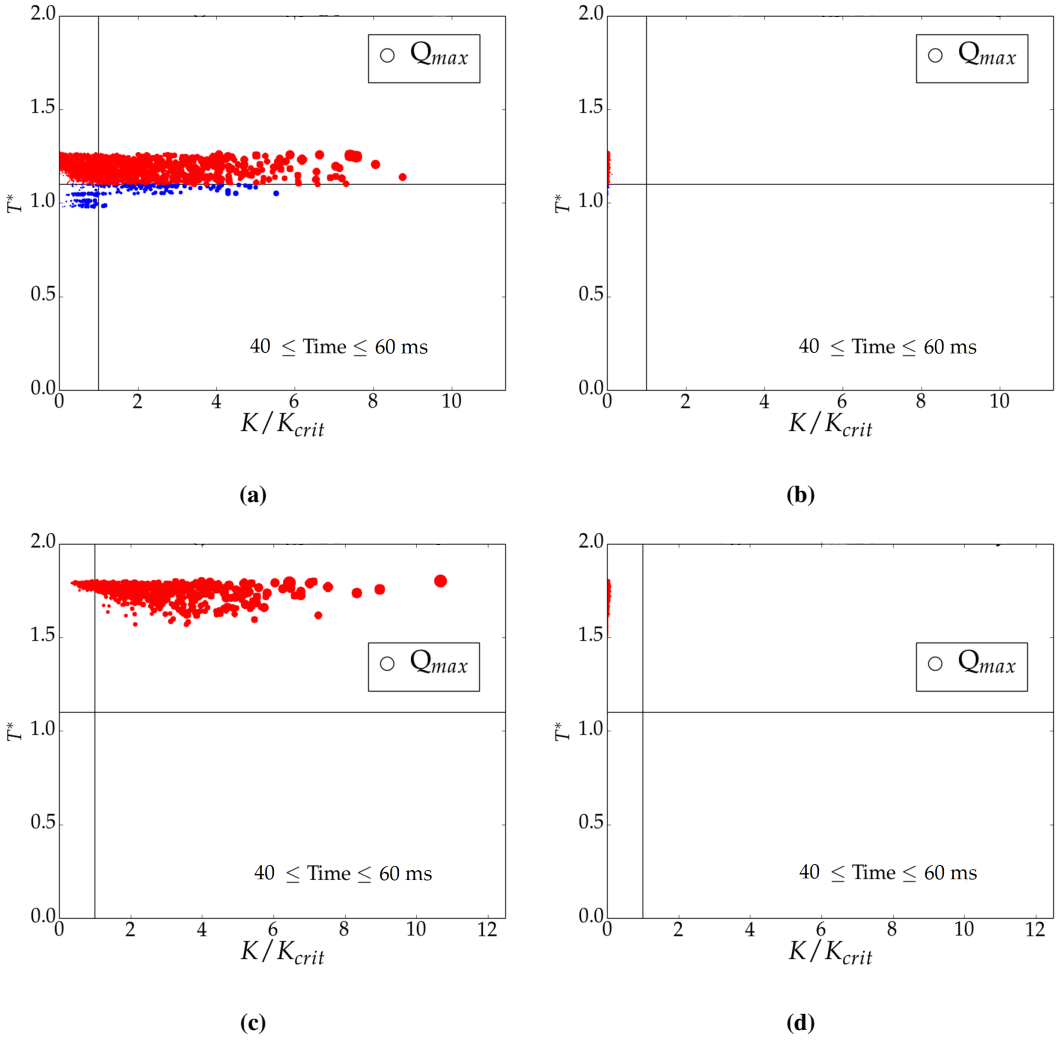

Figure 5.21: *6H - water injection - Specific exchanged energy: t200f100 primary (a) and secondary droplets (b), Q_{max} = 6.83e^{05} $^{J}/_{kg}$. t400f400 primary (c) and secondary (d) droplets, Q_{max} = 1.38e^{06} $^{J}/_{kg}$*

to level out the distribution of both the phases, obtaining low and constant uniformity index UI, calculated for the outlet surface as (5.2).

$$UI = 1 - \frac{\sum_i |Y_{i,j} - \bar{Y}_i| A_j}{2 \sum_j Y_{i,j} A_j} \tag{5.2}$$

where i refers to the ith and A$_j$ to the area of the jth computation face. Fig. 5.22-b reports the evolution of the UI for both the phases in the tested operating conditions, showing unacceptable values also for at t200f100 where the vortex generated by the spray impingement improves the spray mixing without reaching a satisfactory value.

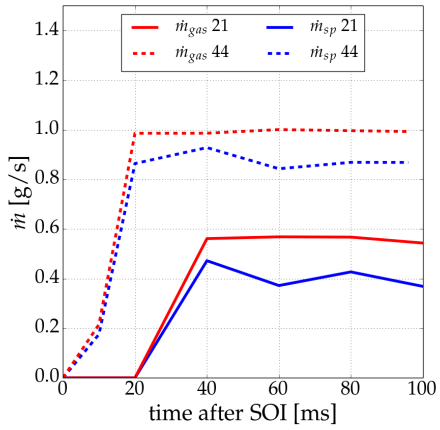

(a)

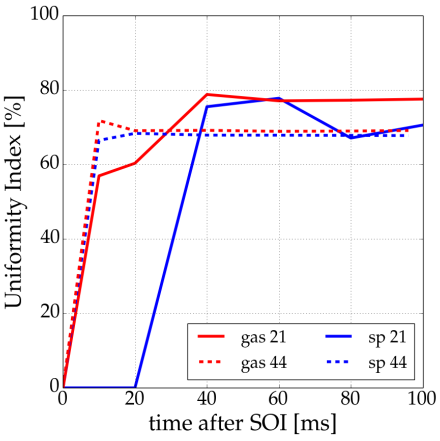

(b)

Figure 5.22: *6H - water injection - Water mass flow rates (a) and their uniformity index on the system outlet patch (b). blue for spray and red for vapor.*

AdBlue® spray simulation

As mentioned in Chapter 3 the characterization of the UWS mixture involves a Rapid Mixing model without considering the thermolysis and hydrolysis of the urea, giving reliable results in the simulation of the spray behavior in cross-flow conditions.

As for the distilled water injection the presence of the solid plate in the channel only slightly affects the behavior of the primary spray. The kinematic properties of the simulated droplets are still compatible with the Phase Doppler Anemometry data, as shown in Fig. 5.23.

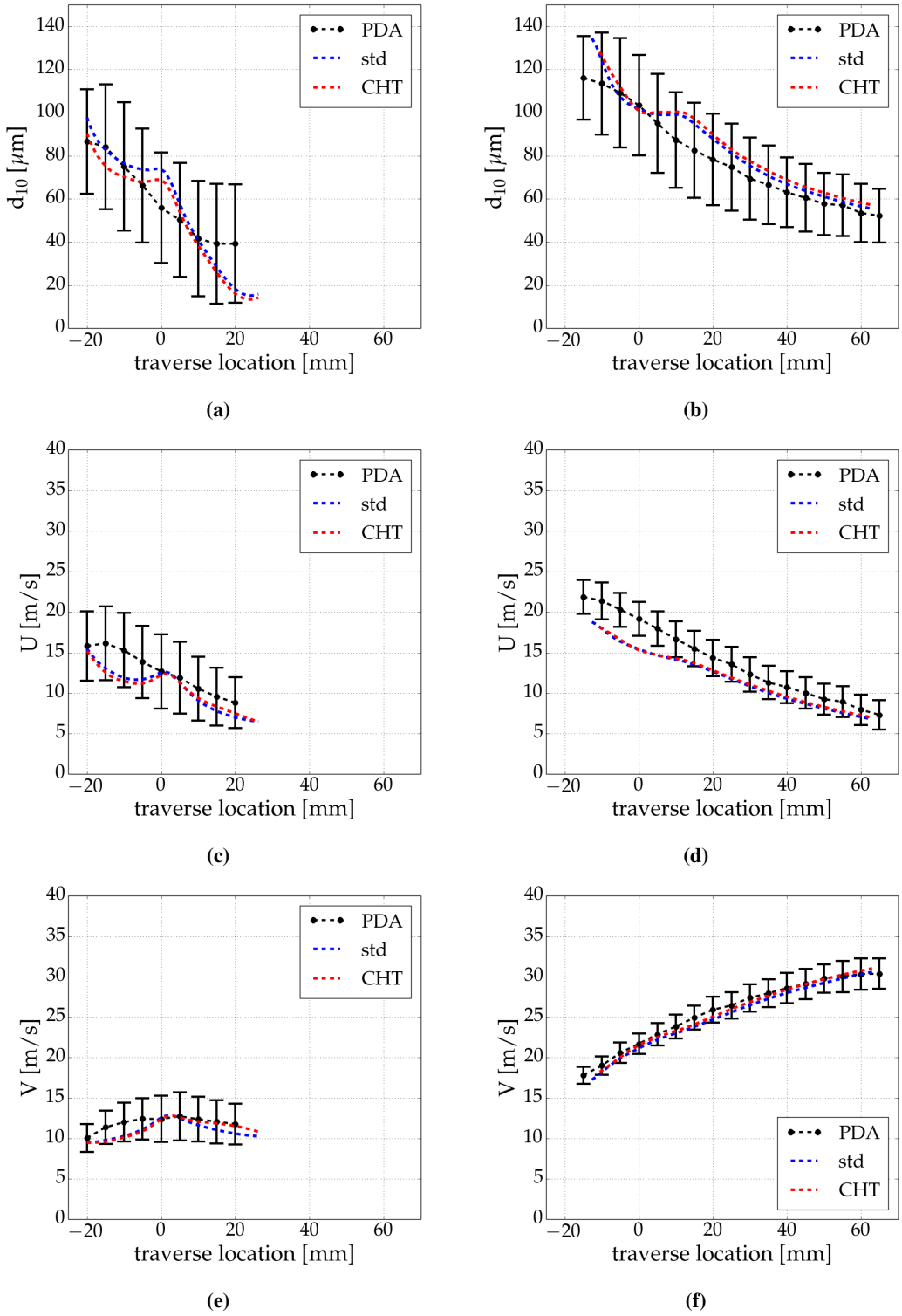

Figure 5.23: *6H - UWS injection - Spray average kinematic parameter profiles. Left: low load (t200f100): d_{10} (a), U (c) and V (e). Right: high load (t400f400): d_{10} (b), U (d) and V (f). The red lines refer to the complete spray-wall treatment on the suspended plate CHT, compared with the standard channel std configuration.*

The qualitative spray pattern retraces the motion highlighted in Fig. 5.9 and 5.10 where the $core$ of the spray remains intact till the impact on the wall, and the $wake$ is dragged by the near-wall gaseous motion.

The mixture composition does not considerably affects the thermal transient of the solid surface, as reported in Fig 5.24. The temporal evolution of the coldest spots in the

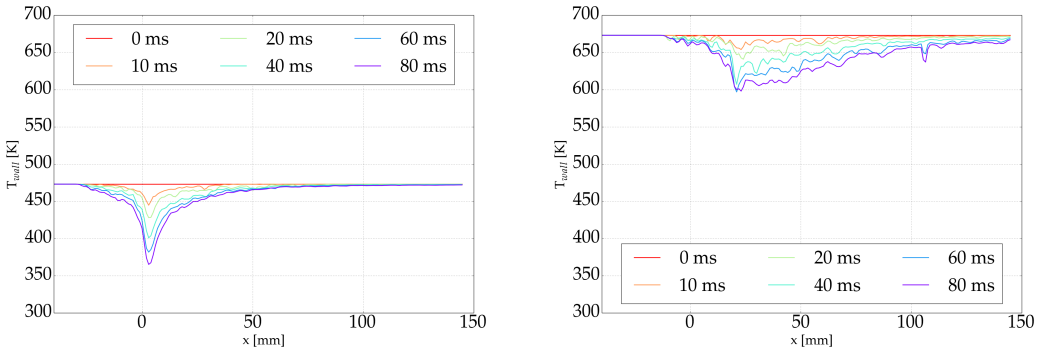

(a) **(b)**

Figure 5.24: *6H - UWS injection - Plate front surface temperature profile on the centerline of the system. t200f100 (a) and t400f400 (b).*

spray thermal footprint is compatible with the distilled water ones, since the heat flux formulation reflects the slight variation of the thermophysical properties of the impinging spray. Also the temperature evolutions at the locations experiencing the highest temperature drop, respectively 3.1 mm and 22.2 mm for t200f200 and t400f400, are consistent with the distilled water injection ones, as shown in Fig. 5.25, remarking that the urea presence in the liquid mixture is negligible in the characterization of the thermo-kinematic behavior the primary and most critical impingement phenomenon. The major difference in the spray-wall interaction is represented by the thermal threshold determining the conditions for a possible wetting of the surfaces. In the definition by [40], it involves a ratio between the temperature of the wall and the saturation temperature of the mixture, and is therefore strictly dependent on the composition of the injected liquid. The absence of urea thermolysis and hydrolisis description in the current description generates an overestimation of the urea fraction in the droplets and a consequent higher wetting threshold. The resulting impact maps, are reported in Fig. 5.26 at 40 ms after the SOI, showing the steady-state spray behavior on the surface.

The absolute and the specific (on the droplet mass) exchanged energy magnitudes are

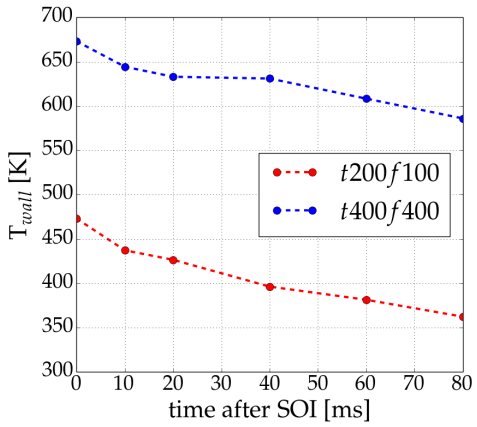

Figure 5.25: *6H - UWS injection - Coldest spot surface temperature evolution.*

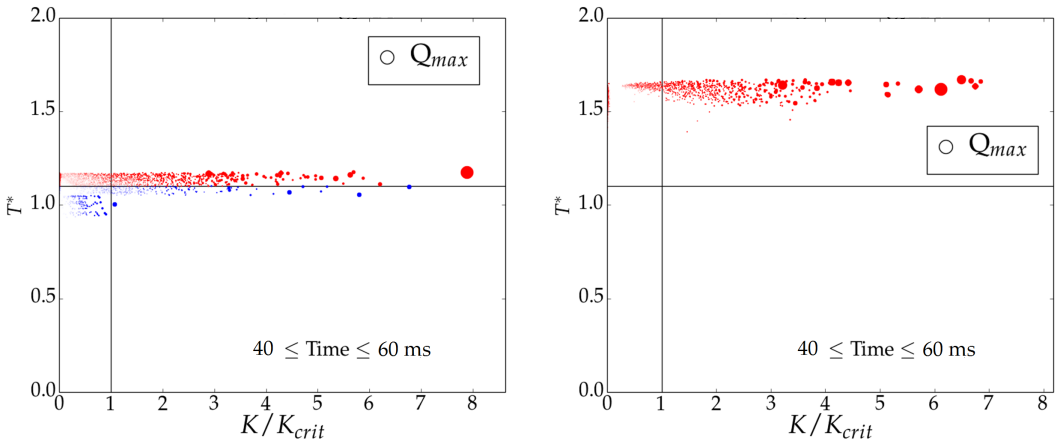

Figure 5.26: *6H - UWS injection - Exchanged energy: t200f100 (a), Q_{max} = 7.87e^{-03} J. t400f400 (b), Q_{max} = 1.22e^{-02} J.*

comparable with the distilled water ones as shown in Fig. 5.27.

The paramount contribution to the spray cooling is represented by the spray core as highlighted by the clear separation between the primary and secondary impact behavior. Also for the UWS droplets, the impact on the walls represents the major break-up source, as depicted in Fig. 5.28-a where the red spheres represent the droplets carrying an urea mass fraction higher than 0.9 for the t400f400 conditions. Their size is proportional to the characteristic parcel diameter, showing that the core of the spray is too dense and cold to allow a notable water evaporation and the consequent ammonia production. The impact-induced atomization acts on the paramount fraction of the

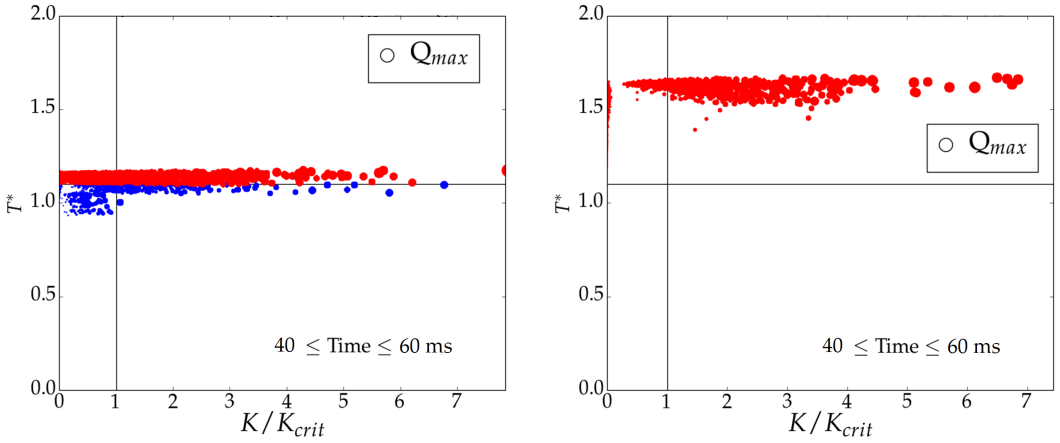

Figure 5.27: *6H - UWS injection - Specific exchanged energy: t200f100 (a), Q_{max} = 6.80e^{05} J. t400f400 (b), Q_{max} = 1.23e^{06} J.*

injected mass providing the prominent phase change source, as shown in Fig. 5.28-b. The urea vapor is not physically consistent with the urea evaporation and reaction, but is a tracker to determine the location of NH_3 formation in a SCR system operation.

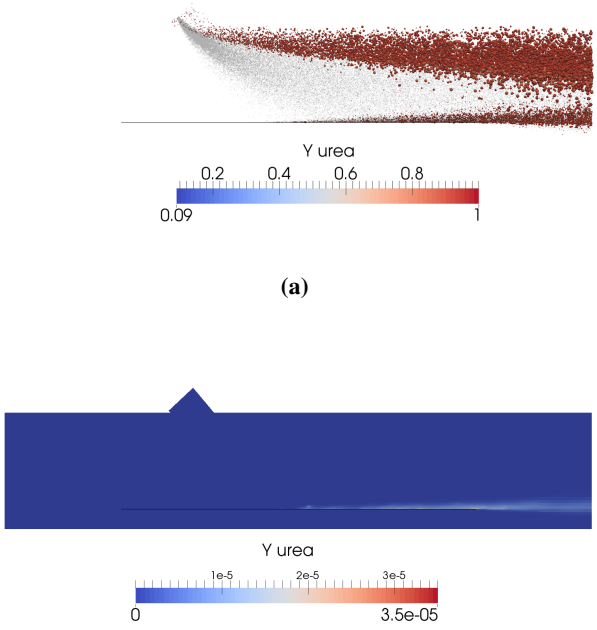

Figure 5.28: *6H - UWS injection - t400f400. Droplets with a Y_{urea} > 0.9 (a) and gaseous urea mass fraction (b) at 40 ms after SOI.*

This behavior is confirmed by the water and urea vapor mass flux patterns on the outlet surface of the simulated domain, reported in Fig. 5.29.

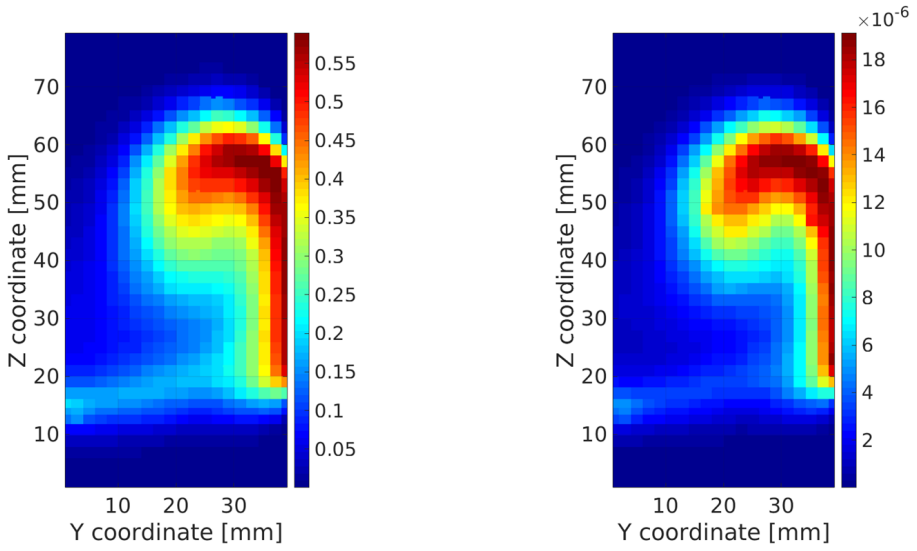

Figure 5.29: *6H - UWS injection - t200f100. Outlet mass flow pattern* $[kg/m^2\ s]$ *for water (a) and urea (b) at t = 40 ms after SOI.*

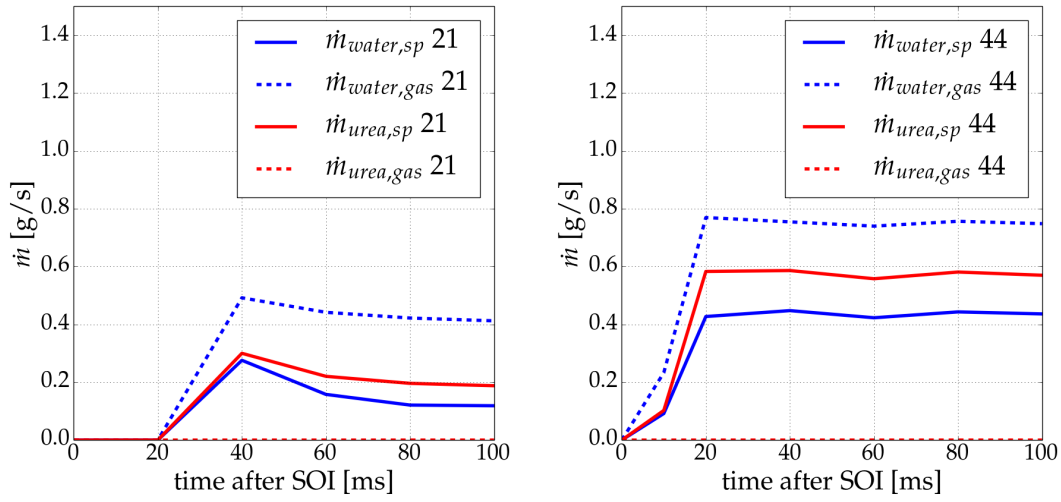

Figure 5.30: *6H - UWS injection - Water and urea vapor and liquid mass flows at the computation domain outlet. t200f100 (a) t400f400 (b).*

The importance of the droplet trajectory deflection is clearer at t200f100, where the swirling motion generated by the spray momentum and the impingement allows the

evaporation of the water fraction and the beginning of the urea conversion within the channel extension at low temperature.
The water evaporation acts as a delay for the generation of the the reacting mixture, especially at low cross flow temperature, where a steep variation of the phase change law has been measured by [103].
The water and urea vapor and liquid mass flow rates at the outlet are reported in Fig. 5.30 for both t200f100 and t400f400, where it is possible to appreciate that the injected water is not completely evaporated, reinforcing the reliability of the proposed representation of the mixture in the system.

The simulation of the liquid injection shows negligible influence of the suspended plate in the droplet kinematic characteristics along their path to the surface (Fig. 5.8). The strong variation in the morphology at the end of the simulated domain ($wake$ region in Fig. 5.10) is therefore due to the direct interaction with the wall, which acts as break-up and thermal energy source (Fig. 5.16) generating the most relevant water vapor stream (Fig. 5.19).
The impingement on the system solid walls becomes an essential phenomenon in the operation of a SCR system, and its optimization represents a key feature in the design of the mixture dosing. In fact, as shown in Fig. 5.15, the destructive impacts generated by the largest and fastest droplets are responsible for the paramount fraction of the exchanged energy with the solid wall. The source term is strong enough to allow the wetting of the surface at low load conditions (t200f100, Fig. 5.15-b) during the first injection event. This result is confirmed by the front surface temperature map (Fig. 5.13), which shows an evident concentration of the spray-derived cooling in the vicinity of the injection axis, where both the maximum K number and the liquid mass loading are predicted.
On the other hand, the secondary droplet further interactions with the walls are negligible in the absolute energy balance of the solid wall (Fig. 5.20-b,d), but considerable in their specific contribution to the spray heating and evaporation (Fig. 5.21).
In closing, the lack of evaporation of the liquid mixture in the analyzed domain high-

lights the urea phase change delay due to the presence of the water fraction (Fig. 5.29). In fact, the absolute contribution of the gaseous urea mass flow rate is negligible (Fig. 5.30), also due to the lack of characterization of the evaporation mechanisms, but is concentrated in the spray wake generated by the interaction with the wall.

CHAPTER 6

Conclusion and Outlook

Pressure-driven injection in quiescent air

Two different injectors operating at the same pressure (9 bar) with water and AdBlue® are experimentally characterized and numerically reproduced. Phase Doppler Anemometry (PDA) represents the main tool for the estimation of the spray features and shows that the six hole nozzle (6H) produces droplets with kinematic characteristics compatible with the three inclined hole ones (3H).

Injecting distilled water and measuring the spray at 32 mm from the nozzle head, the overall Sauter Mean Diameters (d_{32}) are respectively 75.11 μm and 66.35 μm for 6H and 3H, and represent wide drop size distributions ranging from 1 μm to 160 μm. The spray core velocities are comparable, 27 m/s for 6H and 32 m/s for 3H, and both are significantly lower than the Bernoulli limiting values.

The spray pattern is instead very different, reporting a strong cone to cone interaction for 6H that produces a resulting single full cone, and three very dense and separated

streams for 3H, as highlighted through lateral Shadow Imaging (SI).
The influence of the urea fraction in the liquid mixture is tested for 6H, which shows negligible variation in its operation.
The PDA data are used for the initialization of a numerical model for low pressure-driven injectors to be included in the Lagrangian description of the dispersed phase interaction with an Eulerian finite volume description of the surrounding environment. The Discrete Droplet Model (DDM) coupled with a Reynolds Averaged (RANS) treatment of the gas transport equations is chosen, employing the standard $k - \varepsilon$ model to describe the turbulence.
The direct assignment of a drop-size distribution is chosen to initialize the computational parcels properties, since the droplets Weber numbers (We) are lower than the threshold for a significant break-up of the liquid jets. A fit of the spatially distributed data is operated on a Rosin Rammler probability function, weighting the local properties of the droplets on the PDA acquisition data rate and obtaining similar values for the two injectors.
The initialization of the computational parcels mass represents a key point for the reliable description of wide size distributions, and a new approach is proposed: a constant number of droplets is given to each parcel instead of a constant mass, producing a better simulation of the overall spray behavior, avoiding the overestimation of the small droplet influence on the spray pattern and on its interaction with the gaseous environment.
The obtained setup of the injection model shows good agreement with the experimental data in terms of local and global droplet size and velocity distributions.

Pressure-driven injection in cross-flow

The PDA campaign is extended and coupled with previous experimental data to provide the characterization of the spray behavior in an engine-less test rig reproducing a Diesel engine exhaust after-treatment channel, over a wide range of thermal and gas flow rate conditions. The six hole injector is traversed on its centerline at 60 mm from the nozzle head at low load conditions, $T_{gas} = 200° C$ and $\dot{m}_{gas} = 100\, kg/h$, and high load

conditions, $T_{gas} = 400° C$ and $\dot{m}_{gas} = 400\,kg/h$. The increase of momentum and temperature of the gas generates a strong entrainment of the smaller droplets (less than 40 μm), which alters the full cone shape maintained at low load conditions.

A single spray cone produced by the three hole injector is sampled on its centerline at 79 mm from the nozzle head at low and intermediate, $T_{gas} = 300° C$ and $\dot{m}_{gas} = 200\,kg/h$, conditions showing a less evident influence of the cross flow on the average kinematic properties of the droplets. In fact the larger droplets carry a considerable fraction of their initial momentum, reaching the sampling plane with an angle comparable with the injection one.

The effect of the urea presence for 6H is negligible, confirming previous shadow imaging data, and underlining that a large fraction of the liquid mass reaches the sampling plane, without being affected by the cross flow temperature and momentum, and retaining a relevant part of the water fraction.

A simplified computational domain is generated to simulate the square section of the injection chamber, applying the injection models defined in quiescent air to the cross-flow interaction. The proposed setup, coupled with standard Lagrangian spray submodels provides a reliable representation of the spray over the tested conditions. The parcel definition approach provides a better estimation of the droplet size trends, especially at low load conditions, where a wrong representation of the overall size distribution strongly affects also the gaseous phase through the two-way coupling.

Although no urea thermolysis and hydrolisis are introduced in the simulation, reducing the reactivity and phase change of the mixture, the numerical representation of the primary liquid stream is acceptable, confirming that a great fraction of water, inhibiting the conversion of urea, is present in the dense spray core up to high load flow conditions.

Spray-wall interaction

The spray-wall interaction is found to be a fundamental phenomenon to correctly describe the behavior of low pressure-driven injection in a confined environment.

The validated simulation of the spray allows the estimation of the kinematic properties of the impinging spray, well represented by the kinematic parameter K. The core of

the sprays report high values (up to 200) corresponding to strong destructive impacts, which need to be correctly included in the numerical modeling of the system.
Moreover the CFD simulation represents a powerful tool to assess the applicability of a mechanical patternator, built to measure the planar liquid mass distribution in the near wall region. The intrusiveness of the instrument on the flow field development and its interaction with a low pressure-driven spray is estimated, showing less than $10\,\%$ variation of gas flow profile and never more than $15\,\%$ variation in the planar distribution of the spray mass at the sampling location.
The spray model is then tested on the 3H front cone planar mass distribution collected 79 mm from the nozzle head with the patternator. The model predicts a slight stronger shift of the cone location, but shows that the chosen approach for the definition of the computational parcel properties strongly improves the quality of the simulation.
A detailed literature model is added to the CFD library to handle the spray wall interaction, introducing a thermal threshold in the definition of the impingement regimes and improving the characterization of the secondary droplet evolution. The addition of the spray-wall heat transfer description provides the extension of the simulation to the system wall thermal transients, and the introduction of a criterion to assess of the risk of onset of liquid films.
The model behavior is tested on literature data and applied to a single droplet impingement test case, showing that the direct interaction between spray and the wall is the paramount source term in the overall energy balance.

SCR system behavior

A single spray pulse is simulated to characterize an injection transient. The focus is put on the 6H, injecting both distilled water and AdBlue® and introducing a suspended thin stainless steel plate, 14 mm from the bottom plane of the channel, to replicate the thermographic measurements in the test bench, and to reduce the characteristic thermal time of the solid wall. A consistent temperature drop, up to $\approx\ 150^{\circ}\,C$, is experienced by the plate front surface in correspondence of the spray core impingement locations in both the low and high load conditions.

A synthetic representation of the impingement is provided through a re-elaborated impact map, which is based on the a kinematic parameter ratio, $^{K}/_{K_{crit}}$ and a wetting thermal threshold. It shows that for the tested spray, most of the primary interaction are destructive and represent the strongest break-up source in the system, enhancing the liquid-gas exchange surface and promoting the evaporation of the liquid mixture.

Moreover, the secondary droplets, ejected from the impingement, present a small diameter, less than 20 μm, and continue their path to the domain outlet staying close to the solid surface, experiencing a frequent thermal interaction with the wall and spreading the spray cooling effect on a wider area.

On the other hand, a single injection pulse generates the conditions for the onset of liquid deposition, which is not recoverable just with the contribution of the convective heat transfer provided by the gas.

The Urea Water Solution (UWS) behavior is compatible with the distilled water in terms of exchanged heat and kinematic behavior of the spray. The major difference is represented by the increment of the saturation temperature of the mixture, which shifts the wetting threshold towards higher values, highlighting the necessity of an optimal liquid dosing strategy.

A main results of the present thesis is the detailed description of an impingement transient from the point of view of both the spray and the wall. The identification of the spray core location and mass flux is found to be the most relevant parameter to be controlled to improve the system operation. The onset of the liquid film is strictly located in the primary impingement region, and the evaporation of the liquid is strongly dependent on the impact-induced break-up, which is necessary to reach a uniform reacting distribution at the catalyst inlet. This work also provides a validated kinematic and thermal representation of the spray behavior in cross-flow conditions, defining the basis for the introduction of a detailed characterization of the urea thermo-chemical behavior over a wide range of operating conditions.

Bibliography

[1] Fujio Akao, Kazuo Araki, Sigekatsu Mori, and Akira Moriyama. Deformation behaviours of a liquid droplet impinging onto hot metal surface. *Trans. Iron Steel Inst. Jpn.*, 20(11):737–743, 1980.

[2] SW Akhtar and AJ Yule. Droplet impaction on a heated surface at high weber numbers. *ILASS-Europe, Zurich*, page 37, 2001.

[3] John David Anderson and J Wendt. *Computational fluid dynamics*, volume 206. Springer, 1995.

[4] C Arcoumanis and J-C Chang. Heat transfer between a heated plate and an impinging transient diesel spray. *Experiments in Fluids*, 16(2):105–119, 1993.

[5] C. Arcoumanis and P. A. Cutter. Flow and heat transfer characteristics of impinging diesel sprays under cross-flow conditions. *SAE Technical Paper*, SAE International, n. 950448, 1995.

[6] KM Bade and RJ Schick. Volume distribution comparison methods for 1d, 2d, and point measurement techniques. *ILASS Americas*, 2008.

[7] Chengxin Bai and A. D. Gosman. Development of methodology for spray impingement simulation. *SAE Technical Paper*, SAE International, n. 950283, 1995.

[8] Jakov Baleta, Milan Vujanović, Klaus Pachler, and Neven Duić. Numerical modeling of urea water based selective catalytic reduction for mitigation of no x from transport sector. *Journal of Cleaner Production*, 88:280–288, 2015.

[9] Carsten Baumgarten. *Mixture formation in internal combustion engines*. Springer Science & Business Media, 2006.

[10] Theodore L Bergman, Frank P Incropera, David P DeWitt, and Adrienne S Lavine. *Fundamentals of heat and mass transfer*. John Wiley & Sons, 2011.

[11] A Bhattachayya. On a measure of divergence between two statistical population defined by their population distributions. *Bulletin Calcutta Mathematical Society*, 35(99-109):28, 1943.

[12] Felix Birkhold, Ulrich Meingast, Peter Wassermann, and Olaf Deutschmann. Analysis of the injection of urea-water-solution for automotive scr denox-systems: Modeling of two-phase flow and spray/wall-interaction. *SAE Technical Paper*, SAE International, n. 2006-01-0643, 2006.

[13] Felix Birkhold, Ulrich Meingast, Peter Wassermann, and Olaf Deutschmann. Modeling and simulation of the injection of urea-water-solution for automotive scr deno x-systems. *Applied Catalysis B: Environmental*, 70(1):119–127, 2007.

[14] F. V. Bracco. Modeling of engine sprays. *SAE Technical Paper*, SAE International, n. 850394, 1985.

[15] Uladzimir Budziankou, Thomas Lauer, Xuehai Yu, Brian M Schmidt, and Nam Cho. Modeling approach for a wiremesh substrate in cfd simulation. *SAE Technical Paper*, SAE International, n. 2017-01-0971, 2017.

[16] Mark Casarella. Urea dosing systems and controls for light duty diesel applications. *Presentation at SAE Light-Duty Diesel Emissions Symposium*, Ypsilanti, MI, 2011.

[17] BASF Catalogue. Adblue. *Technical Leaflet, M*, 6621:1–6.

[18] YS Cho, SW Lee, WC Choi, and YB Yoon. Urea-scr system optimization with various combinations of mixer types and decomposition pipe lengths. *International Journal of Automotive Technology*, 15(5):723–731, 2014.

[19] A Coghe, GE Cossali, and M Marengo. A first study about single droplet impingement on thin liquid film in a low laplace number range. *ICLASS-95, Nürnberg*, pages 285–293, 1995.

[20] Clayton T Crowe, Martin Sommerfeld, and Yutaka Tsuji. *Multiphase flows with droplets and particles*, volume 2. CRC press Boca Raton, 1998.

[21] Francesco Curto. Experimental investigation of spray-wall impingement process in scr denox automotive catalyst systems. Master's thesis, Politecnico di Milano, 2016.

[22] Thomas E Daubert and Ronald P Danner. *Data compilation tables of properties of pure compounds*. Dep. of chem. engineering, Pennsylvania state univ. University Park (Pa), 1985.

[23] Ruifeng Dou, Zhi Wen, and Gang Zhou. Heat transfer characteristics of water spray impinging on high temperature stainless steel plate with finite thickness. *International Journal of Heat and Mass Transfer*, 90:376–387, 2015.

[24] John K Dukowicz. A particle-fluid numerical model for liquid sprays. *Journal of computational physics*, 35(2):229–253, 1980.

[25] MM Elkotb. Fuel atomization for spray modelling. *Progress in Energy and Combustion Science*, 8(1):61–91, 1982.

[26] GM Faeth. Evaporation and combustion of sprays. *Progress in Energy and Combustion Science*, 9(1-2):1–76, 1983.

[27] Howard L Fang and Herbert FM DaCosta. Urea thermolysis and no x reduction with and without scr catalysts. *Applied Catalysis B: Environmental*, 46(1):17–34, 2003.

[28] Giancarlo Ferrari. *Motori a combustione interna*. Società Editrice Esculapio, 2016.

[29] Joel H Ferziger and Milovan Peric. *Computational methods for fluid dynamics*. Springer Science & Business Media, 2012.

[30] Simon Fischer. *Simulation of the Urea-water-solution Preparation and Ammonia-homogenization with a Validated CFD-model for the Optimization of Automotive SCR-systems*. PhD thesis, TU Wien, 2012.

[31] Simon Fischer, Rene Bitto, Thomas Lauer, Christian Krenn, Johannes Tauer, and Guenther Pessl. Impact of the turbulence model and numerical approach on the prediction of the ammonia homogenization in an automotive scr system. *SAE Int. J. Engines*, 5:1443–1458, 04 2012.

[32] Elke Goos, Alexander Burcat, and Branko Ruscic. Extended third millennium ideal gas and condensed phase thermochemical database for combustion with updates from active thermochemical tables. *URL ftp://ftp. technion. ac. il/pub/supported/aetdd/thermodynamics*, 2010.

[33] OpenFOAM User Guide. Mesh generation with snappyhexmesh.

[34] K Hanjalić, M Popovac, and M Hadžiabdić. A robust near-wall elliptic-relaxation eddy-viscosity turbulence model for cfd. *International Journal of Heat and Fluid Flow*, 25(6):1047–1051, 2004.

[35] RJ Haywood, M Renksizbulut, and GD Raithby. Numerical solution of deforming evaporating droplets at intermediate reynolds numbers. *Numerical Heat Transfer, Part A Applications*, 26(3):253–272, 1994.

[36] Senda Jiro, Masaaki Kobayashi, Seiji Iwashita, and Hajime Fujimoto. Modeling of diesel spray impingement on a flat wall. *SAE Technical Paper*, SAE International, n. 941894, 1994.

[37] Timothy Johnson. Vehicular emissions in review. *SAE Int. J. Engines*, 7:1207–1227, 04 2014.

[38] Timothy Johnson and Ameya Joshi. Review of vehicle engine efficiency and emissions. *SAE Technical Paper*, SAE International, n. 2017-01-0907, 2017.

[39] S Kontin, A Höfler, R Koch, and HJ Bauer. Heat and mass transfer accompanied by crystallisation of single particles containing urea-water-solution. In *23rd Annual Conference on Liquid Atomization and Spray Systems*, 2010.

[40] Dominik Kuhnke. *Spray/wall interaction modelling by dimensionless data analysis*. Shaker, 2004.

[41] Ryoichi Kurose and Satoru Komori. Drag and lift forces on a rotating sphere in a linear shear flow. *Journal of Fluid Mechanics*, 384:183–206, 1999.

[42] Arthur H Lefebvre and Vincent G McDonell. *Atomization and sprays*. CRC press, 2017.

[43] Yujun Liao and P Dimopoulus Eggenschwiler. Experimental investigation of heat transfer characteristics of uws spray impingement in diesel scr. In *16. Internationales Stuttgarter Symposium*, pages 49–58. Springer, 2016.

[44] Yujun Liao, Panayotis Dimopoulos Eggenschwiler, Alexander Spiteri, Lorenzo Nocivelli, Gianluca Montenegro, and Konstantinos Boulouchos. Fluid dynamic comparison of adblue injectors for scr applications. *SAE International Journal of Engines*, 8(2015-24-2502):2303–2311, 2015.

[45] Yujun Liao, Roman Furrer, Panayotis Dimopoulos Eggenschwiler, and Konstantinos Boulouchos. Experimental investigation of the heat transfer characteristics of spray/wall interaction in diesel selective catalytic reduction systems. *Fuel*, 190:163–173, 2017.

[46] Yujun Liao, L Nocivelli, P Dimopoulos Eggenschwiler, and A Spiteri. Experimental investigation of urea-water sprays in selective catalytic reduction (scr) systems. In *15. Internationales Stuttgarter Symposium*, pages 953–966. Springer, 2015.

[47] Tommaso Lucchini, Augusto Della Torre, Gianluca D'Errico, Gianluca Montenegro, Marco Fiocco, and Amin Maghbouli. Automatic mesh generation for cfd simulations of direct-injection engines. *SAE Technical Paper*, SAE International, n. 2015-01-0376, 2015.

[48] Andreas Lundström, Björn Waldheim, Henrik Ström, and Björn Westerberg. Modelling of urea gas phase thermolysis and theoretical details on urea evaporation. *Proceedings of the Institution of Mechanical Engineers, Part D: Journal of Automobile Engineering*, 225(10):1392–1398, 2011.

[49] N. Lévy, S. Amara, and J.-C. Champoussin. Simulation of a diesel jet assumed fully atomized at the nozzle exit. *SAE Technical Paper*, SAE International, n. 981067, 1998.

[50] Amin Maghbouli, Tommaso Lucchini, Gianluca D'Errico, and Angelo Onorati. Effects of grid alignment on modeling the spray and mixing process in direct injection diesel engines under non-reacting operating conditions. *Applied Thermal Engineering*, 91:901–912, 2015.

[51] Samuel L Manzello and Jiann C Yang. An experimental study of a water droplet impinging on a liquid surface. *Experiments in fluids*, 32(5):580–589, 2002.

[52] L Martinelli, RD Reitz, and FV Bracco. Comparison of computed and measured dense spray jets. In *Ninth International Colloquium on Dynamics of Explosions and Reactive Systems (ICDERS), Poitiers, France, July*, pages 3–8, 1983.

[53] Alessandro Montanaro, Luigi Allocca, Michela Costa, and Ugo Sorge. Assessment of a 3d cfd model for gdi spray impact against wall through experiments based on different optical techniques. *International Journal of Multiphase Flow*, 84:204–216, 2016.

[54] Antonio LN Moreira, Joao Carvalho, and Miguel RO Panao. An experimental methodology to quantify the spray cooling event at intermittent spray impact. *International Journal of Heat and Fluid Flow*, 28(2):191–202, 2007.

[55] RA Mugele and HD Evans. Droplet size distribution in sprays. *Industrial & Engineering Chemistry*, 43(6):1317–1324, 1951.

[56] CHR Mundo, M Sommerfeld, and C Tropea. Droplet-wall collisions: experimental studies of the deformation and breakup process. *International journal of multiphase flow*, 21(2):151–173, 1995.

[57] SNA Musa, M Saito, T Furuhata, and M Arai. Evaporation characteristics of a single aqueous urea solution droplet. *ICLASS-2006, Kyoto, Paper ID ICLASS06-195*, 2, 2006.

[58] Makoto Nagaoka, Hiromitsu Kawazoe, and Naomi Nomura. Modeling fuel spray impingement on a hot wall for gasoline engines. *SAE Technical Paper*, SAE International, n. 940525, 1994.

[59] Lorenzo Nocivelli, Gianluca Montenegro, Yujun Liao, Panayotis Dimopoulos Eggenschwiler, John Campbell, and Nicola Rapetto. Modeling of aqueous urea solution injection with characterization of spray-wall cooling effect and risk of onset of wall wetting. *Energy Procedia*, 82:38–44, 2015.

[60] Lorenzo Nocivelli, Gianluca Montenegro, Angelo Onorati, Francesco Curto, Panayotis Dimopoulos Eggenschwiler, Yujun Liao, and Alexander Vogel. Quantitative analysis of low pressure-driven spray mass distribution and liquid entrainment for scr application through a mechanical patternator. *SAE Technical Paper*, SAE International, n. 2017-01-0965, 2017.

[61] Isabella Nova and Enrico Tronconi. *Urea-SCR technology for deNOx after treatment of diesel exhausts*. Springer, 2014.

[62] Angelo Onorati. Internal combustion engines (polimi lecture notes). 2015. Accessed: 2015.

[63] Peter John O'Rourke. Collective drop effects on vaporizing liquid sprays. Technical report, Los Alamos National Lab., NM (USA), 1981.

[64] Steven A Orszag, Victor Yakhot, William S Flannery, Ferit Boysan, Dipankar Choudhury, Joseph Maruzewski, and Bart Patel. Renormalization group modeling and turbulence simulations. *Near-wall turbulent flows*, pages 1031–1046, 1993.

[65] Miguel R Oliveira Panão, António LN Moreira, and Diamantino FG Durão. Effect of a cross-flow on spray impingement with port fuel injection systems for hcci engines. *Fuel*, 106:249–257, 2013.

[66] MRO Panão and ALN Moreira. Thermo-and fluid dynamics characterization of spray cooling with pulsed sprays. *Experimental Thermal and Fluid Science*, 30(2):79–96, 2005.

[67] Kyoungwoo Park, Chol-Ho Hong, Sedoo Oh, and Seongjoon Moon. Numerical prediction on the influence of mixer on the performance of urea-scr system. *WASET Int. J. of Mech., Aero., Industrial and Mechatronics Eng*, 8(5), 2014.

[68] M Pilch and CA Erdman. Use of breakup time data and velocity history data to predict the maximum size of stable fragments for acceleration-induced breakup of a liquid drop. *International journal of multiphase flow*, 13(6):741–757, 1987.

[69] T J Poinsot and SK Lelef. Boundary conditions for direct simulations of compressible viscous flows. *Journal of computational physics*, 101(1):104–129, 1992.

[70] WE Ranz and WR Marshall. Evaporation from drops. *Chemical Engineering Progress*, 48(3):141446, 1952.

[71] RD Reitz and FV Bracco. Mechanism of atomization of a liquid jet. *The Physics of Fluids*, 25(10):1730–1742, 1982.

[72] Rolf D. Reitz and F. V. Bracco. On the dependence of spray angle and other spray parameters on nozzle design and operating conditions. *SAE Technical Paper*, SAE International, n. 790494, 1979.

[73] Rolf D. Reitz and R. Diwakar. Effect of drop breakup on fuel sprays. *SAE Technical Paper*, SAE International, n. 860469, 1986.

[74] ROLFD REITZ et al. Modeling atomization processes in high-pressure vaporizing sprays. *Atomisation and Spray Technology*, 3(4):309–337, 1987.

[75] W. Reuter and F. Terres. Appropriate nox aftertreatment solutions for different mar- kets and applications. 20th aachen colloquium automobile and engine technology. 2011.

[76] Paul Rosin. The laws governing the fineness of powdered coal. *J. Inst. Fuel.*, 7:29–36, 1933.

[77] DT Ryddner and MF Trujillo. A fully resolved uws droplet simulation. In *ILASS-Americas 24th Annual Conference on Liquid Atomization and Spray Systems*, 2012.

[78] Mattia Scala and Elia Siniscalchi. Diesel exhaust fluid injection at low pressure for scr denox after treatment systems : Cfd modeling and validation. Master's thesis, Politecnico di Milano, 2015.

[79] Peter M Schaber, James Colson, Steven Higgins, Daniel Thielen, Bill Anspach, and Jonathan Brauer. Thermal decomposition (pyrolysis) of urea in an open reaction vessel. *Thermochimica acta*, 424(1):131–142, 2004.

[80] Rudolf J Schick. Spray technology reference guide: Understanding drop size. *Spraying Systems Co. Bulletin B*, 459:8–16, 2008.

[81] T-H Shih, WW Liou, A Shabbir, Z Yang, and J Zhu. A new k-epsilon eddy viscosity model for high reynolds number turbulent flows: Model development and validation. 1994.

[82] William A Sirignano. Fuel droplet vaporization and spray combustion theory. *Progress in Energy and Combustion Science*, 9(4):291–322, 1983.

[83] Alexander Spiteri. *Experimental investigation of the injection process in urea-SCR deNOx exhaust gas aftertreatment systems*. PhD thesis, ETH Zürich, 2016.

[84] Alexander Spiteri and Panayotis Dimopoulos Eggenschwiler. Experimental fluid dynamic investigation of urea–water sprays for diesel selective catalytic reduction–denox applications. *Industrial & Engineering Chemistry Research*, 53(8):3047–3055, 2014.

[85] Alexander Spiteri, P Dimopoulos Eggenschwiler, and Y Liao. Comparison of pressure and air-assisted atomizers for urea-scr injection in diesel engine exhaust. In *14. Internationales Stuttgarter Symposium*, pages 911–921. Springer, 2014.

[86] Alexander Spiteri, Panayotis Dimopoulos Eggenschwiler, Yujun Liao, Graham Wigley, Katarzyna A Michalow-Mauke, Martin Elsener, Oliver Kröcher, and Konstantinos Boulouchos. Comparative analysis on the performance of pressure and air-assisted urea injection for selective catalytic reduction of nox. *Fuel*, 161:269–277, 2015.

[87] Donald W. Stanton and Christopher J. Rutland. Modeling fuel film formation and wall interaction in diesel engines. *SAE Technical Paper*, SAE International, n. 960628, 1996.

[88] Gunnar Stiesch. *Modeling engine spray and combustion processes*. Springer Science & Business Media, 2013.

[89] CD Stow and MG Hadfield. An experimental investigation of fluid flow resulting from the impact of a water drop with an unyielding dry surface. In *Proceedings of the Royal Society of London A: Mathematical, Physical and Engineering Sciences*, volume 373, pages 419–441. The Royal Society, 1981.

[90] PA Strakey, DG Talley, and JJ Hutt. Mixing characteristics of coaxial injectors at high gas/liquid momentum ratios. *Journal of Propulsion and Power*, 17(2):402–410, 2001.

[91] Henrik Ström, Andreas Lundström, and Bengt Andersson. Choice of urea-spray models in cfd simulations of urea-scr systems. *Chemical Engineering Journal*, 150(1):69–82, 2009.

[92] T. F. Su, M. A. Patterson, Rolf D. Reitz, and P. V. Farrell. Experimental and numerical studies of high pressure multiple injection sprays. *SAE Technical Paper*, SAE International, n. 960861, 1996.

[93] Michel Trapletti and Andrea Pati. Modellazione multidimensionale dell'evoluzione degli spray per motori ad iniezione diretta e ad accensione comandata. MSc Thesis, Politecnico di Milano, 2015.

[94] Nic van Vuuren, Gabriele Brizi, Giacomo Buitoni, Lucio Postrioti, and Carmine Ungaro. Experimental analysis of the urea-water solution temperature effect on the spray characteristics in scr systems. *SAE Technical Paper*, SAE International, n. 2015-24-2500, 2015.

[95] Achinta Varna, Konstantinos Boulouchos, Alexander Spiteri, Panayotis Dimopoulos Eggenschwiler, and Yuri M Wright. Numerical modelling and experimental characterization of a pressure-assisted multi-stream injector for scr exhaust gas after-treatment. *SAE International Journal of Engines*, 7(2014-01-2822):2012–2021, 2014.

[96] Achinta Varna, Alexander C Spiteri, Yuri M Wright, Panayotis Dimopoulos Eggenschwiler, and Konstantinos Boulouchos. Experimental and numerical assessment of impingement and mixing of urea–water sprays for nitric oxide reduction in diesel exhaust. *Applied Energy*, 157:824–837, 2015.

[97] Henk Kaarle Versteeg and Weeratunge Malalasekera. *An introduction to computational fluid dynamics: the finite volume method*. Pearson Education, 2007.

[98] Alexander Vogel. Experimental investigation of uws spray properties prior to wall impingement. Master's thesis, ETH Zürich, 2016.

[99] LHJ Wachters and NAJ Westerling. The heat transfer from a hot wall to impinging water drops in the spheroidal state. *Chemical Engineering Science*, 21(11):1047–1056, 1966.

[100] A Walker. Current and future trends in catalyst-based emission controi system design. *Presentation at SAE Heavy-Duty Diesel Emission Control Symposium*, Gothenburg, 2012.

[101] DM Wang and AP Watkins. Numerical modeling of diesel spray wall impaction phenomena. *International Journal of Heat and Fluid Flow*, 14(3):301–312, 1993.

[102] Lei Wang, Bengt Sundén, Andreas Borg, and Hans Abrahamsson. Heat transfer characteristics of an impinging jet in crossflow. *Journal of Heat Transfer*, 133(12):122202, 2011.

[103] Tae Joong Wang, Seung Wook Baek, Seung Yeol Lee, Dae Hwan Kang, and Gwon Koo Yeo. Experimental investigation on evaporation of urea-water-solution droplet for scr applications. *AIChE Journal*, 55(12):3267–3276, 2009.

[104] Graham Wigley. Introduction to light scattering and optical diagnostics for the analysis of air flows and fuel sprays: Lessons at loughborough university. Accessed: 2015.

[105] Graham Wigley, Graham K Hargrave, and John Heath. A high power, high resolution lda/pda system applied to gasoline direct injection sprays. *Particle & particle systems characterization*, 16(1):11–19, 1999.

[106] Gareth Williams. Combustion theory. Addison-Wesley, 1985.

[107] Norbert Wruck. *Transientes Sieden von Tropfen beim Wandaufprall*. Shaker, 1998.

[108] N Yadav Indrajit. Adblue: An overview. *International Journal of Environmental Sciences*, 2(2), 2010.

[109] Carl L Yaws. *Chemical properties handbook*. McGraw-Hill,, 1999.

[110] Guanyu Zheng, Adam Fila, Adam Kotrba, and Ryan Floyd. Investigation of urea deposits in urea scr systems for medium and heavy duty trucks. *SAE Technical Paper*, SAE International, n. 2010-01-1941, 2010.

Appendices

APPENDIX $\mathcal{A}$

Thermophysical properties of fluids

Experimental campaign

The properties of liquid water in the experimental campaign are based on tabulated data collected by [10]. Linear interpolation has been used to calculate the values corresponding to temperatures included in the reported range.

Temperature	T	K	273.15	285	290	295
Density	ρ	kg/m^3	1000	1000	999	998
Viscosity	μ	$10^{-6}Ns/m^2$	1750	1225	1080	959
Surface tension	σ	$10^{-3}N/m$	75.5	74.3	73.7	72.7
Specific heat	c_p	kJ/kgK	4.217	4.189	4.184	4.181

Table A.1: *Thermophysical properties of liquid distilled water.*

Appendix A. Thermophysical properties of fluids

According to [83] the reference values for AdBlue® are extracted from [108] and [17] and reported in Tab. A.2

Temperature	T	K	298.15	308.15	313.15	318.15	323.15	328.15
Viscosity	μ	$10^{-6}Ns/m^2$	1400	1050	950	875	805	740
Density	ρ	kg/m^3	1100.01-0.428345·T-1.62819·10^{-3}·T^2					
Surface tension	σ	$10^{-3}N/m$	as for water, Tab. A.1					
Specific heat	c_p	kJ/kgK	8·10^{-3}·T^2+2.7·T+3434.5					

Table A.2: *Thermophysical properties of AdBlue®.*

Numerical simulation

The gaseous phase thermophysical properties are calculated according to different approaches, which are available for the open-source finite volume CFD platform OpenFOAM®. This section provides a short description of the models employed in every simulation.

The dynamic viscosity of a gaseous component is calculated as a function of temperature according to the Sutherland model (A.1)

$$\mu = \frac{A_s \sqrt{T}}{1 + T_s/T} \tag{A.1}$$

where A_s and T_s are the Sutherland coefficient and temperature.

The thermodynamic models used to evaluate the specific heat c_p and the derived properties are functions of temperature through a set of coefficients based on the JANAF tables of thermodynamics in the version provided by [32]. Two sets of coefficients are specified, the first one is valid for temperatures above a common temperature T_c and the second set elsewhere. The values are bounded by a minimum and a maximum temperature. The coefficients a_i defining the dependence of c_p from the temperature are reported in (A.2) and are integrated by two constants, a_5 and a_6 used to evaluate h and s respectively.

$$p_i = \mathcal{R}\left(\left(\left(\left(a_4 T + a_3\right) T + a_2\right) T + a_1\right) T + a_0\right) \tag{A.2}$$

Perfect gas model (A.3) is used as equation of state.

$$\rho = \frac{1}{\mathcal{R}T}\, p \tag{A.3}$$

Ideal mixture of perfect gases is used to describe the composition of the gaseous phase.

The liquid phase is described assuming ideal mixture behavior and Rapid Mixing approach [26, 82]. The ther-

mophysical properties of the pure components are described according to the $NSRDS$ tables [22]. A new set of function is implemented to describe the liquid Urea. The function proposed by [13] is implemented to describe the vapor pressure (A.4) as a function of the liquid temperature.

$$p_v\left(T\right) = \exp 12.06 - 3992/T \tag{A.4}$$

Urea density ρ, latent heat of evaporation h_l, specific heat c_p, dynamic viscosity μ and thermal conductivity k are described according to the formulation and the tabulated data by [109].

APPENDIX B

CFD details and setup

Injection in quiescent air

The simulation of the injection through 6H and 3H is realized on the same computational domain, shown in Fig. B.1.

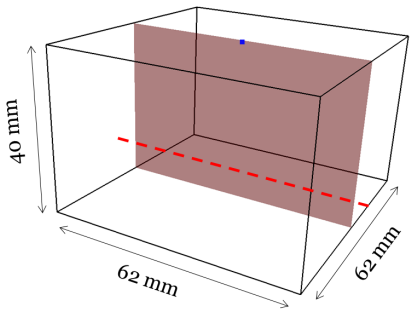

Figure B.1: *Numerical simulation system bounding box.*

Mesh characteristics The box is discretized with hexahedral cells with increasing refinement.

$coarse$ **test case** The basis, named $coarse$ test case involves 9920 cubic cells, with a constant cell size of 2 mm. The symmetry plane face surface is reported in Fig. B.2.

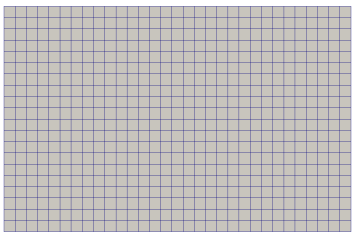

Figure B.2: $coarse$ *mesh.*

mid **test case** One cubic refinement level is applied to the entire domain to generate the mid test case, which involves 78080 cells with a constant cell size 1 mm, as shown in Fig. B.3.

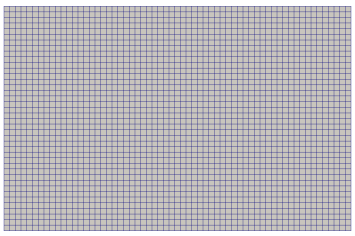

Figure B.3: mid *mesh.*

$fine$ **test case** A further cubic refinement level is applied to the spray path region within a hexagonal base cone, with a 44° aperture. The mesh is defined by 135142 hexahedra and 2025 polyhedra to join the cells with different refinement level. The spray zone cells have a cell size of 0.5 mm, as shown in Fig. B.4. The refinement region includes the whole 6H and 3H sprays.

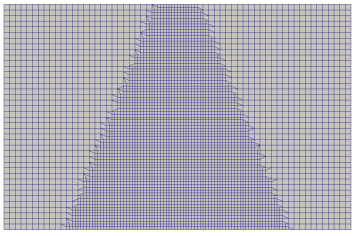

Figure B.4: $fine$ *mesh.*

The larger mesh used to evaluate the effect of the wave-transmissive boundary conditions in Sec. 3.1.3 is based on the $coarse$ test case, extending the domain boundaries (Fig. B.5-a) with 4 mm size cubic cells. The resulting grid is identical to Fig. B.2 in the spray sampling region, and involves a total count of 464850 hexahedra and 3900 polyhedra cells, as shown in Fig. B.5-b.

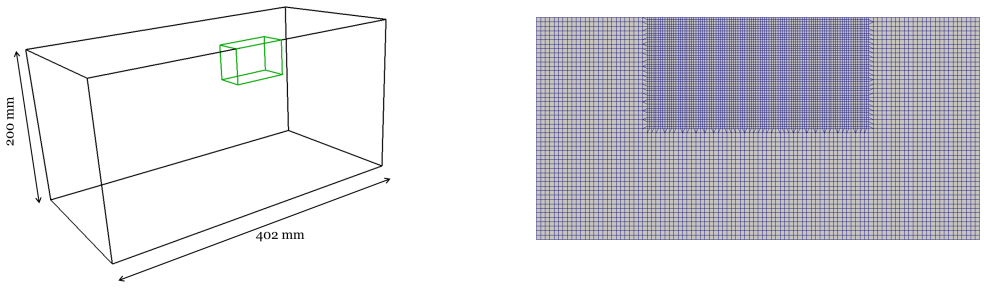

(a) **(b)**

Figure B.5: *Large mesh test case.*

Injector modeling The proposed injection strategy, shared among the three measured injection configurations: 6H-water, 6H-adblue and 3H-water is reported in Tab. B.1.

Injector type	Cone Nozzle injector
Diameter specification	Direct assignment (d_{drop} Rosin-Rammler pdf)
Parcel velocity	Uniform direct assignment
Parcel discretization	Constant number of droplet per parcel
Injection law	Constant profile
Collision model	$none$
Heat transfer model	Ranz Marshall [70]
Mass transfer model	Boiling corrected evaporation
Breakup model	Reitz Diwakar [73]

Table B.1: *Injection and spray submodel summary.*

The injector specification defined by a conical nozzle geometry involves the assignment of a drop size probability function based on the Rosin-Rammler formulation, of a drop velocity and a direction based on a spray cone angle β and a jet deviation angle γ. Tab. B.2 reports the resulting parameters for the single cone of each injector.

	6H-water	6H-AdBlue®	3H-water
RR - scale parameter δ $[\mu m]$	42.11	41.45	38.90
RR - shape parameter n $[-]$	1.406	1.605	1.578
Cone opening angle β $[°]$	36	36	9
Cone deviation angle γ $[°]$	0	0	11
Parcel velocity $[m/s]$	27.4	27.4	32.0
Parcels per second $[1/s]$	2.4 10^6	2.4 10^6	2.2 10^6
Droplets per parcel $[-]$	2.93	3.8	5.61

Table B.2: *Single hole injector model definition.*

The symmetry plane crosses 2 injector holes, halving the mass injected. The parcels hitting the symmetry plane surface, are reflected flipping the normal direction of the trajectory.

Spray in cross-flow

Channel geometry summary Tab. B.3 reports the relation between the traverse location and its horizontal distance from the nozzle location for the characterization of 6H through Phase Doppler anemometry described in Sec. 3.2. The sampling plane is set 60 mm below the the injector location.

Tab. B.4 summarizes the relative and absolute traverse location in the Phase Doppler Anemometry campaign of

traverse	x	distance
$[\#]$	$[mm]$	$[mm]$
0	-20.0	30.35
1	-15.0	35.35
2	-10.0	40.35
3	-5.0	45.35
4	0.0	50.35
5	5.0	55.35
6	10.0	60.35
7	15.0	65.35
8	20.0	70.35
9	25.0	75.35
10	30.0	80.35
11	35.0	85.35
12	40.0	90.35
13	45.0	95.35
14	50.0	100.35
15	55.0	105.35
16	60.0	110.35
17	63.0	113.35

Table B.3: *6H - Measurement reference system relation with the distance from the injector.*

3H. The sampling plane is set 79 mm below the the injector location.

The computational grid employed in the simulation of the spray in cross flow involves a simplification of the test-rig

traverse	x	distance
$[\#]$	$[mm]$	$[mm]$
0	20.0	86.29
1	24.0	90.29
2	28.0	94.29
3	32.0	98.29
4	36.0	102.29
5	40.0	106.29
6	44.0	110.29
7	48.0	114.29

Table B.4: *3H - Measurement reference system relation with the distance from the injector.*

injection chamber, defined by a 80×80 square section duct with the addition of an inclined square channel representing the injectors seat. The different nozzle mount location requires the modification of the system boundary from 6H and 3H. The meshes are reported in Fig. B.6. The simulation domain is cut on the vertical plane corresponding to the channel axis, in accordance to the transversal symmetry of the duct and the injector, to reduce the computational effort.

The hex-dominant grids are generated starting from a structured mesh involving cubic cells with constant size equal

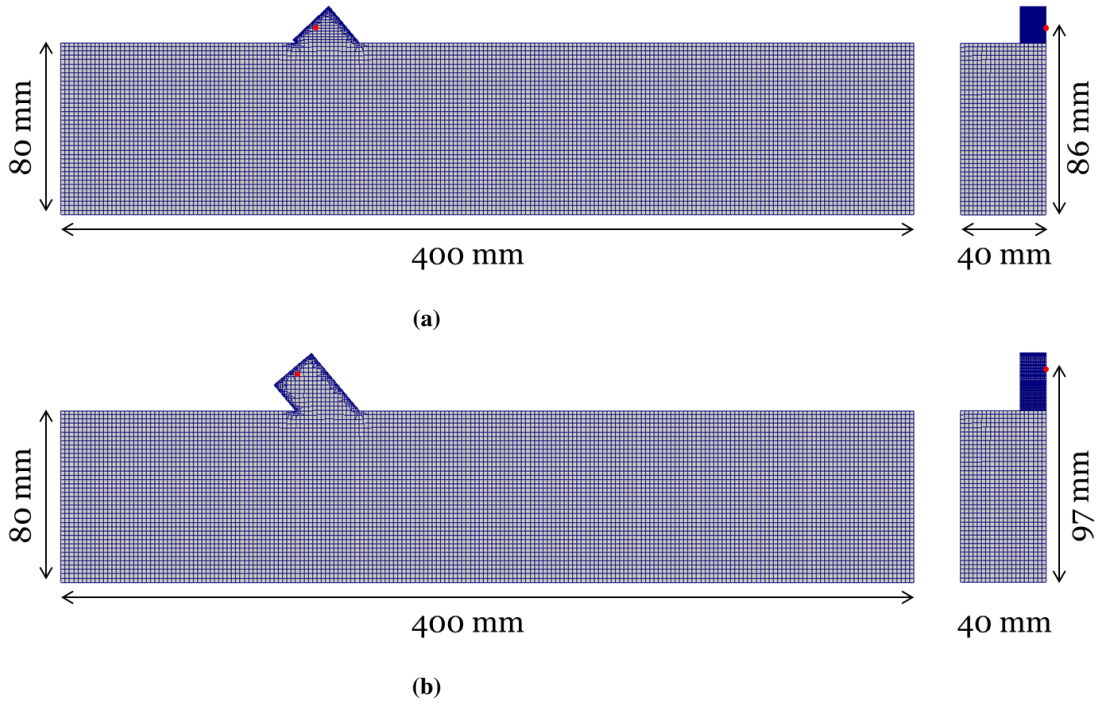

Figure B.6: *Injection chamber computational grid for 6H (a) and 3H (b). The injector location is highlighted by the red dot.*

to 2 mm. The injector channels are generated refining and adapting the grid to the inclined geometry through the use of prisms and polyhedra with $snappyHexMesh$ tool [33]. The resulting 6H grid involves 164464 hexahedra, 1769 prisms, and 1512 polyhedra, with a maximum skewness equal to 1.97 rad, a maximum non-orthogonality equal to

56.1° and a minimum cell volume of $3.210^{-12}\ m^3$. The simulation of 3H is realized on 164120 hexahedra, 2496 prisms and 1704 polyhedra, with a maximum skewness of 1.18 rad, a maximum non-orthogonality equal to 40.3° and a minimum cell volume of $7.410^{-12}\ m^3$.

Impinging fluid mass quantification

The assessment of the mechanical patternator intrusiveness in the flow field is obtained simulating the whole test-rig channel substituting the channel bottom wall with the instrument. The resulting grids are labeled $standard$ and $patternator$ to represent the original channel geometry and the one modified by the probe insertion. The mesh are generated from a base mesh defined by cubic cells with edge size equal to 4 mm, refining and adapting the grid to the solid features with the OpenFOAM® tool $snappyHexMesh$ [33]. Fig. B.7-a shows the $standard$ channel mesh which counts ∼986k cells (hex:726453, prisms:42064, tet wedges: 2964, poly:214291) with a maximum skewness of 4.9 rad and a maximum non-orthogonality equal to 64.9°. The $patternator$ mesh, visible in Fig. B.7-b is composed of 796801 hexahedra, 74114 prisms, 594 tetrahedral wedges and 189242 polyhedra (1.06M cells total). The mesh quality in terms of skewness ans non-orthogonality is consistent with the $standard$ case.

The spray simulations involving the real injection chamber geometry are carried out on a computational domain ex-

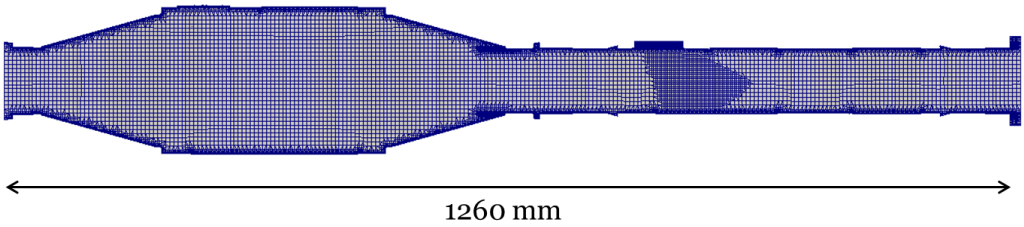

(a)

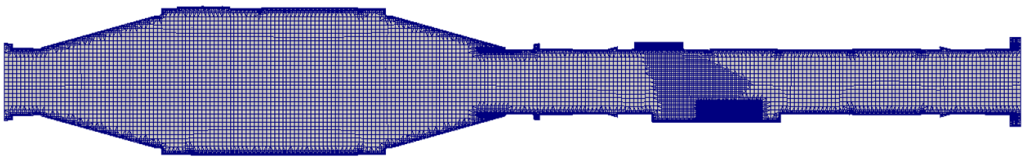

(b)

Figure B.7: *Lateral view of the meshes used to simulate the flow field in the test-bench.* $standard$ *(a) and* $patternator$ *(b).*

tracted from the patternation section of the complete mesh, refined in the near nozzle region and the probe geometry. The resulting mesh are reported in Fig. B.8. The grids are generated with the same approach reported for the whole test-rig one, and are composed of 165k cells for the $standard$ test case and of 422k cells for the $patternator$ one. The skewness and the non-orthogonality are consistent with the flow field meshes.

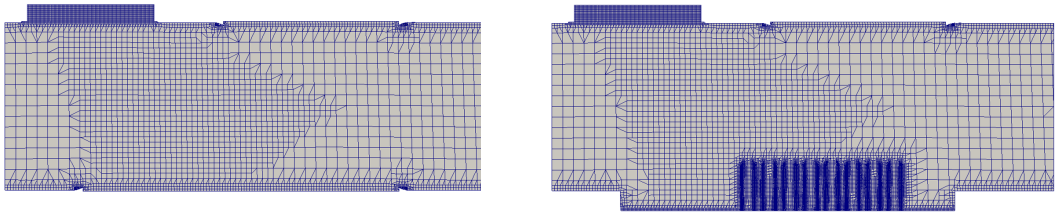

(a) **(b)**

Figure B.8: *Lateral view of the meshes used to simulate the spray development in the test-bench. standard (a) and patternator (b).*

SCR spray heat-transfer

The simulation of the modified test-rig presented in Chapter 5 presents a multi-region case, where a 0.3 mm thick solid plate is introduced in the injection chamber. The basis of the mesh for the six hole injector 6H is reported in Fig. B.6-a. The solid plate is set with the front surface 14 mm above the bottom plate, and is meshed with 8 layers along the thickness and extracted from the gaseous domain. A progressive 3D hex-based grid refinement is applied to the neighborhood of the solid mesh, to reduce the aspect ratio and better represent the gas flow splitting. The final mesh, is reported in Fig. B.9.

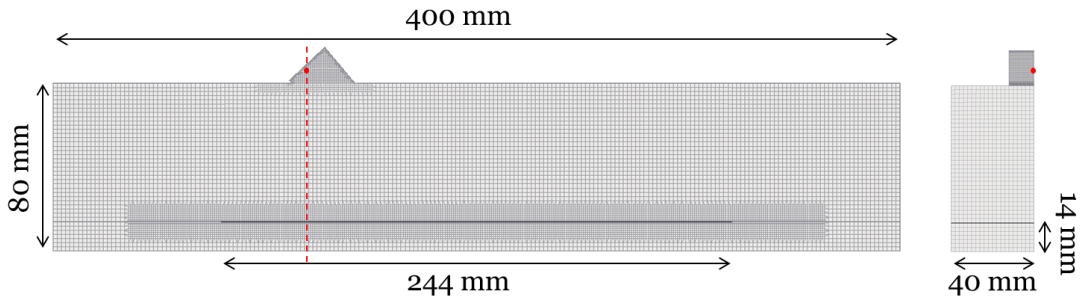

Figure B.9: *6H nozzle: mesh for the spray-wall interaction campaign.*

The solid is meshed with a structured grid composed of 78080 hexahedra with a constant thickness of 0.0375 mm and single face interface area of 1 mm^2. The gaseous domain is discretized with 393697 hexahedra, 1793 prisms and 9296 polyhedra (for a total count of 404786 cells) leading to a maximum skewness of 2.0 rad and a maximum non-orthogonality of 56.1°.